

**NOVEL LIGHT-EMITTING DEVICES OF
SEMICONDUCTOR QUANTUM DOTS AND
CONJUGATED POLYMER
NANOPARTICLES**

A DISSERTATION SUBMITTED TO
THE GRADUATE SCHOOL OF ENGINEERING AND SCIENCE
OF BILKENT UNIVERSITY
IN PARTIAL FULFILLMENT OF THE REQUIREMENTS FOR
THE DEGREE OF
DOCTOR OF PHILOSOPHY
IN
ELECTRICAL AND ELECTRONICS ENGINEERING

By
Talha Erdem
July 2016

NOVEL LIGHT-EMITTING DEVICES OF SEMICONDUCTOR
QUANTUM DOTS AND CONJUGATED POLYMER NANOPARTI-
CLES

By Talha Erdem

July 2016

We certify that we have read this dissertation and that in our opinion it is fully adequate, in scope and in quality, as a dissertation for the degree of Doctor of Philosophy.

Hilmi Volkan Demir(Advisor)

Vakur Ertürk

Dönüş Tuncel

Alper Kiraz

Cleva Owyang Gülgün

Approved for the Graduate School of Engineering and Science:

Levent Onural
Director of the Graduate School

ABSTRACT

NOVEL LIGHT-EMITTING DEVICES OF SEMICONDUCTOR QUANTUM DOTS AND CONJUGATED POLYMER NANOPARTICLES

Talha Erdem

Ph.D. in Electrical and Electronics Engineering

Advisor: Hilmi Volkan Demir

July 2016

Starting with the modern times, lighting has become an essential part of our lives. Today, its share of the total energy consumption reaching 15% should not surprise us. This share further increases when the energy demand for display backlighting is taken into account. Therefore, increasing the efficiency of the lighting sources is of significant importance for decreasing the carbon footprint for a sustainable environment. At this point, light-emitting diodes (LEDs) step forward as the most important candidate for revolutionizing the existing lighting systems; however, the current conventional technologies, which typically employ rare-earth ion based broad-band emitters, are plagued with low photometric efficiency, lack of light quality, and incapability of the spectrum design for application-specific performance.

As a remedy to these problems, in this thesis we study light-emitting diodes of quantum dots that are efficient narrow-band emitters as opposed to phosphors. These colloidal quantum dots allow for the achievement of the light source performance specific to each application. By employing this strength, we first present our design of quantum dot integrated LED display backlight for reducing the adverse effects of the displays on the human biological rhythm while maximizing the color definition. Here we also addressed the need for light sources exhibiting polarization anisotropy for display backlights by hybridizing self-assembled magnetic nanowires and quantum dots. To solve the emission stability problem of the quantum dots in solid-films, we demonstrated the incorporation of the quantum dots within crystalline matrices that act as a barrier against oxygen and humidity and substantially increase their emission stability. Another important strength of this technique has been the preservation of the dispersion quantum efficiencies of the quantum dots in powder form and in solid-films. By employing these material systems, we designed and successfully demonstrated a warm white LED exhibiting successful color rendition capability and large spectral overlap with

the human eye sensitivity function. We also showed that embedding quantum dots into crystalline matrices offers a robust platform to study the excitonic and plasmonic interactions, both of which we utilized for increasing the efficiencies of the quantum dots in crystalline matrices. To meet the need for non-toxic color converter enabling color tuning, we also employed conjugated polymer nanoparticles and studied their near-field interaction with epitaxially grown quantum well nanopillars to boost their emission intensity. We believe that the materials and light sources that we presented in this thesis will enable to reach the targets for realizing high-efficiency but also high-quality light sources for general lighting and displays.

Keywords: White light-emitting diodes (WLED), nanocrystals, quantum dots, conjugated polymer nanoparticles, macrocrystals, excitonics, plasmonics, color science and photometry.

ÖZET

YARI İLETKEN KÜANTUM NOKTACIKLARI VE KONJÜGE POLİMER NANOPARÇACIKLARIN YENİLİKÇİ IŞIK YAYAN AYGITLARI

Talha Erdem

Elektrik ve Elektronik Mühendisliği, Doktora

Tez Danışmanı: Hilmi Volkan Demir

Temmuz 2016

Modern dönemlerde aydınlatma uygulamaları hayat tarzımızın önemli bir parçası haline gelmiştir. Bu sebeple günümüzde aydınlatmanın %15'lere ulaşan ve ekran teknolojileri düşünüldüğünde daha da yükselecek enerji tüketimindeki payı bizi şaşırtmamalıdır. Bu yüzden sürdürülebilir bir çevre için karbon salınımını azaltma noktasında ışık kaynaklarının verimliliğinin artırılması oldukça önemlidir. Bu açıdan ışık yayan diyotlar (LED) var olan aydınlatma sistemlerinin değiştirilmesi için en önemli aday olarak öne çıkmaktadır. Ancak günümüzde yaygın şekilde kullanılan nadir toprak iyonları tabanlı ışığıcı teknolojileri düşük fotometrik verimlilik, düşük ışık kalitesi ve uygulamaya özgü spektrum tasarımına izin vermeyen yapısı nedeniyle halen sorunludur.

Bu sorunlara çözüm olarak bu tez kapsamında fosforların aksine oldukça dar ışımaya bandına sahip kuantum noktalarının tümleştirildiği LED'ler üzerinde yürüttüğümüz çalışmaları sunuyoruz. Bu kuantum noktaları, uygulamaya özgü önemli iyileştirmelere izin vermektedirler. Bu tez çalışmaları kapsamında kuantum noktalarının bu avantajlarından yararlanılarak ekranların insanların biyolojik döngülerine olan olumsuz etkilerini en aza indirecek ve aynı zamanda geniş bir renk gamı da sunacak ekran arka aydınlatması tasarımı sunulmuştur. Bunun dışında, ekranlarda ihtiyaç duyulan polarize ışık kaynaklarının elde edilmesi amacıyla, kendi kendine konumlanan manyetik nanotellerle kuantum noktaları melezlenmiş ve polarizasyon anizotropisi yüksek ışığııcılar elde edilmiştir. Kuantum noktalarının ışımaya kararlılığı sorununu çözmek içinse, onların kristal matrisler içerisine tümleştirilmeleri ve bu kristal matrislerinin oksijen ve nemin kuantum noktalarına ulaşmasında bir engel oluşturduğu gösterilmiştir. Bu yöntemin getirdiği diğer önemli kazanç ise, kuantum noktalarının toz ve katı film halinde çözelti içerisindeki verimliliklerini koruyor olmalarıdır. Bu malzemelerle yüksek renk dönüşümü indisine sahip ve

insan gözünün hassasiyet fonksiyonuyla uyumlu ışma spektrumu olan ılık beyaz LED tasarımı ve gösterimi yapılmıştır. Bunun yanında kuantum noktacık gömülü kristal matrislerinin ekzitonik ve plazmonik etkileşim çalışmaları için elverişli bir ortam oluşturduğu gösterilmiş ve bu etkileşimler kuantum noktacıklarının verimliliklerini daha da artırmak için kullanılmıştır. Ayrıca spektrumu ayarlanabilir toksik olmayan renk dönüştürücülerin geliştirilmesi amacıyla, bu tez kapsamında konjüge polimer nanoparçacıklarıyla da çalışılmıştır. Bu malzemelerin kuantum kuyusu nanosütunlarıyla aralarındaki yakın alan etkileşimleri ışma şiddetlerinin artırılması amacıyla detaylı şekilde incelenmiştir. İnanıyoruz ki; bu çalışmalarımız kapsamında geliştirdiğimiz malzemeler ve ışık kaynakları verimli ve yüksek renk kalitesine sahip genel ve ekran arka aydınlatmasının sağlanması hedeflerine ulaşılmasında katkı sağlayacaktır.

Anahtar sözcükler: Beyaz ışık yayan diyotlar, nanokristaller, kuantum noktacıkları, konjüge polimer nanoparçacıklar, makrokristaller, ekzitonik, plazmonik, renk bilimi ve fotometri.

Acknowledgement

”Bihî, the word that adorns every other word . . .”

As one of the major milestones of my life, herewith I have finished my PhD with this thesis. During this period of my life, I have met a lot of people and I have learned a lot of things from them. I owe many thanks to all of them.

First, I would like to thank my supervisor Prof. Hilmi Volkan Demir. He helped and supported me in every part of my graduate study. We shared a lot of things together, and I have learned a lot of things from him. His guidance and supports have been invaluable for me. I would also like to thank Prof. Dönüş Tuncel, who has supported and helped me during my PhD as a part of our collaboration. In addition, I owe many thanks to Prof. Vakur Ertürk for his support during my PhD. Finally, I would like to thank Prof. Alper Kiraz and Prof. Cleve Ow-Yang for accepting to be in my thesis committee and came from Istanbul to Bilkent for my PhD defence.

Next of course comes my dear-wife and love Zeliha. She has been the most beautiful color of my life. I have always felt her support during this stressful period. In addition to sharing the unprofessional part of our lives, we have also shared our professional lives in Demir Group, which made everything even more brilliant. I cannot find the correct words to thank her enough for her support, presence, love . . .

At this point, I, of course, thank my family: My father and mother, for their supports and patience, and for many things that I cannot put into words. Also I owe many thanks to my brothers that have been with me whenever I need them. I would also like to thank my aunt and her husband, who have never stopped supporting me.

Moreover, I would like to thank Prof. Sedat Nizamoglu and Prof. Evren Mutlugün who have been good friends of mine in addition to being excellent scientists guiding me throughout my graduate study. Their friendship will never be forgotten. I would also like to thank all the past and present members of Demir Group: Ozgun Akyuz, Emre Unal, Emre Sari, Tuncay Ozel, Rohat Melik, Ilkem Ozge Ozel, Asli Yilmaz, Gulis Zengin, Neslihan Cicek, Refik Sina Toru, Can Uran, Cuneyt Eroglu, Onur Akin, Kazim Gurkan Polat, Mustafa Akin Sefunc,

Burak Guzelturk, Aydan Yeltik, Hatice Ertugrul, Sayim Gokyar, Veli Tayfun Kilic, Kivanc Gungor, Ahmet Fatih Cihan, Shahab Akhavan, Yusuf Kelestemur, Yasemin Coskun, Durmus Ugur Karatay, Ozan Yerli, Togay Amirahmadov, Prof. Nihan Kosku Perkgoz, Prof. Urartu Ozgur S. Seker, Pedro Ludwig Hernandez-Martinez, Olga Samarskaya, Vijay Kumar Sharma, Manoj Sharma, Murat Olutas, Savas Delikanli, Didem Dede, Akbar Alipour, Nima Taghipour, Onur Erdem, Mehmet Zafer Akgul, Berkay Bozok, Halil Akcali, Ibrahim Akcali, and Can Firat Usanmaz. It has been a privilege working with all these great people. In addition, I would also like to thank Dr. Marcus Adam and Dr. Nikolay Gaponik from TU Dreden for the excellent collaboration we had.

Finally, I would like to thank TUBITAK BIDEB and SPIE for the financial support.

Contents

1 Introduction.....	1
2 Scientific Background.....	5
2.1 Color Science and Photometry	5
2.2 Quantum Dot Nanophosphors for Lighting and Displays	26
2.3 Conjugated Polymer Nanoparticles	41
2.4 Macrocrystals of Quantum Dots	44
2.5 Nonradiative Energy Transfer	48
2.6 Plasmonics	51
3 Biological Rhythm Friendly Display Lighting with Nanocrystal Quantum Dots	58
3.1 Introduction	58
3.2. Computational Methodology	60
3.3 Results and Discussion	64
3.4 Summary	68
4 Polarization Anisotropy in Self-Assembled Magnetic Nanowire-Quantum Dot Hybrids	70
4.1 Introduction	70
4.2 Experimental Methodology	73

4.3 Results and Discussion	76
4.4 Summary	80
5 Macrocrystals of Quantum Dots for Quality Lighting	81
5.1 Introduction	81
5.2 Experimental Methodology	83
5.3 Results and Discussion	87
5.4 Summary	103
6 Macrocrystals of Nanocrystal Quantum Dots for Fluorescence Enhancement	105
6.1 Introduction	105
6.2 Experimental Methodology	110
6.3 Results and Discussion	113
6.4 Summary	124
7 Stable and Efficient Powders of Nanocrystal Quantum Dots for Color Enrichment	125
7.1 Introduction	125
7.2 Experimental Methodology	127
7.3 Results and Discussion	134
7.4 Summary	146
8 Excitonic Improvement of Colloidal Nanocrystal Emission in Salt Powder Matrix	147
8.1 Introduction	147
8.2. Experimental methods	149
8.3. Results and Discussion	152
8.4 Summary	161
9 Morphology-Dependent Nonradiative Energy Transfer from InGaN/GaN Quantum Well Nanopillars to Conjugated Polymer Nanoparticles.....	163
9.1 Introduction	164

9.2 Experimental Methodology	166
9.3 Results and Discussion	169
9.4 Summary	180
10 Conclusions	182
10.1 Contributions to scientific knowledge	182
10.2. Contributions to the literature	186
10.3 Challenges and future outlook	191
Bibliography.....	194

List of Figures

Figure 2.1. Illustration of the human eye structure along with a zoom-in to the photoreceptors in the retina [18].	7
Figure 2.2. Normalized spectral sensitivities of rods and cones (red, green, and blue). Reproduced with permission from Ref. [20]. © Cambridge University Press 2016.	8
Figure 2.3. Normalized eye sensitivity functions in scotopic (red curve), mesopic (dashed curves), and photopic (blue curve) vision regimes.	9
Figure 2.4. Spectral distribution of the circadian effect function introduced by Gall [35].	14
Figure 2.5. Spectral distribution of the melanopic eye sensitivity function by Enezi et al. [36].	15
Figure 2.6. Color matching functions used in all of the colorimetric calculations.	16
Figure 2.7. (x,y) chromaticity diagram. This color gamut is also known as CIE 1931 chromaticity diagram.	18
Figure 2.8. (u',v') chromaticity diagram. Reproduced with permission from Ref. [20] © Cambridge University Press 2016.	19

Figure 2.9. Illustration of (a) the full CIE $L^*a^*b^*$ chromaticity diagram and (b) a cross-section. Reproduced with permission from Ref. [42]. © Wiley International 2011.....	20
Figure 2.10. Photographs of vegetables and fruits taken with light sources having (a) good and (b) poor color rendition capabilities [44].....	21
Figure 2.11. Reflection spectra of the test color samples (TCS) used for calculating the color rendering index.	22
Figure 2.12. Schematic illustration of a core/shell nanocrystal QD (left) and the corresponding energy band diagram (right).....	28
Figure 2.13. (a) Emission and (b) absorption spectra of the CdSe QDs synthesized at Demir Group laboratories, red-shifting with increasing size.	30
Figure 2.14. Illustration of the setup used for CdTe QD synthesis. Courtesy of Halil Akcali.	33
Figure 2.15. Exemplary photograph showing nonpolar CdSe/CdZnSeS/ZnS QDs synthesized in Demir Group synthesis laboratory.....	34
Figure 2.16. CRI vs. LER relation at CCTs of 2500, 3000, and 3500 K. Reproduced with permission from Ref. [12]. © DeGruyter Publishing 2013.	36
Figure 2.17. CIE 1931 (x,y) chromaticity diagram indicating the NTSC color gamut (white triangle), and color coordinates of QDs having full-width at half-maximum values between 30 and 100 nm with peak emission wavelengths ranging from 460 to 700 nm (black lines). The blue numbers given around the perimeter of the chromaticity diagram are located at the color coordinates of the corresponding monochromatic light. Reproduced with permission from Ref. [12]. © DeGruyter Publishing 2013.....	40
Figure 2.18. Illustration of the conjugated polymer nanoparticle preparation using nano-precipitation, mini-emulsion, and self-assembly techniques. Reproduced with permission from Ref. [63]. © Royal Society of Chemistry 2013.	43

Figure 2.19. Summary of quantum dot nanocrystal (NC) incorporated macrocrystal preparation techniques for NCs in nonpolar organic solvents and in water.....	45
Figure 2.20. Illustration of Dexter-type nonradiative energy transfer.....	48
Figure 2.21. Illustration of Förster-type nonradiative energy transfer.....	50
Figure 2.22. Illustration of a simple geometry allowing for the creation of SPP.	53
Figure 2.23. Illustration of a spherical conducting nanoparticle subject to electric field and induced macroscopic polarization.....	55
Figure 3.1. National Television Standards Committee color gamut (dashed) along with the modified color gamut (line) used in this study. The white dashed regions correspond to allowable chromaticity points of individual color components to realize the targeted color gamut. The black dot in the middle shows the chromaticity point of the blackbody radiator at 9,000 K.....	61
Figure 3.2. (a) Illustration of the computation setup to evaluate the effectiveness of the light source in suppressing melatonin. Our approach is developed based on the three existing models by employing a multi-objective optimization technique. (b) Spectra of the YAG:Ce LED, QD-LED acquiring the targeted color gamut in Figure 3.1 (QD-LED ₁), and QD-LED reproducing the color gamut of the YAG:Ce LED (QD-LED ₂).....	64
Figure 3.3. (a) Circadian performance ($f_{circadian}$) of QD-LED backlit displays together with the percentage area compared to the area of NTSC color gamut. (b) Overlap area of QD-LED color gamut together with the NTSC standard vs. $f_{circadian}$. The blue dashed lines correspond to $f_{circadian}$ of YAG:Ce LED while the green dashed lines correspond to (a) the percentage and (b) the overlap area of color gamut using the YAG:Ce LED backlighting.....	66
Figure 3.4. Average and standard deviations of (a) the peak emission wavelengths (λ) and (b) the full-width at half-maximum ($\Delta\lambda$) values of the spectra that acquire the lowest 1%, 10%, 20%, 50% and 100% values of $f_{circadian}$	68

Figure 4.1. Photoluminescence (red curve) and absorbance (green curve) spectra of the synthesized CdTe QDs. Reproduced with permission from Ref. [124]. © American Institute of Physics 2014.....	73
Figure 4.2. Scanning electron microscope images of the Au/Ni/Au three-segment NWs (a) within the template and (b) on the glass substrate. Reproduced with permission from Ref. [124]. © American Institute of Physics 2014.....	75
Figure 4.3. Illustration of the setup that we used for preparing aligned NW-QD hybrid films. Reproduced with permission from Ref. [124]. © American Institute of Physics.....	75
Figure 4.4. (a) Illustration of our FDTD simulation setup where blue and pink arrows indicate the polarization and propagation of the light, red thin layer represents the CdTe QD layer, and yellow/gray/yellow wires represent the three-segment Au/Ni/Au nanowires. (b) Polarization ratio of the transmitting light that is produced within the CdTe QD layer. (c) Normalized transmission of the light as a function of the average nanowire spacing for single-segment and three-segment nanowires. Reproduced with permission from Ref. [124]. © American Institute of Physics 2014.....	77
Figure 4.5. Optical microscope images of the aligned three-segment nanowires taken from (a) a less dense and (b) a dense region of the hybrid film. Reproduced with permission from Ref. [124]. © American Institute of Physics 2014.....	78
Figure 4.6. Illustration of the setup used for characterizing the optical polarization of QD emission in hybrid films. Reproduced with permission from Ref. [124]. © American Institute of Physics 2014.....	79
Figure 4.7. Photoluminescence spectra at perpendicular (s) and parallel (p) polarizations of the films prepared by hybridizing three-segment Au/Ni/Au NW and CdTe QDs. In (a) 375 μ L and (b) 700 μ L of NW dispersion is used for the thin film preparation. Reproduced with permission from Ref. [124]. © American Institute of Physics 2014.....	80

Figure 5.1. Overview of feasible CRI-LER combinations (black squares) with the experimentally prepared macrocrystals used as color conversion materials on blue LEDs (center). The two PL-spectra on the left and the lower right one show theoretically determined combinations corresponding to the marked points in the center. The upper right PL-spectra and the corresponding red square show the photometric performance of the most optimized final white LED. Reproduced with permission from Ref. [87]. © American Chemical Society 2015..... 89

Figure 5.2. PL-spectra (top) of three different CdSe/CdZnSeS/ZnS QDs and their true color images under UV-excitation at 365 nm (bottom). The QDs are dispersed in CHCl₃ and stored under ambient conditions. Reproduced with permission from Ref. [87]. © American Chemical Society 2015..... 90

Figure 5.3. True color images of three different CdSe/CdZnSeS/ZnS QDs before ((a) and (c)) and after ((b) and (d)) ligand exchange under ambient light (top) and 365 nm UV-excitation (bottom). Reproduced with permission from Ref. [87] © American Chemical Society 2015. 91

Figure 5.4. Photoluminescence (PL) spectra of three different CdSe/CdZnSeS/ZnS QDs dispersed in CHCl₃ (solid lines) and after ligand exchange in H₂O (dotted lines). Reproduced with permission from Ref. [87]. © American Chemical Society 2015. 92

Figure 5.5. True color images of macrocrystals made from the same CdSe/CdZnSeS/ZnS QD batch with either borax ((a) and (c)) or NaCl ((b) and (d)) as host materials. The pictures (a) and (b) have been photographed under ambient light, (c) and (d) under excitation with a 365 nm UV-lamp. Reproduced with permission from Ref. [87]. © American Chemical Society 2015..... 94

Figure 5.6. True color ((a), (d), and (g)) and microscopic ((b), (e), and (h)) images of differently emitting CdSe/CdZnSeS/ZnS QDs incorporated into borax crystals under UV-excitation (365 nm). Graphs (c), (f) and (i) show the corresponding PL-spectra of the initial solutions (black lines) and macrocrystals (red lines). Reproduced with permission from Ref. [87]. © American Chemical Society 2015..... 95

Figure 5.7. Photoluminescence spectra of three different CdSe/CdZnSeS/ZnS QD-based macrocrystals (solid lines) in addition to their spectra after powdering and incorporation into thin films of silicone (dotted lines). Reproduced with permission from Ref. [87]. © American Chemical Society 2015.....	96
Figure 5.8. PL-decay spectra of three different QDs in CHCl ₃ (black squares), H ₂ O (red squares) and after embedding into borax (blue squares). The grey squares always represent the measured prompt. Reproduced with permission from Ref. [87]. © American Chemical Society 2015.....	96
Figure 5.9. TEM images of the green- ((a) and (b)) and red- ((c) and (d)) emitting macrocrystals shown in Figure 4. Overviews (a) and (c) as well as highly magnified images (b) and (d) of the samples prove non-aggregated and well distributed QDs within the matrix. Reproduced with permission from Ref. [87]. © American Chemical Society 2015.....	98
Figure 5.10. Infrared-image of a LED hybridized with macrocrystals in operation. The image was taken after a 15 (left) and 30 (rights) minutes operation using a 1 kHz switching rate, proving that the temperate stays constant slightly above room temperature, not exceeding 35 °C. Reproduced with permission from Ref. [87] © American Chemical Society 2015.....	99
Figure 5.11. PL-spectra of the white LED before and during the stability tests. The white LED was driven at 300 mA and a 1 kHz on/off rate, avoiding significant heat generation. Reproduced with permission from Ref. [87] © American Chemical Society 2015.....	99
Figure 5.12. True color image of a LED (a) prepared using borax powder, which was dried before blending it with the silicone on top of the LED. Photograph (b) and (c) show a LEDs produced using non-dried macrocrystal powder. While (b) shows the porous and non-homogenous silicone encapsulation, (c) displays the minor mechanical stability of such layers. Reproduced with permission from Ref. [87] © American Chemical Society 2015.....	101
Figure 5.13. Thermogravimetric analysis of borax-based macrocrystals. The blue line displays the applied temperature program, with a two-hour isothermic part	

at 70 °C to imitate the curing of the silicone on top of the LED. As prepared macrocrystal powder shows a significant weight loss (black curve), while the pre-dried powder suffers only from a negligible loss at 70 °C. Reproduced with permission from Ref. [87] © American Chemical Society 2015..... 101

Figure 5.14. Photographs (a), (b), and (c) show true color images of our macrocrystals under either ambient illumination with a standard fluorescent lamp (a), with our white LED (b), and under 365 nm UV-excitation. Graph (d) presents the PL-spectra of our white LED within the visible region (solid line) and the used modeled spectra (dotted line), while (e) shows a CIE 1931 diagram with the blackbody radiator (black line, CRI 100) as comparison, our white LED marked with the black cross and an incandescent bulb (grey cross). Reproduced with permission from Ref. [87] © American Chemical Society 2015..... 103

Figure 6.1. True color images of CdTe QDs and Au NPs embedded in macrodimensional sucrose crystals, which shows an efficiency enhancement of 58% through plasmonic interaction, under ambient lighting and ultraviolet illumination along with scanning electron microscopy (middle) and transmission electron microscopy (right) images. Reproduced with permission from Ref. [84]. © Tsinghua University Press and Springer-Verlag Berlin Heidelberg 2015..... 109

Figure 6.2. Absorption spectra of Au NP dispersion in water, in NaCl solution and in sucrose solution along with the true color photos. Reproduced with permission from Ref. [84]. © Tsinghua University Press and Springer-Verlag Berlin Heidelberg 2015..... 109

Figure 6.3. Absorption spectra and true color photographs of the macrocrystals incorporating Au NPs (a) alone and (b) coimmobilized together with CdTe QDs. Reproduced with permission from Ref. [84]. © Tsinghua University Press and Springer-Verlag Berlin Heidelberg 2015..... 110

Figure 6.4. Photoluminescence and absorbance spectrum of as-synthesized CdTe quantum dots (QDs) along with the absorbance spectrum of Au NPs in water and absorbance spectrum of 2.5 mL Au NP incorporated sucrose crystal (~15

mg) dissolved in 5 mL of water. Reproduced with permission from Ref. [84]. © Tsinghua University Press and Springer-Verlag Berlin Heidelberg 2015. 114

Figure 6.5. Time-resolved fluorescence decays and lifetimes (inset) of CdTe QD (2.5 mL) dispersion blended with varying amounts of Au NPs in sucrose solution using which the crystallization was carried out. Reproduced with permission from Ref. [84]. © Tsinghua University Press and Springer-Verlag Berlin Heidelberg 2015..... 116

Figure 6.6. (a) Quantum efficiency corrected photoluminescence spectra of the macrocrystals containing various amounts of Au NPs and 2.5 mL (352.5 nmol) of CdTe QDs, and (b) quantum efficiencies (purple circles) and the field enhancement factors (red triangles) of the corresponding macrocrystals. The purple dashed line indicates the quantum efficiency level when no Au NPs are present in the macrocrystal while the red dashed line stands for a field enhancement factor of unity. Reproduced with permission from Ref. [84]. © Tsinghua University Press and Springer-Verlag Berlin Heidelberg 2015. 117

Figure 6.7. (a)-(e) Time-resolved fluorescence decays of CdTe QDs embedded in plasmonic macrocrystals. All of the crystals were grown using 2.50 mL of CdTe QDs, and the Au NP amounts were increased from 0.125 to 2.50 mL. The reference sample does not include any Au NPs. (f) The lifetimes of the macrocrystals as a function of the Au NP amount used in the crystallization. Black dashed line indicates the lifetime when no Au NPs are present in the macrocrystal. Reproduced with permission from Ref. [84]. © Tsinghua University Press and Springer-Verlag Berlin Heidelberg 2015..... 118

Figure 6.8. (a) SEM and (b) TEM images of the Au NP and CdTe QD incorporated macrocrystals belonging to the macrocrystal prepared using 0.50 mL Au NPs and 2.50 mL CdTe QDs. Some of the QDs in the TEM image are marked with dashed black circles for visual assistance. Reproduced with permission from Ref. [84]. © Tsinghua University Press and Springer-Verlag Berlin Heidelberg 2015..... 122

Figure 6.9. TEM image of a Au NP and CdTe QD incorporated macrocrystals belonging to the macrocrystal prepared using 0.50 mL Au NPs and 2.50 mL

CdTe QDs, which is the same as Figure 6.8(b) with no markers. Reproduced with permission from Ref. [84]. © Tsinghua University Press and Springer-Verlag Berlin Heidelberg 2015..... 122

Figure 6.10. XRD spectra of the composite crystals: (a) XRD spectra of the sucrose macrocrystals having only Au NPs and (b) the spectra of the sucrose macrocrystals with only CdTe incorporated, and the ones grown using mixtures of Au NPs and CdTe QDs. Reproduced with permission from Ref. [84]. © Tsinghua University Press and Springer-Verlag Berlin Heidelberg 2015. 123

Figure 7.1. Photoluminescence spectra of the NCs in the dispersion and that of the same NCs-in-LiCl prepared using 0.3, 0.4, and 0.6 mg (Sample 1, Sample 2, and Sample 3) of the NCs. Reproduced with permission from Ref. [88]. © Royal Society of Chemistry 2015..... 129

Figure 7.2. Illustration of the quantum efficiency measurement methodology: (i) The measurement of the excitation spectrum without sample, (ii) the measurement of the spectrum when the sample is directly excited by the light source, and (iii) the measurement of the spectrum when the sample is excited by the light that scatters from the surface of the integrating sphere. Reproduced with permission from Ref. [88]. © Royal Society of Chemistry 2015..... 133

Figure 7.3. (a) Schematics of NC encapsulation into LiCl salt. The real color images of NC dispersion in THF (b) under ambient lighting and (c) UV illumination at 366 nm. The real color images of the NCs-in-LiCl powders (d) under ambient lighting and (e) UV illumination at 366 nm. Reproduced with permission from Ref. [88]. © Royal Society of Chemistry 2015..... 134

Figure 7.4. Scanning electron microscopy (SEM) images of the LiCl powders (a) without and (b) with NCs (scale bars: 30 μm). Transmission electron microscopy (TEM) images of (c) the as-synthesized NC dispersion in hexane and (d) the NC-in-LiCl powders (scale bars of larger images: 5 nm and inset images: 50 nm). (e) Photoluminescence spectra of the nonpolar NCs in dispersion and the same NCs encapsulated within LiCl ionic salt. Also, absorption spectra of the as-synthesized NCs (dispersion in hexane) and NC-in-LiCl powder film were

provided. Real color photographs of the LiCl encapsulated NC film under (f) ambient lighting and (g) UV illumination at 366 nm. Reproduced with permission from Ref. [88]. © Royal Society of Chemistry 2015.....	135
Figure 7.5. SEM images of (a) the only LiCl powder and (b) NC-in-LiCl powder. Scale bars: 10 μm . Reproduced with permission from Ref. [88]. © Royal Society of Chemistry 2015.....	136
Figure 7.6. TEM image of the NCs within LiCl host. Reproduced with permission from Ref. [88]. © Royal Society of Chemistry 2015.....	137
Figure 7.7. Time-resolved photoluminescence decay curves of the NCs in dispersion and the same NCs encapsulated in LiCl. Reproduced with permission from Ref. [88]. © Royal Society of Chemistry 2015.....	138
Figure 7.8. (a) Schematic image of NC-in-LiCl film preparation onto LED for temperature stability test. (b) Real color images of the NCs-in-LiCl on a blue LED under ambient lighting, UV illumination at 366 nm, and when LED is driven, from left to right. (c) Quantum efficiency variation of the NCs with and without LiCl encapsulation as a function of time when they are integrated on the blue LED driven at a high current level for 96 h (four days). Reproduced with permission from Ref. [88]. © Royal Society of Chemistry 2015.....	141
Figure 7.9. (a) FTIR spectra of the samples of only NCs along with LiCl powders with and without NC incorporation. The zoomed version of the same spectra between the wavenumbers of (b) 2500-3000 cm^{-1} and (c) 1300-1550 cm^{-1} . Reproduced with permission from Ref. [88]. © Royal Society of Chemistry 2015.....	142
Figure 7.10. TGA curves of the NCs, NC-in-LiCl powders, only LiCl powders, and NC drop-casted on LiCl powders. Reproduced with permission from Ref. [88]. © Royal Society of Chemistry 2015.....	143
Figure 7.11. XPS spectra comparison of Li (left) and Cl (right) peaks in only LiCl and NC-in-LiCl samples. Reproduced with permission from Ref. [88]. © Royal Society of Chemistry 2015.....	145

Figure 7.12. XPS spectra comparison of Zn (left) and Cd (right) peaks in the only NCs and NC-in-LiCl samples. Reproduced with permission from Ref. [88]. © Royal Society of Chemistry 2015..... 145

Figure 8.1. Photoluminescence spectra of the green-emitting donor and red-emitting acceptor nanocrystals (shown with green and red continuous lines, respectively) and their absorption spectra (shown with green and red dashed lines, respectively). In the inset, we provide the transmission electron microscopy images of these nanocrystals. Reproduced with permission from Ref. [85]. © Optical Society of America 2016..... 154

Figure 8.2. Photoluminescence spectra of the films prepared using the green-emitting and red-emitting nanocrystal hybrids embedded into LiCl powders. Here, the green-emitting nanocrystals serve as exciton donors while the red-emitting nanocrystals accept excitons. In (a), (c), and (e) the spectra of the only green-emitting nanocrystal embedded powders are given together with the hybrid and only red-emitting acceptor nanocrystal embedded powders prepared using 50, 150, and 250 μL of nanocrystals, respectively. Frames (b), (d), and (f) show the variation of the spectra for the cases where 50 μL of green (donor) nanocrystals are embedded into LiCl together with 50, 150, and 250 μL of acceptor, respectively. The inset images are the real color photographs of these films under ambient (left) and UV lighting (right). Reproduced with permission from Ref. [85]. © Optical Society of America 2016..... 155

Figure 8.3. Time-resolved fluorescence decays of the green-emitting exciton-donating nanocrystals within powders prepared using (a) 25 μL donor nanocrystals (red line) and hybrid of 25 μL donor nanocrystals together with 250 μL red-emitting exciton-accepting nanocrystals (green line), (b) 50 μL donor nanocrystals (red line) and hybrid of 50 μL donor nanocrystals together with 250 μL acceptor nanocrystals (green line), (c) 75 μL donor nanocrystals (red line) and hybrid of 75 μL donor nanocrystals together with 250 μL acceptor nanocrystals (green line), and (d) 100 μL donor nanocrystals (red line) and hybrid of 100 μL donor nanocrystals together with 250 μL acceptor nanocrystals (green line) at the donor emission peaks. Frames (e) and (f) show the TRF decays of the acceptor nanocrystals alone and in hybrid nanocrystal powders.

The black dashed lines are the fitted multiexponential functions on the TRF decays. Reproduced with permission from Ref. [85]. © Optical Society of America 2016.....	157
Figure 8.4. Amplitude-averaged lifetimes of only donor nanocrystal embedded LiCl powders, only acceptor nanocrystal embedded LiCl powders, and powders prepared using donor and acceptor nanocrystals. Frame (a) presents the lifetimes for the incorporated acceptor amount of 50 μ L while in (b) and (c) the illustrated lifetimes stand for the powders prepared using 150 and 250 μ L of acceptor, respectively. Frame (d) presents the NRET efficiency of the hybrid nanocrystal powders for varying acceptor incorporation amounts. Reproduced with permission from Ref. [85]. © Optical Society of America.....	158
Figure 8.5. Emission spectrum of the NRET enhanced nanocrystal embedded LiCl powders at varying currents together with the chromaticity points of the emitted light (inset, left) and luminous efficiency of the device (LE) (inset, right). Reproduced with permission from Ref. [85]. © Optical Society of America 2016.....	161
Figure 9.1. Molecular structure of poly[(9,9-bis{3-bromopropyl}fluorenyl-2,7-diyl)-co-(1,4-benzo-{2,1,3}-thiodiazole)] (PFBT-Br). Reproduced with permission from Ref. [100]. © American Chemical Society 2013.....	166
Figure 9.2. (a) Absorbance and fluorescence spectra of PFBT-Br in THF and PFBT-BR CPNs in water, and (b) absorbance spectra of PFBT-Br CPN film and de-folded PFBT-Br (while preserving the amount of polymers on quartz), together with the photoluminescence of InGaN/GaN QWs. Reproduced with permission from Ref. [100]. © American Chemical Society 2013.....	170
Figure 9.3. (a) Dynamic light scattering (DLS) histogram of PFBT-Br CPNs in water. The average diameter is 69 nm with a polydispersity index of 0.294, (b) the absorption spectrum of PFBT-Br film directly deposited on quartz. Reproduced with permission from Ref. [100]. © American Chemical Society 2013.	171

Figure 9.4. SEM images of (a) PFBT-Br nanoparticles on the nanopillars and (b) PFBT-Br polymer chains on the nanopillars (after the addition and evaporation of THF). The amount is carefully set such that the nanopillars are almost fully covered in both cases to ensure the coverage of the emissive QW region inside the nanopillars. Reproduced with permission from Ref. [100]. © American Chemical Society 2013. 172

Figure 9.5. Illustration of the comparative study: First aqueous dispersion of nanoparticles is drop-casted on the nanopillars and cryogenic time-resolved and steady state fluorescence measurements are taken at 296, 250, 200, 150, and 100 K. Later, THF is drop-wise added onto the nanoparticles on the nanopillars to defold them into polymer chains and then fully evaporated. The same measurements are repeated for the case of open polymers. Reproduced with permission from Ref. [100]. © American Chemical Society. 172

Figure 9.6. Temperature-dependent lifetimes of (a) nanopillars alone, nanopillars in the presence of PFBT-Br CPNs, and nanopillars in the presence of defolded PFBT-Br polymer chains, and (b) temperature-dependent NRET efficiency of the nanopillar-CPN hybrid and nanopillar defolded PFBT-Br hybrid. Black error bars indicate the measurement errors for (a), and the error bars in (b) were calculated using the information in (a). The minimum NRET efficiency was calculated by taking the minimum lifetime value of nanopillar and the maximum donor lifetime of acceptor including system. Similarly, the minimum NRET efficiency was found by using the maximum lifetime value of nanopillar and the minimum donor lifetime of acceptor including system. Reproduced with permission from Ref. [100]. © American Chemical Society 2013. 173

Figure 9.7. Time-resolved fluorescence decay curves of the nanopillars alone, the nanopillars hybridized with PFBT-Br CPNs and those hybridized with PFBT-Br polymer (after the addition and evaporation of THF) at 450 nm at temperatures of 296, 250, 200, 150, and 100 K. Black curves within the colored decay curves are the multi-exponential functions numerically fitted to the experimental data. Reproduced with permission from Ref. [100]. © American Chemical Society 2013. 174

Figure 9.8. Time resolved fluorescence decay curves of PFBT-Br nanoparticles on quartz and on nanopillars, and defolded PFBT-Br polymer chains (after the addition of THF onto nanoparticles) on quartz and on nanopillars at 550 nm at temperatures 296 K, 250 K, 200 K, 150 K, and 100 K. Black lines indicate the fitted multi-exponential curves (4 exponentials). Reproduced with permission from Ref. [100]. © American Chemical Society 2013..... 175

Figure 9.9. Temperature dependent fluorescence lifetimes of PFBT-Br CPNs and defolded PFBT-Br on the nanopillars and quartz. Reproduced with permission from Ref. [100]. © American Chemical Society 2013..... 180

List of Tables

Table 2.1. Common figure-of-merits used for evaluating the performance of white light sources.....	25
Table 3.1. Summary of the spectral parameters for satisfying the color gamut defined in Figure 3.1. λ and $\Delta\lambda$ stand for the peak emission wavelength and full-width at half-maximum, respectively.....	65
Table 5.1. Amount of precursors for the synthesis of three different CdSe/CdZnSeS/ZnS quantum dots (QDs) with an alloyed gradient shell.....	84
Table 5.2. Amounts of Cd within the parental CHCl_3 solutions and the final borax-based mixed crystals, measured using stripping voltammetry. The measurements were conducted using a bismuth film on the electrode for the determination, as described in Ref. [160], [161].....	93
Table 5.3. Average PL-lifetimes and photoluminescence quantum yields (PL-QY) for three QDs in different media. PL-QY values were measured three times and averaged.....	97

Table 6.1. Lifetimes of macrocrystals with varying Au nanoparticle content and fixed CdTe QD concentration (2.50 mL corresponding to 352.5 nmol).	119
Table 7.1. The quantum efficiency of the NCs in dispersion and the same NCs encapsulated in LiCl; their total lifetimes and radiative recombination lifetimes. In addition, the radiative lifetimes of the NCs in vacuum were first calculated by employing the radiative lifetime of the NCs in dispersion, then these values were used to predict the radiative lifetime of the NCs in LiCl matrix according to the empty cavity, virtual cavity, and fully microscopic models.	140
Table 7.2.XPS data for the only NCs, NC-in-LiCl, and only LiCl samples.	144
Table 8.1. The volumes for green- (donor) and red-emitting (acceptor) nanocrystals used for incorporation into LiCl.	151
Table 9.1. Emission (λ_{em}) and absorption (λ_{abs}) peaks and quantum efficiencies (Φ_f) of PFBT-Br in THF and PFBT-Br CPNs in water together with mean diameter, polydispersity index, and zeta potential of the nanoparticles.	170
Table 9.2. Lifetimes (together with χ^2 -values) and energy transfer rates and efficiencies of (i) the hybrid system of the nanopillar and PFBT-Br CPNs and (ii) that of the nanopillar and PFBT-Br defolded polymer chains. τ_{DA} : lifetime of the donor in the presence of acceptor at 450 nm, τ_D : lifetime of the donor (in the absence of the acceptor) at 450 nm, and τ_A : lifetime of the acceptor (in the absence of the donor) at 550 nm.....	175
Table 9.3. Lifetimes of PFBT-Br nanoparticles and polymer chains on quartz at 550 nm.	180

Chapter 1

Introduction

Light has always been an essential part of the human life and is considered an important trigger for the development of culture and science [1]. In modern times, light and light-emitting devices including lamps, lasers, and displays, have become an inseparable part of our lifestyle. Acknowledging this importance of light and underlying scientific breakthroughs, UNESCO announced 2015 as the “International Year of Light and Light-based Technologies”[2].

The significance of light shows itself in its share within the total energy consumption. Decreasing this amount is expected to substantially contribute to the efforts for decreasing the carbon footprint; therefore, there is a strong demand for developing efficient light sources [3]. The research on addressing this need has already started to help decrease the share of the energy consumed by the lighting from ~20% in 2007 [4] to 15% in 2015 [5]. The main driving force for this development has come from the transition from the traditional light sources to the light-emitting diodes (LEDs) [6]. As tabulated by the US Department of Energy [7], an LED based lamp delivering a similar light level of an incandescent lamp consumes only ca. 20% of the energy that the incandescent lamp uses. US Department of Energy predicts that by 2030 the transition to LEDs will enable a

total of ~40% energy saving. In addition to this saving, the bulb lifetime, which is 1,000 h for incandescent lamps reaches 25,000 h for the LED based lamps. This is also an important advantage of using LEDs to decrease the cost [7].

Two main strategies are followed to realize white-light emission using LEDs. The most straightforward approach is the collective use of multiple LED chips each individually emitting in different colors. However, despite being straightforward, this method of producing white light is significantly costly due to the driving electrical circuitry. In addition, different material systems required for such LEDs of varying color components further increases the production complexity and cost. More importantly, the efficiencies of the green and yellow LED chips are very low; therefore, the white LED luminaries using these LED chips suffer from low efficiencies. As a consequence of these problems, multi-chip approach for white light generation could not find ubiquitous use. A more common method for this purpose relies on the hybridization of color converters with LED chips. In this method, a blue or UV LED excites the color converting material that is coated on top of the LED chip. Currently, the most common color converters are the phosphors made of rare-earth ions. These phosphors possessing near unity quantum efficiencies are typically very broad emitters spanning the spectral range from 500 to 700 nm. This spectral broadness allowing for white light generation is, however, their plague because the emission spectra of the phosphors extend toward the spectral region where the human eye is not sensitive anymore. It is also very difficult to fine-tune the spectrum of the LEDs using phosphors to increase the color quality by increasing the color rendition capability and shade of the white light [8], [4]. Another problem associated with these phosphors is the supply problems of the rare-earth elements threatening their future in optoelectronics [9].

At this point, colloidal semiconductor nanocrystal quantum dots step forward as they are synthesized using materials that do not suffer from supply problems and possess high quantum efficiencies accompanied by narrow-band emission making the spectral fine-tuning possible [10]. Using correct combinations of the quantum dots emitting in different colors, it is possible to design the emission spectrum of the white LED so that high color quality and photometric efficiency can be realized simultaneously [11] as opposed to phosphors. The narrow-band

emission of the colloidal quantum dots poses additional advantages for the displays as well. This allows for obtaining very saturated colors compared to broad-band emitters such as phosphors; therefore, the color definition (also known as the color gamut) of the displays can be increased tremendously when quantum dots are employed [12]–[14]. Despite these advantages, however, the quantum dots suffer from low emission stability when exposed to high-photon flux or high temperatures both of which are typical conditions when the quantum dots are hybridized with a high-power LED. In addition to this, obtaining highly-efficient solid-films of the quantum dots is not an easy task. Another problem is that the currently available efficient quantum dots are based on cadmium, which is difficult and costly to recycle for the environmental concerns.

In this thesis, we present our research that we conducted to utilize these aforementioned capabilities of the quantum dots and address their problems we summarized above. After providing a scientific background in Chapter 2, we present our approach to minimize the disrupting effects of the displays on human biological rhythm by using narrow-emitting quantum dots in Chapter 3. In Chapter 4, we present our work in which we hybridized quantum dots with self-assembled magnetic nanowires to obtain anisotropic emitters for display backlights. In Chapter 5, we present our white LED design and implementation in which we incorporated the aqueous colloidal quantum dots within a salt matrix to improve the emission stability. In Chapter 6, we co-immobilized metal nanoparticles with quantum dots to increase the efficiency of the aqueous quantum dots using a robust platform allowing for plasmonic interaction. In Chapter 7, we addressed the need for the aqueous quantum dots to incorporate them into crystalline matrices. The vacuum-assisted method that we present in this chapter allows for the incorporation of the nonpolar quantum dots into salt matrix without phase transfer. This technique enables obtaining powders of quantum dots that possess high quantum efficiency and high emission stability. In Chapter 8, we studied the nonradiative energy transfer dynamics between green- and red-emitting nanocrystal quantum dots in salt matrix and implemented an excitonically improved LED. In Chapter 9, we present our work in which we investigated the morphology dependent nonradiative energy transfer

from the InGaN/GaN quantum well nanopillars to conjugated polymer nanoparticles which make another class of materials allowing for spectrum tuning by controlling the composition [15]. Finally, we conclude the thesis by making final remarks and giving a future outlook in Chapter 10.

Chapter 2

Scientific Background

This thesis work involves the colloidal semiconductor quantum dots and metal nanocrystals along with conjugated polymer nanoparticles for the design and implementation of high-efficiency high-quality light-emitting devices. Before presenting the details of our research work, we find it beneficial to introduce some background information. Within this framework, we first start with an introduction to the color science and photometry. Subsequently, we continue with the physics, synthesis, and applications of the colloidal semiconductor nanocrystal quantum dots, metal nanoparticle and quantum dot incorporating crystalline matrices – the macrocrystals, and conjugated polymer nanoparticles, all of which we have used in this thesis. Finally, we present brief introductory information on nonradiative energy transfer and plasmonic interaction, which are two of the important physical phenomena we studied in this thesis.

This chapter of the thesis is mainly based on T. Erdem and H. V. Demir *Nanophotonics* 2, 1, 57-81 (2013) [12] and partly on T. Erdem and H. V. Demir *Nanophotonics* 5, 1, 74-95 (2016) [16]. Reproduced with permission from DeGruyter Publishing © 2013 and 2016.

2.1 Color Science and Photometry

To evaluate the quality of white light sources, one needs to have quantitative measures, some of which also take the human perception into account. At this point, color science and photometry along with radiometry comes into play. In

this section, we summarize these concepts by first explaining the main features of the human eye. Subsequently, we move to the photometry and discuss different vision regimes depending on the luminance levels. Then we continue with the definitions of the photometric measures used in the lighting community. Finally, we further detail our discussion on the human vision regimes and on the effects of the lighting on human biological rhythm by employing the definitions we present. We discuss the color rendition metrics that indicate how accurate the real colors of the objects are rendered by the light source. Following this, we introduce quantitative definitions of color and then continue with the correlated color temperature which quantifies the shade of the white light and color rendering metrics that evaluate the color rendition accuracy of the light sources.

2.1.1 The human eye and the spectral sensitivity of the vision process

The eye is the sensory organ that provides us with the faculty of visual perception. The outermost layer of the eye is called the cornea, where the light rays first enter (Figure 2.1) [17]. There is an additional curvature in the front part of the cornea contributing to the focusing of the light. The cornea itself is a transparent structure; moreover, tears and mucus solutions have an important role in sustaining its transparency. Light rays passing through the cornea arrive at the anterior chamber, which controls the pressure within the eye ball via a transparent liquid called the aqueous humor. After traversing this liquid region, light rays come to the lens whose main function is to focus the light on the retina.

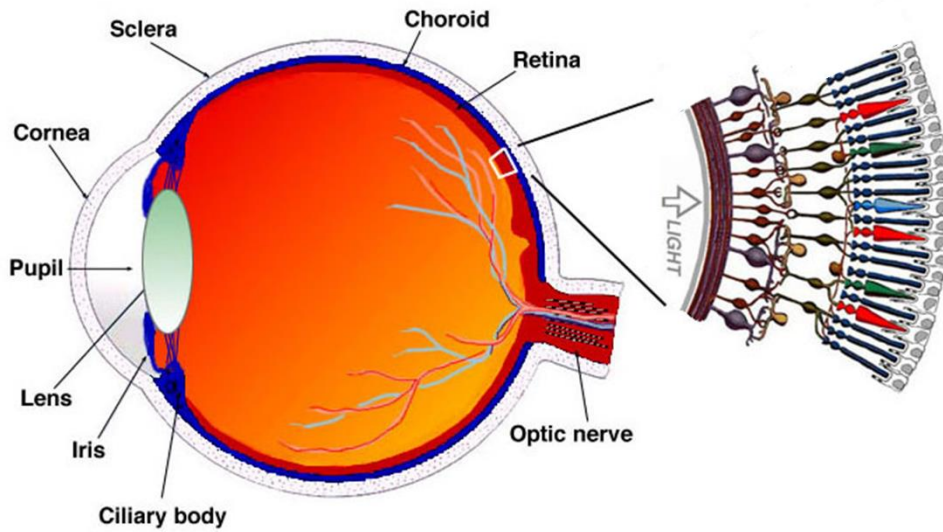


Figure 2.1. Illustration of the human eye structure along with a zoom-in to the photoreceptors in the retina [18].

The innermost part of the human eye is called the retina. It contains the visual neurons, which are the most crucial elements of the vision process. These neurons consist of three main layers: the photoreceptors, intermediate neurons, and ganglion cells [19].

The layer responsible for the light-sensing is called photoreceptors. There are three different types of photoreceptors in the human eye. Two of them are responsible for the visual perception while the remaining one mainly contributes to controlling the human biological rhythm. The photoreceptors that are responsible for the vision are named in accordance with their shapes and called rods and cones. The rod photoreceptors outnumber the cones in the retina and are denser in the regions away from the center of the retina. They have only one type and are very sensitive to light. Their sensitivity spectrum covers a significant portion of the visual regime, but they do not contribute to color differentiation (Figure 2.2). Different than rods, there are three types of cones in our eyes each having a different sensitivity spectrum, which helps brain translating the received optical input as blue, green, and red colors (Figure 2.2) [20].

The difference between cones and rods are not restricted to the difference in their sensitivities, their activities also differ depending on the ambient lighting

levels. At high luminances, cones dominate the visual perception. At lower luminances, on the other hand, cones are not sensitive enough while rods are primarily responsible for vision. As a result, we have a clear color differentiation capability when the ambient lighting is strong while we cannot distinguish colors in the dark or under very dim lighting conditions. The vision regime, in which cones are active, is called the photopic vision and the regime, in which rods dominate the visual perception, is named as the scotopic vision. Between these two, there is another vision regime called the mesopic vision, in which rods and cones contribute to the visual perception simultaneously. Before discussing the importance and limits of this vision regime, we first need to present some basic information that is needed to quantitatively evaluate the lighting-level perception.

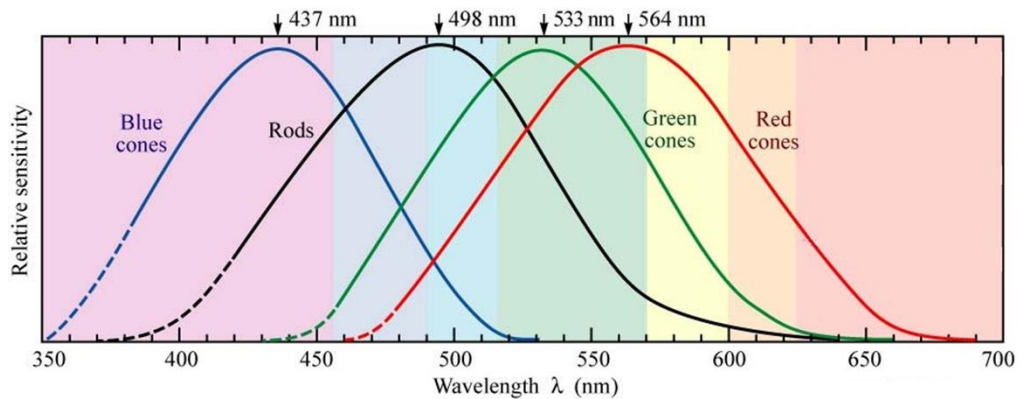


Figure 2.2. Normalized spectral sensitivities of rods and cones (red, green, and blue). Reproduced with permission from Ref. [20]. © Cambridge University Press 2016.

While designing a light source, it is essential to maximize the spectral overlap of the emitted light source with the spectral sensitivity of the human eye. This is because a light source radiating at wavelengths not detectable by the eye cannot contribute to what one sees. Even if the source has a high power conversion efficiency or high optical power, it cannot be accepted as an efficient light source for general lighting applications since the emitted light cannot be sensed. At this point, knowing the sensitivities of the photoreceptors in the human eye is of critical importance. Since the activity of the photoreceptors differ depending on the ambient lighting level, the effective sensitivity of the human eye changes

accordingly. For instance, the sensitivity of the rods peaks at 507 nm while the effective sensitivity of the cones peaks at 555 nm. In the mesopic regime condition, however, both photoreceptors are active, making the human eye sensitivity function differ from the photopic and scotopic eye sensitivity function (Figure 2.3). Here, it is worth mentioning that the eye sensitivity function in the mesopic vision conditions depends on the contributions of the rods and cones to the vision. Since this contribution depends on the lighting level, the mesopic vision sensitivity is also a function of the lighting level, which we will further discuss in the upcoming sections.

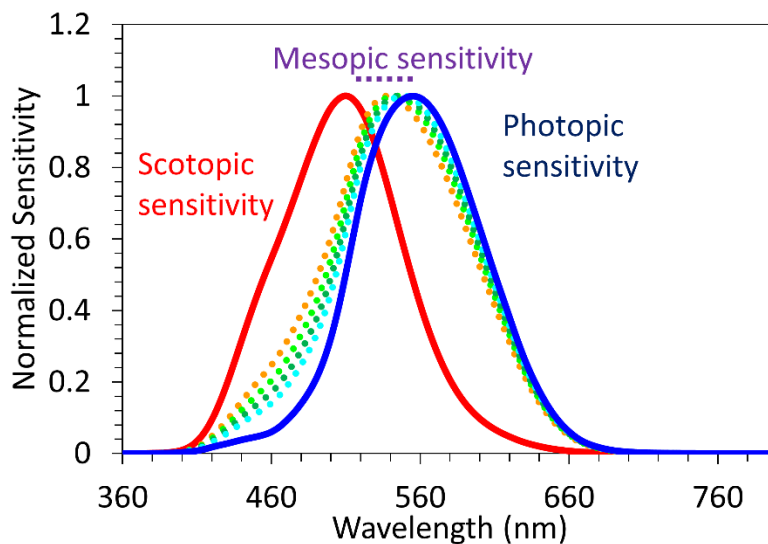


Figure 2.3. Normalized eye sensitivity functions in scotopic (red curve), mesopic (dashed curves), and photopic (blue curve) vision regimes.

2.1.2 Radiometric and photometric quantities

The radiometric measures express the properties of light from the perspective of electromagnetic radiation. On the other hand, photometric measures evaluate the emitted spectrum and power considering the sensitivity of the human eye, and they are essential for commenting on the efficiency of white light sources for general lighting applications.

The first pair of radiometric-photometric quantities that we introduce here is the radiant and luminous flux. Radiant flux is basically the power radiated by a

light source and has units of W_{opt} . The luminous flux (Φ), on the other hand, is defined as the useful optical radiation for the human eye, expressed in units of lumen (lm), and calculated by using Equation 2.1 where $P_R(\lambda)$ and $V(\lambda)$ stand for the spectral radiant flux and photopic eye sensitivity function, respectively.

$$\Phi = 683 \frac{\text{lm}}{W_{\text{opt}}} \int P_R(\lambda) V(\lambda) d\lambda \quad (2.1)$$

Another important radiometric quantity is the irradiance, which is the optical power per unit area and expressed in units of $W_{\text{opt}}/\text{m}^2$. The illuminance is the irradiance subject to the photopic human eye sensitivity function, and it has units of lm/m^2 or equivalently lux. Given the spectral irradiance $P_I(\lambda)$, the illuminance (IL) is expressed as in Equation (2.2). The illuminance is a quantity which is used to assess the effect of the lighting on the human circadian cycle. We will return to this subject toward the end of this section.

$$IL = 683 \frac{\text{lm}}{W_{\text{opt}}} \int P_I(\lambda) V(\lambda) d\lambda \quad (2.2)$$

Among the most important pairs of radiometric-photometric quantities we can include are the radiance and luminance. The radiance is the radiometric quantity denoting the optical power per solid angle per unit area and has the units of $W_{\text{opt}}/(\text{m}^2\text{sr})$. Given the spectral radiance $P_L(\lambda)$, the luminance is calculated using Equation (2.3). Basically, it gives us the amount of optical radiance that is useful for the human eye using the sensitivity function in the photopic regime $V(\lambda)$. It is measured in units of $\text{lm}/(\text{m}^2\text{sr})$, or equivalently cd/m^2 .

$$L = 683 \frac{\text{lm}}{W_{\text{opt}}} \int P_L(\lambda) V(\lambda) d\lambda \quad (2.3)$$

The luminance levels are used for defining the vision regime boundaries. Previously, there has been no consensus regarding these limits until 2010. For example, Osram Sylvania reported the luminance limits of photopic and scotopic vision to be 0.003 and 3 cd/m^2 , respectively [21] whereas Johnson [22] and LeGrand [23] stated that photopic vision begins at a luminance of 5 cd/m^2 .

According to Kokoschka, photopic vision starts at 10 cd/m² [24]. Moreover, the Illuminating Engineering Society of North America (IESNA) puts the boundaries at 0.01 and 3 cd/m² [25], and in 1978, the International Commission for Illumination (Commission Internationale de l’Eclairage, CIE) reported that scotopic vision starts below 0.001 cd/m² [26]. On the other hand, Rea put the scotopic and photopic boundaries at 0.001 and 0.6 cd/m², respectively, in his UPS system [27]. Almost simultaneously, the MOVE consortium suggested the boundaries to be 0.01 and 10 cd/m² [28], [29]. In 2010, a new report on a recommended system of photometry (CIE 191:2010) was published by the CIE, based on the USP and MOVE systems [30]. In this report, the boundary between the scotopic and mesopic vision was given as 0.005 cd/m² and that between the mesopic and photopic vision, as 5 cd/m². Furthermore, the eye sensitivity function in the mesopic vision regime is defined as a linear combination of the photopic and scotopic eye sensitivity functions. The details of this calculation can be found in Ref. [30]. The eye sensitivity functions calculated at various luminances based on this method are presented in Figure 2.3.

In addition to the metrics explained above, the efficiency of the white light sources needs to be evaluated by taking the eye sensitivity function into account. There are two important efficient measures that are used for this purpose. The first one, which expresses the efficiency of the white light spectrum with respect to human perception, is called the luminous efficacy of optical radiation (LER). It is calculated using Equation (2.4) where $P(\lambda)$ and $V(\lambda)$ are the spectral power distribution and photopic eye sensitivity function, respectively. The LER is expressed in units of lm/W_{opt}. The maximum value of the LER is 683 lm/W_{opt}; however, this can only be achieved with a monochromatic light source at 555 nm. A white light spectrum having an LER as high as possible is desirable, as it means less optical energy is radiated at the wavelengths where the eye is not sensitive. In general, white light sources with LERs >350 lm/W_{opt} are considered photometrically efficient [12].

$$LER = \frac{683 \frac{lm}{W_{opt}} \int P(\lambda)V(\lambda)d\lambda}{\int P(\lambda)d\lambda} \quad (2.4)$$

From a device point-of-view, it is essential to evaluate the efficiency of the light source by considering the electrical power consumption. For this purpose, the luminous efficiency (LE), which is defined as the efficiency of the radiated light as perceived by the human eye with respect to the supplied electrical power, P_{elect} , is calculated using Equation (2.5) and it is expressed in units of $\text{lm}/W_{\text{elect}}$. Today, efficient white light sources can reach LEs close to 150 $\text{lm}/W_{\text{elect}}$ [16].

$$LE = \frac{683 \frac{\text{lm}}{W_{\text{opt}}} \int P(\lambda) V(\lambda) d\lambda}{P_{\text{elect}}} \quad (2.5)$$

After obtaining the necessary background information on the photometry of light sources, here we continue with the background information on the effect of lighting on the human circadian rhythm. Around the beginning of this millennium, another photoreceptor in the human eye was found, which is not responsible for vision but instead responsible for the regulation of the circadian cycle, i.e., the daily biological rhythm [31], [32]. This receptor is called the melanopsin which controls the circadian rhythm by secreting melatonin. During the daytime, melatonin secretion is suppressed and a daytime signal is sent to the brain. During the nighttime, melatonin is secreted and a nighttime signal is delivered to the brain.

At this point, it is worth parenthetically noting and discussing the effects of light on the circadian cycle. Since during the daytime, the sun radiates with a significant short-wavelength content compared to the radiation in the evening, it is expected that melatonin suppression is regulated mostly by the blue content of the spectrum. Moreover, insufficient exposure to bluish light in the morning was found to result in a shift in the circadian cycle [33]. Another important point is that the shade of the white light emission affects the circadian cycle. In the case of cool white illumination, the brain receives signals indicating that it is daytime because of melatonin suppression due to the strong blue content, whereas a warm white illumination does not shift the circadian cycle. In other words, the circadian cycle can be manipulated by adjusting the spectrum of the light source and its color temperature. Therefore, especially for home lighting applications,

warm white colors should be selected to avoid the unintended effects of lighting on the circadian rhythm.

Although it is currently well known that the lighting affects the secretion of melatonin contributing to the control of the biological rhythm, it is still controversial how the suppression of melatonin occurs and how lighting affects it. According to Rea, melatonin suppression is affected collectively by rods, cones, and melanopsin [34], while Gall [35] and Enezi [36] employs a simpler model and connects the melatonin suppression only to the effect of lighting on melanopsin since some neurons in the brain robustly react to melanopsin activity but not to that of the cones [37].

In order to quantitatively express the effect of the light sources on the melatonin secretion, Gall introduced the circadian effect function $c(\lambda)$ in 2005, which is shown in Figure 2.4 [35]. This function was empirically calculated using the experimental data of Brainard et al. [38] and Thapan et al. [39]. Subsequently, Gall introduced another quantity, which is known as the circadian effect factor a_{cv} and calculated using Equation 2.6 where $s(\lambda)$ stands for the spectral irradiance and $V(\lambda)$ is the photopic eye sensitivity function. Gall used this quantity to evaluate the relative effect of the light sources on the melatonin suppression. He developed it in a manner that once a_{cv} is known, the relative effects of the light source on the melatonin suppression can be calculated by simply multiplying a_{cv} with the illuminance of the light source.

$$a_{cv} = \frac{\int s(\lambda)c(\lambda)d\lambda}{\int s(\lambda)V(\lambda)d\lambda} \quad (2.6)$$

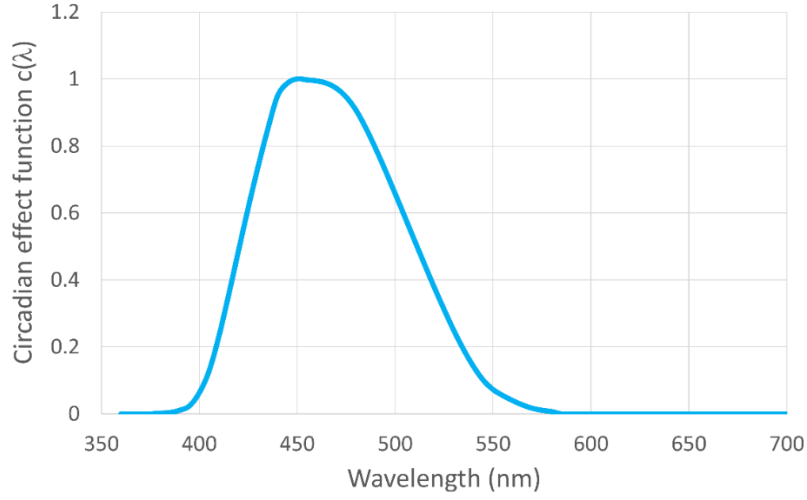


Figure 2.4. Spectral distribution of the circadian effect function introduced by Gall [35].

In 2010 Rea et al. proposed another measure for evaluating the effects of the light sources on the melatonin suppression [34]. This model was further refined in 2012 [40]. Different than the approach of Gall, Rea included the effect of other photoreceptors on the circadian cycle and introduced another metric called the circadian light (CL), which is calculated using Equation 2.7:

$$CL = \begin{cases} 1622 \left[\int M(\lambda) s(\lambda) d\lambda + a_{b-y} \left(\int \frac{S(\lambda)}{mp(\lambda)} s(\lambda) d\lambda - k \int \frac{V(\lambda)}{mp(\lambda)} s(\lambda) d\lambda \right) - a_{rod} \left(1 - e^{-\frac{\int V'(\lambda) s(\lambda) d\lambda}{RodSat}} \right) \right] \\ \quad \text{if } \left(\int \frac{S(\lambda)}{mp(\lambda)} s(\lambda) d\lambda - k \int \frac{V(\lambda)}{mp(\lambda)} s(\lambda) d\lambda \right) \geq 0 \\ 1622 \int M(\lambda) s(\lambda) d\lambda \quad \text{if } \left(\int \frac{S(\lambda)}{mp(\lambda)} s(\lambda) d\lambda - k \int \frac{V(\lambda)}{mp(\lambda)} s(\lambda) d\lambda \right) < 0 \end{cases} \quad (2.7)$$

where $s(\lambda)$ is the spectral irradiance of the light source, $M(\lambda)$ is the melanopsin sensitivity, $S(\lambda)$ is the S-cone fundamental, $mp(\lambda)$ is the macular pigment transmittance, $V(\lambda)$ is the photopic eye sensitivity function, $V'(\lambda)$ is the scotopic eye sensitivity function, RodSat is defined as the half-saturation constant for

bleaching rods and has the value of 6.5 W/m^2 , $k=0.2616$, $a_{b-\eta}=0.6201$, and $a_{rod}=3.2347$.

The third model on the melatonin suppression mechanism developed by Enezi et al. [36] proposes a simpler mechanism. Enezi et al. claims that the responses from the cones can be reduced in the brain and therefore, the signals associated with cones might be ineffective on melatonin suppression. Based on this argument, Enezi et al. introduced the melanopic eye sensitivity function $V_z(\lambda)$, which was plotted in Figure 2.5. Different than Gall model, which was based on the experiments carried out by Brainard [38] and Thapan [39], Enezi et al. employed the photosensitivity of a vitamin A based photopigment while defining $V_z(\lambda)$. After defining $V_z(\lambda)$, the melanopic illuminance (M_ϕ) was calculated using Equation 2.8.

$$M_\phi = 4557 \int s(\lambda) V_z(\lambda) d\lambda \quad (2.8)$$

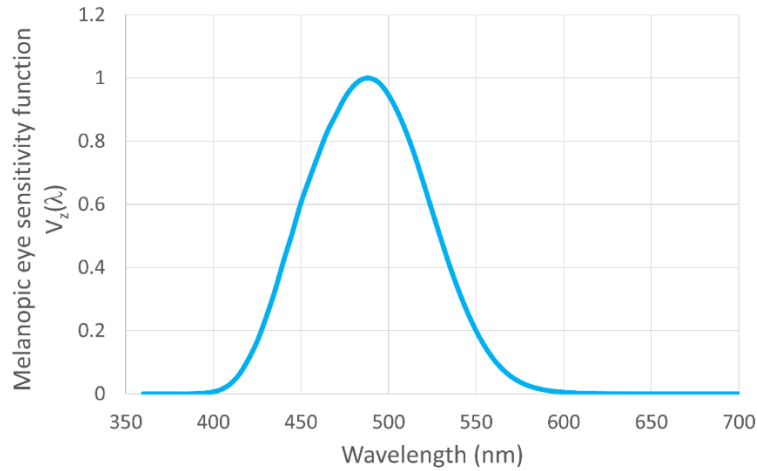


Figure 2.5. Spectral distribution of the melanopic eye sensitivity function by Enezi et al. [36].

2.1.3 Quantifying colors and colorimetric assessment criteria

In addition to the photometric efficiency, it is very important for a light source to exhibit high color quality. Therefore, a quantitative description of color and

its quality is necessary. For this purpose, the CIE introduced three color matching functions: \bar{x} , \bar{y} , and \bar{z} , whose spectral distributions are given in Figure 2.6, using a statistical approach [41].

In order to calculate the color coordinates, we first calculate the so-called tristimulus values, X , Y , and Z by using Equations (2.9)–(2.11) for an arbitrary radiation spectrum of $s(\lambda)$.

$$X = \int_{\lambda} s(\lambda) \bar{x}(\lambda) d\lambda \quad (2.9)$$

$$Y = \int_{\lambda} s(\lambda) \bar{y}(\lambda) d\lambda \quad (2.10)$$

$$Z = \int_{\lambda} s(\lambda) \bar{z}(\lambda) d\lambda \quad (2.11)$$

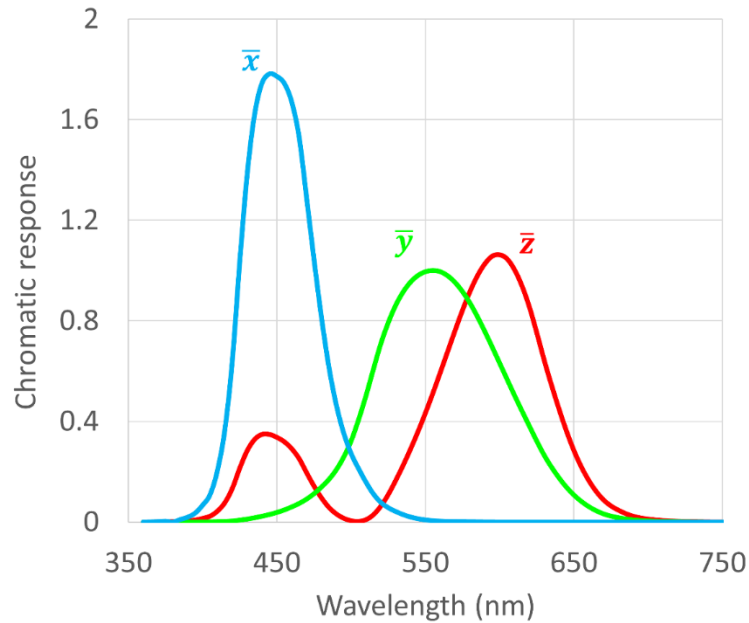


Figure 2.6. Color matching functions used in all of the colorimetric calculations.

The (x, y) chromaticity coordinates, which are also referred to as CIE 1931 chromaticity coordinates, are calculated using Equations (2.12)–(2.14). Since one of the three coordinates is dependent on the other remaining two, this methodology generates a two-dimensional color mapping as presented in Figure 2.7.

$$x = \frac{X}{X + Y + Z} \quad (2.12)$$

$$y = \frac{Y}{X + Y + Z} \quad (2.13)$$

$$z = \frac{Z}{X + Y + Z} = 1 - x - y \quad (2.14)$$

Despite the fact that this color mapping is the most widely preferred chromaticity diagram, it has an inherent problem that the geometric difference between the positions of pairs of colors does not consistently correspond to the perceived difference between the colors leading to nonuniform color distributions. As a solution to this problem, additional color mapping methodologies were proposed by CIE. These are the (u, v) , (u', v') , and $L^*a^*b^*$ chromaticity diagrams.

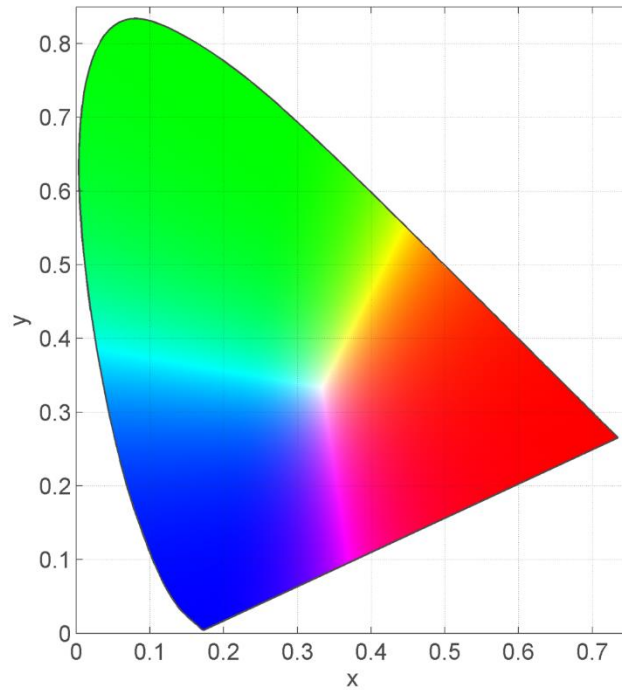


Figure 2.7. (x,y) chromaticity diagram. This color gamut is also known as CIE 1931 chromaticity diagram.

(u,v) and (u',v') coordinates are related to X , Y , and Z color coordinates using Equations (2.15) – (2.17). We present the (u',v') chromaticity diagram in Figure 2.8. As we can clearly see, especially green and red colors are more equally distributed on this diagram.

$$u = u' = \frac{4X}{X + 15Y + 3Z} \quad (2.15)$$

$$v = \frac{6Y}{X + 15Y + 3Z} \quad (2.16)$$

$$v' = \frac{9Y}{X + 15Y + 3Z} \quad (2.17)$$

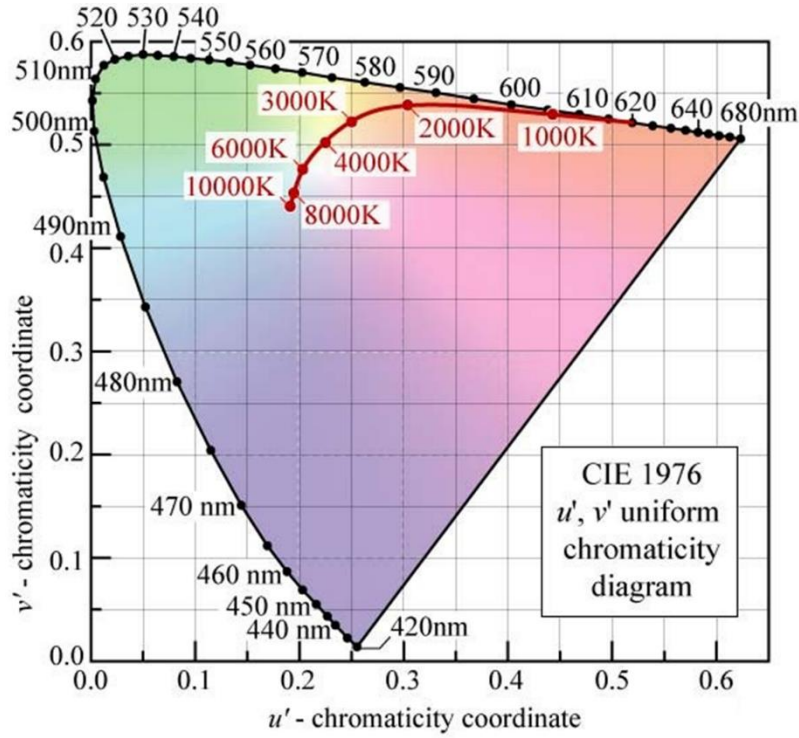


Figure 2.8. (u', v') chromaticity diagram. Reproduced with permission from Ref. [20] © Cambridge University Press 2016.

Despite the improvements on (u', v') chromaticity diagrams in terms of color uniformity, this system still needed to be improved. In addition to this, the existing systems, which do not include the effect of the luminance on the color perception, need to be modified to possess this information. These issues were addressed by CIE in 1976 and ($L^*a^*b^*$) chromaticity diagram was introduced (Figure 2.9). Contrary to the previous systems, ($L^*a^*b^*$) is a three dimensional color space and maps the perceived colors considering the effects of luminance. The corresponding color coordinates are calculated using Equations (2.18)–(2.20), where X_n , Y_n , and Z_n are the nominally white object color stimulus, and calculated using CIE standard illuminant A.

$$L^* = 116(Y/Y_n)^{1/3} - 16 \quad (2.18)$$

$$a^* = 500 \left[\left(\frac{X}{X_n} \right)^{1/3} - \left(\frac{Y}{Y_n} \right)^{1/3} \right] \quad (2.19)$$

$$b^* = 200 \left[\left(\frac{X}{X_n} \right)^{1/3} - \left(\frac{Z}{Z_n} \right)^{1/3} \right] \quad (2.20)$$

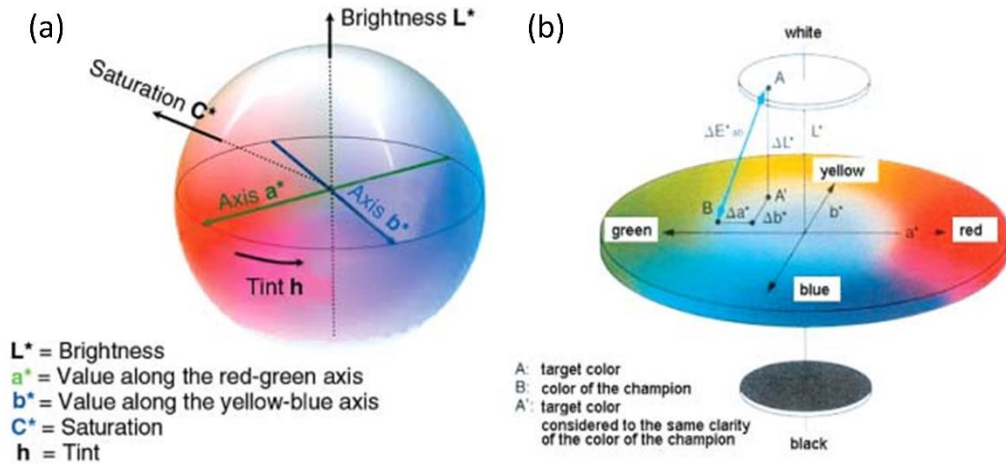


Figure 2.9. Illustration of (a) the full CIE $L^*a^*b^*$ chromaticity diagram and (b) a cross-section. Reproduced with permission from Ref. [42]. © Wiley International 2011.

The chromaticity diagrams offering color uniformity are especially targeted for comparing the colors of different sources. For a white light source, one of the obvious light sources whose color is compared with is the sun. Since the sun can be considered as a blackbody radiator, the shade of the white light radiated by the designed light source can be safely compared with the shade of a blackbody radiator.

The emission spectrum of a blackbody radiator is a function of its temperature. With the same analogy, the shade of the white light of an arbitrary white light source can be characterized by finding the temperature of the blackbody radiator whose color is closest to the color of the light source. This temperature is called the correlated color temperature (CCT). As opposed to the common usage in thermodynamics, high CCTs indicate a cool white-shade since a blackbody radiator at higher temperatures have a stronger bluish color tint. Similarly, a blackbody radiator at lower temperatures have stronger red content components giving its emission a warmer white shade. Traditionally, the CCT of an arbitrary light source is calculated using (u',v') chromaticity diagram (see

Figure 2.8). Incandescent light bulbs have CCTs around 3000 K and fluorescent tubes have varying CCTs from 3000 to 6500 K, whereas the CCT of the sun is close to 6000 K [20]. Having a warmer white shade (between 3000 and 4500 K) is more desirable for indoor lighting applications mainly for avoiding the disturbing effects of cool white light on the human biological clock.

Another parameter for the color quality of a white light source is its capability of rendering the real colors of the objects. This feature of light sources has great importance especially for the indoor lighting applications (Figure 2.10). Moreover, under low ambient lighting such as outdoor lighting, Reynham and Saksvrikrønning indicated that good color rendition helps increasing the road safety by improving the color contrast [43].

This property of the light sources is evaluated by various measures including the color discrimination index [22], cone surface area [23], color rendering capacity [24], feeling of contrast index [25], and flattery index [26]. However, these metrics have not attracted considerable attention in the lighting community to date. Therefore, we will not cover them here in detail and continue with two of the most commonly used color rendition metrics that are the color rendering index (CRI) and the color quality scale (CQS) [21].



Figure 2.10. Photographs of vegetables and fruits taken with light sources having (a) good and (b) poor color rendition capabilities [44].

CRI was first introduced by CIE in 1971 [45] and later in 1995 its calculation method was revised [46]. It makes use of fourteen test samples whose reflection spectra are given in Figure 2.11. The calculation assumes that the reference

white light source, which is in general a blackbody radiator, renders the colors of objects perfectly. The calculation involves evaluating the performance of the test light sources by comparing reflection spectra of the reference and test light sources from the test color samples and calculating the associated color difference between these two light sources. This color difference data was then employed to calculate the CRI whose maximum value is 100 indicating a perfect color rendition capability. Its minimum value is -100 which indicates the worst color rendition performance. During the CRI calculation, a color rendering index value specific to each test sample is obtained. The general color rendering index is calculated by using the first eight test samples while the remaining six samples define the specific CRI. In general, a light source possessing CRI >90 is considered to successfully render the real colors of objects [12].

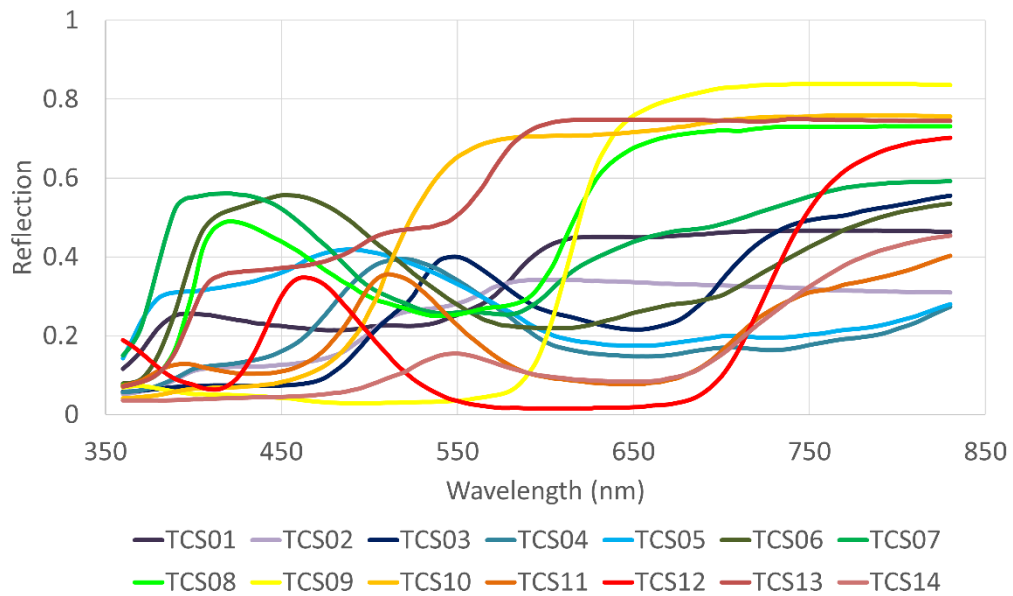


Figure 2.11. Reflection spectra of the test color samples (TCS) used for calculating the color rendering index.

Calculation of CRI starts with the determination of (u, v) coordinates of the reflection from the test sample i using the reference (dubbed with ref) and test light sources. Using Equations 2.21 and 2.22, (u, v) coordinates are transformed to (c, d) coordinates.

$$c = (4 - u - 10v) / v \quad (2.21)$$

$$d = (1.708v + 0.404 - 1.481u) / v \quad (2.22)$$

Subsequently, $(u_{test,i}^{**}, v_{test,i}^{**})$ coordinates are found using Equations (2.23) and (2.24).

$$u_{test,i}^{**} = \frac{10.872 + 0.404 \frac{c_{ref}}{c_{test}} c_{test,i} - 4 \frac{d_{ref}}{d_{test}} d_{test,i}}{16.518 + 1.481 \frac{c_{ref}}{c_{test}} c_{test,i} - \frac{d_{ref}}{d_{test}} d_{test,i}} \quad (2.23)$$

$$v_{test,i}^{**} = \frac{5.520}{16.518 + 1.481 \frac{c_{ref}}{c_{test}} c_{test,i} - \frac{d_{ref}}{d_{test}} d_{test,i}} \quad (2.24)$$

where $(u_{test}^{**}, v_{test}^{**})$ are given in Equations (2.25) and (2.26).

$$u_{test}^{**} = \frac{10.872 + 0.404c_{ref} - 4d_{ref}}{16.518 + 1.481c_{ref} - d_{ref}} \quad (2.25)$$

$$v_{test}^{**} = \frac{5.520}{16.518 + 1.481c_{ref} - d_{ref}} \quad (2.26)$$

The color shifts for each sample (ΔE_i^{**}) are calculated using Equations (2.27) – (2.30).

$$\Delta L^{**} = \left[25(Y_{ref,i})^{1/3} - 17 \right] - \left[25(Y_{test,i})^{1/3} - 17 \right] = L_{ref,i}^{**} - L_{test,i}^{**} \quad (2.27)$$

$$\Delta u^{**} = 13L_{ref,i}^{**}(u_{ref,i} - u_{ref}) - 13L_{test,i}^{**}(u_{test,i}^{**} - u_{test}^{**}) \quad (2.28)$$

$$\Delta v^{**} = 13L_{ref,i}^{**}(v_{ref,i} - v_{ref}) - 13L_{test,i}^{**}(v_{test,i}^{**} - v_{test}^{**}) \quad (2.29)$$

$$\Delta E_i^{**} = \sqrt{(\Delta L^{**})^2 + (\Delta u^{**})^2 + (\Delta v^{**})^2} \quad (2.30)$$

Following the computation of the color shift, CRI for each test sample is calculated using Equation (2.31). Finally, the general CRI can be found using Equation 2.32.

$$CRI_i = 100 - 4.6\Delta E_i^* \quad (2.31)$$

$$CRI = \frac{1}{8} \sum_{i=1}^8 CRI_i \quad (2.32)$$

Despite the fact that CRI still remains as the most frequently used measure of color rendition, it suffers from various issues [47]–[49]. One of them is the utilization of an improper uniform color space. Another issue is the assumption that the used reference sources render the colors perfectly is not always correct at very low and very high CCTs. These problems cause inaccurate results especially for the light sources having saturated color components. In addition to this, the arithmetic mean used during the calculation of CRI allows for the compensation of a low CRI value belonging to a certain test sample by the high CRIs of other test samples.

These problems of CRI are later addressed by Davis and Ohno who introduced the color quality scale (CQS) as an alternative to CRI [21]. CQS and CRI both employ the same reference sources. However, the CQS makes use of fifteen commercially available Munsell samples, all having highly saturated colors. This selection is based on the observation that a light source successfully rendering the saturated colors also successfully renders the unsaturated colors successfully [47]. This is especially important for the narrow-band emitters such as LED and nanocrystal-based light sources that we cover in this thesis. Different than CRI, CQS employs the $L^*a^*b^*$ color space, which is a more uniform color space compared to (u,v) color space. Another improvement in CQS compared to CRI is the addition of a saturation factor that neutralizes the effect of increasing the object chroma under the test illuminant with respect to a reference source. Furthermore, CQS does not allow the compensation of a poorly rendered test source by other successfully rendered sources by calculating the root-mean-square of individual color differences. Another fine-tuning in CQS compared to CRI is the change of the scale from the range of -100 to 100 to the

range of 0 to 100. Finally, in CQS a correction for the low CCTs is introduced, and the final value of the CQS is determined. Since the calculation of the CQS is very similar to that of the CRI, here we do not present the equations necessary for the CQS calculations and encourage the readers to look through Ref. [47] for further details.

Up to here, we have covered the main concepts of color science and photometry, which are frequently used in designing white light sources. The most widely used figure-of-merits in color science and photometry are summarized in Table 2.1 and a short description for each figure-of-merit along with their units is provided to assist the reader.

Table 2.1. Common figure-of-merits used for evaluating the performance of white light sources.

Figure of Merit	Unit	Short Description
Color Rendering Index (CRI)	None	Indicates how good the real colors of the illuminated objects are rendered
Color Quality Scale (CQS)	None	by the light source
Correlated Color Temperature (CCT)	K	Indicates the shade of the white light source – warm to cool white
Luminous Efficacy of Optical Radiation (LER)	lm/W _{opt}	Indicates the overlap between the human eye sensitivity curve and the light source spectral power density per generated optical power
Luminous Efficiency (LE)	lm/W _{elect}	Indicates the overlap between the human eye sensitivity curve and the light source spectral power density per supplied electrical power
Luminance (L)	cd/m ²	Indicates the overlap between the human eye sensitivity and the light source spectrum per unit solid angle per area – can be considered as perceived brightness under photopic

vision conditions		
Illuminance (IL)	lm/m ²	Indicates the overlap between the human eye sensitivity and the light source spectrum per area
Mesopic Luminance (L_{mes})	cd _{mes} /m ²	Indicates the spectral overlap between the human eye sensitivity and the light source spectrum— can be considered as perceived brightness under mesopic vision conditions

2.2 Quantum Dot Nanophosphors for Lighting and Displays

Within the last few decades, we have witnessed a tremendous progress in the optoelectronic devices made of semiconductor materials. Further structural engineering of these materials have introduced additional features that cannot be realized in bulk counterparts. Colloidal semiconductor nanocrystal quantum dots (QDs) are good examples for these structurally engineered semiconductors. By tuning their sizes, their effective bandgaps can span a broad range of wavelengths covering parts of ultraviolet, visible, and near infrared regimes. As a result, the optical features of these materials can be tuned by adjusting their size and size distribution. This property of QDs has enabled the development of new types of lasers, light-emitting diodes (LEDs), solar cells, and photodetectors [12], [16].

From the perspective of white LEDs, these materials offer great potential as they allow for optimization of the photometric and colorimetric properties of the device, because of the narrow emission band of QDs together with the positioning of the peak emission wavelength within the visual spectra band. This further provides the ability to accommodate multiple QD emitters finely tuned

one by one to collectively generate the targeted spectrum. Also, the broadband absorption of QDs remove the constraint for the excitation wavelength as long as it is sufficiently below the band edge, whereas this is one of the main concerns for conventional phosphors with narrower absorption bands. In this section of this thesis, we will briefly describe the nanocrystal synthesis, and finally summarize previous studies including our efforts on their use for indoor and outdoor lighting as well as display backlighting.

2.2.1 Physical properties of nanocrystal quantum dots

As the dimensions of pieces of materials come close to their exciton Bohr radii, the quantum mechanics emerge as the governing mechanisms. Semiconductor QDs are excellent examples of this phenomenon. When we decrease the size of a semiconductor structure down to ~ 10 nm as in the case of semiconductor QDs, we start to approach the typical extent of electron and hole wavefunctions [50]. As a result, the electron and hole wavefunctions start to be confined with decreasing size due to high energy barrier of the surrounding medium. From a simplistic point-of-view, the resulting quantum mechanical system is similar to a finite quantum well problem, and discrete energy levels dictate the material properties. A schematic illustration of a quantum dot is given below in Figure 2.12 along with the corresponding energy band diagram.

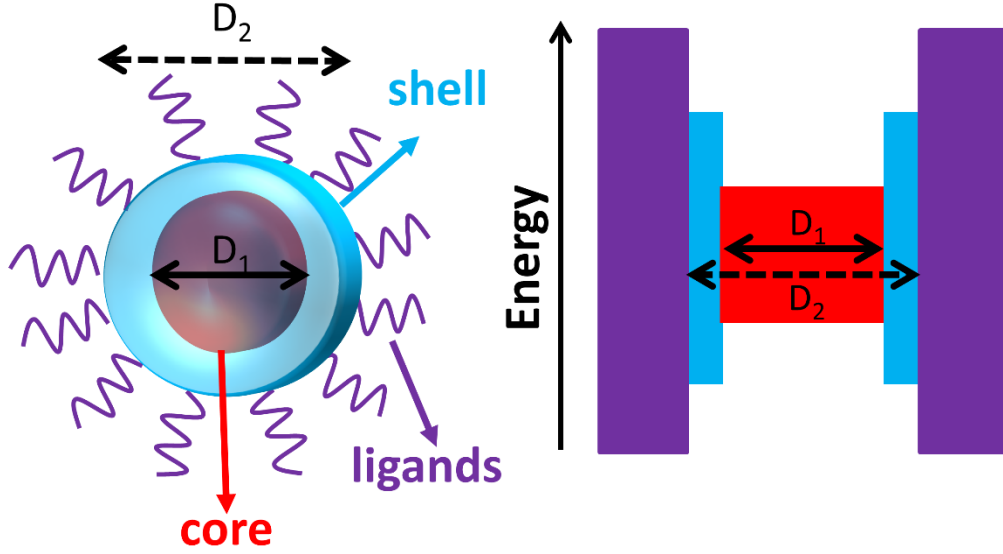


Figure 2.12. Schematic illustration of a core/shell nanocrystal QD (left) and the corresponding energy band diagram (right).

The exciton Bohr radius (r_B) of a typical bulk semiconductor can be calculated using Equation 2.33 where \hbar is the reduced Planck's constant, e is the electron charge, ϵ is the permittivity, and m_e and m_h are the electron and hole effective masses, respectively [51].

$$r_B = \frac{\hbar^2 \epsilon}{e^2} \left(\frac{1}{m_e} + \frac{1}{m_h} \right) \quad (2.33)$$

When we calculate r_B for a typical semiconductor used for QDs such as CdSe, we find it to be ca. 5 nm. Considering that the size of a typical QD is ~ 10 nm, the particle remains in the weak confinement regime [50]. As a result, the energy of the exciton can be expressed as in Equation 2.34.

$$E_{nml} = E_g - \frac{R_y^*}{n^2} + \frac{\hbar^2 \chi_{ml}^2}{2Ma^2} \quad (2.34)$$

In this equation, E_g stands for the bulk bandgap energy; n , m , and l are the quantum numbers; R_y^* stands for the exciton Rydberg energy, which is equal to $e^2/(2\epsilon r_B)$; M is the mass; a indicates the size of the particle, and χ_{ml} stands for the roots of the Bessel function. It is here worth noting that the second term arises from the electron-hole Coulomb interaction and the third term describes the

states due to the center of mass motion in the presence of an external potential barrier.

Equation 2.34 clearly shows the size-dependent transition energies that grow with decreasing particle size. This can be easily observed in the emission and absorption spectra of the QDs. As the size decreases, a significant blue shift is observed in the emission spectrum of the semiconductor material compared to the bulk case. For example, a bulk CdSe crystal has an emission peak at 713 nm, whereas its quantum dots can emit at around 500 nm. Another interesting feature of the QDs is that this blue shift is strongly dependent on the size of the material. As the size of the QD decreases, the emission peak moves to higher energies corresponding to shorter wavelengths as a result of the narrowing well width. On the other hand, the bandwidth of the emission spectrum is strongly dependent of the size distribution of the QDs and the density of the trap states. As with the emission, the absorption features also exhibit a size-dependent behavior. As the size of the QD decreases, the absorption starts at higher photon energies or equivalently shorter wavelengths. As an example, we present the emission and absorption spectra of CdSe QDs synthesized in our laboratory in Figure 2.13.

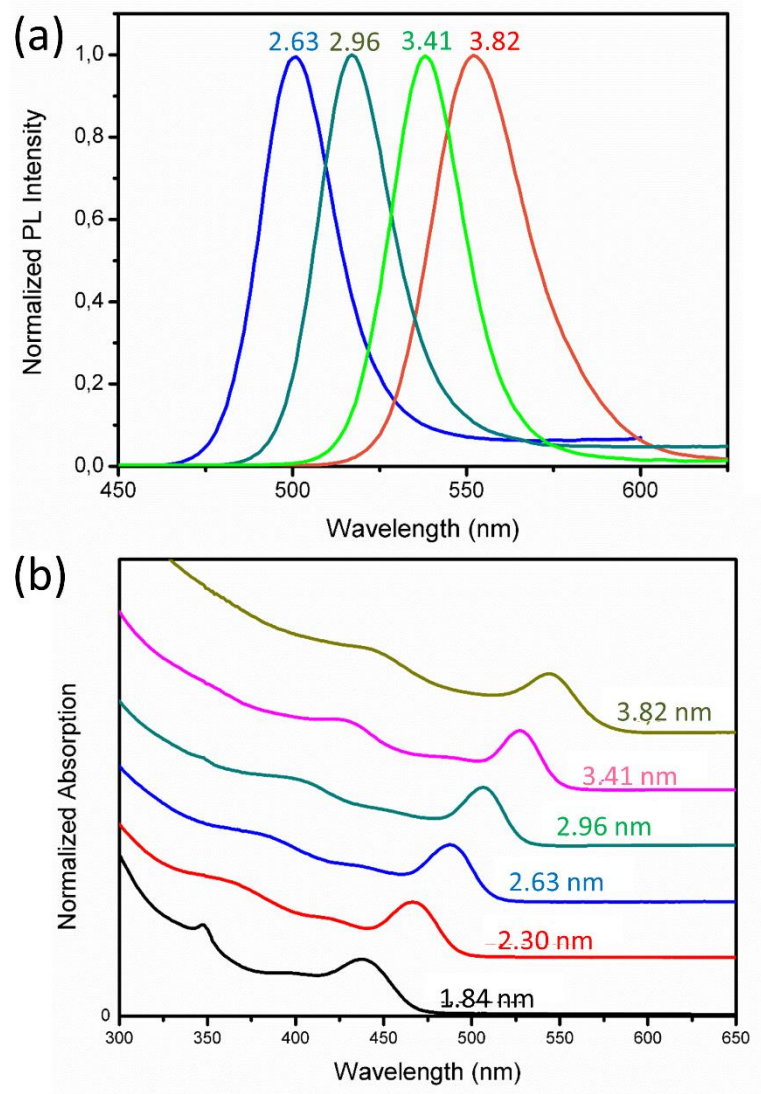


Figure 2.13. (a) Emission and (b) absorption spectra of the CdSe QDs synthesized at Demir Group laboratories, red-shifting with increasing size.

2.2.2 Colloidal synthesis of semiconductor quantum dots

In this thesis, we are interested in the colloidal QDs that are prepared via wet chemistry. The quantum confinement effects that depend on the size of the QD are controlled by adjusting the synthesis parameters such as temperature, growth time, and reactants. A common method for preparing non-colloidal QDs, which

are not used in this thesis, is the use of thin-film epitaxial growth techniques. In this method, the island of an energetically narrow bandgap material is surrounded by a matrix with a wider energy bandgap. However, in contrast to their colloidal counterparts, their epitaxy is very expensive due to high-temperature processing, their growth over large areas is not possible, and they require a substrate for the growth; therefore, their deposition on the LED chips as color converters is a challenge [12].

Colloidal nanocrystal QDs can be synthesized and dispersed in polar solvents, like water, as well as in non-polar solvents such as hexane, toluene, and chloroform. A good review of the synthesis of these materials can be found in Refs. [52], [53]. There are several possible materials that can be used for QD synthesis. Among them, CdS, CdSe, CdTe, ZnS, ZnSe, ZnTe, HgTe, PbSe, PbS, and InP can be given as common examples. However, using only core generally does not result in a high photoluminescence quantum efficiency, which is defined as the emitted number of photons per absorbed photon. To enhance the emission capabilities of the QDs, a core/shell material system is preferred. In this system, an additional material having a higher bandgap surrounds the core. A careful choice of coating material decreases the lattice mismatch, leading to increased quantum efficiency [52]; as a result, more efficient QDs can be synthesized. Today, efficiencies of more than 90% have been reported using colloidal approaches [9]. Typical material choices are CdSe/CdS, CdSe/CdS/ZnS, CdSe/ZnS, PbSe/PbS, CdTe/CdSe, CdSe/ZnTe, and InP/ZnS. Another material system that has attracted attention in recent years is doped quantum dots. These QDs consist of a semiconductor core doped with a transition metal. The absorbing material is the semiconductor, while the emission occurs through the dopants. As a result, the emission spectrum of the QDs and their absorption spectrum are separated, which in turn decreases the reabsorption problem [54]. Common core-QDs are InP, CdSe, CdS, and ZnSe, and common transition metals acting as the emission centers are Cu and Mn.

Within the framework of this thesis work, we have utilized mainly two different QD synthesis techniques. The first synthesis was carried out in aqueous environment and the resulting CdTe core QDs that are coated with thioglycolic acid (TGA) ligands are dispersed in water. The second class of the QDs that we

used in this thesis involves a hot-injection based technique. With this technique we grew CdSe/CdZnSeS/ZnS core/alloyed shell/shell QDs that can be dispersed in nonpolar solvents thanks to their oleic acid ligands.

For the synthesis of CdTe nanocrystal QDs dispersed in water, we follow Ref. [55]. In this synthesis, the TGA molecules having thiol groups which have the tendency to bind to the Cd atoms, serve as the stabilizer and makes them dispersible in water. The synthesis that we carried out in our laboratories uses aluminum telluride (Al_2Te_3) as Te source, cadmium perchlorate hexahydrate ($\text{Cd}(\text{ClO}_4)_2 \cdot 6\text{H}_2\text{O}$) as the Cd source, thioglycolic acid (TGA) as the surfactant, water as the synthesis environment and dispersion medium in addition to sodium hydroxide (NaOH) used to set the pH of the solution, sulfuric acid (H_2SO_4) to carry the Te atoms to the reaction mixture, and iso-propanol ($\text{C}_3\text{H}_7\text{OH}$) for the cleaning. We synthesize these nanocrystals in a three-neck reaction flask while continuously stirring. For a typical synthesis we dissolve 4.59 g of $\text{Cd}(\text{ClO}_4)_2 \cdot 6\text{H}_2\text{O}$ in 500 mL of water. Subsequently, 1.3 g of TGA is added to the reaction mixture and NaOH is added to the mixture dropwise until the pH is set to 11.8. 0.8 g of Al_2Te_3 is placed in a second two-neck flask that is connected to the reaction mixture. First, Ar is flown through the system for removing the dissolved oxygen so that the Te-source does not oxidize. Subsequently, 10-12 mL of H_2SO_4 (0.5 M) is added dropwise on top of the Te-source so that H_2Te gas is generated and flown by Ar flow into the reaction mixture containing the Cd-source (Figure 2.14). To start the growth of the QDs, we heat up the mixture until the boiling point. The first products are green-emitting QDs while the synthesized QDs grow with time and emit in yellow then red color.

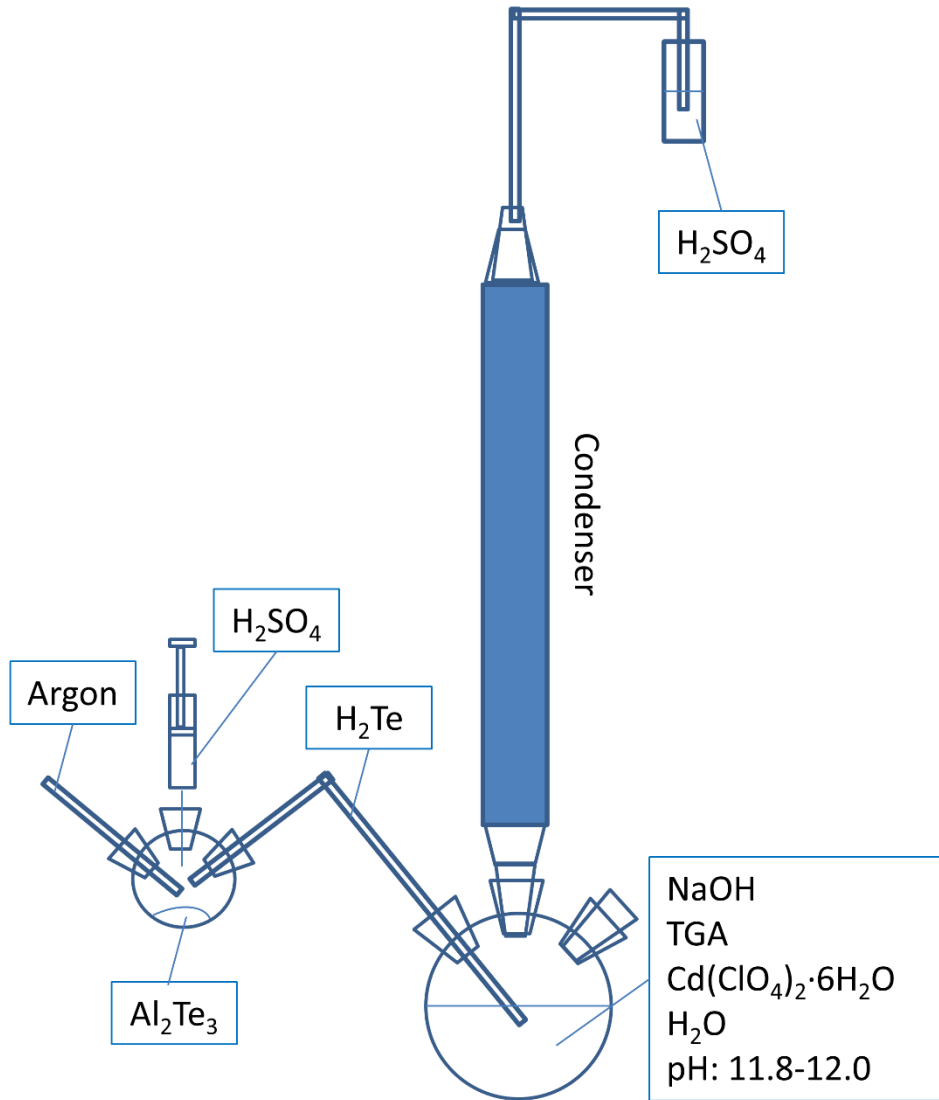


Figure 2.14. Illustration of the setup used for CdTe QD synthesis.

The quantum efficiency of these QDs dispersed in water remain in general below 60%. However, core/alloyed-shell/shell QDs can possess much higher quantum efficiencies. For this purpose, we also synthesized these QDs for the studies presented in this thesis. We follow Ref. [56] for the synthesis of CdSe/CdZnSeS/ZnS QDs. In a typical synthesis, we use cadmium oxide (CdO)

as the Cd-source, zinc acetate as the Zn source, sulfur as the sulfur source, selenium as the Se source, oleic acid as the ligand, and trioctylphosphine (TOP) and 1-octadecene (1-ODE) as solvents. We start the synthesis by dissolving 0.4 mmol of CdO and 4 mmol of zinc acetate in 5.6 mL of oleic acid and 20 mL of 1-ODE in a 50 mL three-neck flask. To remove impurities, we keep the mixture in vacuum for 2 h at 100 °C under vigorous stirring. Subsequently, we heat the reaction mixture to 310 °C under argon flow. When we reach this target temperature, we quickly inject the solution of 0.1 mmol of Se powder and 4 mmol of S powder in 3 mL of TOP to the reaction flask. After 10 min of growth, we cool down the reaction mixture to room temperature (Figure 2.15) and clean the synthesized nanocrystals by precipitation using hexane/acetone mixture. After cleaning, the QDs are dispersed in nonpolar solvents such as hexane and toluene.



Figure 2.15. Exemplary photograph showing nonpolar CdSe/CdZnSeS/ZnS QDs synthesized in Demir Group synthesis laboratory.

2.2.3 Quantum dots for lighting and displays

QDs having narrow band emission and spanning the whole visible regime offer strong opportunities for designing high-quality light sources [12], [57]–[59].

However, optimization of the white light spectrum is a complicated task that needs to be carried out in a manner specific to the application. For example, the design of an indoor light source requires successful color rendering, good spectral overlap with the human eye sensitivity function, and a warm white shade. On the other hand, a spectral design for outdoor lighting has different performance criteria. In this case, for example, the luminance has to be increased considering the changes in the eye sensitivity in the mesopic lighting levels. In addition, road lighting with a high CRI is thought to increase visual perception while driving. Since each application has different figure-of-merits and some applications have complicated trade-offs between the performance criteria, the emitters should be selected carefully for each specific application. For this purpose, narrow emitters such as QDs offer great potential, as they enable high flexibility in the spectral design, leading to high-quality light sources. In this part of the thesis, we summarize our previous studies regarding the spectral design for indoor and outdoor applications using nanocrystal QDs as color-converter materials.

In order to obtain high quality light sources for indoor lighting exhibiting warm white shade together with high CRI and high LER, the selected color components must be strategically selected. Knowing the trade-offs between these figure-of-merits is also helpful during the design of the light source. For this purpose, we previously carried out computational simulations by modeling the emission of nanocrystal QDs as a Gaussian spectrum [57]. The white light spectrum was generated using four color components, i.e., blue, green, yellow, and red. By changing the peak emission wavelength (WL), the full-width-at-half-maximum (FWHM), and the relative amplitude of each QD color component, in total 237,109,375 QD-integrated white LED (QD-WLED) spectra were tested in terms of photometric performance. Before investigating the results, a two-step threshold was applied. First, the spectra possessing a CRI >80 , an LER >350 lm/W_{opt}, and a CCT <4000 K were selected. These results were used for understanding the trade-offs between the performance metrics of the CRI, CCT, and LER. The second threshold was applied by increasing the CRI limit to 90 and the LER limit to 380 lm/W_{opt}.

The trade-offs between the CRI, LER, and CCT can be summarized in Figure 2.16, where the maximum obtainable CRI decreases as the LER increases. This

trade-off is steeper when operating at a lower CCT for a warmer white shade. Moreover, the maximum obtainable CRI at a given LER requires warmer white shades up to LERs of ~ 370 lm/W_{opt}. After this LER value, the trade-off starts to change, and at even higher LERs, maximum obtainable CRIs are attained at cooler white shades.

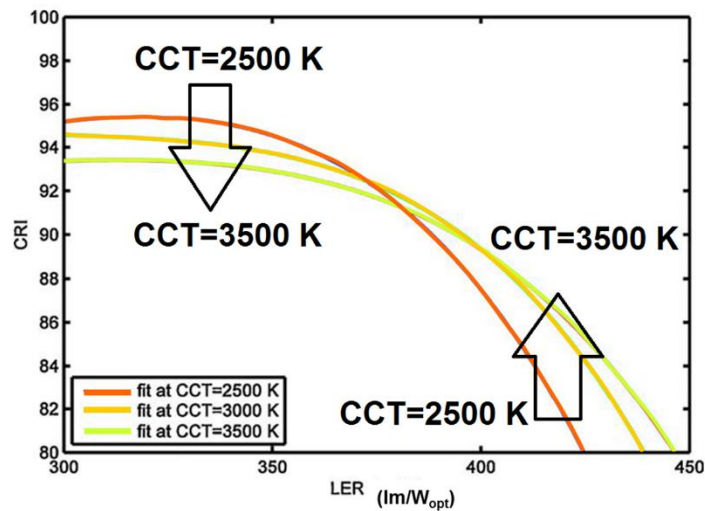


Figure 2.16. CRI vs. LER relation at CCTs of 2500, 3000, and 3500 K. Reproduced with permission from Ref. [12]. © DeGruyter Publishing 2013.

In addition to these trade-offs, Ref. [57] summarizes the spectral requirements for obtaining high CRI and LER values by preserving the warm white emission using QDs. It has been found that the full-width-at-half-maximum of the red color component must be very narrow (~ 30 nm) while its relative amplitude should be strongly dominant in the spectrum ($\sim 430/1000$) and the blue component must remain weak ($\sim 90/1000$). Moreover, another critical parameter is found to be the peak emission wavelength of the red color component, which needs to be located in the proximity of 620 nm. On the other hand, the average values found in the simulations indicate that blue, green, and yellow peak emission wavelengths have to be around 465, 528, and 569 nm, respectively. However, larger standard deviations obtained offer a flexibility in the choice of these peak emission wavelengths without having any significant loss in photometric performance. Similarly, the large FWHM values of these color components offer flexibility in choosing these parameters. Finally, the averages of

the relative amplitudes of the green and yellow components turn out to be 229/1000 and 241/1000, respectively, with standard deviations $>70/1000$. Compared to the standard deviations of blue and red (20/1000 and 49/1000, respectively), it is clear that selection of the green and yellow relative amplitudes is less critical for preserving the photometric performance.

Obtaining a QD integrated white LED spectrum possessing high photometric efficiency and high color quality does not mean that the light source is energy efficient. Therefore, the potential of these devices for energy efficiency has to be investigated separately by considering different architectures of QD films and their quantum efficiencies. We addressed this problem in Ref. [60] where QD integrated white LEDs were modeled as blue LEDs exciting green, yellow, and red QD films. Two basic architectures were studied in which green, yellow, and red QDs were (i) used to form a sequence of three separate coating layers on a blue LED (with green first, followed by yellow, and then red) and (ii) blended together to form a single coating layer on a blue LED. The power conversion efficiencies (PCEs) of the QD integrated white LEDs were calculated by assuming a blue LED chip having a PCE of 81.3% and using a color conversion scheme modeled with feedback loops. The calculations predicted that, when a layered architecture is used, quantum efficiencies of 43%, 61%, and 80% for the QDs are required to achieve luminous efficiencies (LEs) of 100, 150, and 200 $\text{lm}/\text{W}_{\text{elect}}$, respectively, for the spectra possessing an $\text{LER} \geq 380 \text{ lm}/\text{W}_{\text{opt}}$, a $\text{CRI} \geq 90$, and a $\text{CCT} \leq 4000 \text{ K}$ as in Ref. [57]. Moreover, the suitability of the spectra for the Energy Star and ANSI standards were satisfied, and spectra having an $\text{R9} \geq 70$ have been included in the study. When the blended QD integrated white LED architecture is preferred, the required quantum efficiencies of the QDs need to increase to 47%, 65%, and 82%, respectively. Another important result revealed by this study was the effect of the energy down-conversion on the energy efficiency. It has been found that even if the quantum efficiency of the QDs are 100%, at least 17% of the optical energy is lost due to the Stokes shift as far as the photometrically efficient spectra exhibiting high color quality are considered. This corresponds to an LE of $315 \text{ lm}/\text{W}_{\text{elect}}$ in the case of a perfect blue LED chip with a PCE of 100%.

For outdoor lighting conditions, the shade of the white light is not as significant as in the case of indoor lighting. More importantly, the sensitivity of the eye changes since the vision regime becomes mesopic under the luminance levels of road lighting. Therefore, a photopic luminance calculation, which can be considered as an indicator of the perceived brightness, cannot reveal correct perception information. Instead, the mesopic luminance should be considered by taking the changes in the eye sensitivity function into account.

We carried out a spectral recommendation study considering these points to improve the mesopic luminance employing QD integrated white LEDs [59]. First four different road lighting standards among US and UK standards were chosen having various photopic luminance requirements. The second step of the study has been the investigation of the commercial light sources. For this purpose, the spectra of a cool white fluorescent lamp (CWFL), an incandescent lamp with a CCT of 3000 K, a metal-halide lamp (MH), a high-pressure sodium lamp (HPS), and a mercury vapor lamp (MV) were investigated along with the standard daylight source D65, which is included just for the purpose of comparison with daylight. The results showed that at lower radiances the CWFL achieves the highest mesopic luminance, whereas the HPS takes the lead at higher radiances. In accordance with this information, it has been found that the CWFL is the most efficient commercial light source for the two standards requiring lowest luminances, whereas the HPS becomes the most efficient source for the remaining standards chosen in the study.

To investigate the performance of QD integrated white LEDs, a similar computation approach to Ref. [57] was followed. The QD integrated white LED spectra were generated such that they have the same radiances as the CWFL has for the two standards requiring lowest luminances. For the remaining two conditions, the QD integrated white LEDs having the same radiance as the HPS were generated. In order to reveal the spectral parameters necessary for achieving high mesopic luminance, new thresholds were determined in light of the requirements for mesopic lighting. The spectra that can possess CRI and CQS values at or above 85 and satisfy the chromaticity difference requirements of ANSI [61] were selected.

To reveal the spectral conditions necessary for achieving high mesopic luminance, the average and standard deviations of the parameters, which belong to the QD integrated LED spectra passing the threshold indicated above, were calculated. These results suggest that choosing the blue component close to 460 nm and the red component close to 610 nm is crucial for the increased mesopic luminance with good color rendition. In addition, the weight of the blue component should be around 150/1000, whereas the relative intensity of the red component should be chosen around 450/1000. Furthermore, it is not possible to use broad red emitters without falling below the performance limitations. Therefore, the red component should be designed using narrow-band emitters with bandwidths of ~ 30 nm. The green and yellow color components may have intermediate amplitudes; however, the designer has more flexibility in choosing the parameters of these color components in contrast with the case for blue and red.

In addition to the general lighting applications, QDs also offer great potential for display backlights. This is mainly because of the easiness in color control and narrow emission of QDs, which in turn allow for reproduction of a large number of colors in liquid crystal displays (LCDs). In Figure 2.17, the National Television System Committee (NTSC) standard color gamut, which indicates the subset of all colors that should be generated, is given along with the potential color gamut of displays using QD-integrated backlights. The black lines in the graph stand for the chromaticity coordinates of the QDs emitting between 460 and 700 nm with emission bandwidth values ranging from 30 to 100 nm. Clearly, correct combinations of QDs can exhibit a much larger color gamut than the color gamut standardized by the NTSC. This means that, by using QD-integrated display backlights, more colors can be generated by LCD televisions and, consequently, the quality of the images displayed can be enhanced significantly and richer viewing experience can be achieved.

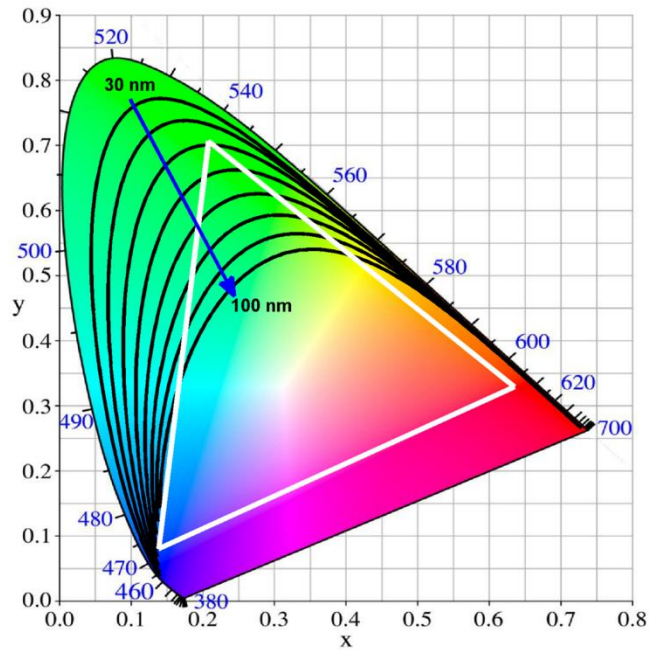


Figure 2.17. CIE 1931 (x,y) chromaticity diagram indicating the NTSC color gamut (white triangle), and color coordinates of QDs having full-width at half-maximum values between 30 and 100 nm with peak emission wavelengths ranging from 460 to 700 nm (black lines). The blue numbers given around the perimeter of the chromaticity diagram are located at the color coordinates of the corresponding monochromatic light. Reproduced with permission from Ref. [12]. © DeGruyter Publishing 2013.

It is worth commenting here on the required properties of the QDs in light of the NTSC color space in Figure 2.18. If a red-green-blue (RGB) light source is designed, the FWHM of the QDs should be at most 50 nm. Otherwise, the green end of the NTSC triangle cannot be included. Moreover, the blue emission should be generated with a source having a FWHM of less than 70 nm. Since the blue color component of QD integrated white LEDs mostly stems from the blue LED, this requirement is not a challenging restriction. In addition, the red QDs emitting around 610 nm can easily satisfy the NTSC color gamut requirements. A QD integrated white LED employing four or more color components can easily achieve color gamuts much larger than the NTSC standards indicate. However, narrow emissions from the green and blue components are still required.

In the discussion above, however, the effects of the filters on the QD emission are omitted. To address this issue, Luo et al.[14] carried out a theoretical study and determined the necessary amplitude, peak emission wavelength, and full-width at half-maximum of QD emission by considering filters used in liquid crystal displays (LCDs) to realize high brightness of the light transmitted through LCD color filters along with a larger color gamut both in CIE 1931 and 1976 color spaces. In this work, the authors calculated the performance of the display by varying the peak emission wavelengths and bandwidths of the blue LED along with green- and red-emitting QDs. The results showed that there is a trade-off between the color gamut and the brightness after considering the transmission spectra of the color filters. As expected, the emitters with narrow emission bandwidths increases the obtained color gamut; however, at the same time this decreases the total overlap with the human eye sensitivity function for the red and blue emitters because of the accompanying shift of the peak emission wavelengths away from 550 nm where the human eye is most sensitive. Therefore, increasing the color gamut comes at the cost of reduced brightness. Considering all of these factors, Luo et al. showed that it is possible to improve the color gamut of the LCD with QD color enrichment by 20% compared to NTSC if the respective peak emission wavelengths of the blue, green, and red components are 447.6, 523.5, and 634.8 nm. The corresponding bandwidths need to be 20, 30, and 30 nm, while the relative amplitudes are 37.3%, 27.8%, and 34.9%, respectively.

2.3 Conjugated Polymer Nanoparticles

Another class of materials that we have used in this thesis work is the conjugated polymer nanoparticles. In this section, we present this material system and their use in light-emitting devices. We will first start with the basic properties of conjugated polymers that are the building blocks of the nanoparticles. Subsequently, we will continue with the conjugated polymer nanoparticles by concentrating on first their preparation techniques and then summarizing their use in optoelectronics.

Polymers are organic molecules consisting of long chains of repeating units. Conjugated polymers are a special structure of polymers in which the carbon

chains undergo sp^2 hybridization [62]. The carbon-carbon bonds in these molecules have a σ -bond occurring between sp^2 orbitals and a π -bond occurring between p_z orbitals. In general, σ -bonds are very strong due to a large overlap of the wavefunction. Therefore, these bonds have a significantly large electronic bandgap and low free electron densities making them electronically and optically inactive. An important function of these bonds is to serve as the backbone of the molecular structure. On the other hand, the wavefunction overlap in π -bonds is rather small making the bonds weaker and forming electronically more active structures especially in polymers having long chains. Theoretical calculations predict almost zero bandgap if all the σ -bonds were of equal lengths. However, in practice, the length of the σ -bonds differs, which results in opening a bandgap for π -bonds. The typical bandgaps of conjugated polymers are around 1.5-3.0 eV enabling optical activity for visible light.

Conjugated polymer nanoparticle (CPNs) are the nanoparticles produced using these polymers. Among their main advantages we can count relatively high quantum yield, high photostability, low toxicity, and cost-effectiveness [15], [63]. Furthermore, the applicability of these CPNs can be controlled by adding various functional or backbone molecules [63], [64]. Their optical features can be tailored by controlling their sizes and aggregation. In general, increasing the size or aggregating the nanoparticles results in increased interchain and intrachain interactions, which consequently increases the nonradiative energy transfer, decreases the quantum yield, and red-shifts the emission spectrum [65], [66]. Attaching functional groups is also known to affect their optical properties [63]. These nanoparticles in general have very broad emission spectra compared to QDs; however, their absorption spectra remain significantly narrow different than the QDs [15]. CPNs have found applications in color-converting LEDs [64], [67]–[69], in organic LEDs [70], [71], solar cells [72]–[74], and bio-imaging [75], [76]. In this thesis, we investigated the nonradiative energy transfer from InGaN/GaN nanopillars to CPNs and also their polymers. We present our work in Chapter 9.

There are three techniques for preparing the CPNs, which are illustrated in Figure 2.18 [63]. The first one is called the nano-precipitation method. It involves dissolving polymers in a good solvent and rapidly injecting this solution into a

poor solvent for the polymers while strongly sonicating. Since the conjugated polymers suddenly experience the presence of the poor solvent, they tend to aggregate and form nanoparticles. Experimental studies indicate that the diameter of the formed nanoparticle increases with increasing conjugated polymer concentration [66], [77]. The second method of CPN formation is called the mini-emulsion technique. In its essence, both techniques are very similar. In both methods, polymers are dissolved in a good solvent and quickly added to a poor solvent under sonication to trigger the nanoparticle formation. However, nano-precipitation method makes use miscible solvent pairs while immiscible solvents are used in mini-emulsion technique. In both techniques surfactants may also be employed to obtain a more stable nanoparticle dispersion. The third technique is the self-assembly method, which employs the electrostatic interaction between polymers of opposite charges. In this technique, these polymers are first separately dissolved and then mixed under continuous stirring. The resulting material is then collected by high-speed centrifugation [65].

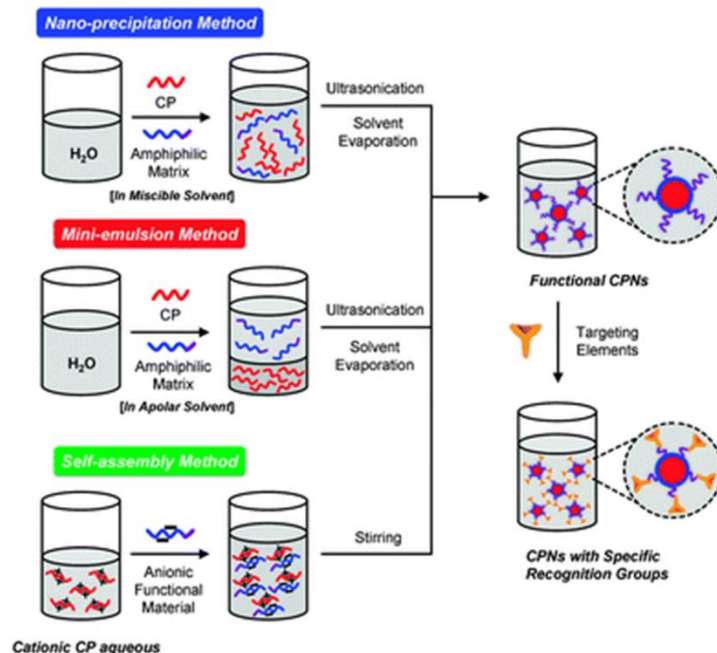


Figure 2.18. Illustration of the conjugated polymer nanoparticle preparation using nano-precipitation, mini-emulsion, and self-assembly techniques. Reproduced with permission from Ref. [63]. © Royal Society of Chemistry 2013.

2.4 Macrocrystals of Quantum Dots

To date high-performance white LEDs using NCs for color-conversion that simultaneously enable successful color rendition capability and optimal spectral overlap with the human eye sensitivity function along with a warm-white shade have been reported [78], [11]. Moreover, electronic displays employing NCs as color converters have been developed and commercialized, e.g., by Samsung [79], [80], Sony [81], and Amazon [82]. Despite their successful deployment, NCs still typically suffer from decreasing quantum yields in their solid films within polymeric encapsulants and low emission stability on LED chips driven at high currents. The rigid conditions during the direct hybridization process of NCs with these host materials are known to degrade the NC emission. Furthermore, the diffusion of oxygen and humidity through the encapsulating materials is another important concern especially when the NCs are subjected to heat, for example, when intimately integrated with LEDs and these hybrid devices are driven at high current densities.

As a remedy to these problems, a new promising method has been proposed by Otto et al.[83] for the incorporation of the NCs into crystalline host matrices, which enables high quantum yields in powder form and solid films together with significantly improved photo- and thermal-stability of the NC emission. The powders of these mixed macrocrystals have further been shown to possess excellent compatibility with the epoxies widely used for encapsulating color converters by the industry. This is an important strength of this material system for the LED and display producers. In addition, we showed these NC-macrocrystals to provide a robust platform for studying environment-sensitive interparticle interactions such as plasmonics [84] and excitonics [85], [86], which we will also present in this thesis in detail in addition to a high-quality white LED demonstration [87] and the development of a green-emitting high-efficiency macrocrystal powder having high emission stability [88]. An interesting application of these materials has also been shown by Kalytchuk et al.[89] as sensitive thermometers using strong variations observed in the emission spectrum of the macrocrystals as a function of the temperature.

To date, CdTe NCs in water [83], CdSe/CdZnSeS/ZnS NCs in water [90] and nonpolar solvents with an alloyed gradient shell [86], [88] and Au nanoparticles in water [84] have been successfully incorporated into macrocrystals. In addition, the incorporation of Cd-free InZnP/ZnS NCs in water have been reported as well [91]. Salts including NaCl, KCl, KBr,[83] borax,[87] and LiCl[88] have been employed as host matrices along with organic crystalline hosts including sucrose [84] and anthracene [86]. In these previous works, the nanoparticles were embedded into the host matrix using one of the three main strategies reported in the literature, which are schematically displayed in Figure 2.19: (i) direct incorporation of NCs via slow solvent evaporation, (ii) vacuum-assisted NC incorporation, and (iii) liquid-liquid-diffusion-assisted-crystallization. For the crystallization process, the colloidal stability of the NCs within the concentrated solution of the host material needs to be high enough to ensure proper, non-aggregated incorporation of the nanocrystals. If the colloidal stability is low, using a host with lower ionic strength in solution [87] or reducing the time needed for the crystallization might be helpful [88], [91].

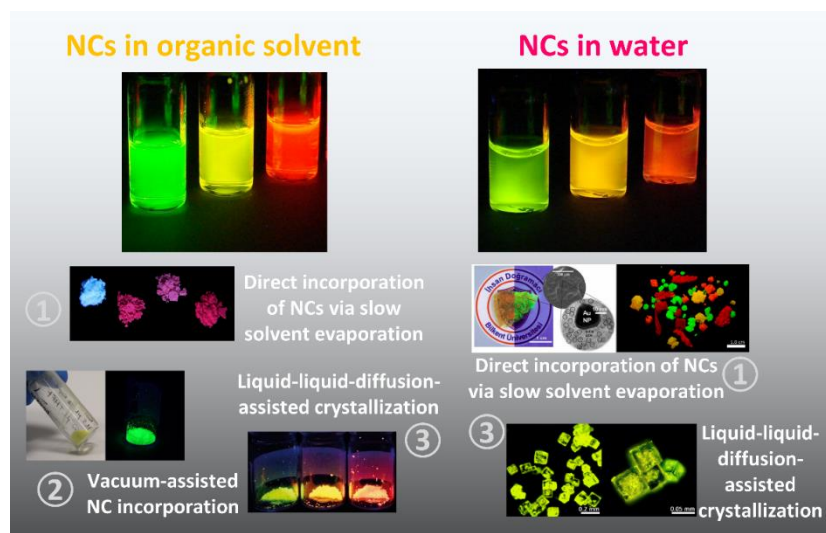


Figure 2.19. Summary of quantum dot nanocrystal (NC) incorporated macrocrystal preparation techniques for NCs in nonpolar organic solvents and in water.

The first method is based on the incorporation of water-soluble NCs (e.g., CdTe) into conventional ionic salt crystals [83] such as sodium chloride (NaCl),

potassium chloride (KCl), and potassium bromide (KBr) or non-ionic molecules such as sucrose [84]. In these works, the mixed macrocrystals of NCs were obtained by blending a saturated salt solution with a batch-specific amount of the NCs. The solutions were kept at 30 °C to promote the evaporation of H₂O and the crystallization was finished when the parental solutions turned colorless. Interestingly, a change from the cubic structure to the octahedral shape was observed when NaCl was utilized as the host matrix. Such different morphology of the host material can be attributed to the free stabilizing agents (TGA or MPA) within the NC-salt solution mixture, which are well known to alter the shape of NaCl crystals from cubic to octahedral [92]. Furthermore, MPA-stabilized NCs turned out to be generally more stable in saturated salt solutions than their TGA-stabilized counterparts. As TGA-capping allows for a better control on the synthesis of CdTe NCs emitting in green to orange spectral regions, efficient incorporation of strongly emitting TGA-capped CdTe NCs into salt matrices is possible. Finally, adjusting the pH of the saturated salt solution and adding small amounts of additional free stabilizer, reproducible incorporation of such NCs is feasible [93].

As a variation of this approach, alternative host matrices were employed to reduce the ionic strength of the saturated salt solutions. For example, sugar, which is a non-ionic organic molecule forming large crystals, has been shown to allow for the simultaneous incorporation of CdTe NCs together with Au nanoparticles [84]. Since the incorporation of citrate-capped metal nanoparticles was not possible using ionic hosts due to the induced aggregation, the utilization of sugar enabled plasmonic interactions occurring between NCs and metal nanoparticles, which will be further discussed in Chapter 6 of this thesis. Alternatively, borax (Na₂B₄O₇ · 10H₂O) has been used to immobilize core/alloyed-shell NCs following a ligand exchange with mercaptopropionic acid (MPA). Since it has a reduced ionic strength in comparison to alkali halides, higher NC colloidal stability in the crystallization mixture could be realized. More importantly, higher amounts of NC incorporation into macrocrystals have been successfully reported [87]. We will present this work in Chapter 5 of the thesis. To incorporate the NCs dispersed in organic solvents, anthracene has

been employed by utilizing the solubility of anthracene in chloroform, which can simultaneously disperse oleic acid capped NCs [86].

The second method provides a fast pathway for the incorporation of NCs dispersed in organic solvents into the inorganic or organic molecules without a prior ligand exchange. In this technique, NCs dispersed in organic solvents are directly incorporated into the organic solvent-soluble salts such as lithium chloride (LiCl) [85], [88]. In these reports dry tetrahydrofuran (THF) was used to dissolve LiCl, which is also a relatively good solvent for the NCs. In order to incorporate NCs into LiCl, the NCs were dried, re-dispersed in THF, and mixed with LiCl-saturated THF solution. Subsequently, the solvent was evaporated quickly in a vacuum chamber, resulting in a complete mixed macrocrystal formation within a few minutes. We employed this technique for obtaining high-efficiency, high-stability green-emitting powders [88], and further studied the exciton transfer between green- and red-emitting NCs in LiCl host matrix [85].

The third method is the liquid-liquid-diffusion-assisted crystallization (LLDC) [91] relying on the solubility difference of inorganic salts in solvents with various polarities. In this technique, due to the reduced solubility of NaCl in water by the interdiffusion of the orthogonal solvent, the crystallization can be completed in less than one day lowering the time needed to produce mixed macrocrystals by more than one order of magnitude in comparison with the crystallization techniques based on the slow evaporation of solvent [83]. Therefore, a mixture of NC solution and NaCl was placed below a layer of methanol, allowing the methanol to diffuse into the NC-layer and be stored for roughly 15 h. Moreover, by adapting a two-step seed-mediated LLDC, the direct application of oil-based NCs for co-crystallization with salts without a prior phase transfer into water was achieved. Here, NaCl-saturated methanol was added to the NCs in chloroform (CHCl_3) forming initially mixed macrocrystal seeds, which were then redispersed in pure methanol. In the second step, NaCl dissolved in H_2O was injected under the seed-methanol layer and stored for 15 h for the crystal growth.

2.5 Nonradiative Energy Transfer

In this part of the thesis, we are interested in near-field interactions that we employ to improve the emission capabilities of the colloidal semiconductor materials. The first interaction that we cover is the nonradiative energy transfer (NRET). There are two main mechanisms of this interaction. The first one is called the Dexter energy transfer, which is also known as the electron exchange energy transfer [94]. As presented in Figure 2.20, once the donor is excited, an electron-hole pair is formed. If the donor and acceptors are close enough, the wavefunctions may overlap, which allows for the transfer of the donor electron to acceptor and the hole of the acceptor to donor. It is here worth noting that this transfer is subject to spin conservation rules. As a result, the acceptor becomes in the excited state while the donor molecule turns to the ground state. Since the extend that the wavefunctions of nano-emitters can spread are in general limited with the dimensions of the nanoparticles, this phenomenon can only take place at very short distances less than a few nanometers [95]. As shown in Equation 2.35, the Dexter energy transfer rate (γ_{Dexter}) has an exponential dependence on distance (r). The transfer rate is a function of the van der Waals radii (L) and it is proportional to a constant (K) expressing the orbital interactions and the spectral overlap of the donor emission and acceptor absorption spectrum (J) (see Equation 2.36). In this equation, $\epsilon_A(\lambda)$ stands for the spectral molar extinction coefficient of the acceptor and $f_D(\lambda)$ is the normalized emission spectrum of the donor.

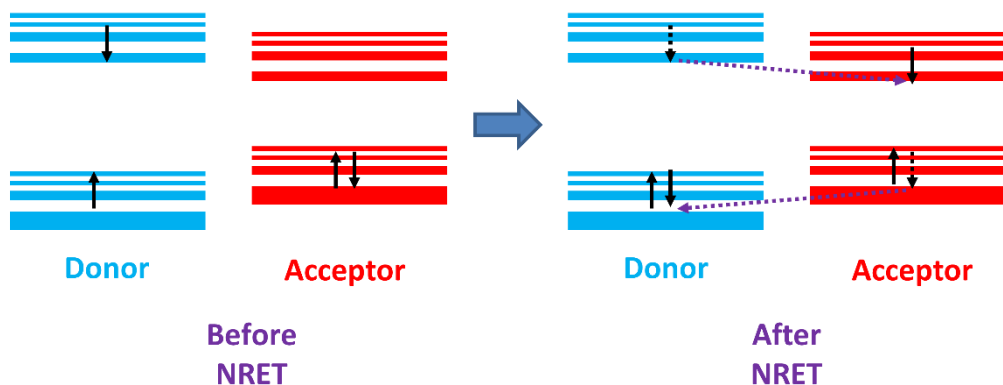


Figure 2.20. Illustration of Dexter-type nonradiative energy transfer.

$$\gamma_{Dexter} = KJe^{-2r/L} \quad (2.35)$$

$$J = \int \varepsilon_A(\lambda) f_D(\lambda) \lambda^4 d\lambda \quad (2.36)$$

Since the Dexter energy transfer is another recombination mechanism for the donor in addition to radiative and nonradiative recombinations, the total exciton recombination rate of the donor increases when energy transfer takes place. The rate of the energy transfer (γ_{Dexter}) can be calculated by using Equation 2.37 where the total donor recombination rates in the presence and absence of the acceptor ($\gamma_{total,DA}$ and $\gamma_{total,D}$, respectively) are equal to $1/\tau_{DA}$ and $1/\tau_D$, respectively. The energy transfer efficiency (η), which is also called the quantum efficiency of the energy transfer process, can be expressed as in [Equation 2.38](#).

$$\gamma_{Dexter} = \gamma_{DA} - \gamma_D = 1/\tau_{DA} - 1/\tau_D \quad (2.37)$$

$$\eta = \frac{\gamma_{Dexter}}{\gamma_{DA}} = 1 - \frac{\tau_{DA}}{\tau_D} \quad (2.38)$$

The energy transfer process also affects the fluorescence spectrum. Upon the occurrence of this electron exchange transfer, the donor emission is quenched since the donor turns to the ground state without emission while acceptor emission is expected to strengthen owing to the generation of an acceptor exciton.

The second nonradiative energy transfer mechanism that we would like to cover in this part of the thesis is the Förster resonance energy transfer (FRET). Different than the Dexter energy transfer, FRET process relies on the transfer of exciton (Figure 2.21); therefore, it is also called as the exciton transfer. From an electromagnetic interaction perspective, FRET involves the electromagnetic coupling between donor and acceptor emitters [96], [97]. According to classic electromagnetic theory, an electron hole pair can be modeled as a dipole with a dipole moment of \bar{p} . The resulting electric field in polar coordinates can be expressed as given in Equation 2.39- 2.41 where n is the refractive index and κ is the dipole orientation factor. The first terms in the brackets of Equations 2.40 and 2.41 denote near-field interactions between a donor-acceptor pair [98]. Since the relation between energy and electric field is quadratic, the dependence of this nonradiative energy transfer follows $1/r^6$ dependence. However, this is only valid when the acceptor is a point dipole. This dependence becomes $1/r^5$ for one

dimensional acceptors and $1/r^4$ for two dimensional acceptors [99]. Without losing generality, from this point on we will assume point sources and use $1/r^6$ dependence.

$$\bar{E}_A = E_r \hat{r} + E_\theta \hat{\theta} \quad (2.39)$$

$$E_r = \frac{2}{n^2} \left\{ \frac{1}{r^3} - i \frac{\kappa}{r^2} + \frac{\kappa^2}{r^2} \right\} \sin \theta p \quad (2.40)$$

$$E_\theta = \frac{1}{n^2} \left\{ \frac{1}{r^3} - i \frac{\kappa}{r^2} + \frac{\kappa^2}{r^2} \right\} \cos \theta p \quad (2.41)$$

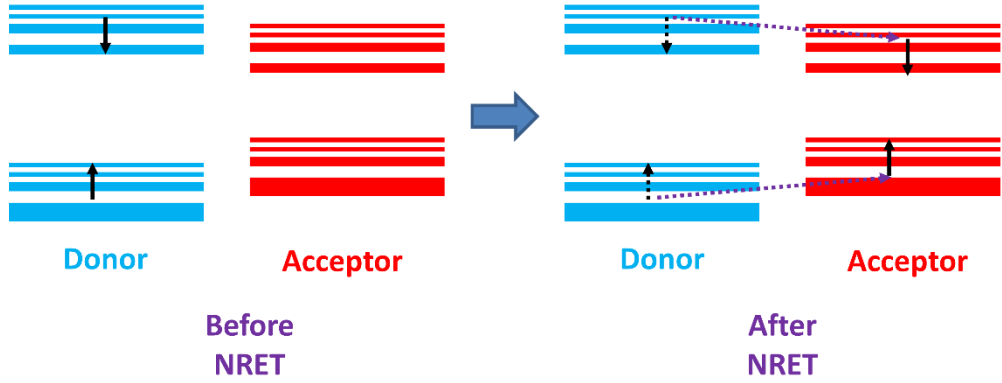


Figure 2.21. Illustration of Förster-type nonradiative energy transfer.

The distance dependence of the FRET efficiency (η_{FRET}) is given in Equation (2.42) where R_0 is defined as the Förster distance at which the FRET efficiency is half.

$$\eta_{FRET} = \frac{1}{1 + \frac{r^6}{R_0^6}} \quad (2.42)$$

The rate of the FRET process (γ_{FRET}) depends on the orientations of donor and acceptors, which is expressed using the dipole orientation factor κ , the overlap integral J given in Equation 2.36, refractive index of the medium n , the lifetime of the donor in the absence of acceptor τ_D , and the distance r as shown in Equation 2.43 [95].

$$\gamma_{FRET} = \frac{9\kappa^2 c^4}{8\pi\tau_D n^4 r^6} J \quad (2.43)$$

The Förster distance, on the other hand, shows dependence on the donor quantum efficiency Φ in addition to the overlap integral J , the refractive index n , and the dipole orientation factor κ as given in Equation 2.44.

$$R_0^6 = 8.79 \times 10^{23} \frac{\kappa^2 \Phi J}{n^4} \quad (2.44)$$

The FRET rate γ_{FRET} can be calculated from the total recombination rate of the donor in the presence ($\gamma_{\text{DA}}=1/\tau_{\text{DA}}$) and absence of the acceptor ($\gamma_{\text{D}}=1/\tau_{\text{D}}$) as given in Equation 2.45. Subsequently, the FRET efficiency can be calculated as shown in Equation 2.46.

$$\gamma_{\text{FRET}} = \gamma_{\text{DA}} - \gamma_{\text{D}} = 1/\tau_{\text{DA}} - 1/\tau_{\text{D}} \quad (2.45)$$

$$\eta_{\text{FRET}} = \frac{\gamma_{\text{FRET}}}{\gamma_{\text{DA}}} = 1 - \frac{\tau_{\text{DA}}}{\tau_{\text{D}}} \quad (2.46)$$

Similar to the Dexter energy transfer, the donor emission quenches when FRET takes place. Therefore, it is also possible to measure the FRET efficiency using the donor emission intensities as given in Equation 2.47 where I_{D} and I_{DA} are the donor emission intensities in the absence and presence of acceptor, respectively.

$$\eta_{\text{FRET}} = 1 - \frac{I_{\text{DA}}}{I_{\text{D}}} \quad (2.47)$$

The most ubiquitous use of FRET has been in bio-imaging, sensing, and investigation of intermolecular interactions [95], [97]. However, within the last fifteen years the use of FRET has been extended toward optoelectronics for the purposes of increasing the efficiencies in light-emitting devices [58] and in solar cells [95]. In this thesis work, we employed the FRET interaction for increasing the emission capabilities of conjugated polymer nanoparticles by interacting them with InGaN/GaN quantum well nanopillars [100] and also for increasing the long wavelength emission intensity in the QD integrated salt powders [85].

2.6 Plasmonics

The second type of near-field interaction that we employed in this thesis work to improve the emission capability of the nano-emitters is plasmonics. In its broadest sense, plasmonics is the science investigating the light-matter

interactions with a focus on charge density oscillations. Here, we first explain why electron oscillations occur using classic electromagnetics. Subsequently, we provide a brief overview of surface plasmon polaritons and then continue with the localized surface plasmons. Finally, we finish this section by discussing the plasmonic fluorescence enhancement.

The high free electron concentration of the metals allows us to study their optical properties by using the free electron gas model [101]. The first step of this modeling process is writing an equation of motion as given in Equation 2.48 where m_e is the electron mass, e is the electron charge, \bar{E} is the electric-field, $\bar{u}(t)$ is the position vector, and γ is the damping factor used for modeling the damping via collisions. The final term on the left hand side of the equation describes the interband transitions characterized by bound electron with a resonance frequency of ω_0 .

$$m_e \ddot{\bar{u}} + m_e \gamma \dot{\bar{u}} + m_e \omega_0^2 \bar{u} = -e\bar{E} \quad (2.48)$$

Assuming a time-harmonic displacement of the electrons in the form of $\bar{u}(t) = \bar{u} \exp(-i\omega t)$, $\bar{u}(t)$ becomes as given in Equation 2.49.

$$\bar{u}(t) = \frac{e\bar{E}}{m_e \omega^2 + i\omega\gamma - m_e \omega_0^2} \quad (2.49)$$

Since the macroscopic polarization \bar{P} is given by $\bar{P} = -ne\bar{u}$ where n is the electron density and the dielectric displacement vector, which is related to the electric field and polarization by $\bar{D} = \epsilon_0 \bar{E} + \bar{P} = \epsilon_0(\epsilon_1 + i\epsilon_2)\bar{E}$, we obtain the real and imaginary parts of the dielectric constant as given in Equations 2.50 and 2.51 where ω_p is the plasma frequency and equals to $ne^2/\epsilon_0 m_e$. These equations show that dielectric function in metals show a clear resonance behavior, which can be characterized as a Lorentzian function. As a result of this resonance behavior, we observe improved absorption and field enhancement at a certain range of frequencies whose bandwidth is basically governed by γ .

$$\epsilon_1 = 1 - \frac{\omega_p^2(\omega^2 - \omega_0^2)}{(\omega^2 - \omega_0^2)^2 + \gamma^2 \omega^2} \quad (2.50)$$

$$\varepsilon_2 = \frac{\omega_p^2 \gamma \omega}{(\omega^2 - \omega_0^2)^2 + \gamma^2 \omega^2} \quad (2.51)$$

After briefly introducing the source of the resonance behavior in metals, now we briefly discuss the surface plasmon polaritons (SPPs), which are extensively employed in sensing, imaging, and optoelectronics [101]–[104]. SPPs are electromagnetic fields that are perpendicularly confined at the interface of a dielectric and conductor while propagating along the interface. The observed propagation of SPPs stems from the coupling of an external electromagnetic field to the oscillations of electrons at the interface. A simple geometry allowing for the creation of SPPs is illustrated in Figure 2.22. The structure consists of a dielectric region for $z > 0$ having a real dielectric function of $\varepsilon_{dielectric} > 0$ and a conducting region for $z < 0$ having a real dielectric function of $\varepsilon_{conductor} < 0$ at the frequencies of interest.

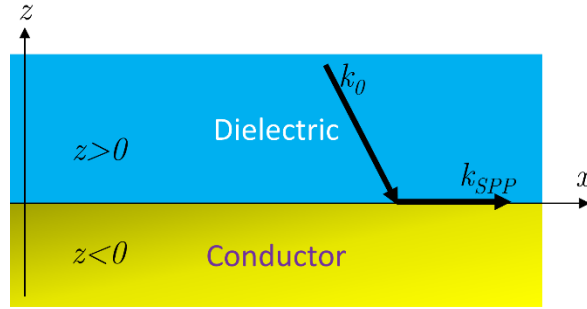


Figure 2.22. Illustration of a simple geometry allowing for the creation of SPP.

As described in Ref. [101] for the TM mode, the continuity condition enforces the relation described by Equation 2.52, where $k_{dielectric}$ and $k_{conductor}$ are the wavenumbers in dielectric and conductor regions, respectively.

$$\frac{k_{dielectric}}{k_{conductor}} = -\frac{\varepsilon_{dielectric}}{\varepsilon_{conductor}} \quad (2.52)$$

Another condition that relates the wavenumber of the propagating mode (k_{SPP}) to the dielectric functions and wavenumbers stems from the wave equation for the TM modes given by Equation 2.53. As a result, we obtain the relations described in Equation 2.54 and 2.55 where k_0 is the free-space wavenumber.

$$\frac{\partial^2 H_y}{\partial z^2} + (k_0^2 \epsilon - k_{SPP}^2) H_y = 0 \quad (2.53)$$

$$k_{dielectric}^2 = (k_{SPP}^2 - k_0^2 \epsilon_{dielectric}) \quad (2.54)$$

$$k_{conductor}^2 = (k_{SPP}^2 - k_0^2 \epsilon_{conductor}) \quad (2.55)$$

Solving Equations 2.52, 2.54, and 2.55 together gives the dispersion relation of the SPPs, which is provided in Equation 2.56.

$$k_{SPP} = k_0 \sqrt{\frac{\epsilon_{dielectric} \epsilon_{conductor}}{\epsilon_{dielectric} + \epsilon_{conductor}}} \quad (2.56)$$

At this point it is worth mentioning that the solutions of the wave equation only allows for the TM modes at the interface; thus, no TE modes can be confined at the dielectric-conductor interface [101]. After this derivation of the SPP dispersion relation, the most obvious observation is that at a fixed wavenumber SPPs can be formed at smaller frequencies. At very high wavenumbers, the frequency of the oscillations asymptotically approaches a frequency ω_{SP} , which is called the surface plasmon frequency and remains below ω_p . For further details on SPP, the reader can refer to Refs. [51], [101].

Different than SPPs, LSPs do not propagate; instead, they exist because of the spherical surface of nanoparticles that restores forces enabling the oscillation of the applied electromagnetic field. We start our discussion by assuming a spherical conductor having a radius of R and a dielectric constant of $\epsilon_{conductor}$. For the sake of simplicity, we assume the medium where the metallic sphere is placed to have a uniform dielectric constant of $\epsilon_{dielectric}$ and consider the applied electric field to be $\vec{E} = E_0 \hat{z}$ (Figure 2.23). Considering the symmetry of the particle, the potentials in the interior (Φ_{in}) and exterior (Φ_{out}) of the particle become as given in Equations 2.57 and 2.58, respectively [105].

$$\Phi_{in} = -\frac{3\epsilon_{dielectric}}{\epsilon_{conductor} + 2\epsilon_{dielectric}} E_0 \cos \theta \quad (2.57)$$

$$\Phi_{out} = -E_0 r \cos \theta + \frac{\epsilon_{conductor} - \epsilon_{dielectric}}{\epsilon_{conductor} + 2\epsilon_{dielectric}} E_0 R^3 \frac{\cos \theta}{r^2} \quad (2.58)$$

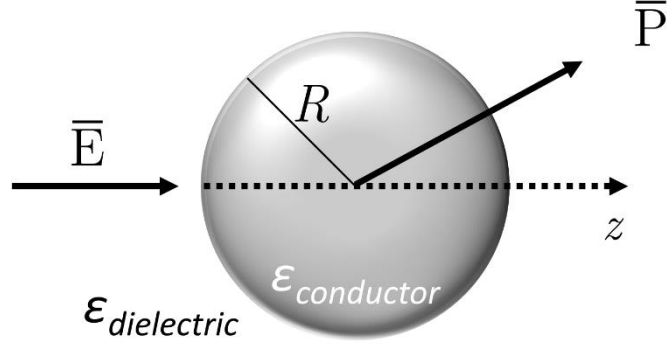


Figure 2.23. Illustration of a spherical conducting nanoparticle subject to electric field and induced macroscopic polarization.

According to Maier [101], Φ_{out} occurs due to the superposition of the excitation field and the dipole formed in the metallic sphere. This allows us to state the outside potential using a dipole moment \bar{p} as described by Equations 2.59 and 2.60.

$$\Phi_{out} = -E_0 r \cos \theta + \frac{\bar{p} \cdot \bar{r}}{4\pi\epsilon_0\epsilon_{dielectric}r^3} \quad (2.59)$$

$$\bar{p} = 4\pi\epsilon_0\epsilon_{conductor}R^3 \frac{\epsilon_{conductor} - \epsilon_{dielectric}}{\epsilon_{conductor} + 2\epsilon_{dielectric}} \bar{E}_0 \quad (2.60)$$

Using the relation of $\bar{p} = \epsilon_0\epsilon_{conductor}\alpha\bar{E}_0$ where α is the polarizability, we obtain Equation 2.61. From this calculation, we see that the polarizability acquires a resonance when $|\epsilon_{dielectric} + 2\epsilon_{conductor}|$ is minimized.

$$\alpha = 4\pi R^3 \frac{\epsilon_{conductor} - \epsilon_{dielectric}}{\epsilon_{conductor} + 2\epsilon_{dielectric}} \quad (2.61)$$

The calculation of polarizability also allows us to find scattering (C_{sca}) and absorption (C_{abs}) cross-sections, which are given by Equations 2.62 and 2.63, respectively [106]. Because the nanoparticle possesses a resonant behavior in its polarizability, this resonance enhancement is also transferred to the scattering and absorption cross-sections.

$$C_{sca} = \frac{8\pi k^4}{3} R^6 \left| \frac{\epsilon_{conductor} - \epsilon_{dielectric}}{\epsilon_{conductor} + 2\epsilon_{dielectric}} \right|^2 \quad (2.62)$$

$$C_{abs} = 4\pi k R^3 \text{Im} \left[\frac{\epsilon_{conductor} - \epsilon_{dielectric}}{\epsilon_{conductor} + 2\epsilon_{dielectric}} \right] \quad (2.63)$$

This resonant behavior also impacts the electric fields in the interior (\bar{E}_{in}) and exterior (\bar{E}_{out}) of the nanoparticle in the near-field regime, which are given by Equations 2.64 and 2.65, where \hat{n} is the unit vector directed toward a point of interest [105].

$$\bar{E}_{in} = \frac{3\epsilon_{dielectric}}{\epsilon_{conductor} + 2\epsilon_{dielectric}} \bar{E}_0 \quad (2.64)$$

$$\bar{E}_{out} = \bar{E}_o + \frac{3\hat{n}(\hat{n} \cdot \bar{p}) - \bar{p}}{4\pi\epsilon_0\epsilon_{conductor}r^3} \quad (2.65)$$

This resonant enhancement in the outer region of the nanoparticle is the source of the resonance enhancement occurring in the near-field of the metal nanoparticles. Since the radiative recombination rate is proportional to the electric field intensity, resonance enhancement is expected when an emitter is placed in the vicinity of a metal nanoparticle. The enhancement factor is defined as the ratio of the electric field intensities around the nano-emitter in the presence and absence of the metal nanoparticle [107]. However, at the same time another near-field interaction, which is the nonradiative energy transfer, may act as the quencher of the emission process because of the overlap between the fluorescence spectrum of the emitter and the absorption spectrum of the metal nanoparticle.

Govorov et al. studied the conditions under which the fluorescence enhancement is the dominant interaction and under which the nonradiative energy transfer is stronger [107]. He found that when the nano-emitter is surrounded by metal nanoparticles, the nonradiative energy transfer is the dominant interaction causing the emission to quench. On the other hand, the fluorescence enhancement becomes stronger in the case that the metal nanoparticle is surrounded by the nano-emitters. Another important finding of this study is that the fluorescence enhancement is more probable if the quantum efficiency of the emitter is low. The enhancement becomes more and more improbable as the quantum efficiency increases.

At this point, it is also worth mentioning another mechanism for increasing the emission intensity via plasmonic coupling. When the metal nanoparticle is excited by optical excitation, the electric field intensity in the near-field of this nanoparticle intensifies. When an emitter, which is capable of absorbing this enhanced electromagnetic field at the excitation frequency, is placed in the

vicinity of the metal nanoparticle, the total amount of the absorbed energy is expected to increase. As a result, we expect the fluorescence intensity of the emitter to increase. Different than the previous case, here we do not expect the quantum efficiency of the nano-emitter to increase by assuming that other nonradiative transitions remain unchanged as long as we stay in the linear regime.

In our thesis work we employed the fluorescence enhancement phenomenon described above to increase the quantum efficiency of the green-emitting CdTe QDs, which we co-immobilize within a crystalline matrix together with Au nanoparticles [84]. We present the details of this study in Chapter 6.

Chapter 3

Biological Rhythm Friendly Display Lighting with Nanocrystal Quantum Dots

Acquiring a balanced circadian rhythm, which is also known as the daily biological rhythm, plays a critical role for human health [108]. For example, it is known that a regular day/night routine helps reducing seasonal affective disorder [109], increasing the concentration of nightshift workers [110], and helping teenagers to start the day earlier [111]. Disruption of the regular daily rhythm, on the other hand, is linked to health problems including depression [112] and even some cancer types [113]. Therefore, the human daily biorhythm (i.e., circadian rhythm) has to be considered while designing devices that have the capability to shift the biological clock. In this chapter of the thesis, we approach this problem from the perspective of a display backlight design using nanocrystal (NC) quantum dot (QD) based color converters and find that nanocrystal enrichment may lead to a substantially reduced effect on body clock.

3.1 Introduction

The backbone of our study lies on the discovery of a third photoreceptor in the human retina called the intrinsically photosensitive retinal ganglion cell (ipRGC) [32]. Different than their sister photoreceptors cones and rods, the main function of ipRGCs is to help the suprachiasmatic nuclei to control the circadian cycle through melatonin secretion although rods and cones were shown to provide input to ipRGCs in the absence of melanopsin, though at a reduced level [31], [114]. While the secretion of the melatonin occurs under dark ambiance through its interaction with suprachiasmatic nuclei to send the “night” signal to the body, it ceases upon the exposure of ipRGC to light at a sufficient level and for a

sufficient duration. Hence, prolonged exposure to display backlights [115], whose spectra match the sensitivity curve of the ipRGCs, may severely affect the melatonin secretion during the night. Consequently, the circadian cycle is affected in a delaying or advancing manner [108]. In 2011, Figueiro et al. reported that the cathode ray tube computer screens cause a slightly suppressed melatonin secretion after two hours of exposure in the night [116]. Moreover, inclusion of the blue LED light of 40 lux was found to significantly decrease the melatonin concentration. Another study of the same group further reported that the use of tablets for two hours before the sleep decreased the melatonin concentration in the saliva by 23% [117]. Furthermore, an additional blue light impinging on the eye was shown to suppress the melatonin concentration by 66%. In an independent study, Cajochen et al. compared the effects of the LED and fluorescent backlighting on the circadian cycle [118]. They found that the LED backlighting hinders and delays the melatonin secretion compared to a fluorescent lamp backlit display after five hours of exposure in the night.

Since the current LED backlighting technology is far from circadian rhythm friendliness [116]–[118], adding the feature of circadian compatibility to the backlight spectrum in a systematic manner is an important but hitherto disregarded design problem. Current software based solutions such as F.lux [119] and Redshift [120] try to solve this problem by adjusting the correlated color temperature of the backlight according to that of the sun depending on the location and time of the day. However, this method undesirably changes the colors produced by the display and its performance may change from display to display. Therefore, a systematic approach starting from understanding the display backlighting is necessary to address the circadian rhythm friendliness problem while avoiding these aforementioned issues.

The design of a circadian rhythm friendly display requires the fine-tuning of the backlight spectrum, which cannot be accomplished using broadband emitters like phosphors that are commonly used as the color converters in display backlights. Furthermore, their broad emission spectrum limits the color span, which is not a desirable aspect for a display. On top of these, emerging supply problems of the rare earth elements, which are the building blocks of the color converting phosphors, have further raised questions for their sustainable use [9].

As discussed earlier in the thesis, the multi-chip approach employing the integration of individual LED chips emitting different colors suffers mainly from the high cost and increased complexity of production. As a remedy to the problems, nanocrystal quantum dots that are narrow-band color converters step forward [57], [10], [121]. Their narrow-band emission and tunability of the emission color via material and size engineering allow for careful spectral design, which leads to the fine-tuning of the backlight spectrum for various applications [12], [16], [58] together with the broadening of the color span [122].

In this study, we introduced the perspective of daily biorhythm friendliness to our colloidal quantum dot integrated LED (QD-LED) designs using the circadian models of Rea [34], Enezi [36], and Gall [35]. Our findings elucidated a 33% weaker effect of the designed QD-LEDs on the circadian rhythm when the color span provided by the QD-LED is the same as that of the YAG:Ce LED. Furthermore, if the quantum dots are selected correctly to realize the color coverage of National Television Standards Committee (NTSC), the designed QD-LED backlight exhibits a 34% wider color gamut together with a 4.1% reduced effect on the circadian rhythm compared to YAG:Ce LED backlight. These findings show that QD-LEDs are excellent candidates for realizing these circadian rhythm friendly backlights thanks to the spectral tunability and purity of these nanocrystal quantum dots.

3.2. Computational Methodology

Our calculations constituted of two major steps. The first one is the determination of the QDs, utilizing which NTSC standards can be satisfied (Figure 3.1) by considering the color filters used in LCDs. In our calculations, we modelled the emission of QDs and the pump LED using Gaussian functions and generated the spectrum of a three-color mixing backlight. The peak emission wavelength of the blue (short wavelength) component was varied between 400 and 495 nm with a 5 nm step. Similarly, the emission wavelengths of the green (middle wavelength) and red (long wavelength) components were varied between 500-595 nm (for the green) and 600-700 nm (for the red), again with 5 nm step sizes. Moreover, the bandwidth of the emission spectra was varied between 20 and 50 nm with 5 nm steps. It was found out that even a bandwidth of 20 nm of

the red QDs cannot satisfy the NTSC condition for red, which is also the case for red LED chips. Therefore, we varied the red point condition by equating the chromaticity point of a regular red LED used for LCD backlighting. Also considering the effect of color filters, the red chromaticity point condition was moved to $(0.6918, 0.3047)$. The resulting color gamut is represented in Figure 3.1 as continuous black lines while the chromaticity points of the allowed color components were shown as the white region on the same figure. The allowed color region indicates the blue, green, and red chromaticity points that ensure the coverage of the targeted color gamut.

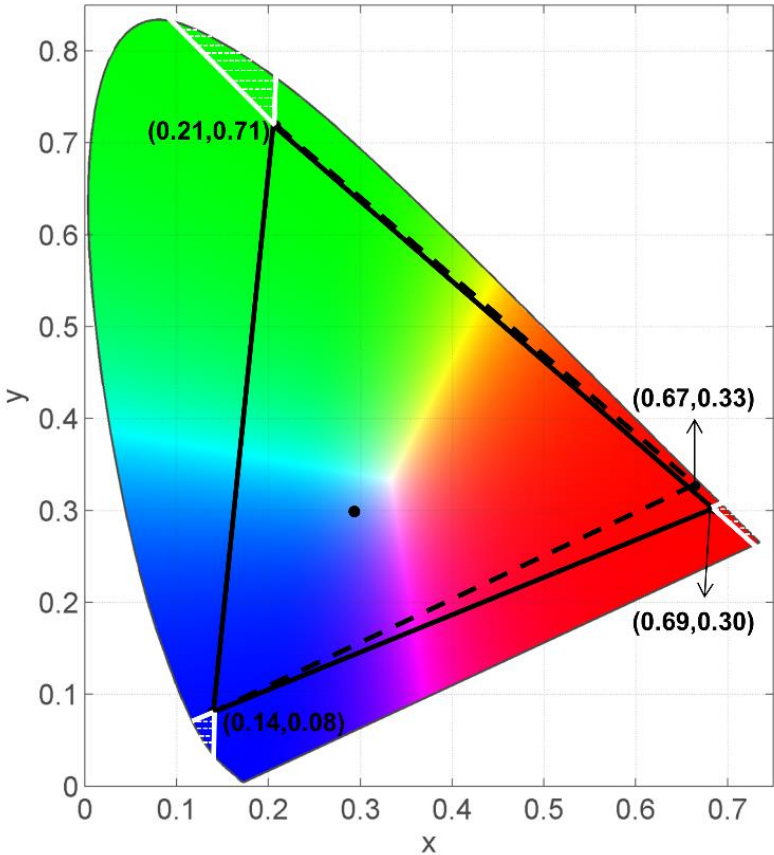


Figure 3.1. National Television Standards Committee color gamut (dashed) along with the modified color gamut (line) used in this study. The white dashed regions correspond to allowable chromaticity points of individual color components to realize the targeted color gamut. The black dot in the middle shows the chromaticity point of the blackbody radiator at 9,000 K.

After the identification of the color components, which can be realized using QDs and satisfy the targeted color gamut conditions after passing the color filters, we design the white QD-LEDs suitable for a display using the requirements listed in Lumileds Application Note [123]. Accordingly, we set the correlated color temperature (CCT) of the backlight to 9,000 K and the luminance to 180 cd/m² by finding the required amplitudes of each color components using a supervised learning algorithm. Considering a typical viewing angle of 2.6 sr stated in Lumileds Application Note [123], the corresponding illuminance becomes 468 lm/m². Finally, a YAG:Ce phosphor integrated LED possessing the same illuminance at the same CCT was used to compare with the QD-LED backlit displays.

As the second step of the study, we calculated the effectiveness of the light sources in suppressing melatonin and compared with a YAG:Ce phosphor integrated LED. The circadian performance of the displays was evaluated using all the three different existing models in the literature. The first approach known as the circadian light (CL) method was developed by Rea et al. [34] In this model, it is aimed to reveal the effect of light on the circadian rhythm by considering the contributions of the visual photoreceptors in addition to the ipRGC. However, opponents of this method argue that the effect of visual photoreceptors could be reduced by central processing [36] considering that some neurons in the brain robustly react to melanopsin activity but not to that of cones [37]. The method developed by Gall employs this idea and evaluates the effects of lighting on the human circadian response by using a circadian effect function [35], which was empirically defined using the melatonin suppression measurements of Brainard [38] and Thapan [39]. Later, in 2011 Enezi et al. conducted experiments on mice and defined the melanopic spectral efficiency function [36]. These three models were later comparatively studied by Rea et al., and it was concluded that there is no experimental finding to reject one model in favor of another [40]. Thus, we made use all of these circadian rhythm models in this thesis work.

However, all of these models present their outputs in numbers of different scales. Thus, bringing these results to the same scale is strictly necessary to make a healthy comparison. For this reason, we performed a scaling operation to

each model similar to the one conducted in Rea et al. [40]. We divided the resulting numbers of the test spectrum to the circadian response of standard illuminant A at 468 lm/m² for each of the models, i.e., the circadian light (CL) developed by Rea [34], the circadian effect factor developed by Gall [35], and the melanopic sensitivity developed by Enezi [36]. Since all these models need to be treated equally, we employed a multi-objective optimization by defining a utopia point indicating no melatonin suppression. The normalized values of circadian light (CL), circadian effect factor (CEF), and melanopic sensitivity function (Mel) constituted the dimensions of the circadian response.

Finally, the performance of each QD-LED spectrum was evaluated by calculating the Euclidean distance from the utopia point, which designates the performance of a hypothetical light source causing no disruption on the circadian rhythm for all of these three models. Spectra taking the closest position to the utopia point were considered as the most circadian rhythm friendly QD-LED designs. The equation used in the calculations of circadian distance ($f_{circadian}$) is shown in Equation 3.1 and its calculation methodology is illustrated in Figure 3.2(a). At this point, it is important to mention that CL model accounts for an exposure duration of one hour, while the remaining two models do not put any restriction on the exposure duration. Therefore, our quantitative results should be evaluated considering this one-hour duration; however, our spectral designs should qualitatively possess circadian rhythm friendliness for longer exposure durations as well.

$$f_{circadian} = \sqrt{\left(\frac{CEF(QD)}{CEF(III A)}\right)^2 + \left(\frac{Mel(QD)}{Mel(III A)}\right)^2 + \left(\frac{CL(QD)}{CL(III A)}\right)^2} \quad (3.1)$$

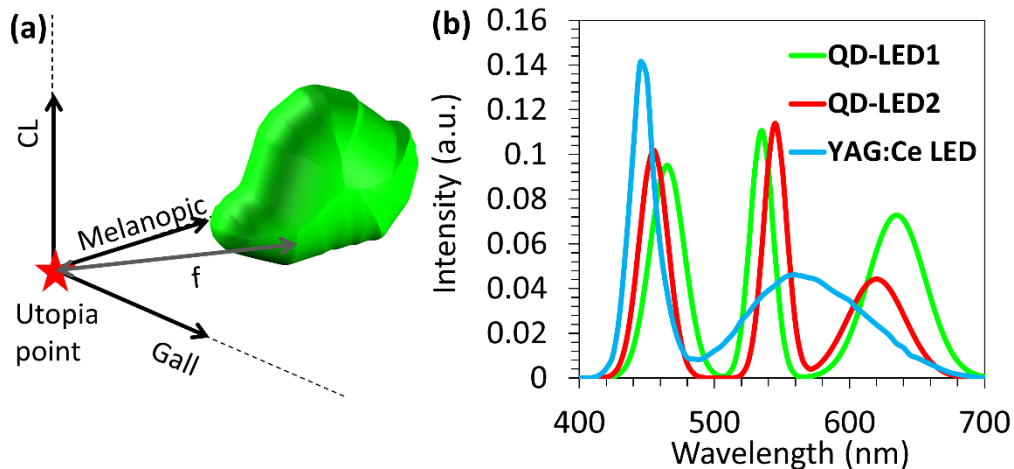


Figure 3.2. (a) Illustration of the computation setup to evaluate the effectiveness of the light source in suppressing melatonin. Our approach is developed based on the three existing models by employing a multi-objective optimization technique. (b) Spectra of the YAG:Ce LED, QD-LED acquiring the targeted color gamut in Figure 3.1 (QD-LED₁), and QD-LED reproducing the color gamut of the YAG:Ce LED (QD-LED₂).

3.3 Results and Discussion

The first point that deserves attention in our analyses is the spectral requirement results regarding the satisfaction of the targeted color gamut (Table 3.1). These calculations revealed that the blue color (short wavelength) component is allowed to acquire only 465 and 470 nm as the peak emission wavelength among the simulated range of 400-495 nm (with the 5 nm step size). When 465 nm is chosen, the minimum and maximum allowed full-width at half-maximum values ($\Delta\lambda$) are 30 and 50 nm, respectively. On the other hand, the selection of 470 nm as the blue emission peak requires the use of more saturated colors having $\Delta\lambda \leq 30$ nm. When the green color components (middle wavelength) are considered, the allowed peak emission wavelengths turn out to be in the range of 525-535 nm within the investigated interval of 500-595 nm. As opposed to the case of blue, the green color component requires high color purity having a $\Delta\lambda$ of 20 nm, which is the narrowest $\Delta\lambda$ used in our computation. When the peak emission wavelength is chosen to be 525 nm, the largest allowed bandwidth turns out to be 30 nm. This value increases to 45 and 40 nm in the case that 530 and 535 nm

are selected, respectively. For the red color component (long wavelength), the allowed peak emission wavelengths span a wider range between 625 and 650 nm within the calculation range of 600-700 nm. It was found out that high purity red color is allowed between 625 and 635 nm indicated by a minimum $\Delta\lambda$ of 20 nm. However, further increase of the peak emission wavelength towards 650 nm enforces the emission to acquire a larger minimum $\Delta\lambda$ of 30, 40, and 45 nm for the peak emission wavelengths of 640, 645, and 650 nm, respectively. The allowed maximum $\Delta\lambda$ values also vary as the peak emission wavelengths change. If the peak wavelength of the red emission is 625 nm, then the maximum allowed bandwidth becomes 25 nm. As the peak emission wavelength increases to 630 nm, the maximum $\Delta\lambda$ increases to 40 nm. Finally, a further increase of the peak wavelength was found out to shift the allowed $\Delta\lambda$ further to 50 nm.

Table 3.1. Summary of the spectral parameters for satisfying the color gamut defined in Figure 3.1. λ and $\Delta\lambda$ stand for the peak emission wavelength and full-width at half-maximum, respectively.

	λ (nm)	$\Delta\lambda$ (nm)
Blue	465	30,35,40,45,50
	470	20,25,30
Green	525	20,25,30
	530	20,25,30,35,40,45
	535	20,25,30,35,40
Red	625	20,25
	630	20,25,30,35,40
	635	20,25,30,35,40,45,50
	640	30,35,40,45,50
	645	40,45,50
	650	45,50

The circadian performance of the spectra presented in Table 3.1 was calculated as described in Section 3.2. The minimal circadian effect ($f_{circadian}$) was realized when the peak emission wavelengths of blue, green, and red color components are 465 nm, 535 nm, and 635 nm, respectively. The full-width at

half-maximum values turned out to be 30, 20, and 50 nm for the same color components. The spectrum corresponding to this QD-LED (QD-LED₁) can be found in Figure 3.2. The same calculations were carried out for the YAG:Ce phosphor integrated white LED. The results show that the QD-LED₁ exhibited a circadian performance value ($f_{\text{circadian}}$) down to 4.32 while that of the YAG:Ce integrated LED was 4.50 (Figure 3.3) while the color gamut of the QD-LED₁ covers 107.5% of the area that NTSC requires. On the other hand, the area that can be covered by the YAG:Ce LED remains only at 80.4% of the area required by NTSC. When the color gamut of the YAG:Ce LED is targeted during the QD-LED design, the resulting QD-LED (QD-LED₂) reduces $f_{\text{circadian}}$ by 33% to 3.03, whose spectra are given in Figure 3.2. This QD-LED constitutes of blue, green, and red components emitting at 455, 545, and 620 nm, respectively, with respective full-width at half-maximum values of 25, 20, and 50 nm.

The overlap area with NTSC color span is also presented in Figure 3.3. This overlap is a very crucial quantity because this indicates the ability to define the colors in accordance with the NTSC specifications. The results show that the color-gamut of the QD-LED₁ overlaps almost perfectly as indicated by the reproduction of 99.2% of the NTSC color gamut while YAG:Ce integrated LED only overlaps with 87.3% of the NTSC standards.

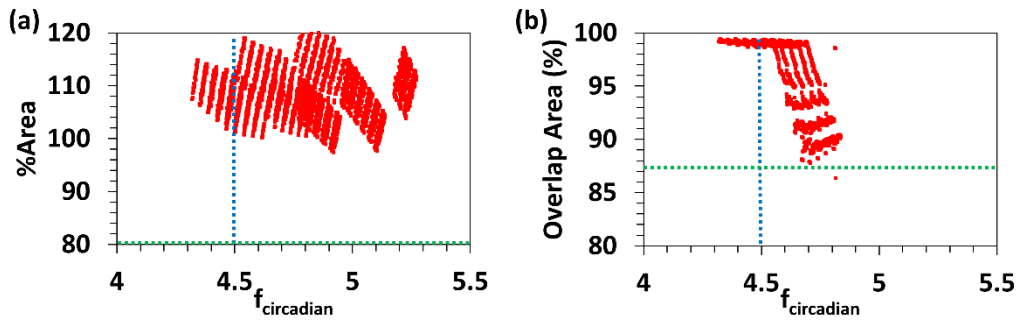


Figure 3.3. (a) Circadian performance ($f_{\text{circadian}}$) of QD-LED backlit displays together with the percentage area compared to the area of NTSC color gamut. (b) Overlap area of QD-LED color gamut together with the NTSC standard vs. $f_{\text{circadian}}$. The blue dashed lines correspond to $f_{\text{circadian}}$ of YAG:Ce LED while the green dashed lines correspond to (a) the percentage and (b) the overlap area of color gamut using the YAG:Ce LED backlighting.

As Figure 3.3 suggests, the QD-LEDs possess the potential to cause weaker disruptions on the circadian rhythm compared to the YAG:Ce LED; however, if not correctly designed, QD-LEDs can also adversely affect the circadian rhythm. Therefore, it is of significant importance to know which spectral parameters (the peak emission wavelength and the full-width at half-maximum) are necessary for realizing circadian rhythm friendly displays. To reveal this information, we sorted the spectra given in Table 3.1 according to their $f_{circadian}$ values. In Figure 3.4, we illustrate the average and standard deviations of the spectral parameters having the lowest 1%, 10%, 20%, 50% and 100% values of $f_{circadian}$. Here, 0 nm standard deviation of the blue wavelength for the spectra possessing the lowest 1%, 10%, and 20 % values of $f_{circadian}$ indicates that the selection of the blue peak emission wavelength at 465 nm is very critical for the best circadian performance. Similarly, 535 nm turned out to be the critical wavelength for the green component as its standard deviation remains at 0 nm for the spectra possessing the lowest 1% and 10% of $f_{circadian}$. On the other hand, the red component offers large flexibility in the design of QD-LED backlight with a standard deviation of ca. 6.9 nm around the average wavelength of 636 nm. The investigation of the full-width at half-maximum values provides additional valuable information. It turns out that the bandwidth of the blue emission is strictly required to be 30 nm while that of the green component is also equally critical to be as narrow as possible acquiring a full-width at half-maximum of 20 nm as their corresponding low standard deviations of 0 nm and 1.4 nm show for the spectra having the lowest 1% $f_{circadian}$. The investigation of the red component, on the other hand, draws a different picture. The average of the bandwidth for the red components of circadian friendly spectra becomes around 36 nm with a large standard deviation of ~ 10 nm. This information brings us to the conclusion that the selection of red component provides significant flexibility for the design of the circadian rhythm friendly backlight using QDs compared to the blue and green color components.

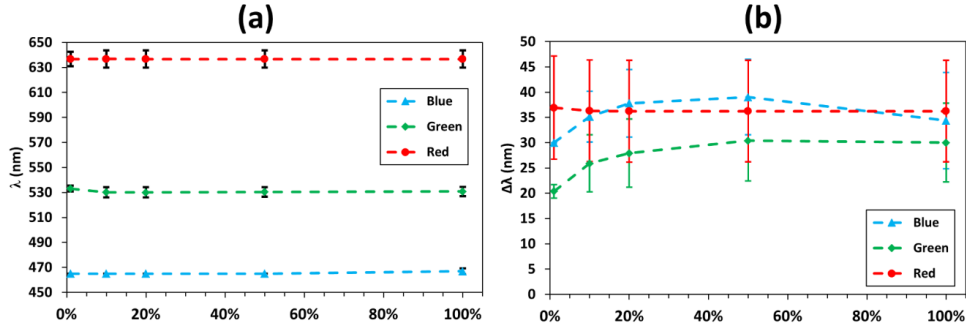


Figure 3.4. Average and standard deviations of (a) the peak emission wavelengths (λ) and (b) the full-width at half-maximum ($\Delta\lambda$) values of the spectra that acquire the lowest 1%, 10%, 20%, 50% and 100% values of $f_{\text{circadian}}$.

3.4 Summary

In summary, in this chapter of the thesis we investigated the potential of quantum dot integrated LED backlit displays considering their effect on the daily biological rhythm. The strategy that we present here is the first account of a circadian cycle friendly display backlight. By presenting the circadian rhythm friendliness perspective, we believe that the displays of the future will provide a healthier working and entertainment environment for the users.

For this purpose, here we first calculated the required spectral properties of the emitters so that the intended NTSC color gamut can be reproduced by employing quantum dots. Subsequently, we evaluated the effect of backlighting on the circadian rhythm using three existing circadian cycle models: circadian light, circadian effect factor, and melanopic sensitivity function. The results show that compared to widely preferred YAG:Ce phosphor integrated LEDs, QD-LEDs can exhibit 33% weaker circadian disrupting effect when both acquire the same color gamut. When the QD-LED is required to cover the whole NTSC color gamut, then the corresponding circadian performance is enhanced by 4.1% in addition to a 34% improvement in the achievable color gamut compared to that of a YAG:Ce LED.

Furthermore, our results indicated that, if the NTSC color gamut is targeted, a circadian rhythm friendly backlighting should acquire blue and green peak emission wavelengths at 465 and 535 nm, respectively, together with respective

bandwidths of 30 and 20 nm. On the other hand, the red color component offers large flexibility to the designer as indicated by 6.9 nm and 10 nm standard deviations around the peak emission wavelength of 636 nm and full-width at half-maximum of 36 nm, respectively, which is exactly in contrast to high color-quality general lighting. On the other hand, if the color gamut of the YAG:Ce LED is targeted using a QD integrated LED, the emission wavelengths of the QDs should be at 455, 545, and 620 nm with bandwidths of 25, 20, and 50 nm for blue, green, and red color components, respectively.

Chapter 4

Polarization Anisotropy in Self-Assembled Magnetic Nanowire-Quantum Dot Hybrids

In this chapter of the thesis, we move from the discussion on the effect of color conversion on the human biological rhythm in electronic displays to our efforts on obtaining backlighting sources having high-polarization ratio color conversion for displays. Our motivation in this work has been to avoid the need for polarizers in the liquid crystal display systems and eventually to contribute to the efforts of increasing the optical efficiency in the displays. The work that we present here is based on C. Uran, T. Erdem, B. Guzelturk, N. Kosku Perkgöz, S. Jun, E. Jang, and H. V. Demir, *Appl. Phys. Lett.* 105, 14, 141116 (2014) [124]. Reproduced with permission from American Institute of Physics © 2014.

4.1 Introduction

Optical polarizers that have the capability of transmitting the light at a certain polarization while blocking the light possessing orthogonal polarization are among the essential passive components for numerous applications including plasmonic sensing [125], imaging [126], and liquid crystal displays (LCDs) [127]. The polarizers are employed in plasmonic sensing applications for generating the surface plasmon polaritons (SPPs) using polarized light [128] since the SPPs can only be excited with light having a certain polarization [101]. In the imaging applications, the polarizers are typically utilized for improving the details of the image by only allowing for the transmission of the light of a well-defined polarization [14]. The need for polarizers in LCDs arises due to the optical features of the liquid crystals that are employed to modulate the optical transmission of polarized light in displays. In a typical LCD, the light generated

by the backlight source arrives first the polarizer. Then the liquid crystals change (e.g., twist) the polarization of this light, which hits the second polarizer, translating the polarization change to the amplitude change. This contributes to image formation pixel-by-pixel together with the color filters that are placed on top of the liquid crystals. The light transmission by the liquid crystals can be modulated only if the light is strongly polarized. This means that theoretically at least 50% of the incident optical power is wasted, which increases about 75% in a typical display [129]. Considering the current wide-spread use of LCDs, globally we are wasting huge amounts of energy. However, if we could obtain a light source that is capable of producing light preferably at a single polarization, then we will not need polarizers, which offers increased efficiencies and decreased production costs of displays.

Until today, there have been numerous attempts to develop light sources emitting at least dominantly in a preferred polarization. For this purpose, wire-grid polarizers [130], [131], special resonant cavities [132] and plasmonic cavities [133], and anisotropic crystals [86], [134] have been employed. Especially, from the perspective of obtaining light dominantly in a preferred polarization, wire-grid polarizers have stepped forward. For example, Zhang et al. achieved a polarization ratio of 7 by fabricating gratings on top of InGaN-based LED using electron beam lithography technique [135]. Even higher polarization ratios have been achieved by Ma et al. as 50 [136]. However, the drawbacks of these demonstrations are the need for advanced, expensive, time-consuming, and usually low-throughput fabrication techniques including focused ion beam lithography [137], electron beam lithography [138], and nanoimprint lithography [139] to produce parallel grids of metals with periodicities comparable or smaller than the wavelength [131]. Therefore, there is a strong demand for less complicated and less costly fabrication techniques that enable improved polarization ratios of the emitters. Owing to their solution processing capabilities, colloidal materials are good candidates for this purpose. However, the challenge is to control their assembly so that the polarization anisotropy can be supported within the film of colloids. To address this important point, Ozel et al. decorated the surface of a quartz substrate with negatively charged gold nanoparticles and CdTe QDs by employing electrostatic interaction with

positively charged polymers to form plasmonic cavities [133]. The architecture successfully increased the ratio of perpendicular (s) to parallel polarizations of the QD emission to 1.7. However, despite the successful self-assembly of colloids, which is obviously a high-throughput and low-cost technique, the resulting s/p-polarization ratio did not increase sufficiently.

To further increase the s/p-polarization ratio by employing colloidal materials, we study a hybrid morphology consisting of a thin CdTe QD film coupled with magnetically aligned multi-segmented Ni/Au nanowires (NWs). The ferromagnetic character of these NWs that stem from the use of Ni enables the formation of aligned NW films upon application of an external magnetic field. The utilization of the template-assisted synthesis of NWs allows for their production in higher amounts and their magnetic field assisted self-assembly enables us to obtain their aligned thin films covering large areas. Prior to our work, the alignment of NWs was studied using Langmuir-Blodgett [140], dielectrophoresis [141], [142], and magnetic field assisted [143], [144] techniques. However, these works employed either relatively complex setups such as Langmuir-Blodgett troughs or predefined electrodes for the application of electric and magnetic fields.

Different than these works, here we show a significantly simpler method of alignment to decrease the cost of fabrication and increase the area of the deposition. In this study, we placed the NWs in a polymeric host between commercially available magnets to align them while the film was slowly drying on the substrate without the requirement for a pre-defined electrode or surface functionalization. This enables obtaining aligned NW films in large areas and studying the effect of the NWs on the polarization of the incorporated emitters. For a proof-of-concept demonstration, we hybridized the CdTe QDs as isotropic light-emitters within the aligned three-segment Au/Ni/Au NWs to obtain polarized light. The polarization ratio of this composite material system reached 15 proving the potential of the presented technique for next-generation LCD backlighting.

4.2 Experimental Methodology

4.2.1 Synthesis of CdTe QDs

The synthesis of the red-emitting CdTe QDs were carried out as explained in Chapter 2 of this thesis. Briefly, after solving $\text{Cd}(\text{ClO}_4)_2 \cdot 6\text{H}_2\text{O}$ (4.59 g) in water (500 mL), we added thioglycolic acid (TGA) (1.33 g) to the solution. Subsequently, to set the pH of the solution to 12, we added NaOH solution dropwise by continuously monitoring the pH of the system. In a separate glassware (see Figure 2.14), we placed Al_2Te_3 (0.8 g) under Ar flow for one hour to clean the material. Subsequently, we added H_2SO_4 solution (0.5 M) dropwise on the Al_2Te_3 to obtain H_2Te gas, which carries Te atoms for the reaction mixture under Ar flow. Then, we heated the mixture until it boiled and continued the reaction for 20 hours to obtain red-emitting CdTe NCs in water. The photoluminescence and absorbance spectra of these QDs are presented in Figure 4.1.

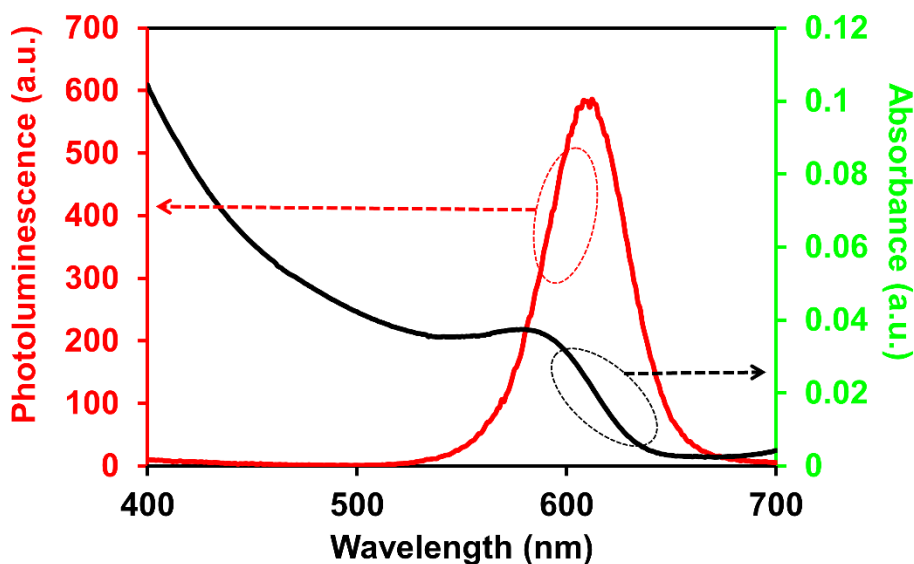


Figure 4.1. Photoluminescence (red curve) and absorbance (green curve) spectra of the synthesized CdTe QDs. Reproduced with permission from Ref. [124]. © American Institute of Physics 2014.

4.2.2 Synthesis of segmented Au/Ni/Au NWs

In our synthesis on NWs, we used a Whatmann Anodisc membrane having a pore density of 10^9 cm^{-2} as the template. We grew the NWs using an electrodeposition technique. Briefly, we first thermally evaporated a 200 nm thick silver layer, which will serve as the back electrode, on the backside of the template. We used mesh platinum as the counter electrode and placed it 5 cm above the template within a glass tube. We first deposited 2 μm thick silver using the silver bath (TechniSilver E-2, Italgalvano, 11.5% potassium silver cyanide) to clog the branching portion of the membrane, then we deposited $\sim 1.5 \mu\text{m}$ of gold segments on silver layer using Orotemp 24 (6.87% potassium aurocyanide) as the gold bath under a current of -1.6 mA. We subsequently rinsed water to clean unreacted chemicals from the template and then deposited the Ni segment of 7 μm length again under -1.6 mA current flow in Ni bath, which consists of nickel sulfamate (20-35%), nickel bromide (0.5-1.5%), and boric acid (1-3%). The average nickel growth rate has been 1.5 nm/s. We cleaned the template with water again and deposited the second gold segment of $\sim 1.5 \mu\text{m}$ length using the method we described above. The average gold deposition rate has been 2 nm/s. Once the deposition was finished, we removed the silver back electrode by etching it with HNO_3 solution (30%) and then removed the alumina membrane by dissolving it within NaOH (3 M). To separate the NWs from the remainings of alumina membrane in the solution, we centrifuged the mixture three times in DI water at 3000 rpm. The scanning electron microscope (SEM) images of the synthesized NWs are presented in Figure 4.2.

4.2.3 Preparation of the hybrid film and its alignment

We used two neodymium magnets with dimensions of 5 mm \times 10 mm \times 40 mm separated by 2 cm for the alignment of the NWs. We measured the generated magnetic field to be 400 Gauss. Before the alignment, we first mixed the synthesized multi-segment NWs (500 μL) with poly(vinyl pyrrolidone) (PVP, 750 μL) and the synthesized CdTe QDs (1600 μL) with PVP (1200 μL) separately. We first drop-casted the NW mixture (375 and 500 μL) on a glass substrate, which was placed between the magnets, and left the film drying under magnetic

field. After the film dried, we drop-casted 500 μL of the mixture containing QDs and again left the film for drying. The illustration of the film structure and the setup are presented in Figure 4.3 along with the optical microscope images of the prepared films.

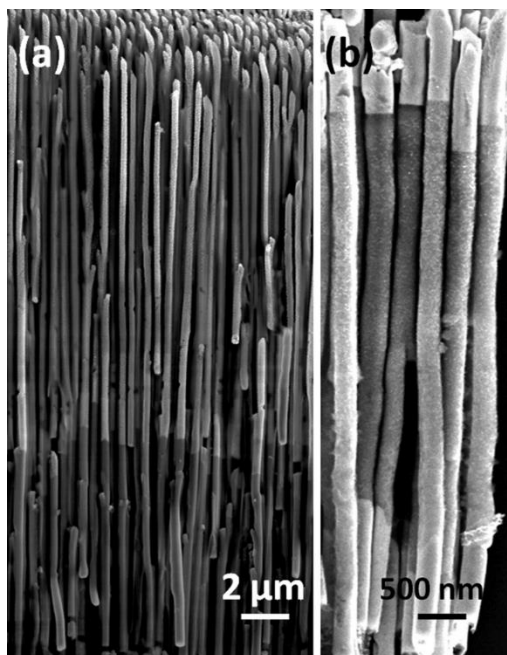


Figure 4.2. Scanning electron microscope images of the Au/Ni/Au three-segment NWs (a) within the template and (b) on the glass substrate. Reproduced with permission from Ref. [124]. © American Institute of Physics 2014.

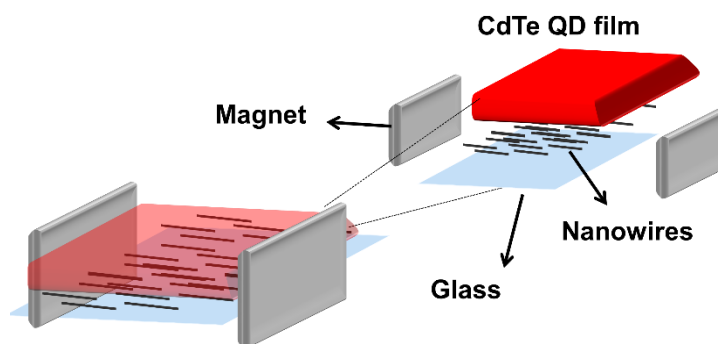


Figure 4.3. Illustration of the setup that we used for preparing aligned NW-QD hybrid films. Reproduced with permission from Ref. [124]. © American Institute of Physics.

4.3 Results and Discussion

Applying a magnetic field to the nanowires magnetizes the nickel parts of the NWs. This magnetization induces magnetic domains that interact with the applied magnetic field and causes a torque so that the NWs are aligned along the applied field. We can relate the induced magnetic moment on NWs (L) using $L=mlH\sin\theta$, where m stands for the dipole strength, l is the length of the ferromagnetic segment, H is the magnetic field intensity, and finally, θ is the angle between the long axis of the NWs and the applied magnetic field [143]. This relation states that if we employ nanowires with longer nanowire segments or apply stronger magnetic field, the induced magnetic moment leading to torque on the nanowires strengthens. As a result, the NWs will tend to align along the external field forming a grid-like architecture that resembles wire-grid polarizers and has the potential to reflect one polarization of light strongly while transmitting the other.

We evaluated the potential of this methodology by modeling this aligned NW architecture using a numerical full electromagnetic solver. For this purpose, we employed the Lumerical's finite difference time domain (FDTD) software and calculated the polarization dependent emission of the hybrid films comprising of NWs and CdTe QDs (Figure 4.4). In our simulations we tested the polarization of the hybrid films by using first three segment Au/Ni/Au NWs hybridized with CdTe QDs. The simulated NW morphology was similar to the synthesized one and consisted of a 7 μm long Ni segment and two 1.5 μm long Au segments below and above the Ni segment. The second NW morphology we tested was single-segment NWs of Ni having a length of 10 μm . The refractive index of the CdTe QD layer was first measured using ellipsometry and these values were used in our simulations. We structured our simulation so that the light emitted by the QDs propagate through the randomly positioned but aligned NWs. While positioning the NWs randomly, we set the average period of the NW separation to 250, 300, 350, and 400 nm. To study the polarization of the CdTe emission, we monitored the transmission of the QD emission separately at perpendicular and parallel polarizations.

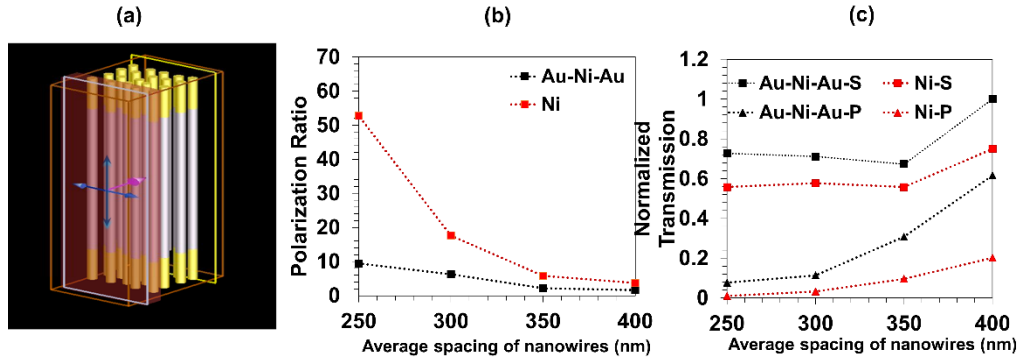


Figure 4.4. (a) Illustration of our FDTD simulation setup where blue and pink arrows indicate the polarization and propagation of the light, red thin layer represents the CdTe QD layer, and yellow/gray/yellow wires represent the three-segment Au/Ni/Au nanowires. (b) Polarization ratio of the transmitting light that is produced within the CdTe QD layer. (c) Normalized transmission of the light as a function of the average nanowire spacing for single-segment and three-segment nanowires. Reproduced with permission from Ref. [124]. © American Institute of Physics 2014.

When the optical polarization and the long axis of the NWs are aligned, electromagnetic field emitted by the QD strongly interacts with the conductive NWs leading to absorption and scattering. On the other hand, the light polarized perpendicular to the long axis of the NWs interacts with the NWs significantly less leading to improved transmission. The results of our simulations presented in Figure 4.4 confirm our expectations and reveal optical anisotropy for both three-segment and single-segment nanowires. We reckoned that the polarization ratios tend to increase at shorter inter-nanowire spacing. The polarization ratios that we can achieve can get values up to 10 and 50 for the three-segment and single-segment nanowires, respectively. However, in the case of single-segment Ni NWs, the transmission is considerably less than the three-segment Au/Ni/Au NWs.

In addition to the transmission advantage of three-segment NWs, they also pose experimental advantages. We observed that single-segment Ni nanowires tend to break while removing the silver layer at the backside of the template. In contrast with single-segment nanowires, three-segment Au/Ni/Au NWs are more robust owing to the strengthened Au-Ni contact during post-thermal baking.

Therefore, we decided to continue our experiments with the three-segment NWs. In our experiments, we also employed poly(vinyl pyrrolidone) (PVP) as the host polymer for both QDs and nanowires. This host matrix avoided the quenching of the QD emission during solid-film formation and increased the viscosity of the mixture so that the NWs did not move toward the magnets while the film dried. We first formed the films of the NWs within PVP. After this film dried, we drop-casted the CdTe QD layer on top of the NW layer and the film was dried overnight. Our optical microscopy images clearly revealed that the alignment of the NWs took place along the direction of the applied magnetic field (Figure 4.5(a) and (b)). However, we observed that we could not perfectly avoid the non-uniformities, which we attribute to the random nature of the alignment process. As a result, we expect that these non-uniformities place an upper bound on the feasible polarization ratio.

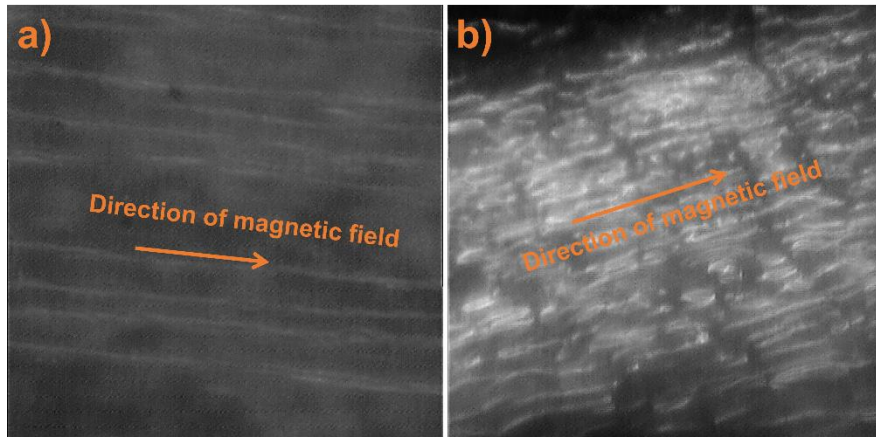


Figure 4.5. Optical microscope images of the aligned three-segment nanowires taken from (a) a less dense and (b) a dense region of the hybrid film. Reproduced with permission from Ref. [124]. © American Institute of Physics 2014.

After forming the NW-QD hybrid films, we recorded their polarization-dependent photoluminescence spectra using the system illustrated in Figure 4.6. We excited these hybrid films with a laser emitting at 375 nm and collected the light through a linear polarizer, monochromator, and a photomultiplier tube. We rotated the polarizer to record the emission intensities at perpendicular and

parallel polarizations of the light emitted by the QDs and transmitted through the array of NWs.

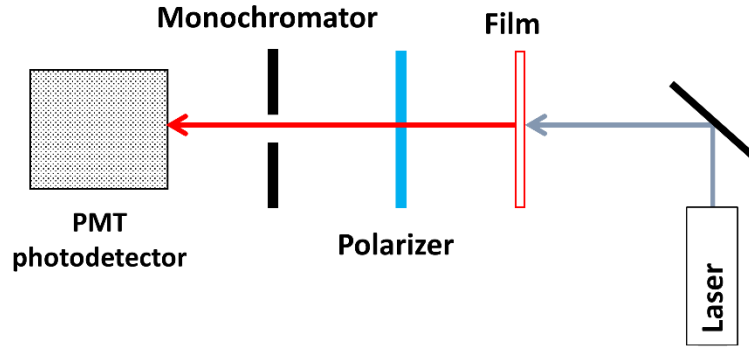


Figure 4.6. Illustration of the setup used for characterizing the optical polarization of QD emission in hybrid films. Reproduced with permission from Ref. [124]. © American Institute of Physics 2014.

Our results indicated that the bare CdTe QD film without NW hybridization possesses a s/p polarization ratio close to unity. In the hybrid films, however, we observed strong polarization-dependent emission intensities (black and red curves) as shown in Figure 4.7. We also reckoned that the polarization ratio given in blue in Figure 4.7 can reach 10 and becomes ~ 8 at the emission peak for the hybrid film prepared using 375 μL of NW:PVP mixture. Furthermore, we found out that increasing the amount of NW:PVP film used during the film formation significantly contributes to increasing the emission polarization up to 16, which takes values close to 15 at the peak of the QD emission. In the light of our simulations, we attribute this observed behavior to the decreased NW spacing at increased NW amounts utilized in solid-film. We also observed an unusually broad spectrum of the polarization ratio, which we again attribute to the randomness of the NW alignment and imperfect distribution in the solid-film.

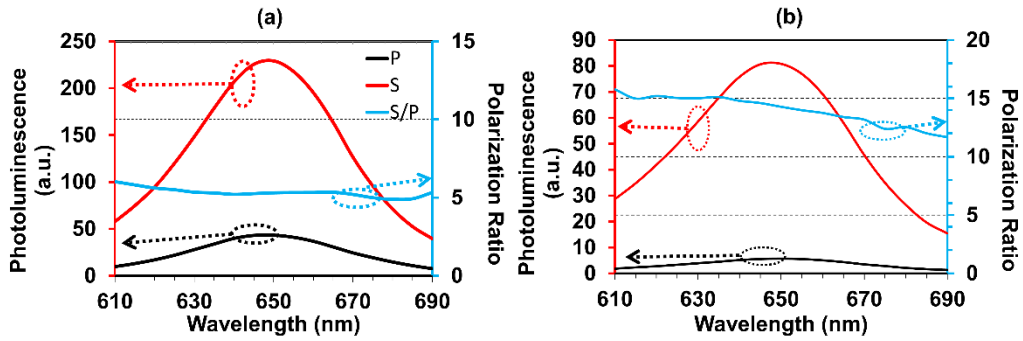


Figure 4.7. Photoluminescence spectra at perpendicular (s) and parallel (p) polarizations of the films prepared by hybridizing three-segment Au/Ni/Au NW and CdTe QDs. In (a) 375 μL and (b) 700 μL of NW dispersion is used for the thin film preparation. Reproduced with permission from Ref. [124]. © American Institute of Physics 2014.

4.4 Summary

In this work, we proposed and demonstrated a new simple methodology for obtaining polarized emission by employing the self-assembly of magnetic nanowires hybridized with semiconductor QDs under magnetic field. We observed that the application of magnetic field makes the nanowires self-assemble along the field direction. Thus, the nanowires act as wire-grid polarizers that significantly improve the anisotropy of the QDs that are otherwise isotropic emitters, which was also confirmed by the numerical analyses carried out using finite difference time domain electromagnetic simulations. Our experiments showed that it is possible to obtain polarization ratios above 15 using this technique, which offers significant advantages for displays owing to its simplicity and low cost. We believe that this present work will open up new opportunities in using magnetic field assisted self-assembly techniques for increasing the polarization anisotropy of the emitters that are especially of significant importance for display applications.

Chapter 5

Macrocrystals of Quantum Dots for Quality Lighting

In this chapter of the thesis, we present our work on the development of the high-quality light-emitting diodes using color-converting quantum dots incorporated into borax macrocrystals. In this work, we first determined the spectral conditions required for achieving high color quality and high photometric efficiency. Subsequently, we synthesized the green- and red-emitting quantum dots and incorporated them into borax macrocrystals. Using their photoluminescence features, we refined our numerical calculations and determined the necessary features of yellow-emitting quantum dot incorporating macrocrystals. Based on these findings we synthesized yellow-emitting quantum dots and incorporated them into borax macrocrystals. Employing green-, yellow-, and red-emitting macrocrystals, we prepared a white light-emitting diode and characterized its colorimetric and photometric properties in addition to the stability tests. Below, we present the details of this work that we covered in M. Adam*, T. Erdem*, G. M. Stachowski, Z. Soran-Erdem, J. F. L. Lox, C. Bauer, J. Poppe, H. V. Demir, N. Gaponik, A. Eychmüller, *ACS Appl. Mater. Inter.* 7, 41, 23364-23371 (2015) [87] (*equal contribution). Reproduced with permission from American Chemical Society © 2015.

5.1 Introduction

Today's commercially available white light-emitting diodes (LEDs) are mainly suffering from low color rendering index (CRI) due to their color-converting phosphors. Those are based on rare-earth doped oxides with a broad tail reaching the deep-red part of the spectra where the human eye is not sensitive thus not providing a sufficient amount of detected red photons in the visible region [8], [4]. One solution to overcome this issue is the use of fluorescent colloidal semiconductor quantum dots (QDs) as color-converters. Discovered

during the 1980's [145], [146], QDs provide the ability to alter chemical and physical properties than their bulk counterparts such as the band gap tunability with their size enabled by size-dependent quantum confinement effects [147]. Therefore, emitters with a tunable emission peak accompanied by a narrow full-width at half-maximum (FWHM) spanning a significant portion of the electromagnetic spectrum can be obtained using the same material [53]. Their applications as color converters on LEDs [12], [58], [148]–[150] as well as active emitting layers [151]–[153] have been successfully demonstrated; however, in both cases their well-known limited stability against oxidation and decomposition remains as a challenge to overcome. In our previous publication [83], we addressed this problem by incorporating the QDs into ionic matrices, e.g. NaCl and KCl and drastically improved their photostability while preserving or, under the right conditions, increasing their photoluminescence quantum yield (PL-QY) [154].

Although these QD incorporating salt macrocrystals (also called QD-salt mixed crystals) proved to be suitable as color conversion materials [83], [84], [91], [93], [155], [156], only proof-of-concept white LEDs without any photometric optimization were shown. In this manuscript, we carried out a model-experimental feedback approach to prepare QD incorporating salt macrocrystals, which can be used to produce white LEDs with high luminous efficacy of radiation (LER), high CRI and a correlated color temperature (CCT) comparable to the incandescent bulb. First, we used the model to identify the spectral requirements for high quality lighting employing QD photoluminescence (PL) spectra, which were then implemented in the subsequent QD synthesis. By comparing the experimental spectra at each intermediate stage with the model, we optimized the color quality and photometric efficiency of the final white LED. In addition to this, here we benefitted for the first time from the reduced ionic strength of borax in water compared to NaCl allowing significantly higher loading of QDs into crystals making the implementation of the designed white LEDs possible. Finally, we showed that the encapsulation of the QDs in salt crystals provides outstanding emission stability integrated with LEDs driven at high currents.

5.2 Experimental Methodology

5.2.1 Model for spectral evaluation

To maximize the photometric performance of the white LEDs, we carefully designed the spectra of the LEDs prior to experiments so that appropriate QDs can be used with the correct amounts. For this purpose, we benefitted from the results of our previous study [11] as the starting point. In our calculations, we modelled the emission of the QDs as a Gaussian function unless we do not use the experimentally measured photoluminescence spectra. In our designs, we tried to maximize the CRI, which indicates how good the real colors of the objects are rendered, and LER, which indicates how good the spectrum of the light source overlaps with the eye sensitivity curve. Furthermore, a special emphasis was given to generate white light with a warm white shade acquiring a CCT below 4500 K. According to our previous results, only a tiny fraction of all possible color combinations yields LED-spectra where $\text{CRI} > 90$, $\text{LER} > 330 \text{ lm/W}_{\text{opt}}$, and $\text{CCT} < 4500 \text{ K}$ were met simultaneously. Based on these results, here we designed a four color white LED composed of a blue LED pumping green-, yellow-, and red-emitting QD macrocrystals to generate white light. According to the recommendations provided at this step, we first synthesized green- and red-emitting QDs and grew their macrocrystals. Considering the measured photoluminescence spectra of these macrocrystals, the required peak emission wavelength of the yellow color component was determined to achieve $\text{CRI} > 90$, $\text{LER} > 330 \text{ lm/W}_{\text{opt}}$, and $\text{CCT} < 4500 \text{ K}$. Based on these results, we synthesized yellow-emitting QDs and grew their macrocrystals. Using the measured photoluminescence spectra of the green-, yellow-, and red-emitting macrocrystals, we calculated their necessary relative amplitudes for high quality white light generation.

5.2.2 Synthesis of QDs

All chemicals used were of analytical grade or of the highest purity available. All aqueous solutions were prepared from Milli-Q water (Millipore). CdSe/CdZnSeS/ZnS QDs with an alloyed gradient shell were synthesized

according to a previous publication [157], using slight modifications of the synthetic protocol. All amounts used for the synthesis can be found in Table 5.1.

Table 5.1. Amount of precursors for the synthesis of three different CdSe/CdZnSeS/ZnS quantum dots (QDs) with an alloyed gradient shell.

	Green QD	Yellow QD	Red QD
CdO	0.3 mmol (38.5 mg)	1.8 mmol (231.1 mg)	1.0 mmol (127.5 mg)
Zn(OAc) ₂	4.0 mmol (733.9 mg)	2.6 mmol (477.0 mg)	2.0 mmol (367.0 mg)
Oleic acid	5.5 mL	5.5 mL	5.0 mL
ODE	20.0 mL	20.0 mL	23.2 mL
Se	0.25 mmol (19.7 mg)	1.00 mmol (84.2 mg)	0.20 mmol (15.8 mg)
S	3.50 mmol (112.0 mg)	2.45 mmol (78.7 mg)	2.00 mmol (64.1 mg)
TOP	3.0 mL	3.2 mL	Se: 0.2 mL + 1.6 mL ODE S: 1 mL
DDT	-	-	0.3 mL

For green-emitting (530 nm) and yellow-emitting (570 nm) QDs, a defined amount of CdO, Zn(OAc)₂, oleic acid (OA) and 1-octadecene (ODE) were placed in a 50 mL three-necked flask. The mixture was degassed for 1 h and backfilled with inert gas at 100 °C. After heating to 310 °C, defined amounts of S and Se dissolved together in trioctylphosphine (TOP) were rapidly injected into the flask accompanied with a temperature reduction to 300 °C. After 10 min., the QD solution was cooled to room temperature, quenched with 20 mL of CHCl₃, and followed by two washing steps with an excess of acetone.

For red-emitting (617 nm) QDs, CdO, Zn(OAc)₂, OA and ODE were placed in a 50 mL three-necked flask and degassed for 1 h at 100 °C. After backfilling with inert gas and heating to 300 °C, Se dissolved in TOP and ODE was

injected rapidly into the flask, followed by a dropwise addition of 1-dodecanethiol (DDT) after 30 s. 20 min. later, S dissolved in TOP was added dropwise to the reaction solution, while holding the mixture at 300 °C for further 10 min. The QD solution was cooled to room temperature, quenched with 20 mL of CHCl₃ and washed two times with acetone and isopropanol. Finally, the QDs were redispersed in 4 mL of CHCl₃ to gain a concentrated solution for the ligand exchange and characterization.

5.2.3 Ligand exchange

Long chain aliphatic acids on the QDs surface were exchanged with short chain thiols using a modified protocol of Ref. [158]. 30 µL of concentrated QDs solution were diluted with 500 µL CHCl₃ and mixed with a 0.2 M aqueous mercaptopropionic acid (MPA) solution at pH of 10. After shaking vigorously for 4 h, phases were separated and the aqueous phase was used without further purification.

5.2.4 Preparation of QD incorporating salt macrocrystals

2 mL of freshly ligand exchanged QD solution was mixed with 10 mL of saturated disodium tetraborate decahydrate Na₂B₄O₇ · 10 H₂O (Borax) solution, modifying our previous report [154]. The mixture was stored at 30 °C in an oven for about one week, until the parental solution turned colorless. Resulting macrocrystals were rinsed with cold water for cleaning, dried, and stored under ambient conditions.

5.2.5 Preparation of white LED

To prepare white LEDs, borax-based macrocrystals were milled to a fine powder and varying amounts of the powders emitting in different colors were blended with a two component silicone resin (ACC Silicones) on top of a blue-emitting commercial InGaN LED. The mixture was hardened for 2 h at 70 °C, forming a homogeneous phosphor layer.

5.2.6 Preparation of thin sheets for transmission electron microscopy (TEM)

Structural characterization of QD incorporating salt macrocrystals was performed using TEM. Prior to imaging, green- and red-emitting macrocrystals were embedded into histological resin (Kulzer), which was prepared by mixing resin and cross-linker with a ratio of 15:1. In order to initiate the cross-linking process, samples were exposed to UV light at 254 nm for 15 min and then stored at room temperature for complete solidification. After one week, sheets of 200 nm thickness were obtained using a Leica ultramicrotome. Cross-sections were transferred onto a Lacey carbon coated 200 mesh copper grid and TEM images were recorded by a FEI Tecnai G2 F30 transmission electron microscope.

5.2.7 Characterization

UV-Vis absorption measurements were performed on a Cary 50 spectrophotometer (Varian). PL spectra were recorded using a FluoroMax-4 spectrofluorometer (Horiba Jobin Yvon) at room temperature. PL-QY measurements of as-prepared and ligand-exchanged QDs were performed according to reference [159], using Rhodamine 6G and Rhodamine 101 (both Radiant Dyes Laser) in ethanol (Uvasol, Merck) [159]. Photoluminescence lifetime (PL-LT) spectra were recorded using a Fluorolog-3 spectrofluorometer (Horiba Jobin Yvon) equipped with a pulsed LED diode and a time-correlated single-photon counting (TCSPC) module at room temperature. Average PL-LTs were calculated at the time, when the initial signal intensity was reduced to 10000/e. Absolute PL-QY measurements were performed using a FluoroLog-3 spectrofluorometer (Horiba Jobin Yvon) equipped with a Quanta- ϕ integrating sphere. Thermogravimetric analyses were performed on a TGA/DSC1 STAR^F System (Mettler Toledo) using alumina crucibles and pressured air as purging gas. Stripping voltammetric analysis were performed on a home-built three-electrode system, using glassy carbon as the working-electrode, Hg/HgCl₂ as the reference electrode and Pt as the auxiliary-electrode. In-situ, the target analyte as well as a bismuth film were deposited on and stripped off the working

electrode. The analyte concentration was determined by applying the standard addition method using a Cd standard solution [160], [161].

5.2.8 Temperature tests

We measured the temperature of the LED chips using an FLIR A655sc infrared camera. The LEDs were operated using a square wave at a frequency of 1 kHz at 300 mA.

5.3 Results and Discussion

5.3.1 Photometric modeling

We used the photometric calculations as the feedback tool for the design of our white LED. The first step of our work has been determination of the number of color components. According to Tsao [3], four color components, i.e., blue, green, yellow, and red are required for achieving high-quality white light. In our previous work, we had determined the required wavelengths, relative amplitudes, and full-width at half-maximum values of the QD emitters [11]. In the light of this prior work, here we chose to use a blue LED emitting at 460 nm, green-emitting QDs with a peak emission around 530-540 nm, and red-emitting QDs with a peak emission around 620 nm. Although the necessary condition for the yellow peak wavelength to achieve high quality lighting was found to be 570-580 nm, we chose to fine-tune the white LED spectrum using the yellow component to compensate experimental deviations. For this purpose, we grew green- and red-emitting QD macrocrystals and recorded their photoluminescence spectra before preparing the yellow-emitting QD macrocrystals. Our calculations showed that employing the blue LED together with green- and red-emitting macrocrystals cannot provide high LER and high CRI together with warm white shade at the same time, confirming the results of Ref. [3].

Furthermore, to determine the conditions for high-quality white light, we calculated the required peak emission wavelength of the yellow color component by making use of the PL spectra of the green- and red-emitting macrocrystals

along with that of the blue LED. Since the material composition and the synthesis methodology of the yellow-emitting QDs are similar to those of the green-emitting QDs, we selected the full-width at half-maximum values of the yellow-emitting QDs to be the same as that of the green-emitting QDs. Our calculations revealed that the peak emission wavelength around 570 nm results in realizing $\text{CRI} > 90$, $\text{LER} \sim 350 \text{ lm/W}_{\text{opt}}$, and $\text{CCT} < 3000 \text{ K}$, all at the same time. Based on this information, yellow-emitting macrocrystals emitting at 573 nm were grown. In the center of Figure 1, possible CRI-LER combinations of the modeled LEDs based on experimentally prepared macrocrystals are shown as black squares, while the blue background is a guide for the eye showing feasible combinations. The PL-spectra display exemplarily chosen possible combinations of the four colors and their corresponding photometric performance.

Subsequently, the required relative amplitudes of the color components were determined using the experimental emission spectra of the QD macrocrystals and the blue LED to be $2/9$ for both the blue and green components, $1/9$ for the yellow component, and $4/9$ for the red color component to achieve high color quality and photometric performance. Based on these calculations, a white LED made of these macrocrystals was prepared simultaneously achieving $\text{CRI} = 91$, $\text{LER} = 341 \text{ lm/W}_{\text{opt}}$, and $\text{CCT} = 2720 \text{ K}$, marked as a red square in the center and the corresponding PL-spectrum shown in the upper right corner of Figure 5.1.

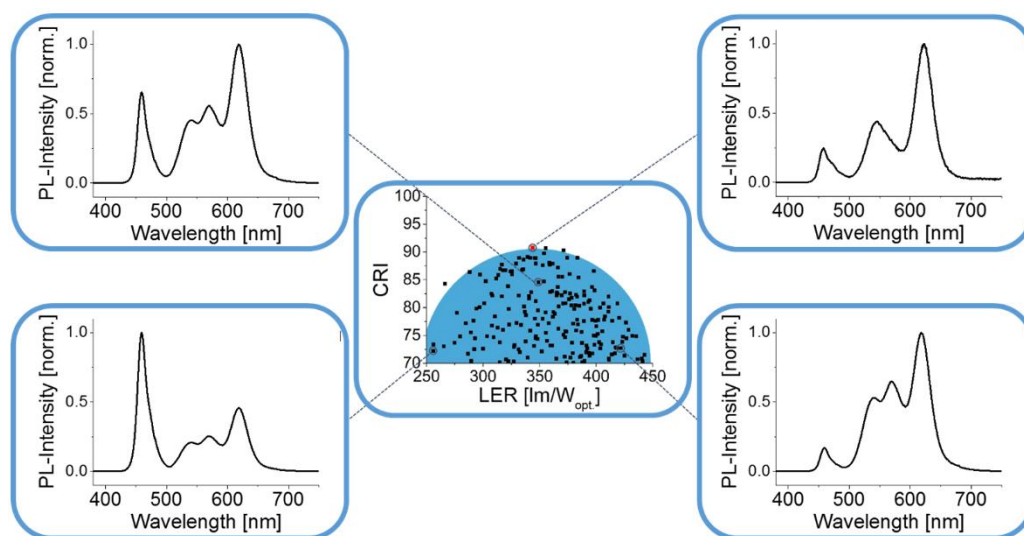


Figure 5.1. Overview of feasible CRI-LER combinations (black squares) with the experimentally prepared macrocrystals used as color conversion materials on blue LEDs (center). The two PL-spectra on the left and the lower right one show theoretically determined combinations corresponding to the marked points in the center. The upper right PL-spectra and the corresponding red square show the photometric performance of the most optimized final white LED. Reproduced with permission from Ref. [87]. © American Chemical Society 2015.

5.3.2 QD synthesis and characterization

Oil-based CdSe/CdZnSeS/ZnS QDs with an alloyed gradient shell were used, since they show a better tunability in the higher energy part of the spectrum and a smaller FWHM in the low energy region compared to aqueous based CdTe QDs while preserving high stability and PL-QY. In Figure 5.2, the PL-spectra of the resulting QDs are shown, with emission maxima at 530, 570, and 617 nm, FWHM of 40, 30, and 30 nm and PL-QY of 38.5%, 40.2%, and 42.6% for green, yellow, and red, respectively. These FWHM are in agreement with the requirements of high quality lighting as described in Ref. [11]. Below the PL-spectra in Figure 5.2, a photograph of the QD solutions under UV excitation shows their bright, pure color emission. Since Cd-based materials possess an inherent toxicity, their use in general applications is highly restricted. Nevertheless, if the benefits of using Cd-based materials strongly exceeds the risks, their application can be permitted by the legislature, as it is going to

happen for the use of Cd-based QDs in display and general lighting color conversion applications within the European Union [162].

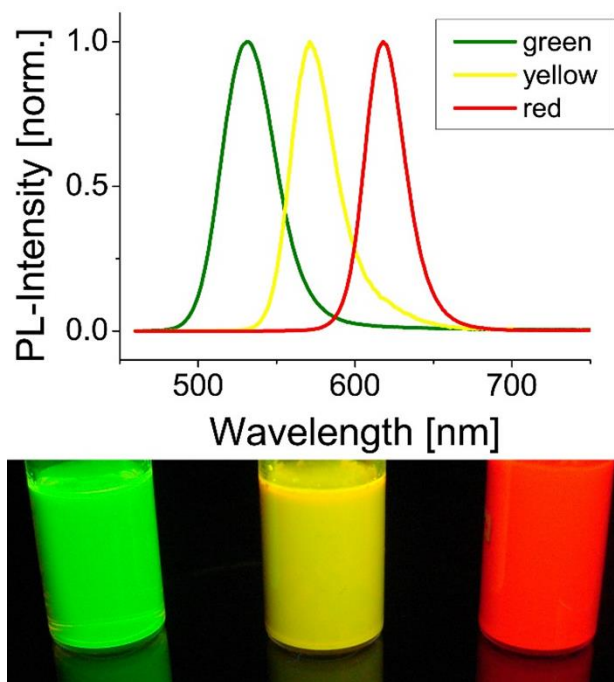


Figure 5.2. PL-spectra (top) of three different CdSe/CdZnSeS/ZnS QDs and their true color images under UV-excitation at 365 nm (bottom). The QDs are dispersed in CHCl_3 and stored under ambient conditions. Reproduced with permission from Ref. [87]. © American Chemical Society 2015.

The used oil-based QDs are stabilized by OA and TOP and are not soluble in the saturated, aqueous borax solution. Therefore, a phase transfer together with a ligand exchange towards the short chain thiol MPA is necessary. As it can be seen from Figure 5.3, QDs are transferred towards the initially colorless aqueous phase, preserving their pure color and intense emission (Figure 5.3(d)). The transfer is quantitative, yielding a colorless CHCl_3 phase and no aggregated particles, proving well stabilized, ligand exchanged QDs. Both shape and position of the PL-spectra stay constant during the procedure, as it can be observed in Figure 5.4. During the ligand exchange, non-ideal surface passivation is achieved, which causes a typical decrease of the PL-QY to roughly 50 % of the initial value [158], [163].

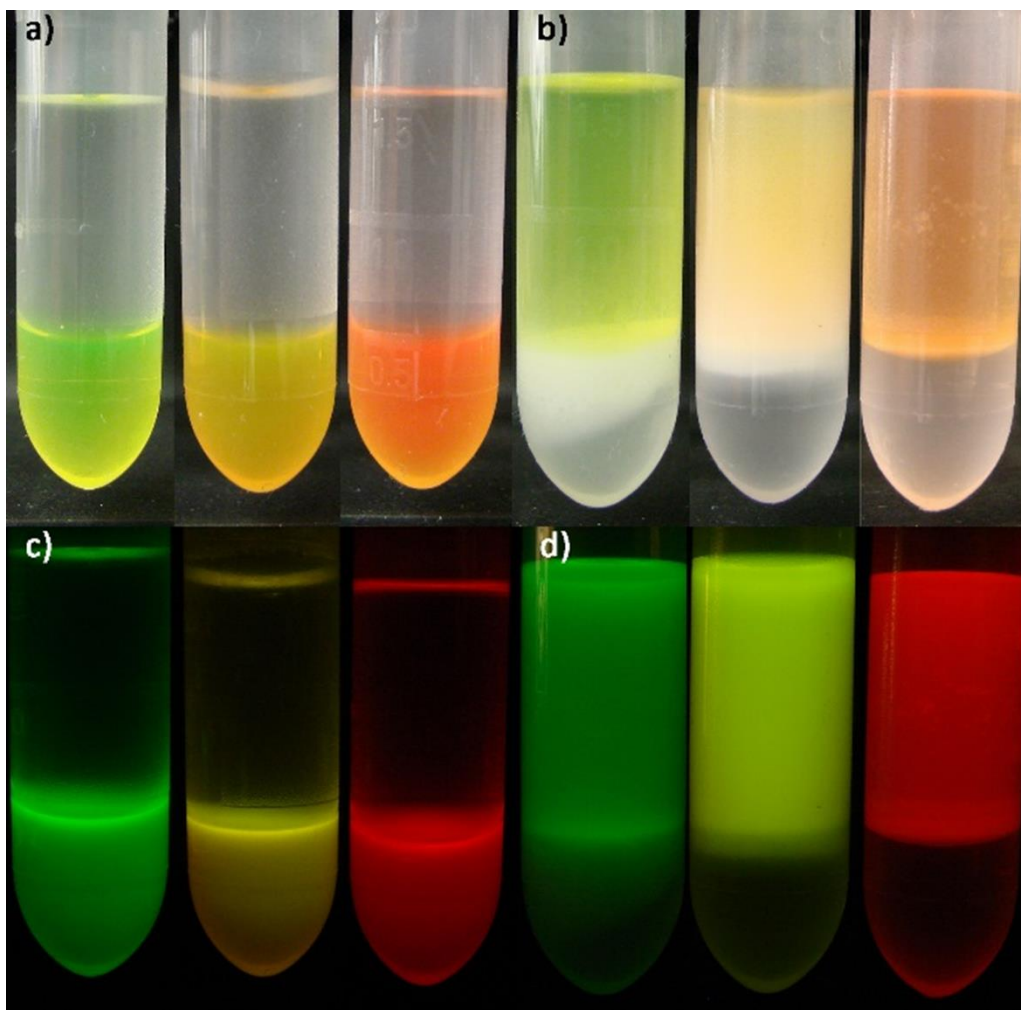


Figure 5.3. True color images of three different CdSe/CdZnSeS/ZnS QDs before ((a) and (c)) and after ((b) and (d)) ligand exchange under ambient light (top) and 365 nm UV-excitation (bottom). Reproduced with permission from Ref. [87] © American Chemical Society 2015.

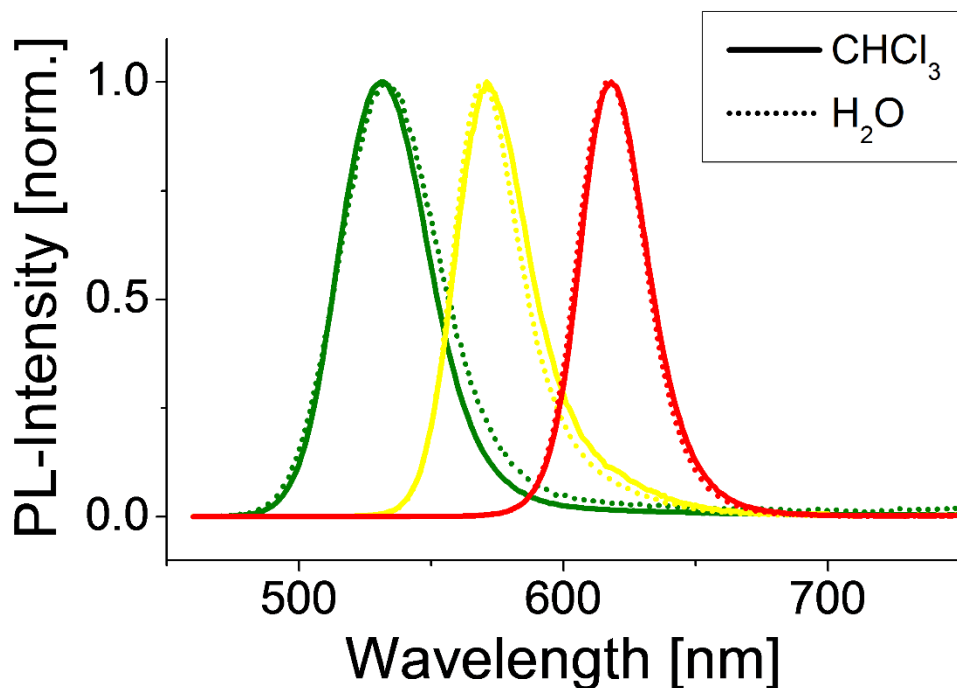


Figure 5.4. Photoluminescence (PL) spectra of three different CdSe/CdZnSeS/ZnS QDs dispersed in CHCl₃ (solid lines) and after ligand exchange in H₂O (dotted lines). Reproduced with permission from Ref. [87]. © American Chemical Society 2015.

5.3.3 Mixed crystal preparation

Embedding the ligand exchanged QDs into NaCl is known to be non-trivial, since their stability, in comparison to initially aqueous based CdTe QDs, is lower [154]. Using NaCl as a host, only macrocrystals with small loading amounts of QDs can be obtained, as it is shown in Figure 5.5. To overcome this problem, either our different crystallization procedure liquid-liquid diffusion assisted crystallization (LLDC) [91] or another host material can be used. Since the LLDC allows for a QD loading level that is non-sufficient for highest quality color conversion, borax is used as the host material in thesis work here. Due to its much lower solubility in water in comparison to NaCl (0.13 mol/L compared to 6.14 mol/L, respectively)[164], the ionic strength of the saturated borax solution is much lower than for saturated NaCl-solutions. Therefore, the stability of the ligand exchanged QDs is much higher within the borax solution. On the

other hand, using the same amount of QDs per mL of saturated solution, the QD loading within the resulting macrocrystals is higher. Stripping voltammetry measurements (Table 5.2) showed a 3.4 times higher amount of Cd and thereby QDs within borax in comparison to NaCl based macrocrystals prepared from the same batch of ligand exchanged QDs.

Table 5.2. Amounts of Cd within the parental CHCl_3 solutions and the final borax-based mixed crystals, measured using stripping voltammetry. The measurements were conducted using a bismuth film on the electrode for the determination, as described in Ref. [160], [161].

Sample	Amount of Cd
Green in CHCl_3	$c = 44.75 \text{ mmol/L}$ $c = 5.03 \text{ g/L}$
Green in borax	$b = 1.17\text{E-}06 \text{ mol/g mixed crystal}$ Ratio $1.31\text{E-}04 \text{ g/g mixed crystal}$
Yellow in CHCl_3	$c = 15.88 \text{ mmol/L}$ $c = 1.78 \text{ g/L}$
Yellow in borax	$b = 9.26\text{E-}08 \text{ mol/g mixed crystal}$ Ratio $1.04\text{E-}05 \text{ g/g mixed crystal}$
Red in CHCl_3	$c = 276.28 \text{ mmol/L}$ $c = 31.06 \text{ g/L}$
Red in borax	$b = 2.52\text{E-}07 \text{ mol/g mixed crystal}$ Ratio $2.84\text{E-}05 \text{ g/1 g mixed crystal}$
Comparison Borax-NaCl	$c = 4.95\text{E-}06 \text{ mol/g in Borax}$ $c = 1.44\text{E-}06 \text{ mol/g in NaCl}$

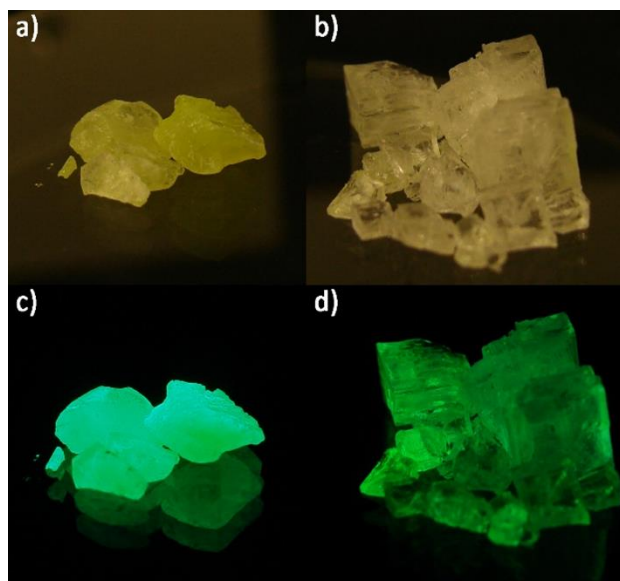


Figure 5.5. True color images of macrocrystals made from the same CdSe/CdZnSeS/ZnS QD batch with either borax ((a) and (c)) or NaCl ((b) and (d)) as host materials. The pictures (a) and (b) have been photographed under ambient light, (c) and (d) under excitation with a 365 nm UV-lamp. Reproduced with permission from Ref. [87]. © American Chemical Society 2015.

In Figure 5.6, the resulting borax based macrocrystals are displayed. As it can be seen from the microscopic images in Figure 5.6 ((b), (e), and (h)), the QDs are equally distributed within the matrix. The corresponding PL-spectra show that upon incorporation the pure color emission does not change, but a small red shift of the emission maxima occurs. This shift is accompanied with the change of the surrounding dielectric media from water to salt matrix [83], [154]. Spectra in Figure 5.6(f) shows a reproducible slight red tailing, indicating aggregated QDs upon incorporation into borax. Such broadening, in the case of the yellow component, does not reduce the overall quality of the color converter. To ensure that the spectral properties of the macrocrystals will not change upon milling and incorporation into the silicone, thin layers of powder encapsulated into the silicone resin were prepared. The corresponding spectra can be found in Figure 5.7, showing no change during the silicone embedding process. For all samples, PL-LT and PL-QY measurements were conducted in CHCl_3 , H_2O and borax, corresponding results are shown in Figure 5.8 and Table 5.3.

As expected from recent studies on macrocrystals [91], [154], [155], all samples show a stronger change in PL-QY than PL-LT over all steps (and thereby changes of surrounding media), while both figures exhibit similar trends. Such behavior was previously discussed in the literature [165], considering the fact that both PL-QY and PL-LT data arise from ensemble measurements of QDs revealing multiexponential decay kinetics. In such ensembles, PL-LT measurements are commonly dominated by the strongest luminescent component, while PL-QY measurements account also for weakly emitting (or dark) QDs due to their absorbance and reflect most likely a broad distribution in PL-QY. Therefore, until today, no straightforward correlation between the QDs PL-QY and PL-LT was found, as it is, on the other hand, well known for molecular emitters [166]. Secondly, the results are in good agreement with the findings of our recent mixed crystal PL-QY study [154]. An encapsulation of CdSe/CdZnSeS/ZnS QDs into an ionic matrix does not lead to a pronounced increase in PL-QY, since no passivating CdCl_x can be formed on the QD surface.

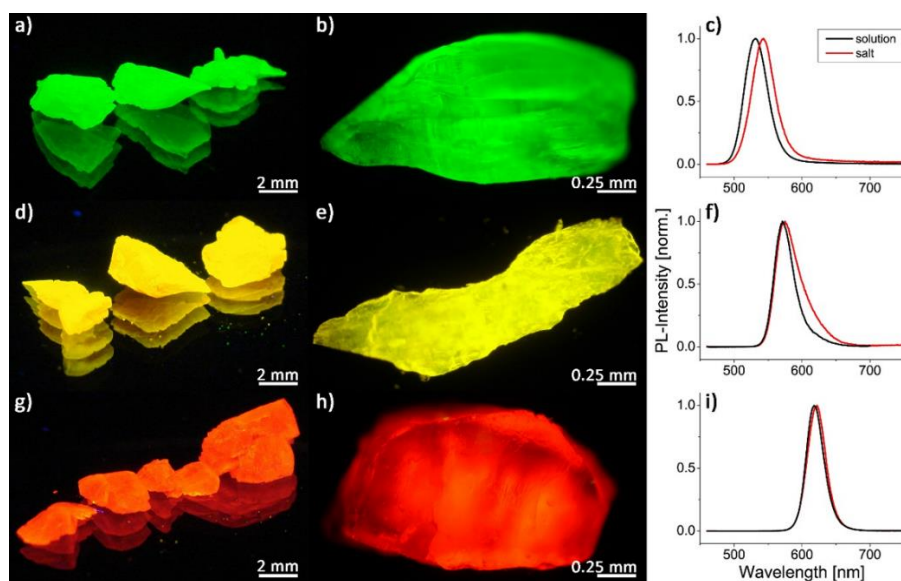


Figure 5.6. True color ((a), (d), and (g)) and microscopic ((b), (e), and (h)) images of differently emitting CdSe/CdZnSeS/ZnS QDs incorporated into borax crystals under UV-excitation (365 nm). Graphs (c), (f) and (i) show the corresponding PL-spectra of the initial solutions (black lines) and macrocrystals (red lines). Reproduced with permission from Ref. [87]. © American Chemical Society 2015.

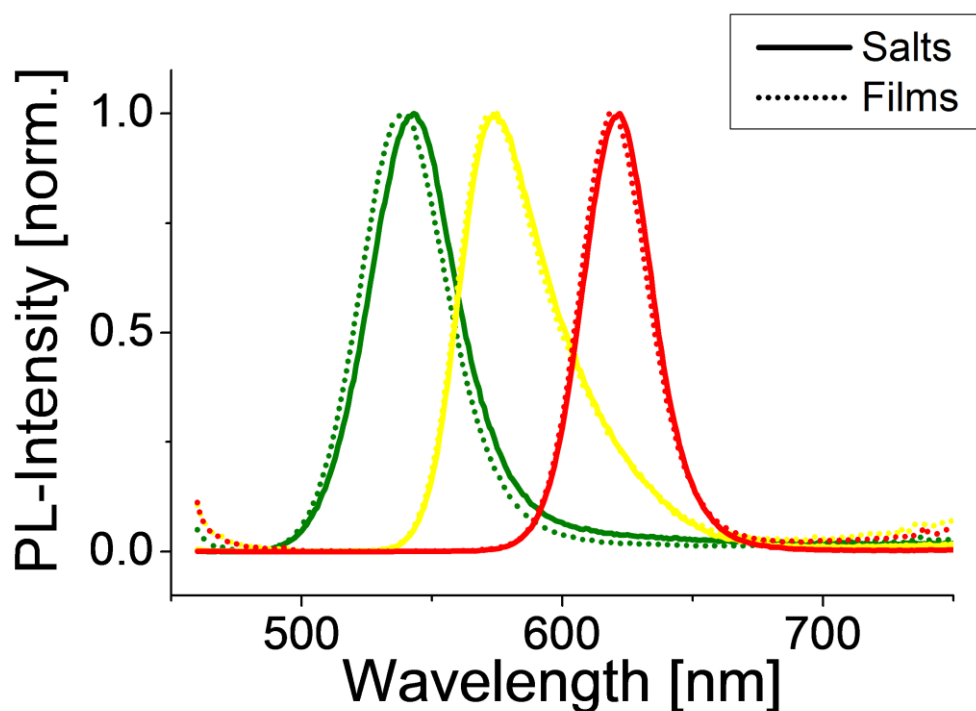


Figure 5.7. Photoluminescence spectra of three different CdSe/CdZnSeS/ZnS QD-based macrocrystals (solid lines) in addition to their spectra after powdering and incorporation into thin films of silicone (dotted lines). Reproduced with permission from Ref. [87]. © American Chemical Society 2015.

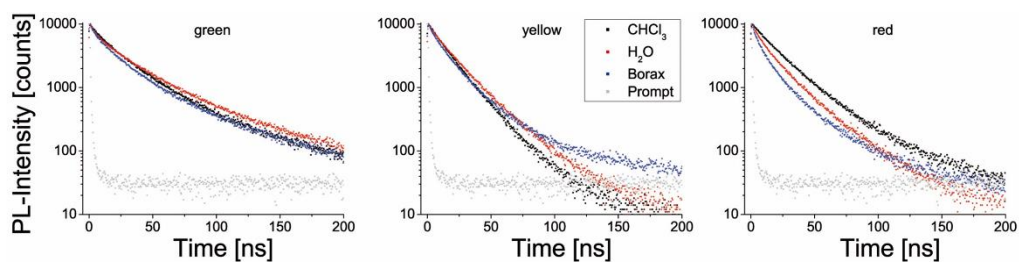


Figure 5.8. PL-decay spectra of three different QDs in CHCl_3 (black squares), H_2O (red squares) and after embedding into borax (blue squares). The grey squares always represent the measured prompt. Reproduced with permission from Ref. [87]. © American Chemical Society 2015.

Table 5.3. Average PL-lifetimes and photoluminescence quantum yields (PL-QY) for three QDs in different media. PL-QY values were measured three times and averaged.

	Green QD	Yellow QD	Red QD
τ in CHCl_3	21.9 ns	16.5 ns	21.6 ns
τ in H_2O	21.2 ns	17.4 ns	14.7 ns
τ in Borax	17.6 ns	14.1 ns	9.9 ns
PL-QY in CHCl_3	38.50%	40.30%	42.60%
PL-QY in H_2O	23.80%	16.60%	17.60%
PL-QY in Borax	30.20%	15.70%	14.00%

To verify that the QDs are well dispersed within the borax matrix, the macrocrystals were embedded within a resin and cut into thin sheets using an ultramicrotome. This step proved to be necessary, since directly adding the macrocrystals (or powders thereof) on top of the TEM-grid resulted in fast and complete melting of the macrocrystals under electron beam exposure [83]. The images in Figure 5.9 show well separated and non-aggregated QDs within the salt matrix, which is in good agreement with the results from the optical characterization methods. It should be highlighted that only using these thin sheets, imaging of QDs within an inorganic crystal matrix at atomic resolution, showing the crystallographic planes of the QDs is possible. Although a similar approach was used for QDs within NaCl-based macrocrystals [91], only borax proved to be suitable as a stable matrix under electron beam exposure, allowing such high magnifications.

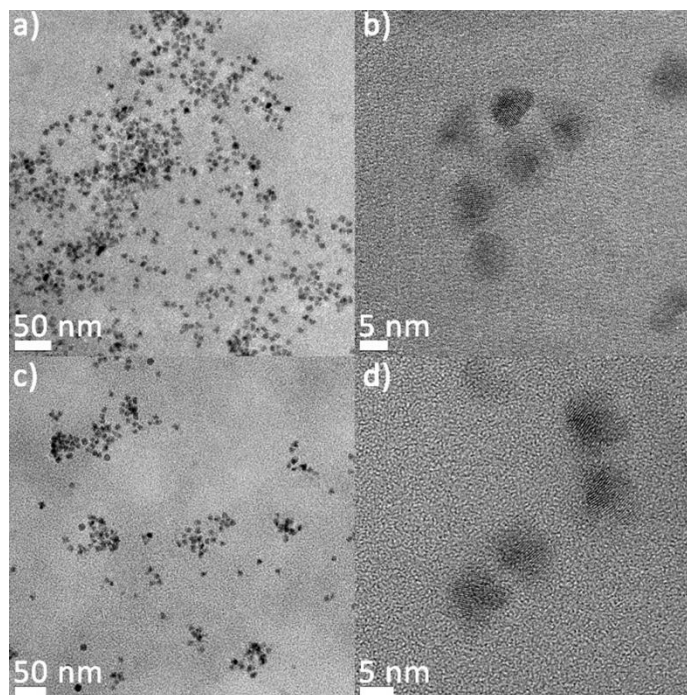


Figure 5.9. TEM images of the green- ((a) and (b)) and red- ((c) and (d)) emitting macrocrystals shown in Figure 4. Overviews (a) and (c) as well as highly magnified images (b) and (d) of the samples prove non-aggregated and well distributed QDs within the matrix. Reproduced with permission from Ref. [87]. © American Chemical Society 2015.

5.3.4 Stability tests of the white LED

The emission intensity of the QD macrocrystals were recorded by hybridizing them on a blue LED driven at 300 mA for 96 h (4 days). To avoid pronounced heat generation, the LED was placed on an aluminum plate for passive cooling and operated with a 1 kHz on/off rate. Under these conditions, the LED temperature stayed below 35°C (see Figure 5.10) while a continuous operation would cause an increase to 72°C which would reduce the overall stability of the emissive layer. Figure 5.11 displays the PL-spectra recorded during the investigation. The intensity of the mixed crystal emission decreases only slightly, which is in good agreement with our recent findings on the PL-stability of the macrocrystals under intense illumination [83]. Therefore, the macrocrystals outcompete all other QD packaging approaches in terms of photostability, verifying their suitability in color conversion applications. It should be noted

that the macrocrystals were grown under ambient conditions. For commercialization, preparation under inert atmosphere could be beneficial, preventing the incorporation of dissolved O₂ and might be a crucial step to further increase the overall photostability.

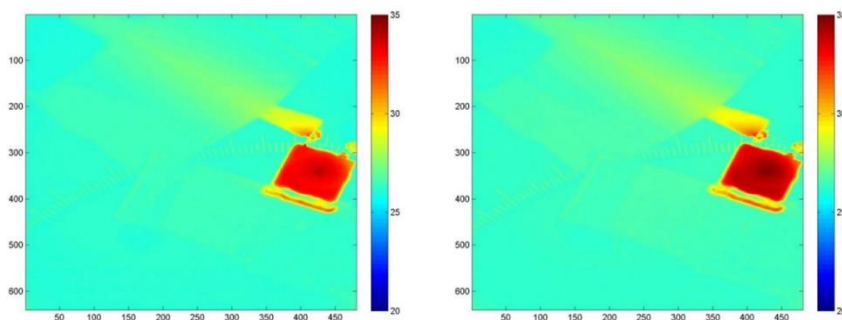


Figure 5.10. Infrared-image of a LED hybridized with macrocrystals in operation. The image was taken after a 15 (left) and 30 (rights) minutes operation using a 1 kHz switching rate, proving that the temperate stays constant slightly above room temperature, not exceeding 35 °C. Reproduced with permission from Ref. [87] © American Chemical Society 2015.

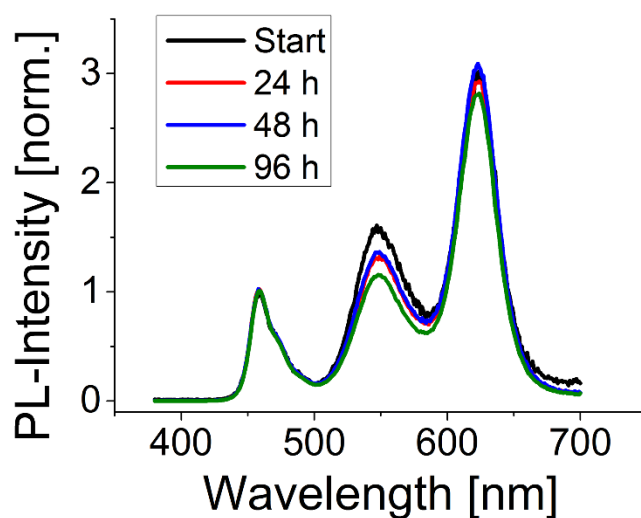


Figure 5.11. PL-spectra of the white LED before and during the stability tests. The white LED was driven at 300 mA and a 1 kHz on/off rate, avoiding significant heat generation. Reproduced with permission from Ref. [87] © American Chemical Society 2015.

5.3.5 White LED preparation

To produce our final white LED, the macrocrystals discussed above were milled to a fine powder, dried and defined amounts of green (20 mg), yellow (8 mg) and red (16 mg) converters were blended together with a two-component, industrial standard silicone resin.

During the first preparations, a raising in the powder-silicone mixture was observed, causing an inhomogeneous and porous conversion layer, as shown in Figure 5.12(b). These layers showed minor mechanical stability (Figure 5.12(c), conversion layer after holding with tweezers) and provided only weak protection of the fine powder against oxygen and water-vapor diffusion, yielding a change of the white LEDs spectra within days. Borax, unlike the other matrices NaCl, KCl etc. we used, crystallizes as a decahydrate. As it can be seen from the thermo gravimetric analyses of borax based macrocrystals in Figure 5.13, part of the crystal water is released at 70 °C, the curing temperature of the silicone. Gently drying the mixed crystal powder under vacuum at 70 °C before blending it with the silicone ensures that no further crystal water is released during curing, yielding a smooth and rigid conversion layer as shown in Figure 5.12(a). Removing parts of the crystal water during the drying step also reduces the overall mass of mixed crystal powder needed, enabling the formation of smaller conversion layers.

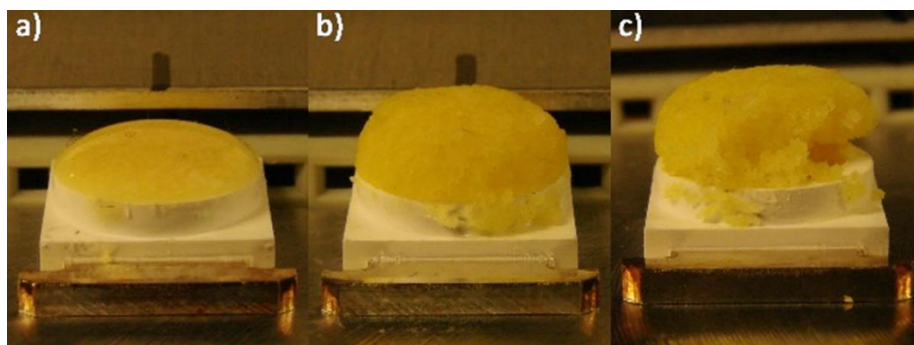


Figure 5.12. True color image of a LED (a) prepared using borax powder, which was dried before blending it with the silicone on top of the LED. Photograph (b) and (c) show a LEDs produced using non-dried macrocrystal powder. While (b) shows the porous and non-homogenous silicone encapsulation, (c) displays the minor mechanical stability of such layers. Reproduced with permission from Ref. [87] © American Chemical Society 2015.

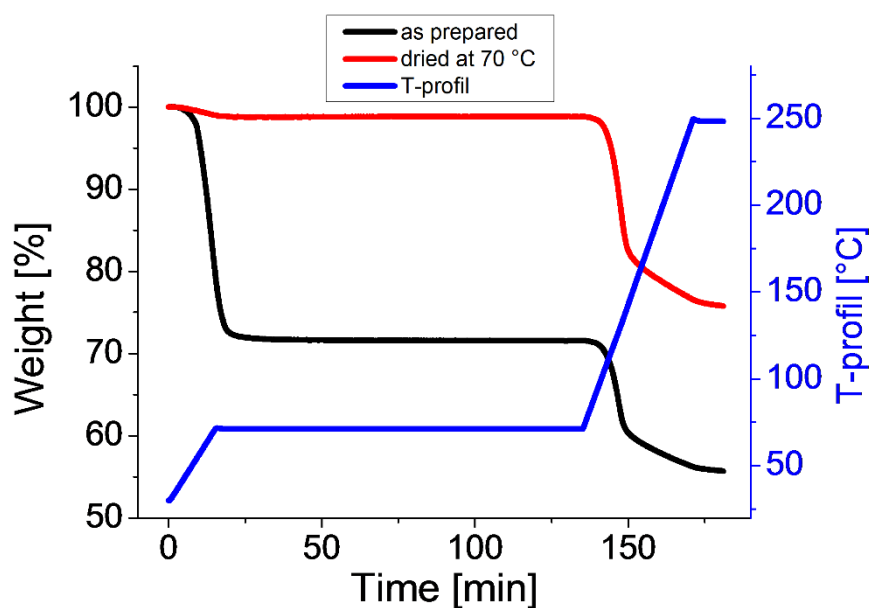


Figure 5.13. Thermogravimetric analysis of borax-based macrocrystals. The blue line displays the applied temperature program, with a two-hour isothermic part at 70 °C to imitate the curing of the silicone on top of the LED. As prepared macrocrystal powder shows a significant weight loss (black curve), while the pre-dried powder suffers only from a negligible loss at 70 °C. Reproduced with permission from Ref. [87] © American Chemical Society 2015.

By adjusting the amounts of green-, red-, and yellow-emitting powder, the hue of the final device can be tuned to a warm white. Figure 5.14(d) shows the emission spectrum of the resulting warm-white LED achieving a CCT of 2720 K, a CRI of 91 and a LER of 341 lm/W_{opt}, simultaneously. These values combine a warm-white hue, which is comparable to an incandescent bulb (CCT ~ 2800K), while preserving the high efficiency of the solid-state lighting devices and giving a color rendering that matches industrial requirements [167]. Furthermore, it overcomes the CRI = 90 barrier of QD based LEDs for the first time simultaneously reaching LER > 340 lm/W_{opt} with a warm-white shade, exceeding the current state-of-the art in literature [121]. In Figure 5.14(e), the position of the LEDs spectra within the CIE 1931 diagram (x=0.4557, y=0.4056) and a blackbody radiator are marked with the cross and the black curve, respectively. Figure 5.14(a) shows the QD incorporating salt macrocrystals, which we used to produce our white LED under the illumination of a standard fluorescent lamp. In comparison, the same image was taken in the darkened room, just illuminated by our white LED (Figure 5.14(b)). Here, especially the red crystals show a more saturated color in comparison to Figure 8a, which is due to the LED's much higher amount of emitted red light in comparison to the fluorescent lamp. Since most of today's commercially available white LEDs also lack a sufficient amount of red within their emission spectra, the fluorescent lamp can be used as a comparison. Figure 5.14(c) shows the same image taken under 365 nm UV-excitation, proving the intense and pure color emission of the macrocrystals.

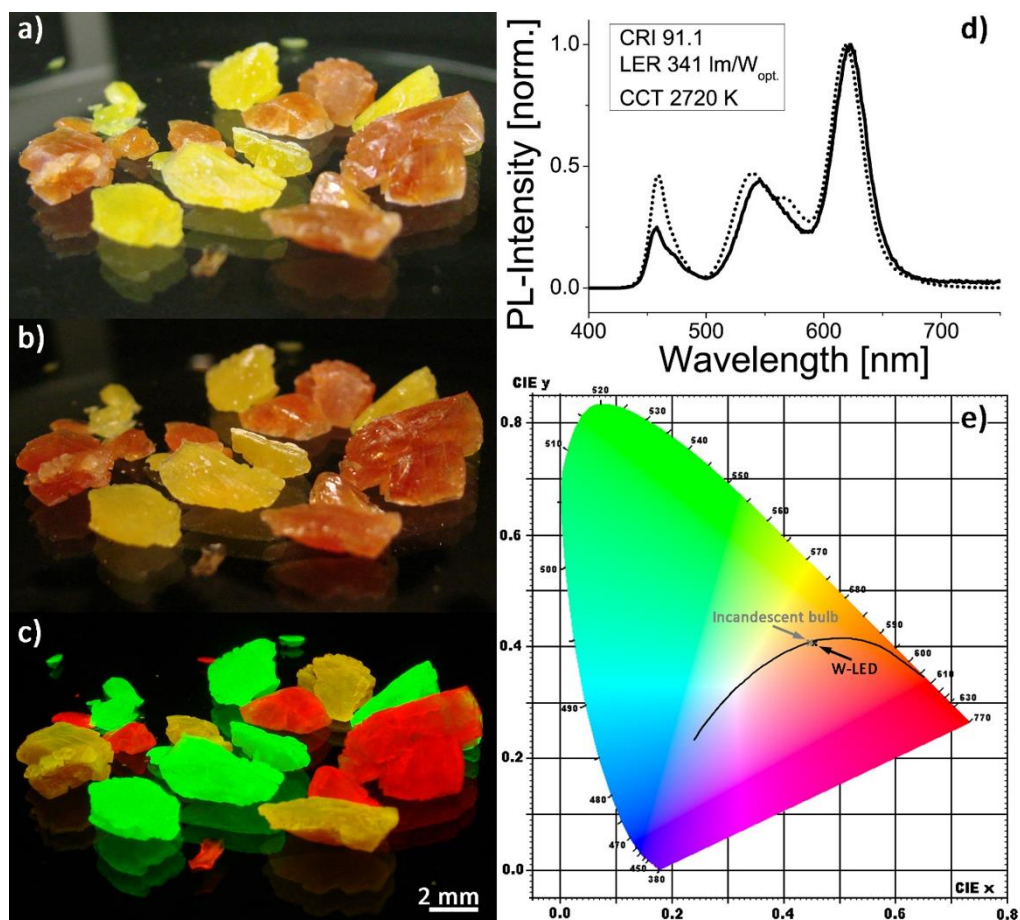


Figure 5.14. Photographs (a), (b), and (c) show true color images of our macrocrystals under either ambient illumination with a standard fluorescent lamp (a), with our white LED (b), and under 365 nm UV-excitation. Graph (d) presents the PL-spectra of our white LED within the visible region (solid line) and the used modeled spectra (dotted line), while (e) shows a CIE 1931 diagram with the blackbody radiator (black line, CRI 100) as comparison, our white LED marked with the black cross and an incandescent bulb (grey cross). Reproduced with permission from Ref. [87] © American Chemical Society 2015.

5.4 Summary

In summary, we presented a model-experimental feedback approach to synthesize CdSe/CdZnSeS/ZnS QDs with an alloyed gradient shell whose emission spectra match the requirements of high-quality white light luminaires. These QDs were successfully phase-transferred and incorporated in borax-based macrocrystals,

which provide a rigid and air-tight ionic matrix while assuring a high loading density of QDs. Within a stability test, these macrocrystals showed a strongly enhanced stability in comparison to pure QDs, proving their applicability as color converters. Throughout all steps, intermediate results were reviewed with the spectral model to ensure their applicability as color-conversion materials. Finally, by hybridizing green-, yellow-, and red-emitting macrocrystals onto a blue LED, we prepared a white LED with a correlated color temperature of 2720 K, a color rendering index of 91.1 and a luminous efficacy of optical radiation of 341 lm/W_{opt}, which altogether make very high performance.

Chapter 6

Macrocrystals of Nanocrystal Quantum Dots for Fluorescence Enhancement

In this chapter of the thesis, we present our efforts on developing robust and cm-dimensional plasmonic structures facilitating colloidal metal nanoparticles. In our study, we incorporated gold nanoparticles into sucrose macrocrystals to obtain large and robust crystals possessing plasmonic features. We further co-immobilized these metal nanoparticles together with colloidal semiconductor QDs to investigate the plasmonic interaction between these colloidal nanoparticles. We observed that at the correct concentration of the gold nanoparticles in the macrocrystals, we can increase the quantum efficiency of the QDs substantially within the macrocrystals. These results suggest that such plasmonic crystals are promising candidates for large-scale robust platforms to embed plasmonic nanoparticles.

This chapter of the thesis is mainly based on T. Erdem, Z. Soran-Erdem, P. L. Hernandez-Martinez, V. K. Sharma, H. Akcali, I. Akcali, N. Gaponik, A. Eychmüller, and H. V. Demir, *Nano Research* 8, 3, 860-869 (2015) [84]. Reproduced with permission from Tsinghua University Press and Springer-Verlag Berlin Heidelberg © 2015.

6.1 Introduction

Plasmonics attract significant attention in various branches of science and technology including biology [103], [168], physics [169]–[171], chemistry [172], and photonics [173]. Basically, this field of study deals with the oscillation of free charges on the metallic surfaces. When excited at the correct frequency, these free charges start to oscillate in resonance with the incoming light. In the case of

metal nanoparticles (NPs), these oscillating charges – called localized surface plasmons – can enhance the electromagnetic field locally but strongly, which in turn gives rise to the attractive features of plasmonics such as enhanced absorption, fluorescence, and scattering [169] in addition to improvements of the nonlinear properties [173]. The fluorescence enhancement through localized surface plasmons, about which we present a proof-of-concept study using macrocrystals of nanocrystals in this chapter of the thesis, emanates from the increased radiation probability of near-by emitters as a result of the localized electromagnetic field [174]. Consequently, substantial improvements in the quantum efficiency become possible.

An experimental realization of these improvements associated with plasmonics necessitates metallic structures to be produced with nanometer dimensions, which requires either the use of lithography tools like electron beam and focused ion beam lithography or colloidal synthesis. Among the limitations associated with the lithography approaches, one can count the difficulties and high cost of the fabrication process. In addition, the total size of the samples prepared with these techniques remains generally in the micrometer range, which strongly restricts the use of plasmonic structures in applications requiring large dimensions such as lasers and light-emitting diodes. Furthermore, integration and transfer of these structures to functional devices turn out to be another challenge related to this fabrication method.

The colloidal synthesis approach, on the other hand, offers an inexpensive and easy way to obtain metal nanoparticles for plasmonics studies. By carefully selecting the surfactant molecules attached to these nanoparticles, their interaction with other molecules or structures can be easily tailored in liquid environments. Nevertheless, the use of these colloidal nanoparticles in solid state applications is challenging because of the problems in controlling the plasmonic interactions between the metal nanoparticles and other materials. Although the layer-by-layer assembly of nanoparticles enables the preparation of highly controlled films [175], the thickness of the films remains mostly below 100 nm significantly limiting possible device applications. Methods allowing for preparing films of larger thicknesses like spin-coating and drop-casting, however, cannot

prevent the aggregation of colloidal nanoparticles, which avoids the use of plasmonic interaction in a controlled manner.

As a remedy to these problems, here we present metal nanoparticle embedded sucrose crystals that acquire centimeter scale dimensions and exhibit a robust plasmonic character suitable for integration in large-scale applications. This material system can be used in various optical systems such as color-converting coatings of LED luminaries and color enrichment films of LCD display backlighting units using approaches including powdering and encapsulation in polymers and epoxies that will protect them from external effects like humidity and heat to a certain degree. Furthermore, using pieces of individual macrocrystals, which are selected during or after crystal growth, is another possible simple integration scheme. These sucrose crystals were grown by hybridizing them with gold nanoparticles (Au NPs) so that the plasmonic nature of the metal nanoparticles is maintained. Furthermore, plasmonic fluorescence enhancement of green CdTe quantum dots (QDs) was demonstrated by hybridizing them with gold nanoparticles within these sucrose crystals (Figure 6.1).

Different from previous reports of QD embedded macrodimensional salt crystals (i.e., macrocrystals) [83], [87], [89], sucrose was deliberately chosen here because of the absence of ions in its aqueous solution, since ions in a salt solution strongly trigger aggregation of gold nanoparticles [176]. This causes the plasmonic peak of the absorption spectrum to broaden significantly as soon as NaCl solution is introduced to the gold nanoparticle dispersion while the color of the mixture turns from pink to gray. As a result, at the end of the crystallization in the presence of salt ions, the initial plasmonic peak of gold nanoparticles in the absorption spectrum completely vanishes (see Figure 6.2). Sucrose, on the other hand, successfully protects the plasmonic fingerprints of the gold nanoparticles first in the dispersion (see Figure 6.2) and later in the crystal form (Figure 6.3).

Here, this hybrid composite material obtained in centimeter scales was shown to increase the quantum efficiency of the green CdTe QDs from 24% up to 38% by 58% via plasmonic coupling as the concentration of Au nanoparticles

increases. In this particular case, the lifetime of the emitter decreased from 11.0 to 7.39 ns indicating the plasmonic character of the efficiency improvement. Moreover, a further increase of the Au NP content while keeping the QD content the same caused strong quenching of quantum efficiency down to 4.6% together with an increase in the lifetime up to 12.6 ns.

Employing the information of quantum efficiency and photoluminescence lifetime, we carried out a detailed theoretical analysis to identify the origin of the changes in the photophysical features of the macrocrystals. We found out that the increase of the field enhancement factor plays a crucial role in the fluorescence enhancement. On the other hand, the fluorescence quenching was attributed to the decrease of the field enhancement factor below unity, as also reported by Teng *et al.* [177] while the effect of nonradiative energy transfer from CdTe QDs to Au NPs remained weaker. Bearing in mind its simplicity, inexpensiveness, and robustness, we believe that this new composite material may find applications in various fields of science, especially in optics and photonics, requiring solid materials with large dimensions that employ plasmonic interaction.

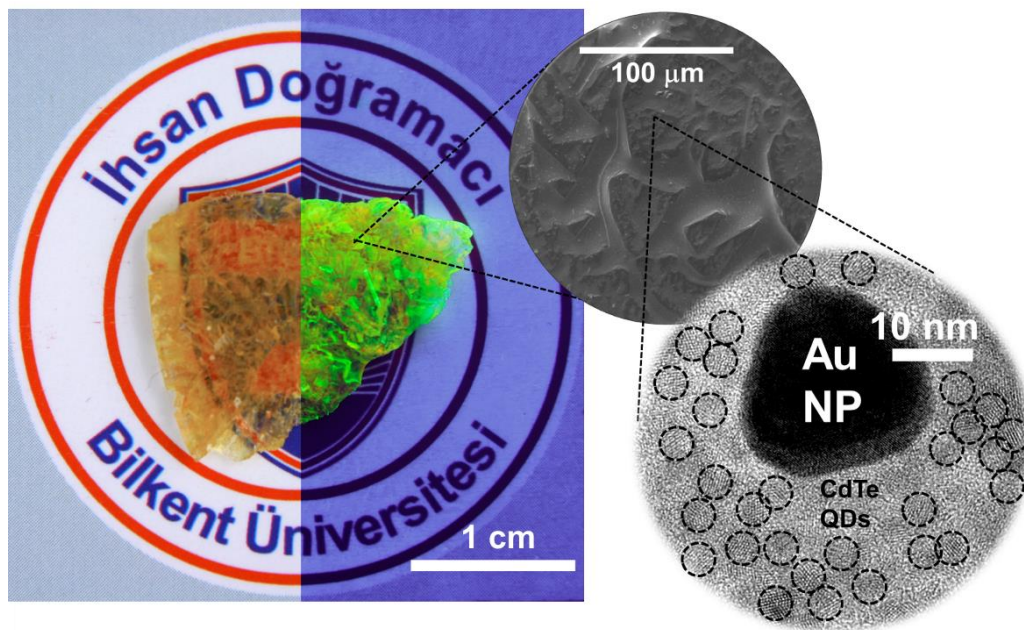


Figure 6.1. True color images of CdTe QDs and Au NPs embedded in macrodimensional sucrose crystals, which shows an efficiency enhancement of 58% through plasmonic interaction, under ambient lighting and ultraviolet illumination along with scanning electron microscopy (middle) and transmission electron microscopy (right) images. Reproduced with permission from Ref. [84]. © Tsinghua University Press and Springer-Verlag Berlin Heidelberg 2015.

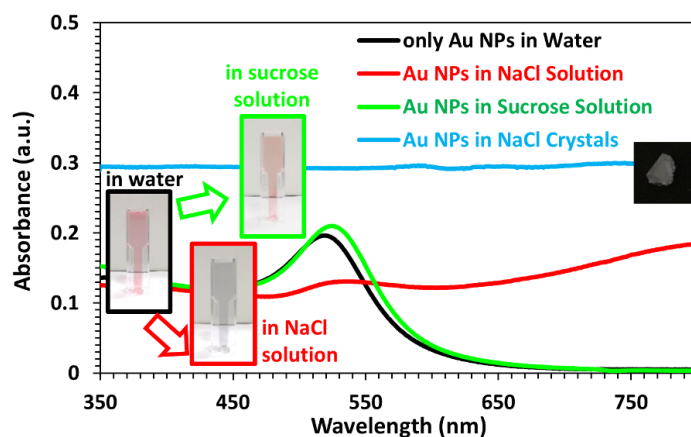


Figure 6.2. Absorption spectra of Au NP dispersion in water, in NaCl solution and in sucrose solution along with the true color photos. Reproduced with

permission from Ref. [84]. © Tsinghua University Press and Springer-Verlag Berlin Heidelberg 2015.

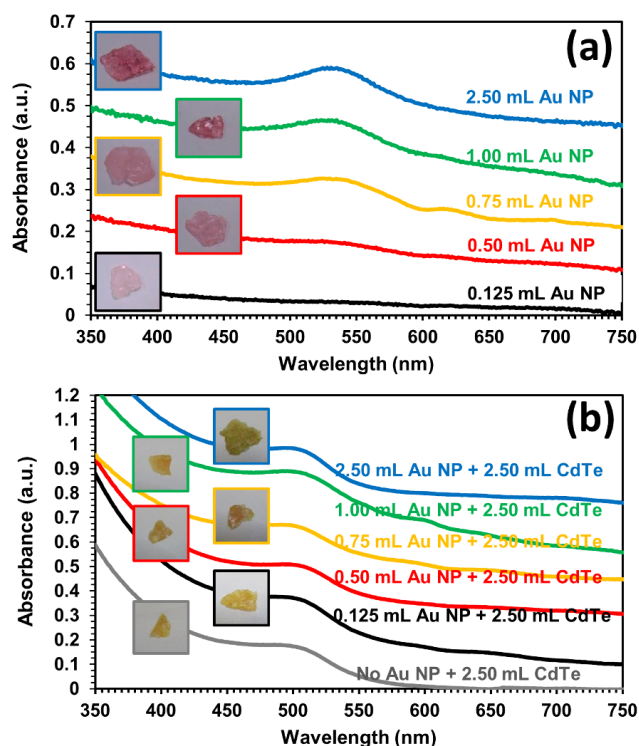


Figure 6.3. Absorption spectra and true color photographs of the macrocrystals incorporating Au NPs (a) alone and (b) coimmobilized together with CdTe QDs. Reproduced with permission from Ref. [84]. © Tsinghua University Press and Springer-Verlag Berlin Heidelberg 2015.

6.2 Experimental Methodology

6.2.1 Synthesis of CdTe QDs and Au NPs

The synthesis of CdTe QDs was carried out according to the procedure reported in Chapter 2 [55]. A typical synthesis starts with the dissolution of $\text{Cd}(\text{ClO}_4)_2 \cdot 6\text{H}_2\text{O}$ (5.5 mmol) in Milli-Q water (Millipore) (250 mL) followed by the addition of thioglycolic acid (7.15 mmol). Subsequently, the pH of the solution was adjusted to 12 by adding of NaOH (1 M) solution dropwise. Before the synthesis, the mixture was placed in a three-neck flask and kept under argon

flow for 30 min. The Te-precursor was transferred to the mixture via the addition of H_2SO_4 (0.5 M, 10 mL) on to Al_2Te_3 (0.916 mmol) under slow argon flow. Finally, the atmosphere of the synthesis was changed to air and the synthesis was started after heating the mixture to 100 °C. For obtaining small QDs possessing green emission, the synthesis was stopped within the first 5 minutes. The size and concentration of the QDs were calculated according to Ref. [178] as ~1.8 nm and 141 μM , respectively.

The gold nanoparticles used in this study were synthesized using the citrate reduction approach [179]. In a typical synthesis, $\text{H}[\text{AuCl}_4]_{33}\text{H}_2\text{O}$ solution (0.2% w/v, 2.5 mL) in Milli-Q water (50 mL) was heated. Once the solution started to boil, sodium-citrate solution (1% w/v with 0.05% w/v citric acid, 2 mL) was added under vigorous stirring. After approximately 10 minutes of boiling, the synthesis was finished and the solution was cooled down. The absorption spectrum of the synthesized Au NPs is given in Figure 6.4. The size and concentration of the as-synthesized Au NPs were calculated according to Ref. [180] and found to be ~15 nm and 2.5 nM, respectively.

6.2.2 Growth of sucrose macrocrystals

Sucrose stock solution for the crystallization studies was prepared by dissolving sucrose (260 g) in Milli-Q water (500 mL). For the crystal growth, the sucrose solution (10 mL) was mixed with CdTe QDs (2.50 mL) and the desired amount of Au NPs. In this study, samples including 0.125, 0.50, 0.75, 1.00, and 2.50 mL of Au NPs were employed. For the sake of simplicity, here we used the volume of the added Au NP and CdTe QD into the crystallization mixture as the amounts. In terms of particle numbers, the amount of QDs used in the study corresponds to 352.5 nmol and the amounts of Au NPs used become 0.78, 1.56, 2.34, 3.13, and 15.6 pmol. The prepared mixture was dropped into a petri dish (diameter 6 cm) in an environment where the vibration is minimal. Vibration was further minimized using a 30 Duro Sorbothane vibration isolation pad. Within approximately 10 days, QD and Au NP embedded sucrose crystals were obtained. At the end of the crystallization, the whole surface of the petri dish

was covered with sucrose crystal pieces, laterally in centimeter scales. The thickness of the crystal formation was ~2-3 mm.

6.2.3 Optical characterizations

The absorption measurements were carried out using a Cary 100 spectrophotometer. The quantum efficiency measurement of the crystals was carried out by placing the crystals on a blue LED (Avago ASMT) emitting at 460 nm and calculating the absorbed and emitted number of photons using an integrating sphere and a ZVision spectrophotometer. In solution quantum efficiency of the QDs were measured using Rhodamine 6G as the standard reference dye whose quantum efficiency is 95%. The absorbances of the QD and the reference dye were equated between 460 and 480 nm and below an absorbance of 0.1 to minimize the self-absorption effects. Subsequently, the emissions of QD and dye were collected using a Cary Eclipse fluorescence spectrophotometer by exciting at the wavelength where their absorbances were equated. The quantum efficiency was found by comparing the total number of photons emitted by the reference dye and the QDs. Time-resolved fluorescence spectra were obtained by employing a PicoHarp 200 time-resolved single photon counting system (PicoQuant) and the 1/e value of the maximum photon count was reported as the lifetime.

6.2.4 Structural characterizations

The crystal structure of the macrocrystals, which were fine-powdered by using a mortar before the X-Ray diffraction (XRD) measurement, was determined by a Panalytical X'pert Pro Multi-purpose X-Ray Diffractometer operated at 45 kV and 40 mA with CuK α radiation and a diffracted beam monochromator. XRD spectra were taken from 10° to 50° of the 2 θ angle with a step size of 0.01°.

The structural morphology of the as-grown QD and Au NP embedded sucrose macrocrystals was further investigated using a FEI Quanta 200 FEG scanning electron microscope (SEM) under high vacuum. The crystals were coated with 4 nm of Au/Pd to minimize the charging of crystals before imaging.

QDs and Au NPs within the macrocrystals were imaged using a transmission electron microscope (TEM). In order to obtain thin sections, the macrocrystals were embedded into an Araldite 502 epoxy resin [181]. Following the curing of epoxy at 60 °C, macrocrystal embedded epoxy was sectioned using a Leica ultramicrotome. Subsequently, sections in ethanol were transferred onto a Lacey carbon coated 200 mesh copper grid and TEM images were recorded by a FEI Tecnai G2 F30 TEM.

6.3 Results and Discussion

The as-synthesized CdTe QDs exhibited a peak emission wavelength of 523 nm, while their first exciton band in the absorption spectrum was located at 476 nm (Figure 6.4). In the absence of the metal NPs, the emission peak of CdTe QDs in the sucrose macrocrystals shifted to ~534 nm. Furthermore, a clear plasmon peak was monitored at 522 nm in the absorption spectrum of the Au NPs in water (Figure 6.4). Despite mixing the Au NP dispersion with sucrose solution, the plasmonic features of the nanoparticles were protected except for causing a slight red shift and a slightly enhanced absorption (see Figure 6.2). When Au NPs were embedded into the sucrose crystals, the plasmonic absorption peak was observed to shift further to 532 nm (see Figure 6.3).

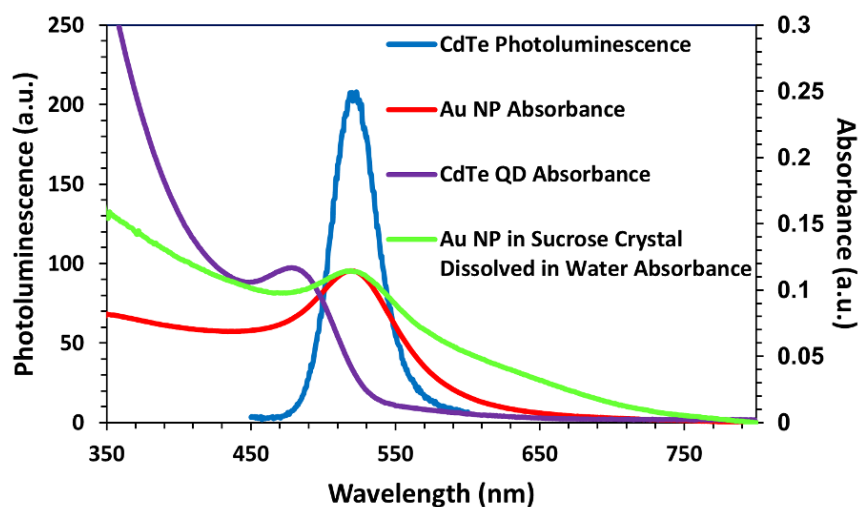


Figure 6.4. Photoluminescence and absorbance spectrum of as-synthesized CdTe quantum dots (QDs) along with the absorbance spectrum of Au NPs in water and absorbance spectrum of 2.5 mL Au NP incorporated sucrose crystal (~15 mg) dissolved in 5 mL of water. Reproduced with permission from Ref. [84]. © Tsinghua University Press and Springer-Verlag Berlin Heidelberg 2015.

This red shift and absorption enhancement in the absorption peak of the Au NP is attributed to the difference of the refractive indices of water ($n_{\text{water}}=1.33$) and sucrose crystal ($n_{\text{sucrose}}=1.56$) [182], and was confirmed using the simulation tool extinction, scattering and absorption efficiencies of single and multilayer nanoparticles at <http://nanohub.org>. The absorption spectra of the sucrose crystals with and without CdTe QDs and with different amounts of Au NPs are presented in Figure 6.3.

In this proof-of-concept demonstration, these Au NPs and CdTe QDs were intentionally chosen so that the plasmonic peak of the Au NP absorption and photoluminescence of QDs overlap to reveal a strong plasmonic interaction in this composite material system. Nonetheless, there is no physical or chemical restriction of applying this system to other organic and inorganic emitters and metal NPs of other sizes, shapes, and materials, which further widens its applicability.

We observe that the plasmonic absorption peaks for low concentrations of Au NPs are barely recognizable; however, they appear very strong when the Au NP content is further increased. This observation shows that Au NPs retain their plasmonic features within the sucrose crystals as opposed to the case of embedding them in salt macrocrystals where we observed a distinct color change of the mixture from pink to gray right after the preparation of the mixture due to the aggregation of Au NPs in the presence of positive ions (see Figure 6.2).

On the other hand, when the Au NPs and CdTe QDs are crystallized together with sucrose, the absorption spectra do not reveal a certain qualitative difference compared to the crystals without Au NPs. However, the bumps at longer wavelengths that occur due to the interaction of Au NPs with each other can still be observed. The true-color photographs of Au NP embedded crystals in this figure clearly show that the pink color of Au NPs associated with the plasmonic effect is maintained in sucrose crystal. To further confirm that the metal nanoparticles in sucrose crystals preserve their plasmonic character without severe aggregation, ~15 mg of 2.50 mL Au NP incorporated sucrose crystal was re-dissolved in 5 mL of water. The absorption spectrum of this dissolved crystal (Figure 6.5) indicates that the plasmonic peak retains its position in spite of a slight broadening, which suggests that the permanent aggregation of Au NPs in sucrose remains limited.

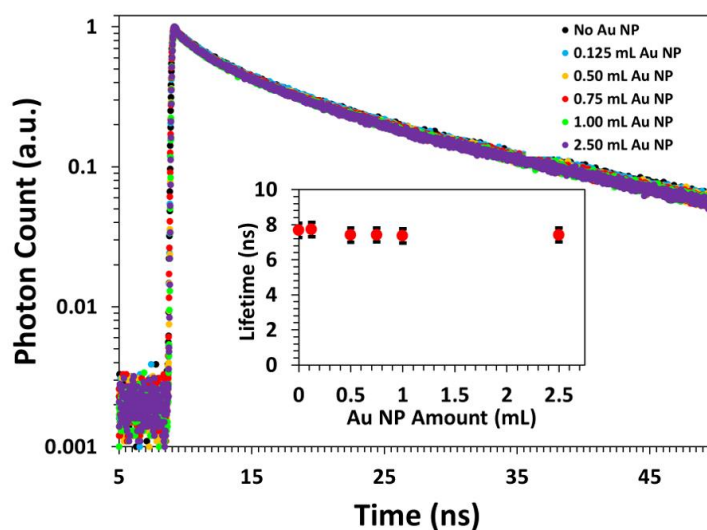


Figure 6.5. Time-resolved fluorescence decays and lifetimes (inset) of CdTe QD (2.5 mL) dispersion blended with varying amounts of Au NPs in sucrose solution using which the crystallization was carried out. Reproduced with permission from Ref. [84]. © Tsinghua University Press and Springer-Verlag Berlin Heidelberg 2015.

Subsequent to the absorption of the macrocrystals, their fluorescence quantum efficiency was measured to be 24% for the sample with no Au NPs and 2.50 mL (352.5 nmol) CdTe QDs while the quantum efficiency of the CdTe QDs is 20% in water (for the sake of simplicity, volumes used in the crystallization are preferred to particle amounts). This increase in the quantum efficiency was also observed in the work of Rogach *et al.*, and possibly stem from the better surface passivation of QDs within crystal [183]. For the cases of 0.125 mL (0.39 pmol) and 0.50 mL (1.56 pmol) of Au NP incorporation together with 2.50 mL (352.5 nmol) CdTe QDs, we observed enhanced quantum efficiencies of 29% and 38%, respectively. In other words, the respective quantum efficiency enhancement of the QDs turned out to be 21% and 58% for these two cases. Further increase of the Au NP amount caused a decrease in the quantum efficiency of the macrocrystals, as also theoretically suggested by Govorov *et al.* [107], to 22%, 4.6%, and 6.9% when 0.75 mL (2.34 pmol), 1.00 mL (3.13 pmol), and 2.50 mL (15.6 pmol) of Au NP were employed together with 2.50 mL (352.5 nmol) CdTe QDs, respectively. The quantum efficiency corrected

photoluminescence spectra belonging to these macrocrystals are presented in Figure 6.6 along with the measured quantum efficiencies. The analysis of Figure 6.6 reveals that the emission of the macrocrystals around the plasmonic peak of the Au NP was increased compared to the other parts of the emission spectrum for the crystals having fluorescence enhancement. This observation indicates that the enhancement in the emission is very likely to stem from the localized surface plasmons of Au NPs. For the crystals experiencing quenching the emission spectrum should exhibit a decrease in the emission intensity around the same wavelength range (~ 532 nm). However, such an observation is not straightforward from the spectra belonging to the corresponding crystals.

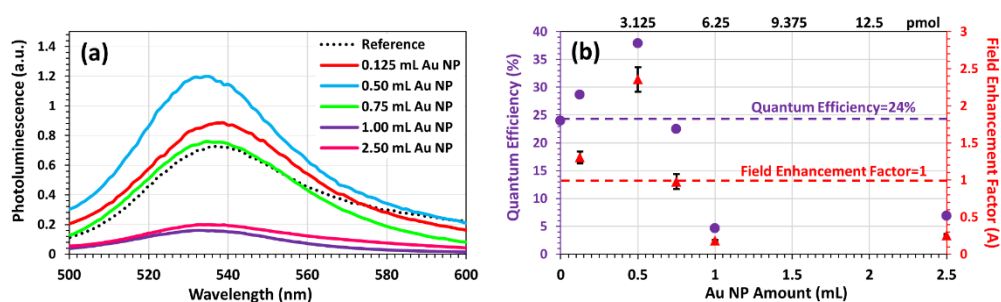


Figure 6.6. (a) Quantum efficiency corrected photoluminescence spectra of the macrocrystals containing various amounts of Au NPs and 2.5 mL (352.5 nmol) of CdTe QDs, and (b) quantum efficiencies (purple circles) and the field enhancement factors (red triangles) of the corresponding macrocrystals. The purple dashed line indicates the quantum efficiency level when no Au NPs are present in the macrocrystal while the red dashed line stands for a field enhancement factor of unity. Reproduced with permission from Ref. [84]. © Tsinghua University Press and Springer-Verlag Berlin Heidelberg 2015.

At this point, a lifetime analysis is crucial to clearly identify changes in the quantum efficiency when Au NPs are introduced into the macrocrystals. For this purpose, we measured the time-resolved photoluminescence decays of the composite macrocrystals and revealed the lifetime kinetics (Figure 6.7 and Table 6.1). The results show that the lifetimes shorten compared to the case of no metal NPs present when there is a fluorescence enhancement while the opposite is valid in the case of fluorescence quenching. The reference sample containing no

Au NPs but prepared using 2.50 mL of CdTe QDs exhibited a photoluminescence lifetime of 11.0 ns, while the lifetimes of 0.125 mL and 0.50 mL Au NP and the same amount of QD including macrocrystals (the ones experiencing fluorescence enhancement) became 10.1 and 7.39 ns, respectively. 0.75, 1.00, and 2.50 mL Au NP incorporated macrocrystals, which experienced fluorescence quenching, possessed lifetimes of 10.6, 11.6, and 12.6 ns, respectively. These observations together with the increase in quantum efficiency can be explained using plasmonic interactions between the QDs and the Au NPs, and the results are strongly in agreement with the study of Teng *et al.* [177] where lifetime shortening (lengthening) was observed in the case of plasmonic fluorescence enhancement (quenching) of Eosin Y on gold nanostructures fabricated employing electron beam lithography. In our experiment, only the sample including 0.75 mL of Au NP does not obey the trend indicated above. However, the quantum efficiency and lifetime of this sample turned out to be very close to the sample containing no metal nanoparticle, therefore, also the 0.75 mL metal nanoparticle containing macrocrystals can be considered to follow the same trend.

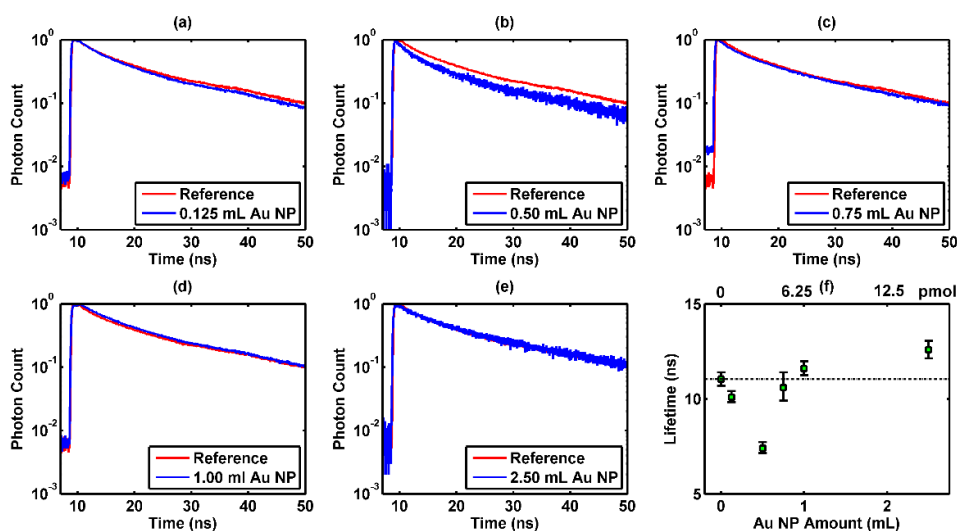


Figure 6.7. (a)-(e) Time-resolved fluorescence decays of CdTe QDs embedded in plasmonic macrocrystals. All of the crystals were grown using 2.50 mL of CdTe QDs, and the Au NP amounts were increased from 0.125 to 2.50 mL. The reference sample does not include any Au NPs. (f) The lifetimes of the

macrocrystals as a function of the Au NP amount used in the crystallization. Black dashed line indicates the lifetime when no Au NPs are present in the macrocrystal. Reproduced with permission from Ref. [84]. © Tsinghua University Press and Springer-Verlag Berlin Heidelberg 2015.

For a deeper understanding of the system, we start the analyses of the results with the definition of quantum efficiency that is the ratio of the radiative recombination rate (γ_{r0}) to the sum of the radiative and nonradiative recombination (γ_{nr0}) rates in the absence of the metal nanoparticles (Equation 6.1).

$$\eta_0 = \frac{\gamma_{r0}}{\gamma_{r0} + \gamma_{nr0}} \quad (6.1)$$

Table 6.1. Lifetimes of macrocrystals with varying Au nanoparticle content and fixed CdTe QD concentration (2.50 mL corresponding to 352.5 nmol).

Sample	Lifetime (ns)
Only 2.50 mL CdTe QD	11
Error +/-	0.35/0.35
0.125 mL AuNP + 2.50 mL CdTe QD	10.1
Error +/-	0.26/0.32
0.50 mL AuNP + 2.50 mL CdTe QD	7.39
Error +/-	0.26/0.32
0.75 mL AuNP + 2.50 mL CdTe QD	10.6
Error +/-	0.70/0.80
1.00 mL AuNP + 2.50 mL CdTe QD	11.6
Error +/-	0.35/0.38
2.50 mL AuNP + 2.50 mL CdTe QD	12.6
Error +/-	0.45/0.46

When there is a metal nanoparticle in the proximity of the emitter, interactions start to occur between the emitter and metal nanoparticle. The electric field (E) around the metal nanoparticle is enhanced upon the generation of localized surface plasmons, and this strengthened field is felt by the

nanoparticle whose radiative recombination rate (γ_r) is modified as $\gamma_r = A\gamma_{r0}$ where A is the field enhancement factor defined by the ratio of the total electric field intensity of the emitter in the presence ($E_{MNP \text{ present}}$) and absence ($E_{MNP \text{ absent}}$) of metal nanoparticles (Equation 6.2).

$$A = \frac{\int |E_{MNP \text{ present}}|^2 dV}{\int |E_{MNP \text{ absent}}|^2 dV} \quad (6.2)$$

Furthermore, the interaction of the emitter and metal nanoparticles opens another path for the excitons generated in the QDs to the metal nanoparticles as a nonradiative energy transfer ($\gamma_{nr,metal}$). Assuming that the intrinsic nonradiative channels are not affected as suggested by Govorov *et al.* [107], the total recombination rate and fluorescence quantum efficiency are modified in the presence of metal nanoparticles as in Equations 6.3 and 6.4, respectively.

$$\gamma_{total} = A\gamma_{r0} + \gamma_{nr0} + \gamma_{nr,metal} \quad (6.3)$$

$$\eta = \frac{A\gamma_{r0}}{A\gamma_{r0} + \gamma_{nr0} + \gamma_{nr,metal}} \quad (6.4)$$

In our experiments, we observed that in the case of fluorescence enhancement ($\eta > \eta_0$), $\gamma_{total} > \gamma_{total,0}$ where $\gamma_{total,0} = \gamma_{r0} + \gamma_{nr0}$; and $\gamma_{total} < \gamma_{total,0}$ in the case of fluorescence quenching ($\eta < \eta_0$). When the fluorescence enhancement is observed, the field enhancement factor A should be larger than unity so that the ratio of $A\gamma_{r0}$ to the total decay rate γ_{total} increases. As a result, an increase in the total recombination rate should be observed, which confirms our experimental findings stated above. On the other hand, the fluorescence quenching can be realized with an increase in the total recombination rate if this increase is larger than the increase of the radiative recombination rate. Nevertheless, our experimental results indicate a different behavior; in our case, the total recombination rate decreases. This can only happen if the field enhancement factor decreases below unity, which is the case in our study (Figure 6.6(b)) and was explained theoretically by the dynamic screening effect in Ref. [107]. An investigation of $\gamma_{nr,metal}$ together with A revealed that the decrease of the total decay rate in the case of fluorescence quenching was mainly driven by the decrease of A below unity. Our calculations showed that the decrease in the radiative emission rate

cannot be compensated by the increase in nonradiative energy transfer rate; as a result, we observe a strong lifetime lengthening when the quantum efficiency decreases strongly.

Since plasmonic coupling is strictly distance dependent [101], [107], the plasmonic interaction between the metal NPs and QDs in the dispersion is expected to be much weaker due to the increased interparticle distance in dispersion compared to the case of solid crystals. To reveal this effect, we investigated the emission dynamics of CdTe QDs in the dispersion mixture using which the crystallization was carried out by employing time-resolved fluorescence. As expected, the fluorescence decay curves presented in Figure 6.5 indicated no significant change in the QD emission dynamics upon the inclusion of the metal nanoparticles in the dispersion. This confirms that the interaction between metal nanoparticles and quantum dots is strongly distance dependent and strengthens in solid crystals as a result of decreased interparticle distance.

The structural characterizations of the composite macrocrystals were carried out using scanning electron microscopy (SEM), transmission electron microscopy (TEM), and X-Ray diffraction (XRD). The SEM image presented in Figure 6.8 (a) shows that the composite structure has clear crystal facets with varying sizes. On the other hand, the TEM image shown in Figure 6.8(b) indicates that the CdTe QDs and the Au NPs are in close proximity, which is necessary for the plasmonic interaction. In Figure 6.8(b), some of the QDs are marked with black circular indicators for visual assistance. To reveal the general distribution of the QDs in the matrix, the same figure was presented without black circles in Figure 6.9. Figure 6.8(b) shows that the QDs may form small aggregates in some regions. However, the optical characterizations reveal that this aggregation does not cause a net decrease in the quantum efficiency of the QDs mainly because of a better surface passivation of the QDs [154] and the plasmonic interaction.

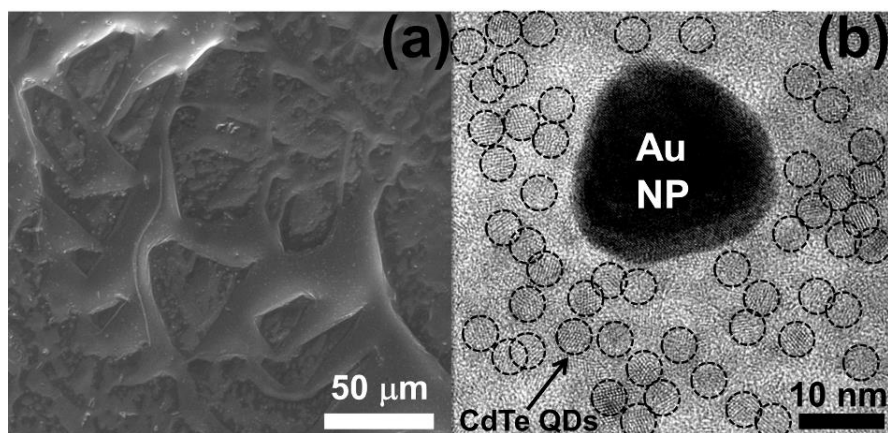


Figure 6.8. (a) SEM and (b) TEM images of the Au NP and CdTe QD incorporated macrocrystals belonging to the macrocrystal prepared using 0.50 mL Au NPs and 2.50 mL CdTe QDs. Some of the QDs in the TEM image are marked with dashed black circles for visual assistance. Reproduced with permission from Ref. [84]. © Tsinghua University Press and Springer-Verlag Berlin Heidelberg 2015.

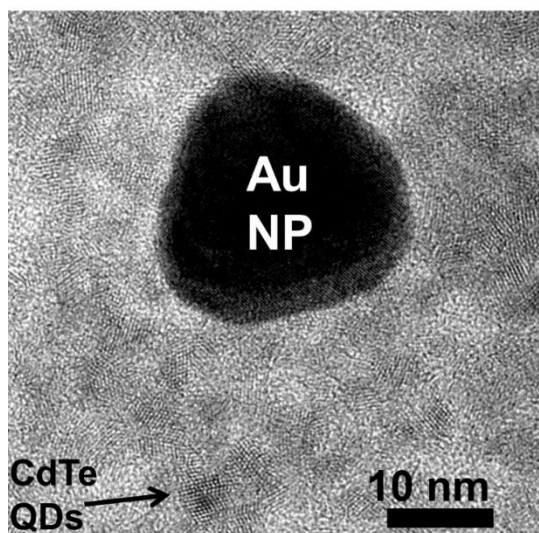


Figure 6.9. TEM image of a Au NP and CdTe QD incorporated macrocrystals belonging to the macrocrystal prepared using 0.50 mL Au NPs and 2.50 mL CdTe QDs, which is the same as Figure 6.8(b) with no markers. Reproduced with permission from Ref. [84]. © Tsinghua University Press and Springer-Verlag Berlin Heidelberg 2015.

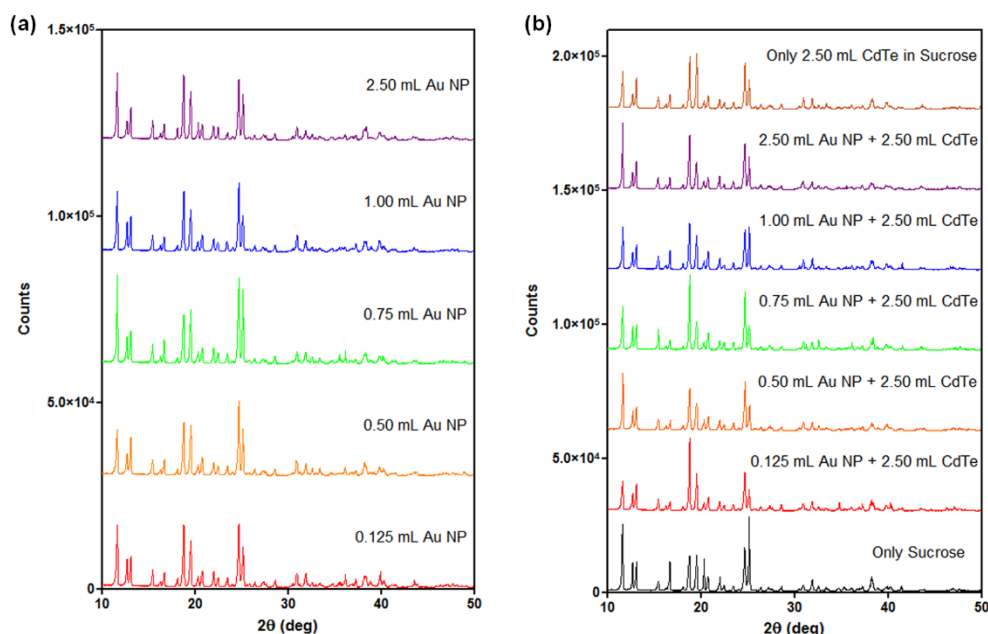


Figure 6.10. XRD spectra of the composite crystals: (a) XRD spectra of the sucrose macrocrystals having only Au NPs and (b) the spectra of the sucrose macrocrystals with only CdTe incorporated, and the ones grown using mixtures of Au NPs and CdTe QDs. Reproduced with permission from Ref. [84]. © Tsinghua University Press and Springer-Verlag Berlin Heidelberg 2015.

The crystal structure investigation of sucrose macrocrystals with embedded CdTe QDs and Au NPs was carried out using XRD (Figure 6.10). The crystal structure of sucrose was identified as monoclinic (JCPDS#24-1977) and polycrystalline. We observe that the crystallinity of sucrose decreases with the addition of Au NPs and/or CdTe QDs. The prominent peaks of sucrose at 11.6° , 16.7° , 20.4° , and 25.2° decrease with the addition of Au NPs and/or CdTe QDs. It was also observed that some orientations ($d=4.53$ and 5.70 Å) of sucrose are preferred over others when Au NPs and/or CdTe QDs were added to it. We do not observe any shift in the sucrose crystal peaks after addition of Au NPs and/or CdTe QDs, which indicates that the macrocrystals are simply a mixture of sucrose, Au NPs, and CdTe QDs. Furthermore, we did not observe any peaks associated with Au NPs and/or CdTe QDs in the XRD spectra. This may be due to the low concentration of Au NPs and/or CdTe QDs in the sucrose macrocrystals, since XRD is not sensitive enough to detect material concentrations of less than ~ 2 at%.

6.4 Summary

In summary, here we demonstrated a robust and large-scale plasmonic composite material system suitable for the integration into various optoelectronic devices. By incorporating gold nanoparticles into sucrose macrocrystals, we showed that the final structure still exhibits the plasmonic features of the metal nanoparticles as opposed to embedding in salts. As a proof-of-concept demonstration of plasmonic fluorescence enhancement in macrocrystals, we also hybridized gold nanoparticles with CdTe quantum dots and co-immobilized them within sucrose crystals. As a result of the plasmonic interplay between the metal nanoparticles and the QDs, the quantum efficiency of the emitter particles was improved by 58% at maximum. The plasmonic character of this enhancement was further verified by the time-resolved fluorescence analyses indicating a lifetime shortening from 11.0 to 7.39 ns. Further increase of the Au NP content in the macrocrystal caused quenching in the quantum efficiency, which through theoretical analyses was attributed to the decrease of the field enhancement factor below unity due to screening effect rather than the nonradiative energy transfer from the QDs to metal nanoparticles. We believe that the results presented in this work can open up the way to novel robust device architectures having large dimensions that employ plasmonic interactions, as a remedy to the dimension restrictions of conventional fabrication and/or assembly methods.

Chapter 7

Stable and Efficient Powders of Nanocrystal Quantum Dots for Color Enrichment

In this chapter of the thesis, we present our efforts on increasing the efficiency and emission stability of the nanocrystal quantum dots incorporated into salt-matrices. Here, we employed LiCl as the host matrix for the encapsulation of the nonpolar nanocrystal QDs without ligand exchange. In this material system we successfully preserved the in-dispersion quantum efficiencies of the nanocrystals. In addition to this, we carried out an emission stability test on LEDs proving the protection capability of the salt matrix against the heat and high photon flux exposure. These results enabled obtaining high-efficiency and high-stability nanocrystal quantum dot emitters suitable for integration into light-emitting diodes and displays as color enrichment.

This chapter of the thesis is mainly based on T. Erdem*, Z. Soran-Erdem*, V. K. Sharma, Y. Kelestemur, M. Adam, N. Gaponik, and H. V. Demir, *Nanoscale* 7, 42, 17611-17616 (2015) [88] (*equal contribution). Reproduced with permission from Royal Society of Chemistry © 2015.

7.1 Introduction

Within the thirty years following their first report [147], colloidal nanocrystal (NC) quantum dots (QDs) have witnessed a tremendous improvement in their synthesis, crystal quality, and quantum efficiency [184]. As a consequence of these developments, as discussed ample times earlier in the thesis, today NCs have been extensively used in various applications from biology [185] to optoelectronics including light-emitting diodes (LEDs) [12], [16], [58], [59] and lasers [186]–[188]. In particular, the tunability of the NC emission and its narrow

bandwidth have attracted significant attention for their use in display backlighting [13] and general lighting [78], [11], [87] as color converters on light-emitting diodes.

Despite their improved quantum efficiencies, the NCs still remain vulnerable to the solid film preparation process using polymer based encapsulants since the quantum efficiencies of the NCs significantly decrease in the polymer film. In addition, due to the continuous exposure to energetic photons and elevated temperatures, the emission intensity of the NCs decreases undesirably on light-emitting diodes (LEDs). Especially, the use of these LEDs for long durations causes significant degradation of NC emission. To improve the emission stability of the NCs, silica coating was proposed; however, this eventually adversely affects the quantum efficiency of the NCs [189]. As an alternative, Otto et al. demonstrated for the first time that aqueous NCs can be incorporated in a single phase process in salt crystals (e.g., NaCl, KCl, etc.) and this improves the emission stability of the NCs [83]. Another study reported by Müller et al. showed that these salt crystals also improve the quantum efficiency of the aqueous NCs [154]. Subsequently, we applied this single-phase approach to plasmonic systems and demonstrated plasmonic fluorescence enhancement of the aqueous NCs this time together with the aqueous metal nanoparticles co-immobilized in sucrose host crystals [84]. In all these previous reports, however, only aqueous NCs (or other aqueous nanoparticles) could be used. In the case of using aqueous NCs, the as-synthesized NCs in water are plagued with intrinsically low quantum efficiencies. Alternatively, high-efficiency nonpolar NCs could be used only after ligand exchange, which also suffers from substantially reduced quantum efficiencies upon the ligand exchange. Therefore, in either case, the quantum efficiency of the resulting ionic salt encapsulated aqueous NCs in a single phase has been a problem. However, the utilization of nonpolar NCs is significantly important because of their high efficiencies and narrow emission bandwidths. Acquiring a narrow emission is very essential for the displays and general lighting applications while high quantum efficiencies in particular in the blue-green colors are needed to address the green gap problem of the epitaxial LEDs [12], [58].

As a solution, here we propose and demonstrate incorporation of the nonpolar NCs directly into LiCl ionic salt without ligand exchange by benefiting from the solubility of LiCl in tetrahydrofuran (THF), which simultaneously disperses these nonpolar NCs. As a proof-of-concept demonstration, we integrated green-emitting CdSe/CdZnSeS/ZnS NCs into LiCl host and characterized their structural and optical properties. In addition, we tested their emission stability on a blue LED operating at 100 mA for 96 h. At the end of the test, the NCs encapsulated in LiCl succeeded to preserve 95.5% of their initial emission intensity while that of the NCs without LiCl encapsulation decreased to 34.7%. To uncover the effect of the LiCl encapsulation on the emission capabilities of the NCs, we reproducibly measured the quantum efficiency of the NCs-in-LiCl host to be 75.1%, which is higher than the quantum efficiency of the same as-synthesized nonpolar NCs in dispersion (73.1%) and the same ones in film without salt encapsulation (67.9%). Subsequently, we investigated the emission dynamics of the NCs-in-LiCl and observed that their radiative decay lifetime is consistent with the theoretical predictions relating the radiative lifetime to the variations of the dielectric environment. Considering all these, we believe that the proposed LiCl encapsulation of the nonpolar NCs will find wide-scale use in light-emitting devices as color enrichment films of display backlights.

7.2 Experimental Methodology

7.2.1 Chemicals

Cadmium oxide (CdO, 99.99 %), zinc acetate ($\text{Zn}(\text{acetate})_2$, 99.9 %), sulfur (S, 99.9%), selenium (Se, 99.99%), potassium bromide (KBr) and lithium chloride (LiCl) were purchased from Sigma-Aldrich in powder form. Oleic acid (OA, 90 %), trioctylphosphine (TOP, 90 %), 1-octadecene (1-ODE, 90 %), dodecanethiol (DDT, 99 %), tetrahydrofuran (THF) and hexane were bought from Sigma-Aldrich and used without any purification.

7.2.2 NC synthesis

CdSe/CdZnSeS/ZnS nanocrystals were synthesized following the method in the literature as described in Chapter 2 [56]. For a typical synthesis, 0.4 mmol of CdO, 4 mmol of Zn(acetate)₂, 5.6 mL of OA and 20 mL of 1-ODE were loaded into a 50 mL three-neck flask. After degassing for 2 h at 100 °C under vigorous stirring, the temperature of mixture was raised to 310 °C under argon flow. At this temperature, 0.1 mmol of Se powder and 4 mmol of S powder both dissolved in 3 mL of TOP were quickly injected into the reaction flask. After 1 min, 0.3 mL of DDT dissolved in 0.8 mL of 1-ODE was injected dropwise and the temperature of the reaction flask was set to 300 °C. Following 10 min of growth, the mixture was cooled down to room temperature and precipitated with hexane/acetone mixture. Finally, the resulting nanocrystals were dissolved in hexane and used for further experiments.

7.2.3 Preparation of the LiCl encapsulated NC powders

Oversaturated stock solution of LiCl was prepared by mixing 1.83 g of LiCl in 50 mL of THF in a glovebox with nitrogen environment. Prior to the encapsulation of the NCs-in-LiCl, hexane of the NC dispersion was evaporated. We optimized the NC amount to maximize their photoluminescence quantum efficiency in the salt (see Section 7.2.4) and chose the sample with 0.4 mg of the NCs to use, which resulted in the highest quantum efficiency of 75.1%, throughout the rest of this work. Before the preparation of NC-in-LiCl powders, the NCs were first dispersed in 250 μ L of THF, and then 1 mL of LiCl stock solution was slowly added on NCs in THF. Subsequently, the samples were placed within a desiccator to completely evaporate the solvent and to obtain the LiCl encapsulated NCs. NC weight percentage in the powders were determined by re-dissolving them in THF and comparing the NC absorbance values with the NC dispersion. The methodology for estimating molar concentration of the NCs inside the powders was explained in Section 7.2.5. Only LiCl powders were obtained using the same procedure without NC addition. The NC-in-LiCl films were prepared by mixing \sim 6.3 mg of the NC embedded LiCl powders with a

commercial two-component epoxy (Bison), which does not require any UV or heat treatment for hardening. Since we aimed to test the stabilities of NC-in-LiCl powders on LEDs at a high current level, we chose this encapsulant on purpose. However, other encapsulants such as commercial silicones and poly(methyl methacrylate), which in general require heat treatment or UV exposure for hardening, can also be used with these powders.

7.2.4 Optimization of NC amount in macrocrystals

The optimization of the NC incorporation amount in the LiCl ionic salt was carried out by integrating 0.3 (Sample 1), 0.4 (Sample 2), and 0.6 mg (Sample 3) of the NCs-in-LiCl. The photoluminescence spectra of these NC-in-LiCl powders were given in Figure 7.1. Their quantum efficiencies were measured as described in the Experimental Methods section to be 65.7%, 75.1%, and 72.5%. In the rest of the study, the samples were prepared by incorporating NCs having this highest quantum efficiency were employed.

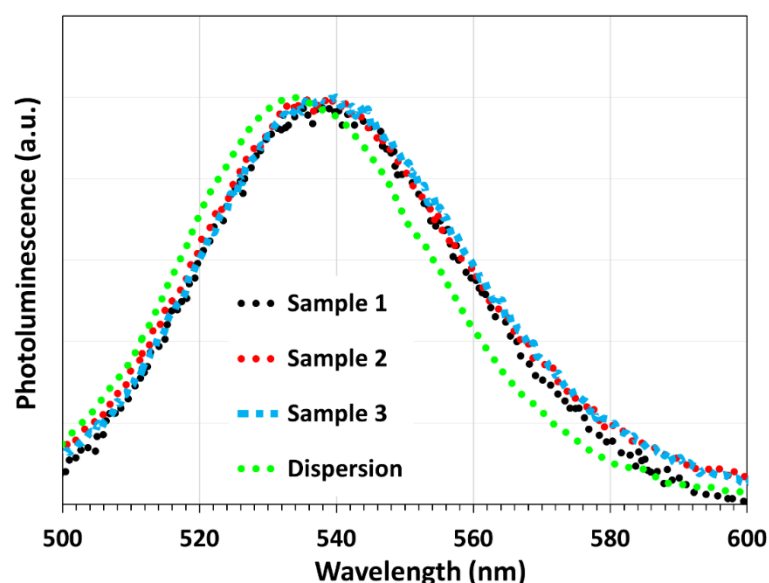


Figure 7.1. Photoluminescence spectra of the NCs in the dispersion and that of the same NCs-in-LiCl prepared using 0.3, 0.4, and 0.6 mg (Sample 1, Sample 2, and Sample 3) of the NCs. Reproduced with permission from Ref. [88]. © Royal Society of Chemistry 2015.

7.2.5 Calculation of the NC molar concentration in LiCl powders

Because in this study we use the alloyed CdSe/CdZnSeS/ZnS NCs, whose exact composition cannot be known, exact determination of the molar concentration is not possible. However, an estimation of this concentration is still possible based on the size of the NCs and the density of the materials constituting the NCs (ignoring the contribution from ligands). We start our calculations with the assumption of spherical nanocrystals having a diameter of ca. 8 nm as determined from the transmission electron microscopy images. This leads to the volume of each individual NC to be $268.1 \times 10^{-21} \text{ cm}^3$. If the NCs were totally composed of CdSe, then their molecular weights would be $9.39 \times 10^8 \text{ mg/mol}$. If the material were CdS and ZnSe, then the molecular weights of the NCs would be $7.79 \times 10^8 \text{ mg/mol}$ and $8.51 \times 10^8 \text{ mg/mol}$, respectively. If the NCs were made of ZnS, then the corresponding molecular weights turn out to be $6.60 \times 10^8 \text{ mg/mol}$. Because the maximum and minimum molecular weights were obtained for CdSe and ZnS cases, the correct molecular weight should be between these two cases. Since we know the weight of the NCs inside 1 mg of the NC-in-LiCl powders to be 0.0122 mg, then the amount of the NCs inside 1 mg of powder turns out to be $\sim 13.0 \text{ pmol}$ for CdSe assumption and $\sim 18.4 \text{ pmol}$ for ZnS assumption.

7.2.6 Structural characterizations

Scanning electron microscopy (SEM): The LiCl and NC-in-LiCl powders were imaged employing an FEI Quanta 200 FEG SEM. Samples were prepared by placing approximately 2 mg of only LiCl and NC embedded LiCl powders onto a carbon tape. Following 4 nm of Au/Pd coating, the samples were imaged under high vacuum.

Transmission electron microscopy (TEM): The TEM images of the green-emitting CdSe/CdZnSeS/ZnS nanocrystals and NC embedded LiCl powders were taken using a FEI Tecnai G2 F30 transmission electron microscope. For this

purpose, TEM sample of NCs and NC embedded LiCl powders were prepared by drop-casting of diluted NC dispersion in hexane and powder dispersion in pure ethanol on a 200 mesh copper grid, respectively.

Fourier transform infrared spectroscopy (FT-IR): Chemical differences of the NCs with and without LiCl encapsulation were investigated using a Shimadzu DR-8101 Fourier transform infrared spectrometer. The sample of the NCs without LiCl encapsulation was prepared by drop-casting 50 μL of the NC dispersion on a KBr pellet. The KBr pellets of only LiCl and NC incorporated LiCl powders were prepared by mixing 7.5 mg of the powders with 111.8 mg of KBr powder. Spectra of pellets were recorded between the wavelengths of 400-4000 cm^{-1} .

Thermal gravimetric analyses (TGA): TGA was performed using a TA Instruments TGA Q500 thermal gravimetric analysis tool. We carried out TGA on the samples of only NC, only LiCl, and NC-in-LiCl powders. In addition, we drop-casted NCs in hexane on only LiCl powders and physically mixed the NCs with LiCl powders after evaporation of hexane. Prior to measurement, LiCl including samples were warmed to 100 $^{\circ}\text{C}$ under a nitrogen atmosphere, held at 100 $^{\circ}\text{C}$ for 15 min to discard the moisture and cooled to room temperature (RT). After 15 min waiting at RT, the temperature was ramped up to 980 $^{\circ}\text{C}$ at the heating rate of 10 $^{\circ}\text{C min}^{-1}$. Different than powders, only NC sample was heated directly to 980 $^{\circ}\text{C}$ with the same heating parameters. All measurements were performed under inert nitrogen environment.

X-ray photoelectron spectroscopy (XPS): XPS measurements were performed using a Thermo K-Alpha XPS spectrometer by referencing it to C 1s peak at ~ 285 eV. The spectra corresponding to Zn, Cd, Cl, Li, Se, and S were recorded.

7.2.7 Steady-state and time-resolved fluorescence spectroscopy

Steady-state photoluminescence spectra of NC dispersion and NC-in-LiCl film were taken using a Spectral Products monochromator integrated Xenon lamp as the excitation source, a Hamamatsu integrating sphere, and an Ocean Optics

Maya 2000 spectrometer. Time-resolved fluorescence spectra were taken using a PicoHarp 200 time-resolved single photon counting system (PicoQuant). A pulsed laser emitting at 375 nm was employed as the excitation source and the time difference between the time of the maximum photon count and the time of 1/e of maximum photon count was reported as the lifetime.

7.2.8 Quantum efficiency measurements

The quantum efficiency measurements were carried out at an excitation wavelength of 460 nm using a Spectral Products monochromator integrated Xenon lamp, a Hamamatsu integrating sphere, and an Ocean Optics Maya 2000 spectrometer using the following method, also previously described by deMello et al.[190] This technique involves three steps: (i) the measurement of the spectrum when no sample is placed in the integrating sphere, (ii) the measurement of the spectrum when the sample is directly illuminated by the excitation source, and (iii) the measurement of the sample when the sample is not directly illuminated by the light source of the integrating sphere. Here, in step (ii), the sample was placed with a slight oblique angle as suggested. In step (iii), the sample was rotated so that only the scattered light excites the sample. In [Figure 7.2](#), an illustration of this technique is presented and the quantum efficiency (η) is calculated using Equation 7.1. In this equation, E stands for the excitation part of the spectrum while L stands for the emission part of the measured spectrum. The subscripts i, ii, and iii indicate the measurement steps described above.

$$\eta = \frac{L_{ii} - E_{ii}L_{iii}/E_{iii}}{\left(1 - E_{ii}/E_{iii}\right)E_i} \quad (7.1)$$

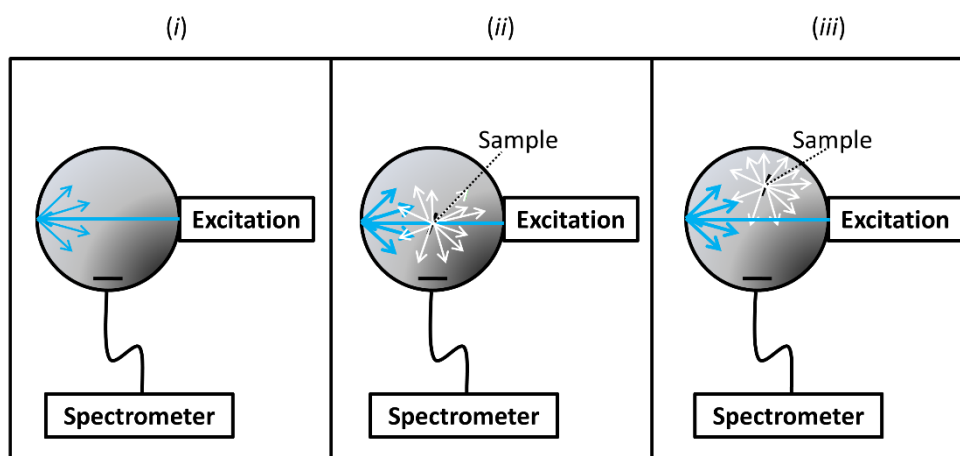


Figure 7.2. Illustration of the quantum efficiency measurement methodology: (i) The measurement of the excitation spectrum without sample, (ii) the measurement of the spectrum when the sample is directly excited by the light source, and (iii) the measurement of the spectrum when the sample is excited by the light that scatters from the surface of the integrating sphere. Reproduced with permission from Ref. [88]. © Royal Society of Chemistry 2015.

The accuracy of the measurement setup was tested using Rhodamine 6G dissolved in ethanol with an optical density <0.1 at 460 nm. We measured a quantum efficiency of 94.7%, which is in agreement with the standard value of 95%.

7.2.9 Emission stability tests

The emission stability of the films was tested by investigating the emission intensity of the NCs with and without LiCl encapsulation on an Avago ASMT blue LED driven at 100 mA for 96 h (four days). The NCs with LiCl encapsulation were coated on the LED chip using the two-component epoxy. As the control group, the NCs without LiCl were coated on the blue LED by first drop-casting the NCs on the LED and then the epoxy was added and blended with the NCs following the evaporation of the solvent.

7.3 Results and Discussion

We integrated nonpolar NCs-in-LiCl powders as described in the Experimental Methodology section and Figure 7.3. Briefly, we mixed the oversaturated LiCl solution (in THF) with NCs dispersed in THF in a nitrogen environment. Subsequently, the solvent was evaporated under vacuum and consequently NC encapsulated powders were obtained. The NC weight percentage in these powders was determined to be ~1.22%. Further structural characterizations were performed using scanning electron microscopy (SEM) and transmission electron microscopy (TEM) (Figure 7.4).

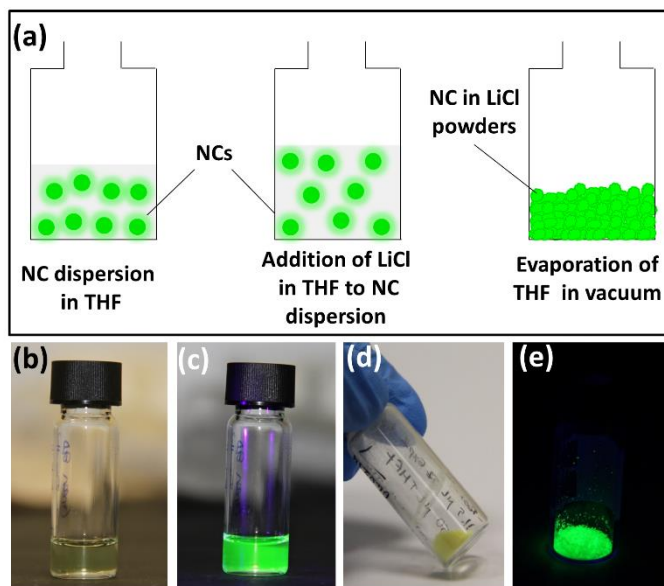


Figure 7.3. (a) Schematics of NC encapsulation into LiCl salt. The real color images of NC dispersion in THF (b) under ambient lighting and (c) UV illumination at 366 nm. The real color images of the NCs-in-LiCl powders (d) under ambient lighting and (e) UV illumination at 366 nm. Reproduced with permission from Ref. [88]. © Royal Society of Chemistry 2015.

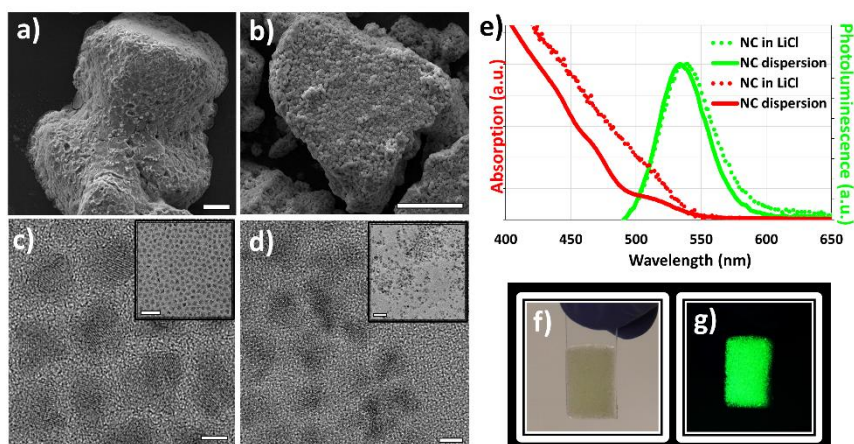


Figure 7.4. Scanning electron microscopy (SEM) images of the LiCl powders (a) without and (b) with NCs (scale bars: 30 μm). Transmission electron microscopy (TEM) images of (c) the as-synthesized NC dispersion in hexane and (d) the NC-in-LiCl powders (scale bars of larger images: 5 nm and inset images: 50 nm). (e) Photoluminescence spectra of the nonpolar NCs in dispersion and the same NCs encapsulated within LiCl ionic salt. Also, absorption spectra of the as-synthesized NCs (dispersion in hexane) and NC-in-LiCl powder film were provided. Real color photographs of the LiCl encapsulated NC film under (f) ambient lighting and (g) UV illumination at 366 nm. Reproduced with permission from Ref. [88]. © Royal Society of Chemistry 2015.

The SEM images of the representative LiCl powders with and without NC loading show that the size of the powders is in general less than 200 μm for both of the cases with and without NC loading and they do not exhibit crystal facets as opposed to slower crystallizations previously studied in other media [84]. This is mainly due to the fast evaporation of the solvent (THF in this case) under vacuum. Another interesting feature is the occurrence of small grape-like structures on the powders containing NCs while such an observation cannot be made for the LiCl powders without NC loading (Figure 7.5(a),(b)). Here it is worth noting that the NCs are small and cannot be imaged using SEM. Each of these grape-like structures most likely includes many NCs inside. We think that these grape-like structures may possibly take a role in preventing full aggregation of the NCs within LiCl and thus avoid the quenching of the NCs.

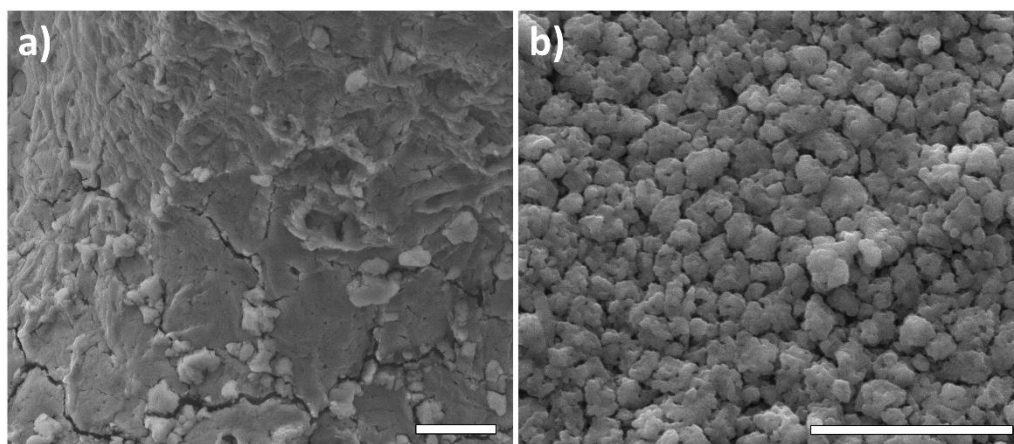


Figure 7.5. SEM images of (a) the only LiCl powder and (b) NC-in-LiCl powder. Scale bars: 10 μm . Reproduced with permission from Ref. [88]. © Royal Society of Chemistry 2015.

Furthermore, we used TEM to image the NCs without LiCl and the NCs incorporated in LiCl (Figure 7.4(c)-(d)). These images show that the size of our as-synthesized NCs is approximately 8 nm. In addition, we imaged the NC-in-LiCl powder (Figure 7.4(d) and Figure 7.6 for a larger image) and observed that the NCs in LiCl tend to be localized in some parts of the salt. Finally, having the information of size and concentration of our NCs, we are able to estimate the molar concentration of the NCs inside LiCl host. Our calculation reveals that there are between 13.0 and 18.4 pmol of NCs inside 1 mg of powder.

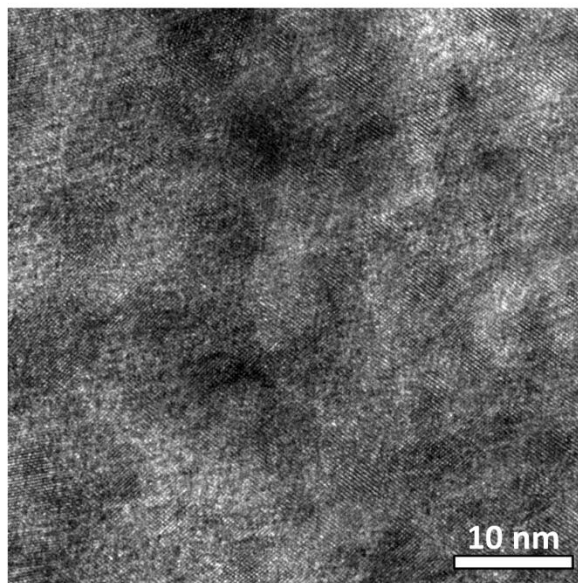


Figure 7.6. TEM image of the NCs within LiCl host. Reproduced with permission from Ref. [88]. © Royal Society of Chemistry 2015.

Following the morphological characterization, we prepared the NC-in-LiCl film using a commercial epoxy that does not require any UV or heat treatment for hardening. Subsequently, we measured the steady-state photoluminescence spectra and quantum efficiencies of the NCs in the dispersion and encapsulated into LiCl host. We observed that the encapsulation of the NCs by the ionic salt causes a slight red shift in the emission spectrum (Figure 7.4(e)) as observed in previous works[83], [154], which can be explained by the limited aggregation of the NCs within LiCl (Figure 7.4(d), Figure 7.6) and also in part by the interactions of dipoles of the NCs with the dipoles of the surrounding medium as also reported by Ibnaouf et al.[191]. The quantum efficiency of the NCs-in-LiCl was measured to be 75.1% while the quantum efficiency of the same NCs in dispersion was found to be 73.0% and that of the NCs without LiCl encapsulation in solid film remained at 67.9%. The observation of this increased quantum efficiency of the nonpolar NCs in the salt matrix agrees well with the previous reports of salt encapsulation of aqueous NCs in NaCl [86], [154].

Here, we also analysed the emission kinetics of the NCs in dispersion and the same NCs encapsulated by the LiCl salt. The measured time-resolved

photoluminescence decays presented in Figure 7.7 revealed a lifetime of 29.1 ns for the NCs dispersed in hexane and 19.4 ns for the NCs encapsulated in LiCl. Using the quantum efficiency (η) information together with the lifetime (τ_{total}), the effective radiative lifetime (τ_{rad}) is predicted using Equation 7.2. This analysis leads to a radiative lifetime of 39.9 ns for the NCs dispersed in hexane while that of the NCs-in-LiCl decreases to 25.8 ns.

$$\eta = \frac{1/\tau_{rad}}{1/\tau_{total}} \quad (7.2)$$

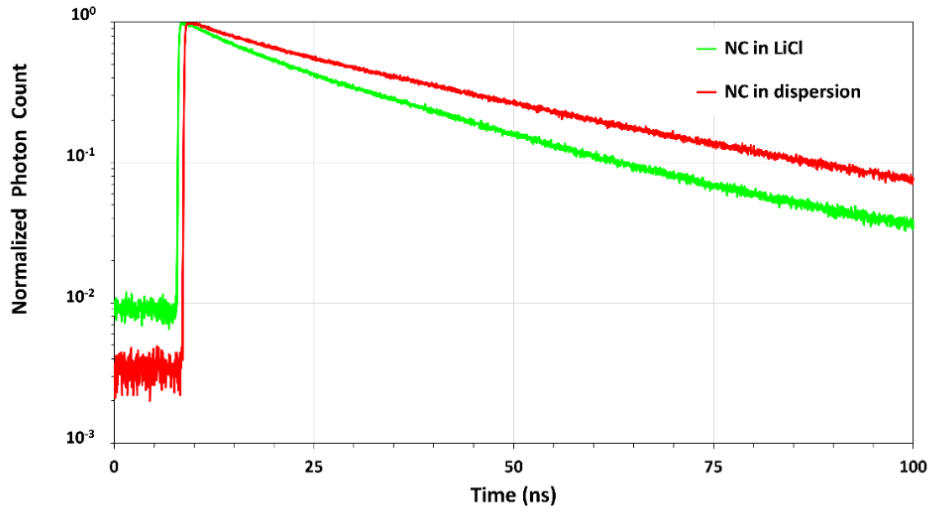


Figure 7.7. Time-resolved photoluminescence decay curves of the NCs in dispersion and the same NCs encapsulated in LiCl. Reproduced with permission from Ref. [88]. © Royal Society of Chemistry 2015.

According to Nienhuis et al.[192], the radiative lifetime is related to the refractive index in the absence of local-field effects as $\tau_{rad} = \frac{\tau_{vac}}{n}$ where τ_{rad} is the radiative lifetime in the dielectric medium, τ_{vac} is the radiative lifetime in the vacuum, and n is the refractive index.

When the dipole is placed in an empty spherical cavity, the radiative lifetime becomes $\tau_{rad} = \left(\frac{3n^2}{2n^2+1}\right)^{-2} \frac{\tau_{vac}}{n}$ according to Glauber et al.[193] This model is called the empty-cavity model.

When the dipole is placed within a cavity with the same refractive index as the host and the dipoles in the cavity do not contribute to the local electric field, the radiative lifetime becomes $\tau_{rad} = \left(\frac{n^2+2}{3}\right)^{-2} \frac{\tau_{vac}}{n}$ according to Knoester et al. [194] This model is called the virtual-cavity model.

Finally, Crenshaw et al.[195] showed that the radiative lifetime becomes $\tau_{rad} = \left(\frac{n^2+2}{3}\right)^{-1} \tau_{vac}$ if the microscopic local-field effects were introduced. This model is called the fully microscopic model.

In our calculations, we first determined the vacuum radiative lifetime of the NCs using the radiative lifetime information of the NC dispersion. Subsequently, we predicted the radiative lifetime of these NCs according to these models as if they were surrounded by LiCl, and compared these results with the measured radiative lifetimes of NC-in-LiCl powders [196]. Subsequently, we predicted the radiative lifetimes of the NCs using this value when they are surrounded by the LiCl matrix and present the results in Table 7.1 in the rows indicated by the names of these models. The computed results show that the predicted experimental and theoretical radiative lifetimes are reasonably close especially when the empty cavity model is considered. Therefore, we can suggest that the dipoles generated in the NCs encapsulated by the LiCl salt experience a radiative recombination that is not significantly affected by the local field of the surrounding medium generating the cavity.

Table 7.1. The quantum efficiency of the NCs in dispersion and the same NCs encapsulated in LiCl; their total lifetimes and radiative recombination lifetimes. In addition, the radiative lifetimes of the NCs in vacuum were first calculated by employing the radiative lifetime of the NCs in dispersion, then these values were used to predict the radiative lifetime of the NCs in LiCl matrix according to the empty cavity, virtual cavity, and fully microscopic models.

	Quantum Efficiency (%)	τ_{total} (ns)	τ_{rad} (ns)
NCs in dispersion	73.0	29.1	39.9
NCs-in-LiCl	75.1	19.4	25.8
Empty cavity model	-	-	28.7
Virtual cavity model	-	-	21.9
Fully microscopic model	-	-	32.5

In addition to the effect of the surrounding dielectric medium on the quantum efficiency, we also expect the ionic salts wrapping the NCs to improve the stability of the NC emission on LEDs. For this purpose, we tested the emission stability of the NC-in-LiCl powders blended with epoxy on a blue LED driven at a high current level (Figure 7.8(a)-(b)) while the NCs without LiCl encapsulation blended with epoxy was our control group. We observed that the efficiency of the NCs without LiCl encapsulation decreased to 34.7% of its initial value after 96 h (four days) of uninterrupted operation while the film of NC-in-LiCl powders successfully preserved 95.5% of its initial quantum efficiency during the same period. In terms of the absolute quantum efficiencies, the quantum efficiency of the NC-in-LiCl powders decreased from 75.1% to 71.7% while that of the NCs without LiCl encapsulation dropped from 67.9% to below 23.6% at the end of the test (Figure 7.8(c)). We attribute this improvement in the emission stability of the NCs on a LED driven at high currents to the formation of a physical barrier against oxygen penetration by LiCl salt limiting the interaction with the ambient environment. This improved stability is of significant importance especially for the display backlighting.

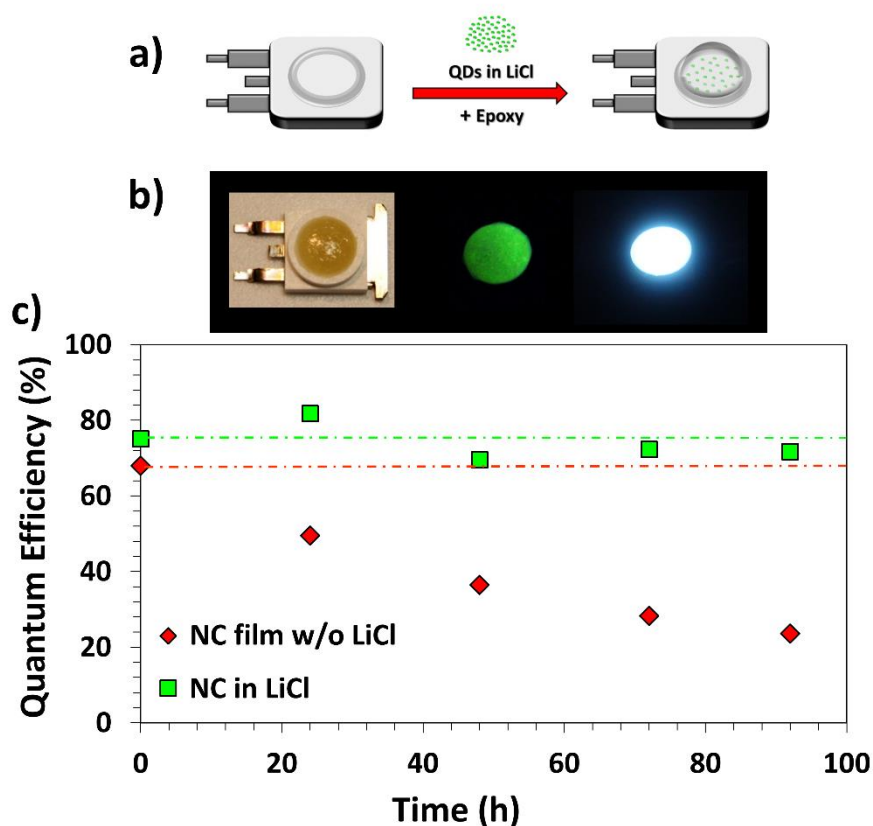


Figure 7.8. (a) Schematic image of NC-in-LiCl film preparation onto LED for temperature stability test. (b) Real color images of the NCs-in-LiCl on a blue LED under ambient lighting, UV illumination at 366 nm, and when LED is driven, from left to right. (c) Quantum efficiency variation of the NCs with and without LiCl encapsulation as a function of time when they are integrated on the blue LED driven at a high current level for 96 h (four days). Reproduced with permission from Ref. [88]. © Royal Society of Chemistry 2015.

To test whether a chemical interaction occurs between the ligands of the NCs and the host medium during crystallization process, we measured the FTIR spectrum of the NCs without LiCl encapsulation, the NCs-in-LiCl, and the only LiCl salt (Figure 7.9). The results show that the FTIR spectrum of the only LiCl is coherent with the literature [197]. In FT-IR spectra of only NCs, which have oleic acid ligands, we observe strong C-H stretching bond around 2860-2924 cm^{-1} and C-H bending bond around 1450-1460 cm^{-1} belonging to the ligands of NC. Although both of the C-H bending and C-H stretching bonds are visible in NC

embedded LiCl samples as well, their intensities are dominated. On the other hand, we expect to observe strong stretching bond belonging to C-Cl around 550-800 cm^{-1} if there were a chemical reaction between the NC ligand and LiCl. However, we could not see any peak around these wavenumbers. This suggests that LiCl only wraps the NCs without forming a C-Cl bonding.

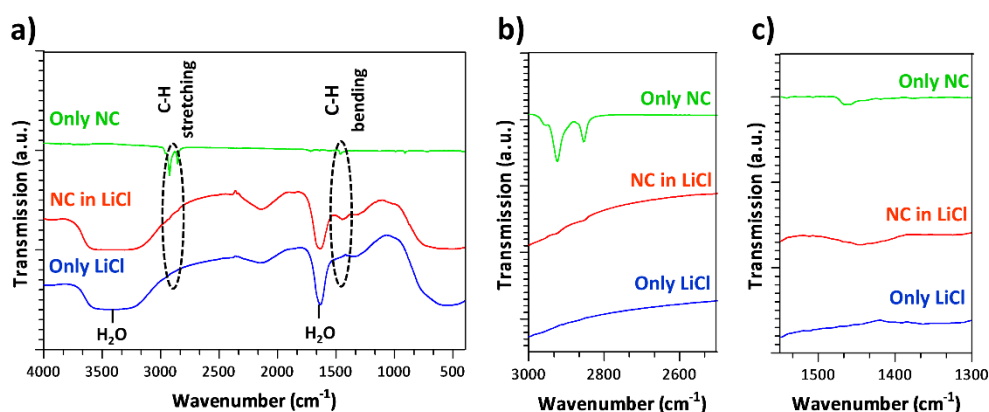


Figure 7.9. (a) FTIR spectra of the samples of only NCs along with LiCl powders with and without NC incorporation. The zoomed version of the same spectra between the wavenumbers of (b) 2500-3000 cm^{-1} and (c) 1300-1550 cm^{-1} . Reproduced with permission from Ref. [88]. © Royal Society of Chemistry 2015.

In order to gain further structural information, we performed thermal gravimetric analysis (TGA) on the samples of only NC, only LiCl, NC-in-LiCl powder and NC drop-casted LiCl powder. As seen from Figure 7.10, oleic acid capped-NCs have multiphase degradation with the increased temperature. Observed weight loss between 30-150 $^{\circ}\text{C}$ and 150-450 $^{\circ}\text{C}$ occurs due to the evaporation of hexane from the sample and degradation of oleic acid ligands [198], respectively. On the other hand, only LiCl, NC-in-LiCl and NC drop-casted on LiCl samples have one-phase degradation and show a similar pattern. Above 600 $^{\circ}\text{C}$, linear mass loss was observed in LiCl including samples. It was attributed to the progressive vaporization of the salt LiCl near its melting point [199]. NC-in-LiCl powders exhibit faster weight loss compared to only LiCl powder. In order to understand whether chemical and physical interaction affects this difference, NC drop-casted on LiCl powder, in which we do not expect any chemical interaction, was also examined. We observed that NC drop-casting

decreased the degradation temperature of the LiCl compared to only LiCl case, which was also the case for the NC-in-LiCl powders. In addition, NC drop-casted LiCl and NC-in-LiCl powders started to degrade at the same temperature and have almost the same temperature stability at the end. Furthermore, we did not observe a strong degradation phase in NC-in-LiCl or NC drop-casted on LiCl powders related to NCs, which is mainly due to low NC incorporation ratio into LiCl powders (~1%). The similarities in the weight loss curves of the NC-in-LiCl powders and NC drop-casted LiCl powders suggest that this fastened evaporation is more likely a physical process rather than an indication of a chemical interaction. In addition, from the TGA curves we could not observe any signature that we can relate to any indication of the NCs-salt chemical interaction. As a result, using TGA, we were not able to identify an obvious chemical interaction between the NCs and the host matrix.

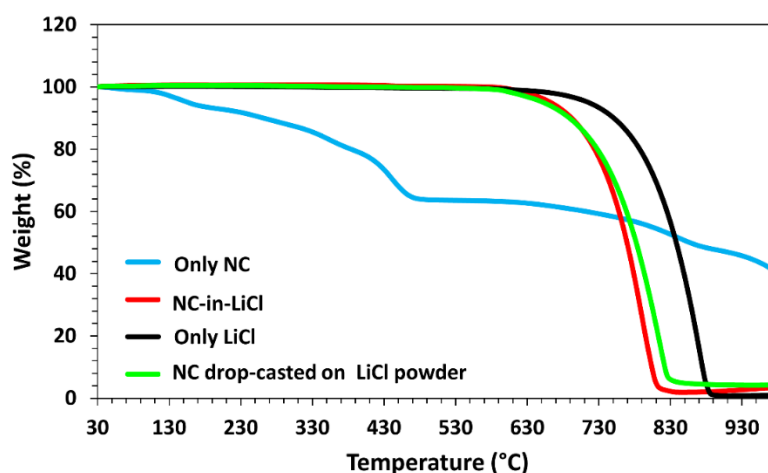


Figure 7.10. TGA curves of the NCs, NC-in-LiCl powders, only LiCl powders, and NC drop-casted on LiCl powders. Reproduced with permission from Ref. [88]. © Royal Society of Chemistry 2015.

To further investigate the interaction of the LiCl with the NCs, we performed X-ray photoelectron spectroscopy (XPS) of only NCs, NC-in-LiCl powders, and only LiCl powders (Figures 7.11 and 7.12). In our experiments, XPS spectra are referenced to the C 1s peak at ~285 eV. For LiCl only (Figure 7.11), in the Li spectra we observed two peaks, which can be assigned to LiCl (56.33 eV) and

Li₂O/Li₂CO₃ (55.24 eV), respectively. Similarly, in the chlorine spectra (Figure 7.11) we observed the Cl 2p doublet (Cl 2p_{3/2} ~ 198.96 eV and Cl 2p_{1/2} ~ 200.7 eV) with an additional peak, which can be assigned to Cl-O/C-Cl (197.1 eV). This additional peak is most probably due to the moisture on LiCl. In the case of the NC-in-LiCl powders, XPS data do not show any new peak, which confirms the absence of any metal chloride (ZnCl₂ or CdCl₂) formation or interaction in the mixture. XPS spectra reveal a small shift (0.4 eV) in the Li and Cl peaks in the mixture (see Table 7.2), which is most probably due to the change in the medium. For the NCs (Figure 7.12), the XPS survey scan indicates the presence of Cd, Se, S and Zn. High resolution XPS spectra of all NC-elements are also obtained to study the interaction with the LiCl salt. For the NCs only, Cd 3d (Cd 3d_{5/2} ~ 405 eV and Cd 3d_{3/2} ~ 411.73 eV) and Zn 2p (Zn 2p_{3/2} ~ 1022.33 eV and Zn 2p_{1/2} ~ 1045.23 eV) doublet has been observed. Similarly, Se 3d (54.15 eV) and S 2p (162.04 eV) peaks are observed. For the mixture (Figure 7.11) we observe a small shift (0.5 eV) in the NC peaks in comparison to the only NC case (see Table 7.2), which is most probably due to the change in the microenvironment of the NCs. XPS results therefore support the notion that the NCs and LiCl form a composite structure and NC incorporation into LiCl is also confirmed by the decrease in the intensity of the NCs peaks in comparison to the only NCs, since XPS is a surface sensitive technique (Figure 7.12). Considering all of these results, here we conclude that XPS measurements did not provide any indication of a notable chemical interaction between the salt medium and the NCs.

Table 7.2.XPS data for the only NCs, NC-in-LiCl, and only LiCl samples.

Element	Only LiCl (eV)	Only NCs (eV)	NC-in-LiCl (eV)	Difference (eV)
Li	56.33	-----	56.78	0.45
Cl	198.96	-----	199.35	0.39
Cd	-----	405	405.52	0.52
Zn	-----	1022.33	1022.84	0.51
Se	-----	54.15	-----	-----
S	-----	162.04	162.6	0.56

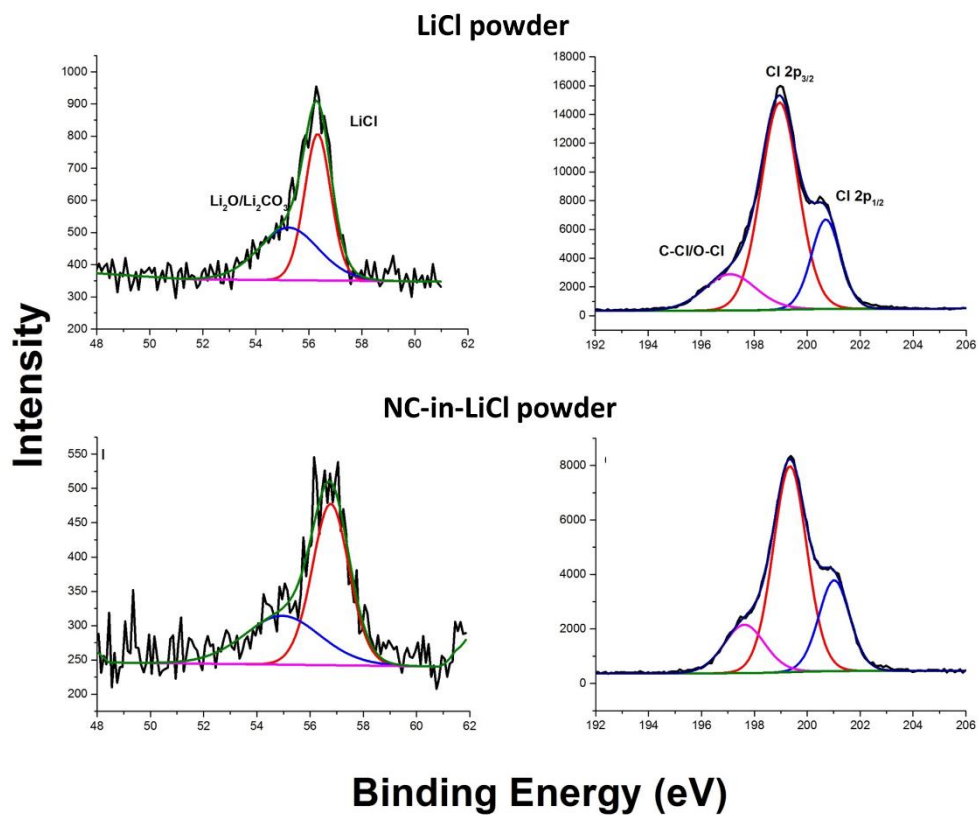


Figure 7.11. XPS spectra comparison of Li (left) and Cl (right) peaks in only LiCl and NC-in-LiCl samples. Reproduced with permission from Ref. [88]. © Royal Society of Chemistry 2015.

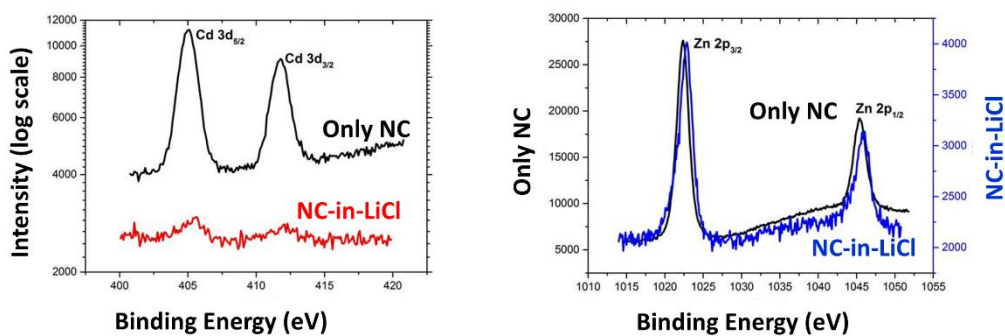


Figure 7.12. XPS spectra comparison of Zn (left) and Cd (right) peaks in the only NCs and NC-in-LiCl samples. Reproduced with permission from Ref. [88]. © Royal Society of Chemistry 2015.

7.4 Summary

In summary, here we present the encapsulation of the colloidal as-synthesized nanocrystals by the LiCl ionic salts in the form of powder, which significantly improves the stability of the encapsulated NCs on LEDs operating at high currents. We also observed that the LiCl encapsulation helps preserving the indispersion quantum efficiency levels of the NCs for use in the color enrichment films. Additionally, unlike the previous reports on the incorporation of the aqueous NCs in salt or sucrose matrices, this method totally removes the need for a ligand exchange of the nonpolar NCs, which are known to otherwise suffer from decreased quantum efficiencies during the phase transfer. Considering all these strong aspects, we believe that the proposed encapsulation technique presented here will find a wide-spread use in the light-emitting diodes of display backlights integrated with NCs as color enrichment films.

Chapter 8

Excitonic Improvement of Colloidal Nanocrystal Emission in Salt Powder Matrix

In this chapter of the thesis, we present our study on the investigation of nonradiative energy transfer (NRET) between green- and red-emitting color converting nanocrystals within LiCl salt matrix. Here, we systematically studied the resulting NRET process by varying donor and acceptor concentrations in the powders. We observed that NRET is a strong function of both of the nanocrystal concentrations and that NRET efficiency increases with increasing acceptor concentration. Nevertheless, with increasing donor concentration in the powders, NRET efficiency was found to first increase but then to decrease. As a device demonstrator, we employed these NRET-improved nanocrystal powders as color-converters on blue light-emitting diodes (LEDs), with the resulting hybrid LED exhibiting a luminous efficiency $>70 \text{ lm/W}_{\text{elect}}$. The proposed excitonic nanocrystal powders potentially hold great promise for quality lighting and color enrichment applications.

This chapter of the thesis is mainly based on T. Erdem*, Z. Soran-Erdem*, Y. Kelestemur, N. Gaponik, and H. V. Demir, *Optics Express* 24, 2, A74-A84 (2016) [85] (*equal contribution). Reproduced with permission from Optical Society of America © 2016.

8.1 Introduction

Semiconductor colloidal nanocrystals, which offer favorable and unique optical properties such as narrow and tunable emission, broad absorption, and high quantum efficiencies [10], have been in the center of interest in numerous fields from biology [185] to photonics [200]. After twenty years of their first colloidal

synthesis, these materials are utilized in various applications including displays [122], [201], sensors [202], solar-cells [203], [204], and illuminants for general [12], [57], [205] and outdoor lighting [59]. Their main Achille's heel is the problems associated with their deterioration occurring due to their moderate stability as well as limited compatibility with the encapsulants and fabrication techniques.

One of the remedies to these problems is the incorporation of nanocrystals into crystalline host matrices of ionic salts as it has been proposed by Otto et al.[83] The effect of this crystallization process on the quantum efficiency was studied by Müller et al. and efficiencies of crystals above the in-dispersion efficiencies were reported [154]. Subsequently, we investigated the plasmonic interaction between nanocrystals and gold nanoparticles within sucrose macrocrystals and reported an improvement of 58% in the quantum efficiency via plasmonic interplay [84]. In these works, however, the host matrix of nanocrystals allows for the incorporation of the nanocrystals dispersed only in water. Therefore, the types and performance of the applicable nanocrystals are strongly limited.

To resolve these handicaps, Soran-Erdem et al. embedded the oleic acid capped nanocrystals into the anthracene matrix, which is a blue-emitting crystalline organic semiconductor material soluble in chloroform [86]. However, the quantum efficiency of the nanocrystals in this material system decreased and the thermal stability of the nanocrystals in anthracene is limited due to the low thermal stability of anthracene. As an alternative to organic crystals, we developed a vacuum-assisted technique for incorporating nanocrystals in nonpolar solvents into LiCl salt without phase transfer. With this technique we significantly improved the emission stability of the nanocrystals and protected their in-solution quantum efficiencies in salt matrix [88].

Since the distance between the nanocrystals embedded into LiCl matrix can be as low as 10 nm [88], this material system can be a good candidate for utilizing nonradiative energy transfer (NRET) in color enrichment films. With the small distance between the nanocrystals allowing for dipole-dipole coupling, high NRET efficiencies can be realized within these powders as opposed to our previous work [86] where low quantum efficiency of anthracene restricted the

efficiency of NRET to red-emitting nanocrystals below 30%. Furthermore, the broad emission spectrum of anthracene, which always exists in the photoluminescence of the macrocrystal, did not allow for fine-tuning the final emission spectrum. This is, however, an important requirement for general lighting and display applications [12].

Since the utilization of only nanocrystals within powders can easily help to control the spectral features of the color converting materials [60], [206], here we aim at developing and demonstrating a material system consisting of dielectric salt encapsulating nanocrystals that undergo NRET among them. For this purpose, here we co-integrated green- and red-emitting nanocrystals into a single LiCl salt matrix for the first time and studied the NRET dynamics between these nanocrystals within the salt powder. We systematically varied the concentration ratios of the green-emitting nanocrystals as the exciton donors to red-emitting nanocrystals as the exciton acceptors by controlling their incorporation amounts. In our experiments, we achieved a maximum NRET efficiency of 53.9%, which is almost twice the value that could be previously obtained in anthracene macrocrystal hosts. Furthermore, we employed these nanocrystal powders on a proof-of-concept light-emitting diode as color conversion film and obtained a high luminous efficiency of 70 lm/W_{elect.} We believe that this present study can possibly pave the way for a wide-spread use of LiCl encapsulation of colloidal nanocrystals on light-emitting diodes for use as robust, efficient phosphor powders compatible with the packaging capabilities of the lighting industry.

8.2. Experimental methods

8.2.1 Chemicals

Cadmium oxide (CdO, 99.99 %), zinc acetate (Zn(acetate)₂, 99.9 %), sulfur (S, 99.9%), selenium (Se, 99.99%) and lithium chloride (LiCl) were purchased from Sigma-Aldrich in powder form. Oleic acid (OA, 90 %), trioctylphosphine (TOP, 90 %), 1-octadecene (1-ODE, 90 %), dodecanethiol (DDT, 99 %), octanethiol,

cadmium oleate, tetrahydrofuran (THF) and hexane were bought from Sigma-Aldrich and used without any purification.

8.2.2 Synthesis of colloidal nanocrystals

Colloidal nanocrystals having peak emission wavelengths of 534 nm (green) and 604 nm (red) were synthesized to be used in this study as exciton-donating and exciton-accepting nanocrystals, respectively. The details of their syntheses were explained below.

8.2.3 Synthesis of green-emitting CdSe/CdZnSeS/ZnS colloidal nanocrystals

For a typical synthesis of CdSe/CdZnSeS/ZnS nanocrystals, we followed the method published by Bae et al. [56] as described in Chapter 2. Briefly, 0.4 mmol of CdO, 4 mmol of Zn(acetate)₂, 5.6 mL of OA and 20 mL of 1-ODE were loaded into a 50 mL three-neck flask. Then, the mixture was degassed for 2 h at 100 °C under vigorous stirring and the temperature of mixture was raised to 310 °C under argon flow. At this temperature, 0.1 mmol of Se powder and 4 mmol of S powder both dissolved in 3 mL of TOP were quickly injected into the reaction flask. Following 10 min of growth, the mixture was cooled down to room temperature and precipitated with hexane/acetone mixture. Finally, the resulting nanocrystals were dissolved in hexane and used for further experiments.

8.2.4 Synthesis of red-emitting CdSe/CdS core/shell colloidal nanocrystals

The synthesis of CdSe/CdS core/shell nanocrystals was carried out following the method reported in Chen et al. [207] For the synthesis of CdSe core, cadmium myristate and selenium dioxide were used as cadmium and selenium precursors, respectively. These chemicals were dissolved in octadecene and evacuated at room temperature for 10-15 minutes. Subsequently, the solution was heated to 240 °C within 10 min. Then, the temperature of the solution was kept at 240 °C for the growth of CdSe cores until the desired size of CdSe cores was obtained.

After the reaction was stopped by decreasing the temperature, as-synthesized CdSe cores were precipitated by using acetone and dissolved in hexane. In the second step, CdSe cores were coated with CdS shell. For this purpose, certain amount of CdSe cores (100 nmol) dissolved in hexane was loaded to a four-neck flask containing 3 mL octadecene and 3 mL oleylamine. After the solution was degassed at 100 °C in order to remove hexane and any other organic residuals, the temperature of the reaction was set to 300 °C for the coating of CdS shell under argon atmosphere. When the temperature reached 240 °C, the calculated amounts of cadmium and S precursors corresponding to six monolayers of CdS were injected at a rate of 3 mL/min. After the injection of shell precursors were completed within two hours at 300 °C, the reaction was stopped and the temperature was decreased to room temperature. As-synthesized CdSe/CdS core/shell nanocrystals were precipitated with acetone and dispersed in hexane.

8.2.5 Preparation of the LiCl encapsulated nanocrystal powders, films, and light-emitting diode

For the preparation of oversaturated LiCl stock solution, 1.83 g of LiCl was dissolved in 50 mL of tetrahydrofuran (THF) in a glovebox with nitrogen environment. Prior to the encapsulation of the nanocrystals in LiCl, the green- and red-emitting nanocrystal concentrations were set to 3.7 mg/mL. Subsequently, hexane of only green- and only red-emitting nanocrystals along with that of their mixtures were evaporated. The volumes of the nanocrystals used in this work were listed below in Table 8.1. After drying the solvent, nanocrystals were dispersed in 250 μ L of THF and 1 mL of LiCl stock solution (36.6 mg) was slowly added. Subsequently, samples were placed within a desiccator to encapsulate the nanocrystals within LiCl powders by completely evaporating THF.

Table 8.1. The volumes for green- (donor) and red-emitting (acceptor) nanocrystals used for incorporation into LiCl.

Volume (μ L)	Green (Donor)				Red (Acceptor)		
	25	50	75	100	50	150	250

The nanocrystal incorporated LiCl powder films were prepared by mixing ~6.3 mg of the powders with a commercial two-component epoxy (Bison). Similarly, the light-emitting diode was prepared by integrating 23 mg of the 50 μL green (donor) and 250 μL red-emitting (acceptor) on an Avago ASMT blue LED using Bison epoxy.

8.2.4 Optical Characterizations

Steady-state photoluminescence spectra of nanocrystal dispersion and nanocrystal incorporated LiCl films were taken using an Ocean Optics Maya 2000 spectrometer equipped with a Hamamatsu integrating sphere, a Spectral Products monochromator at an excitation wavelength of 460 nm and a Xenon lamp as the excitation source.

Absorption spectra of green-emitting and red-emitting nanocrystal solutions were taken using Carry 100 UV-Vis spectrometer. However, the absorption spectrum of the nanocrystal embedded LiCl powders could not be measured reliably due to the scattering problem.

The photoluminescence lifetimes of the films were taken using a PicoHarp 200 time-resolved single photon counting system (PicoQuant). A pulsed laser emitting at 375 nm was employed as the excitation source. Three exponentials were fitted to the decay curves and amplitude averaged lifetimes were reported as the lifetime.

8.3. Results and Discussion

In this thesis, we investigated for the first time the nonradiative energy transfer from green- to red-emitting nanocrystals that are immobilized within a salt matrix. Here we benefitted from the solubility of LiCl in THF which simultaneously can disperse nanocrystals as well. This enabled the incorporation of the nonpolar nanocrystals into LiCl salt without any ligand exchange. Furthermore, this vacuum assisted salt incorporation of nanocrystals allowed for immobilizing the nanocrystals emitting different colors in close proximity so that nonradiative energy transfer (NRET) can take place.

Toward this aim, we first synthesized green-emitting alloyed core/shell nanocrystals of CdSe/CdZnSeS/ZnS and red-emitting CdSe/CdS core/shell nanocrystals. These as-synthesized nanocrystals exhibited emission peaks at 534 nm and 604 nm, respectively. We note that there is a strong overlap between the emission spectrum of the green-emitting nanocrystals and absorption spectrum of the red-emitting nanocrystals as presented in Figure 8.1. This suggests that NRET is possible from the green-emitting nanocrystals to the red-emitting nanocrystals via dipole-dipole interaction if these nanocrystals are placed in close proximity. Because the distance between nanocrystals can be below 10 nm when they are embedded in LiCl using the technique presented in Ref. [88], NRET from the green-emitting nanocrystals to the red-emitting nanocrystals becomes possible. Therefore, in this work we embedded these nanocrystals into LiCl matrix in varying volumes as shown in Table 8.1.

The concentration of the nanocrystals embedded into powders was calculated by dissolving a certain amount of powders in THF, measuring the absorption spectra of the nanocrystals, and comparing the absorbance of the nanocrystals in the dissolved powders with the absorbance of the nanocrystal dispersion. The results showed that almost all the nanocrystals used were incorporated into LiCl matrix. The estimated molar concentrations of the green-emitting nanocrystals in powders calculated according to Ref. [88] then became ~ 2.68 - 3.82 pmol/mg, ~ 5.36 - 7.64 pmol/mg, ~ 8.04 - 11.5 pmol/mg, and ~ 10.7 - 15.3 pmol/mg for the powders prepared using 25, 50, 75, and 100 μL of nanocrystals, respectively. A similar calculation of the red-emitting nanocrystal powders yielded ~ 8.92 - 10.7 pmol/mg, ~ 26.8 - 32.1 pmol/mg, and ~ 44.6 - 53.5 pmol/mg for 50, 150, and 250 μL of nanocrystals, respectively.

To obtain exciton-transferring nanocrystal embedded LiCl powders, we hybridized these green and red-emitting nanocrystals with the designated amounts stated above prior to their incorporation into LiCl and subsequently carried out the incorporation into salt. In this material system, green nanocrystals act as exciton donors while red nanocrystals serve as exciton acceptors. To assist the reader, we have chosen to use the volumes of the incorporated nanocrystals instead of their weights or molar concentrations throughout the rest of the chapter.

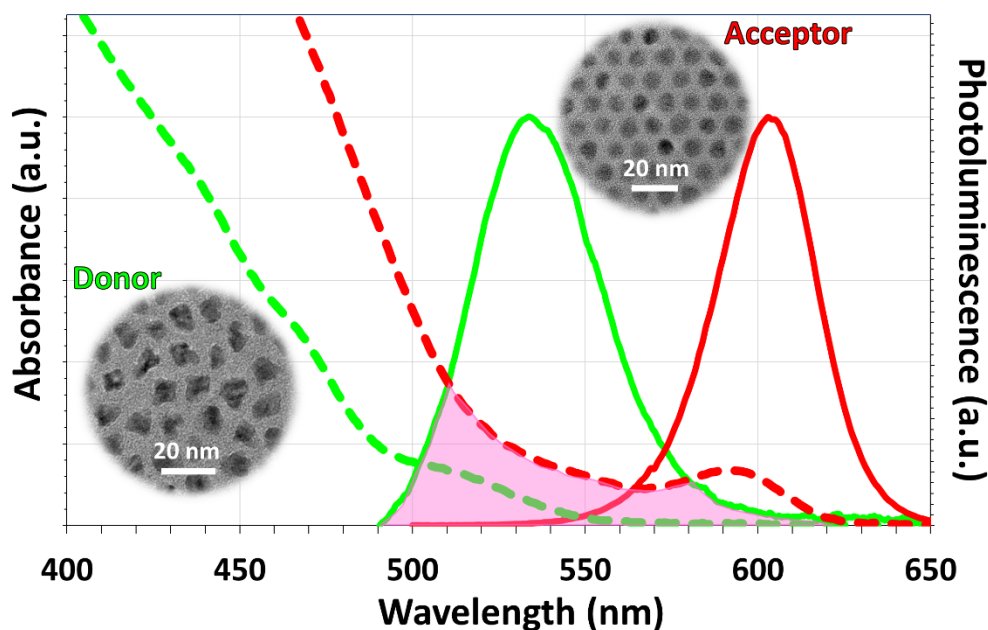


Figure 8.1. Photoluminescence spectra of the green-emitting donor and red-emitting acceptor nanocrystals (shown with green and red continuous lines, respectively) and their absorption spectra (shown with green and red dashed lines, respectively). In the inset, we provide the transmission electron microscopy images of these nanocrystals. Reproduced with permission from Ref. [85]. © Optical Society of America 2016.

Within the framework of our study, we first investigated the photoluminescence of the nanocrystal incorporated powders (Figure 8.2). In the powders with only single color nanocrystal incorporation, we observe a red shift of 2 and 8 nm for green and red nanocrystals in LiCl powders compared to their dispersions, respectively. In addition, we did not observe an apparent red shift in the emission spectra of the nanocrystals with the increasing nanocrystal incorporation amount. If the aggregation of nanocrystals was prominent, however, we would expect increasing red shift of nanocrystal emission with increasing nanocrystal incorporation amount. This shows that the red shift in the emission spectrum is mainly caused by the interaction of the dipoles in the nanocrystals with the surrounding medium [191]. Another observation is the decreasing intensity of the green-emitting nanocrystals when red-emitting nanocrystals are co-immobilized within LiCl powders. In parallel to this, we

observe an increase in the intensity of the red nanocrystals when hybridized with green nanocrystals compared to the intensity of the only red nanocrystals immobilized in LiCl powders.

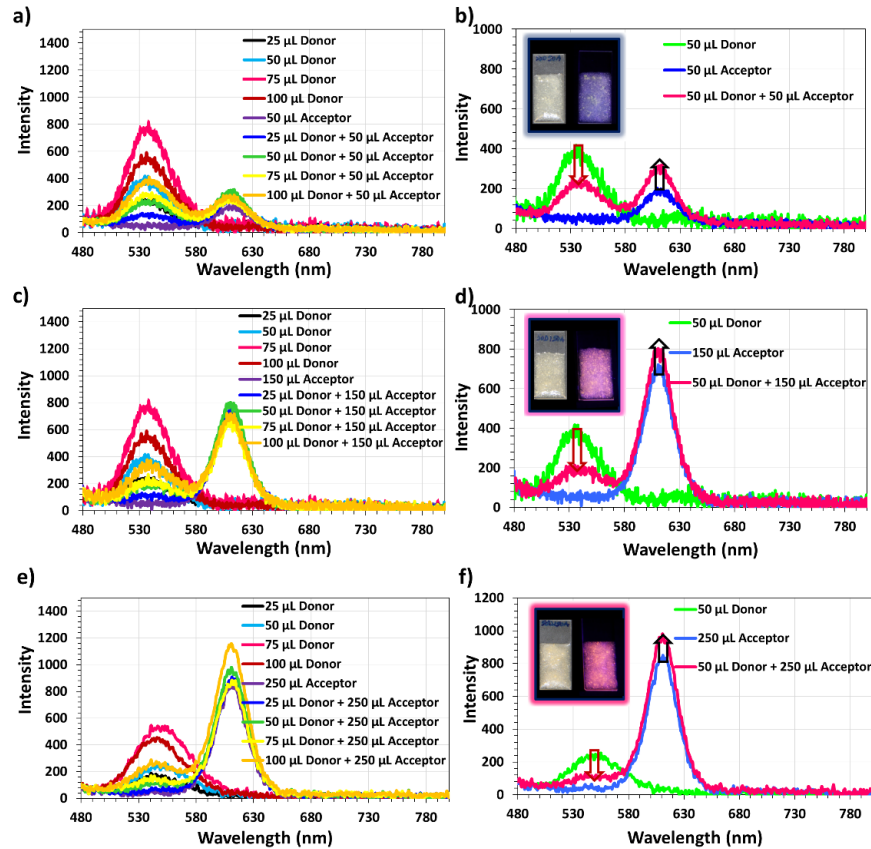


Figure 8.2. Photoluminescence spectra of the films prepared using the green-emitting and red-emitting nanocrystal hybrids embedded into LiCl powders. Here, the green-emitting nanocrystals serve as exciton donors while the red-emitting nanocrystals accept excitons. In (a), (c), and (e) the spectra of the only green-emitting nanocrystal embedded powders are given together with the hybrid and only red-emitting acceptor nanocrystal embedded powders prepared using 50, 150, and 250 μL of nanocrystals, respectively. Frames (b), (d), and (f) show the variation of the spectra for the cases where 50 μL of green (donor) nanocrystals are embedded into LiCl together with 50, 150, and 250 μL of acceptor, respectively. The inset images are the real color photographs of these films under ambient (left) and UV lighting (right). Reproduced with permission from Ref. [85]. © Optical Society of America 2016.

In these hybrid powders, the decrease of the green-emitting nanocrystal intensity along with the increase of the red-emitting nanocrystal intensity can be explained by both the radiative and nonradiative energy transfer. Radiative energy transfer can occur via the absorption of the green light by the red nanocrystals; as a result, the intensity of the green light decreases while the red intensity increases. This process does not require close proximity between the nanocrystals; instead, it only requires the emitted green light to reach the red-emitting nanocrystals that absorb the green light. On the other hand, NRET requires close proximity between green and red nanocrystals within LiCl to transfer the excitons from one emitter to another. These two energy transfer mechanisms can be safely distinguished by time-resolved fluorescence (TRF) spectroscopy. While the radiative energy transfer does not have any effect on the time-resolved decay of the emitter, the occurrence of the NRET can be monitored in the TRF decay of the donor as an acceleration in the decay curve. In addition, slowed-down acceptor decay curves are also expected if the lifetime of the acceptor is comparable to that of the donor lifetime [208]. Since in our system we utilize nanocrystals having similar lifetimes, we expect to observe an increase in the red nanocrystal lifetime simultaneous to decreasing lifetime of the green-emitting donor nanocrystals.

To reveal the emission mechanisms within the LiCl powders incorporating green and red nanocrystals, we measured the TRF decays of the films. In Figure 8.3, we present exemplary decay curves of the hybrid LiCl films prepared using powders incorporating 250 μL of the red-emitting nanocrystals together with 25-100 μL of the green-emitting nanocrystals. Similar trends are observed in the samples prepared by incorporating 50 and 150 μL of red nanocrystals. All of these data indicate a clear acceleration in the time-resolved decay curve of the green nanocrystals in LiCl powders when co-immobilized in LiCl together with the red-emitting nanocrystals while acceptor decays slow down. These observations confirm that NRET takes place between the green-emitting nanocrystals and the red-emitting nanocrystals.

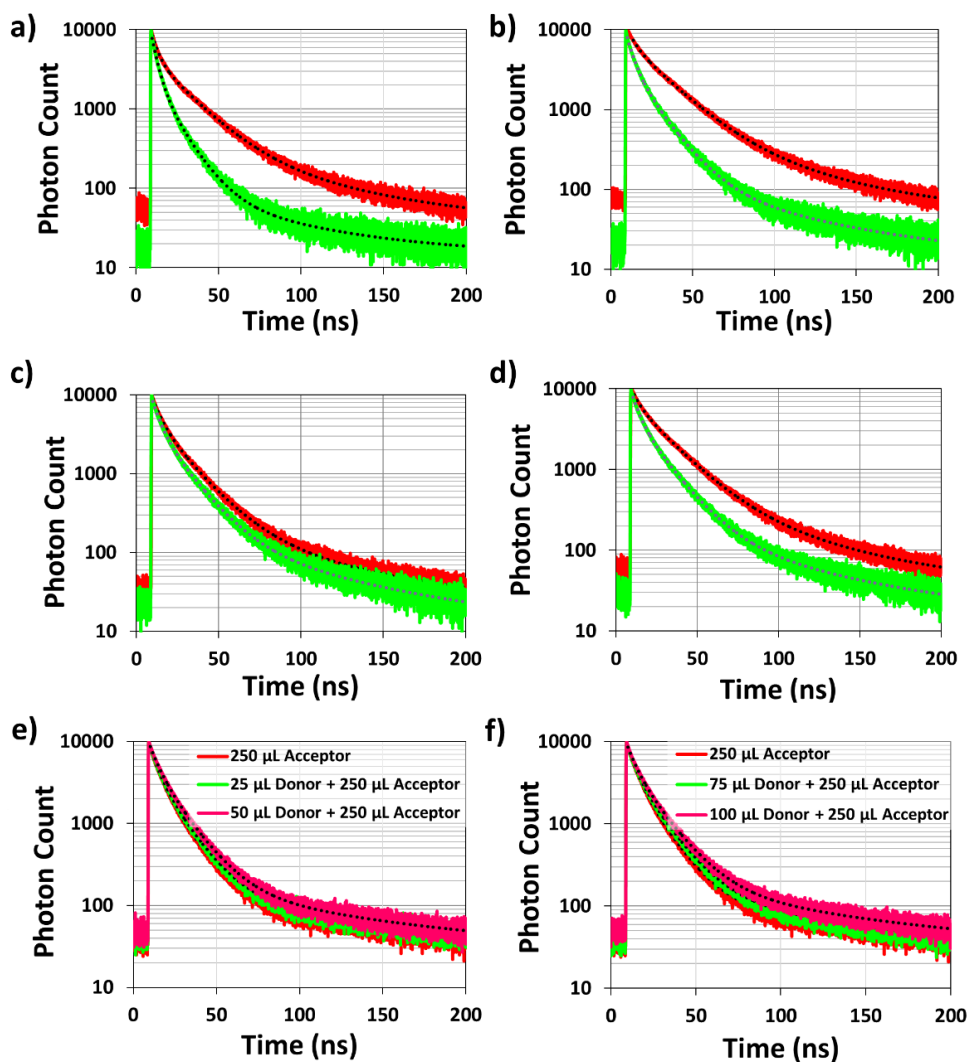


Figure 8.3. Time-resolved fluorescence decays of the green-emitting exciton-donating nanocrystals within powders prepared using (a) 25 μL donor nanocrystals (red line) and hybrid of 25 μL donor nanocrystals together with 250 μL red-emitting exciton-accepting nanocrystals (green line), (b) 50 μL donor nanocrystals (red line) and hybrid of 50 μL donor nanocrystals together with 250 μL acceptor nanocrystals (green line), (c) 75 μL donor nanocrystals (red line) and hybrid of 75 μL donor nanocrystals together with 250 μL acceptor nanocrystals (green line), and (d) 100 μL donor nanocrystals (red line) and hybrid of 100 μL donor nanocrystals together with 250 μL acceptor nanocrystals (green line) at the donor emission peaks. Frames (e) and (f) show the TRF decays of the acceptor nanocrystals alone and in hybrid nanocrystal powders.

The black dashed lines are the fitted multiexponential functions on the TRF decays. Reproduced with permission from Ref. [85]. © Optical Society of America 2016.

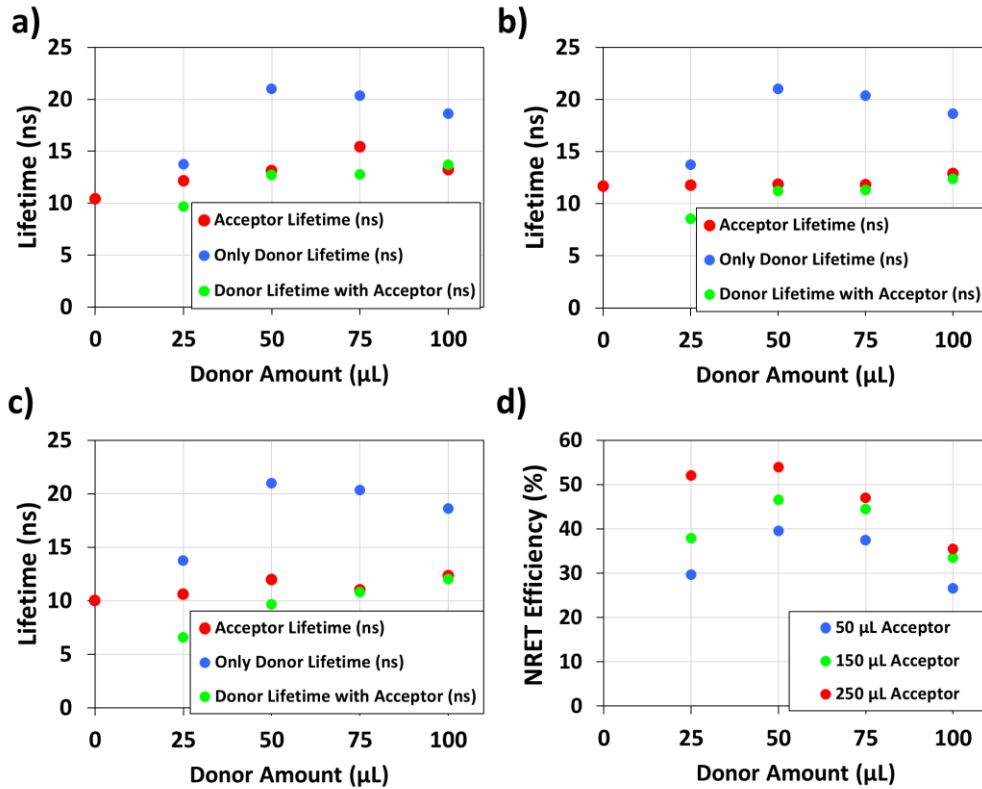


Figure 8.4. Amplitude-averaged lifetimes of only donor nanocrystal embedded LiCl powders, only acceptor nanocrystal embedded LiCl powders, and powders prepared using donor and acceptor nanocrystals. Frame (a) presents the lifetimes for the incorporated acceptor amount of 50 μL while in (b) and (c) the illustrated lifetimes stand for the powders prepared using 150 and 250 μL of acceptor, respectively. Frame (d) presents the NRET efficiency of the hybrid nanocrystal powders for varying acceptor incorporation amounts. Reproduced with permission from Ref. [85]. © Optical Society of America.

To quantitatively analyze the NRET dynamics within the hybrid powders, we fitted the TRF decays with three exponential functions and calculated the amplitude-averaged lifetimes. Subsequently, the efficiency of the NRET process is calculated according to Equation 8.1 where τ_D stands for the donor lifetime in

the absence of the acceptor while τ_{DA} stands for the donor lifetime in the presence of acceptor. These calculated lifetimes are illustrated below in Figure 8.4.

$$\eta = 1 - \frac{1/\tau_D}{1/\tau_{DA}} \quad (8.1)$$

In this figure, we observe that the lifetimes of the green-emitting nanocrystals decrease when they are hybridized with the red-emitting nanocrystals in LiCl compared to the case of only green-emitting nanocrystals embedded within LiCl for all the red-emitting nanocrystal amounts in the hybrid powders. For example, the lifetime of the green-emitting nanocrystals decreases from 21.0 to 9.7 ns when 50 μL green-emitting nanocrystals are embedded into LiCl together with 250 μL of red-emitting nanocrystals. In addition, the red-emitting nanocrystals exhibit a lengthened lifetime in hybrid powders. For instance, the lifetime of the red-emitting nanocrystals increases from 10.0 ns to 12.0 ns following the hybridization of 250 μL red-emitting nanocrystals with 50 μL of green nanocrystals in LiCl. These findings show that excitons are donated from the green-emitting nanocrystals to the red-emitting nanocrystals. It is here worth noting that NRET in such material system might originate from dipole-dipole interaction or charge transfer. However, in our system the high energy barrier occurring due to the LiCl in the medium and ZnS shell of the green nanocrystals blocks the charge transfer [209]. This hypothesis is also supported by the lengthened acceptor lifetimes, which should have shortened if charge transfer occurred between the nanocrystals [208]. Therefore, here we conclude that the main NRET mechanism taking place in our system is Förster-like energy transfer that relies on the dipole-dipole interaction of two emitters.

The NRET efficiencies presented in Figure 8.4(d) exhibit a dependence on the amounts of the incorporated exciton donating green-emitting nanocrystals and exciton accepting red-emitting nanocrystals. As expected, as the amount of the acceptor nanocrystals increases, the efficiency of the NRET process increases for all the donor amounts. This is because the number of acceptors surrounding the donor nanocrystals increases; as a result, the probability of exciton transfer from the donor nanocrystals to the acceptor nanocrystals increases leading to increased NRET efficiencies. On the other hand, for the fixed incorporated

acceptor amounts the NRET efficiency first increases with the increasing donor amount in the powders up to 39.6%, 46.6%, and 53.9% in the samples prepared by mixing 50 μL of the green-emitting donor nanocrystals with 50, 150, and 250 μL of the red-emitting nanocrystals, respectively. Nevertheless, further increase of the donor concentration in the powders is found to decrease the NRET efficiency. This observation can be explained with two effects that possibly work together. The first one is that there are enough acceptors in the close proximity of the donors to transfer their excitons up to a donor concentration around $\sim 5.36\text{-}7.64$ pmol/mg (50 μL); but beyond this concentration a competition starts to occur between the donor nanocrystals to transfer their excitons. As a result, some excitons can be transferred nonradiatively while some of them cannot as the donor concentration in the powders further increases. Consequently, the lifetime of the donor nanocrystals in the nanocrystal hybrid powders converges to the lifetime of the only green-emitting nanocrystal incorporated powders with further increase of donor nanocrystal concentration. The second effect is that after a certain point increasing the donor concentration cannot increase the number of donors which are in close proximity of the acceptors. As a result, the number of the nanocrystals transferring their excitons cannot increase. In this case, further addition of donors would decrease the fraction of the donors undergoing exciton transfer. Consequently, the donor lifetime in the hybrid nanocrystal powders starts to converge to the lifetime of the only green nanocrystal embedded LiCl powders leading to smaller ensemble NRET efficiencies.

This material system of nanocrystal embedded LiCl powders is an excellent system for use on light-emitting devices as color converters because it offers high-efficiency along with the improved stability of nanocrystals [88] and compatibility with the current production facilities of the light-emitting diode (LED) producers. In this work, we also utilized NRET in these powders to realize exciton transferring light-emitting diodes. For this purpose, we integrated about 23 mg of the powders prepared using 50 μL of green- and 250 μL of red-emitting nanocrystals, which achieved the highest NRET efficiency among our samples, on a blue LED emitting at 460 nm. This LED, whose emission spectrum is presented in Figure 8.5, reached a luminous efficiency above 70 lm/W_{elect} in the

violet-purple color regime with chromaticity points around $x=0.32-0.35$ and $y=0.23-0.26$. Considering this performance, we believe that this NRET improved LEDs can be a good alternative for replacing violet LEDs based on epitaxially grown GaN.

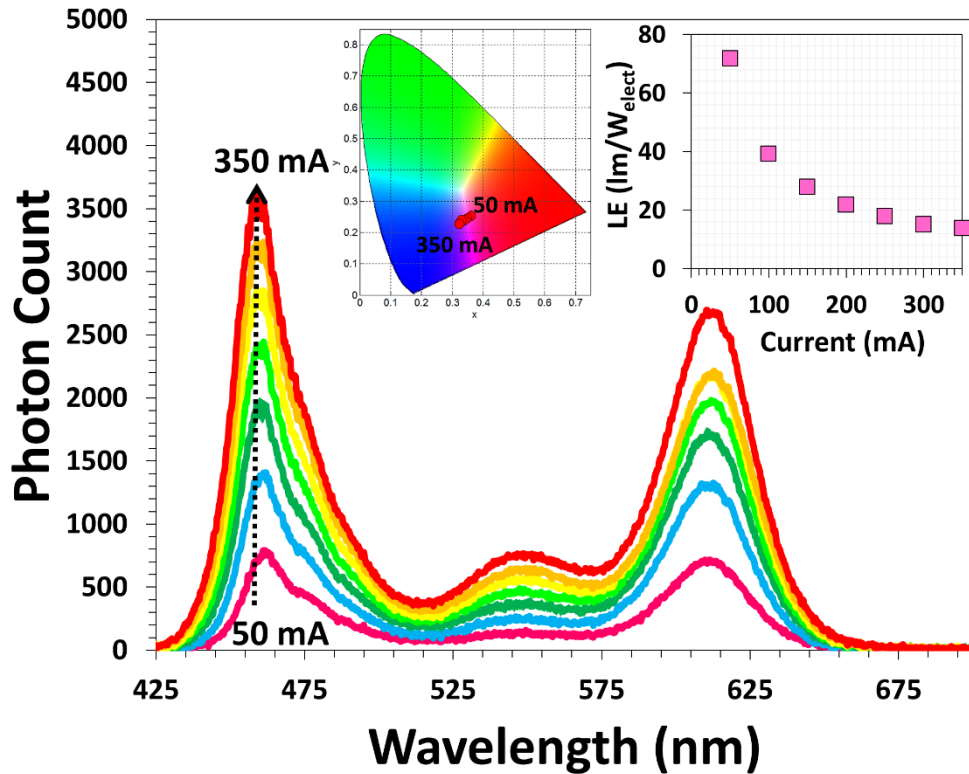


Figure 8.5. Emission spectrum of the NRET enhanced nanocrystal embedded LiCl powders at varying currents together with the chromaticity points of the emitted light (inset, left) and luminous efficiency of the device (LE) (inset, right). Reproduced with permission from Ref. [85]. © Optical Society of America 2016.

8.4 Summary

In summary, here we co-immobilized nonpolar green- and red-emitting nanocrystals into LiCl salt matrix. The short distance between these co-integrated nanocrystals allowed the green-emitting ones to strongly transfer their excitons to the red-emitting ones. For a systematic study, we varied the concentrations of the donor and acceptor nanocrystals within these powders and

studied the NRET efficiency. We observed that the increase of the acceptor incorporation in the powders increases the NRET efficiency because there are more acceptors to receive excitons per donor. On the other hand, the increasing donor concentration in the powders was found first to increase the energy transfer efficiency and then to decrease it, which is attributed to the competition between the donors with increasing donor concentration and to the increased amount of donors immobilized further away from the acceptors. In our powder system, the NRET efficiency reached a maximum level of 53.9% at the donor concentration of $\sim 5.36\text{-}7.64$ pmol/mg and the acceptor concentration of $\sim 44.6\text{-}53.5$ pmol/mg. Subsequent to these analyses, we integrated these NRET-enhanced color-converting nanocrystal powders on blue LEDs. The resulting violet-emitting LED reached a luminous efficiency above 70 lm/W_{elect.} We believe that these excitonic LiCl powders of colloidal nanocrystals, which offer improved stability, robustness, and compatibility to current packaging facilities of the LED industry, can find wide-spread use in lighting and display applications.

Chapter 9

Morphology-Dependent Nonradiative Energy Transfer from InGaN/GaN Quantum Well Nanopillars to Conjugated Polymer Nanoparticles

In this chapter of the thesis, we present our study on the investigation of nonradiative energy transfer (NRET) between conjugated polymer nanoparticles (CPNs) prepared in aqueous dispersion from poly[(9,9-bis{3-bromopropyl}fluorenyl-2,7-diyl)-co-(1,4-benzo-{2,1,3}-thiodiazole)] (PFBT-Br), and InGaN/GaN multiple quantum wells (MQWs) nanopillars to demonstrate a new organic/inorganic class of nanostructured excitonic model system. This hybrid system enables intimate integration for strong exciton-exciton interactions through nonradiative energy transfer (NRET) between the integrated CPNs and MQW pillars. The NRET of these excitonic systems is systematically investigated at varied temperatures. To understand morphology-dependent NRET, PFBT-Br CPNs coating InGaN/GaN MQWs are made to defold into polymer chains by in situ treatment with a good solvent (tetrahydrofuran, THF). The experimental results indicate that NRET is significantly stronger in the case of CPNs compared to their defolded polymer chains. This work may potentially open up new opportunities for the hybrid organic/inorganic systems where strong excitonic interactions are desired for light generation, light harvesting, and sensing applications.

This chapter is based on T. Erdem, V. Ibrahimova, D.-W. Jeon, I.-H. Lee, D. Tuncel, and H. V. Demir, *J. Phys. Chem. C* 117, 36, 18613-18619 (2013) [100]. Reproduced with permission from American Chemical Society © 2013. This work

is a collaboration with Prof. Tuncel's research group at the Department of Chemistry and UNAM, Bilkent University.

9.1 Introduction

Conjugated polymer nanoparticles (CPNs) attract significant attention for important applications including bioimaging [210]–[212], biosensing [213], [214], and optoelectronics [215]–[221]. One of the most attractive features of CPNs is the convenient tunability and control of their properties through the choice and functionalization of the polymer, and the surface modification of nanoparticles. Furthermore, CPNs exhibit low toxicity [222] and their mechanical stability can be enhanced through cross-linking [64]. Their optical properties arise from the controlled conformational changes of the polymer and their aggregation form, rather than the quantum confinement effects, in contrast to inorganic nanoparticles, *e.g.*, colloidal semiconductor quantum dots (QDs) [222]. As a result of these attractive properties, CPNs find use as alternative color convertors, or molecular beacons, in various biotechnology [210], [212], [213] and optoelectronics [64], [215], [218], [219], [222] applications.

The emission of color convertors, including CPNs, can be enhanced *via* the Förster-type nonradiative energy transfer (NRET) (also dubbed as Förster resonance energy transfer, FRET), which basically relies on the exciton-exciton interactions between the donor and acceptor emitters [96]. For example, polymers [223], organic dyes [224], inorganic quantum dots [225], and epitaxial quantum wells [225], [226] have been widely investigated for NRET studies. CPNs were also used in similar studies because of their preferably high absorption cross-sections [15].

Another important class of materials in optoelectronics is the III-nitrides. They are the main building blocks of today's UV, blue, green, and white light-emitting diodes. Using these materials, a wide range of spectral region from the ultraviolet to the green can be covered by controlling their alloy composition. Especially quantum well (QW) architectures are of great importance as they enable spectral tuning and enhancement in the emission quantum efficiency. Since InGaN/GaN quantum wells having a wide bandgap are used for high-

energy photon generation, they are also valuable for studying NRET dynamics. In the literature this type of QWs were used together with both organic and inorganic luminophors. As an example of inorganic material integration on QWs, Achermann *et al.* used epitaxial quantum wells with semiconductor nanocrystal QDs and reached a transfer efficiency of 65% [225]. Later Chanyawadee *et al.* achieved an NRET efficiency of 82% using nanocrystal QDs and QWs having elliptical holes reaching down their wells [227]. In an independent work of Nizamoglu *et al.*, the use of nanopillars housing QWs was also reported to increase the NRET efficiency to 83% [228]. The enhancement in the NRET efficiency is basically enabled by the reduced distance between the QWs and the colloidal QDs in these examples.

In this work, different than the previous reports of our group and others, we studied aqueous dispersions of CPNs made of poly[(9,9-bis{3-bromopropyl}fluorenyl-2,7-diyl)-co-(1,4-benzo-{2,1,3}-thiodiazole)] (PFBT-Br) whose chemical structure is given in Figure 9.1, immobilized into InGaN/GaN QW nanopillar architecture to make a new class of hybrid excitonic model systems consisting of organic and inorganic nanostructures. We observed that nanopillars transfer their excitation energies to CPNs with a substantially higher efficiency compared to their defolded polymer chains at varying temperatures (at 296, 250, 200, 150, and 100 K), while preserving the same number of polymer molecules in the system. We also observed that the NRET efficiency and rate are functions of temperature and decreases with decreasing temperature as a result of stronger exciton localization within InGaN/GaN QW nanopillars at lower temperatures in the case of CPN hybridization. Also, to further identify the effects of morphology directly on the emission kinetics of organic molecules used in this study, we examined the emission decay characteristics of PFBT-Br CPNs and their defolded polymer chains on a quartz substrate. We found that the emission kinetics of CPNs decorating nanopillars and those on quartz are similar whereas the defolded polymer chains exhibit completely different behavior. This study shows that the emission dynamics of CPNs are more immune to environmental and morphological changes than defolded polymer chains are.

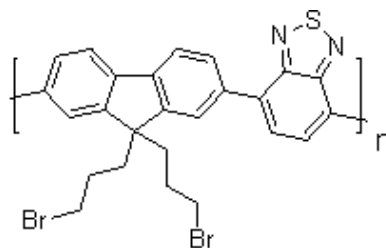


Figure 9.1. Molecular structure of poly[(9,9-bis{3-bromopropyl}fluorenyl-2,7-diyl)-co-(1,4-benzo-{2,1,3}-thiadiazole)] (PFBT-Br). Reproduced with permission from Ref. [100]. © American Chemical Society 2013.

9.2 Experimental Methodology

9.2.1 Synthesis of PFBT-Br

2,1,3-Benzothiadiazole-4,7-bis(boronic acid pinacol ester) (411mg, 1.06 mmol), 2,7-dibromo-9,9-bis(3-bromo-propyl)-9H-fluorene (566 mg, 1.06 mmol) and K_2CO_3 (1.47 g, 10.6 mmol) were dried under vacuum for about 30 min. Subsequently, degassed solvents, tetrahydrofuran (THF) (10 mL), water (10 mL) and toluene (10 mL) were added into the mixture under argon gas. Then, the catalyst, tetrakis(triphenylphosphine) palladium $[Pd(PPh_3)_4]$ was quickly added. After 3 h stirring of the mixture under argon at 80–90°C, the phase transfer catalyst, tetra-n-butylammonium bromide (TBAB), was added. The stirring was continued for another 48 h at 80–90°C to complete the polymerization reaction. The mixture was evaporated under vacuum to obtain a solid residue, which was suspended in water; the water insoluble particles were then collected by suction and dissolved in THF (15 mL) and the solution was precipitated into cold methanol (200 mL). The precipitates were collected by suction and dried under vacuum for 6 h (547 mg, 56%). The synthesis of PFBT-Br can also be found in Ref. [229].

1H NMR (400 MHz, $CDCl_3$, δ) 7.99 (m, 8H, Ar-H), 3.35 (q, 4H, CH_2Br), 2.41 (q, 4H, CH_2), 1.25 (m, 4H, CH_2). GPC: $M_n = 4.5 \times 10^3$ g/mol, $M_w = 1.1 \times 10^4$ g/mol (polystyrene as standard).

9.2.2 Preparation of PFBT-Br nanoparticles

Nanoparticles were prepared by the reprecipitation method [222]. 2 mg of PFBT-Br polymer were dissolved in 10 mL of THF and ultra-sonicated for 15 min. After sonication the solution was filtrated via syringe filter and injected into rapidly stirring 100 mL Milli-Q water (18.2 M Ω) and ultra-sonicated for another 1 h. Vacuum rotary evaporator was used to remove THF to obtain stable nanoparticles. Dynamic light scattering (DLS) measurements showed that the average diameter of the prepared CPNs is 69 nm. Absorption and fluorescence spectra of the polymer and nanoparticles are given in Figure 9.2(a), and DLS results are given in Table 9.1 and Figure 9.3(a). Absorption spectrum of PFBT-Br film on quartz is also recorded (Figure 9.3(b)). We observed that there is no major difference in the photoluminescence between PFBT-Br films prepared directly and prepared by adding THF onto PFBT-Br CPN film and drying it.

9.2.3 Epitaxial growth of InGaN/GaN quantum wells

InGaN/GaN multiple QWs were grown on a sapphire substrate using metal organic chemical vapor deposition (MOCVD). The precursors of Ga, In, and N were trimethylgallium (TMGa), trimethylindium (TMIn), and NH₃, respectively. First the c-plane sapphire substrate was annealed at 1000 °C for 10 min. Subsequently, a buffer layer of GaN was grown at low temperature. Following the buffer layer, an undoped GaN layer (1 μ m) and n-type GaN layer (2 μ m) were grown at 1060 °C. Five pairs of InGaN/GaN QWs were then grown on top of this n-type layer. Finally, a 150 nm thick GaN layer was grown to complete the epitaxial structure.

9.2.4 Preparation of InGaN/GaN QW nanopillars

A 100 nm thick SiO₂ was deposited by plasma enhanced chemical vapor deposition (PECVD) on the epitaxially grown layers, followed by a 10 nm thick Ni thin film deposition using an e-beam evaporator. The formation of Ni clusters was realized upon annealing the epi-wafer at 800 °C for 1 min under N₂ flow. SiO₂ and GaN layers were etched using inductively coupled plasma-reactive ion

etching (ICP-RIE). Ni and SiO₂ regions were then removed using buffered oxide etchant (BOE). Surface passivation was carried out *via* KOH and NH₄S treatment and confirmed by an increased intensity compared to both non-treated and planar cases. The photoluminescence spectrum of nanopillars is given in Figure 9.2(b).

9.2.5 Experimental procedure for NRET characterization

First, time-resolved and steady state photoluminescence measurements of the InGaN/GaN nanopillars were taken at 100, 150, 200, 250 and 296 K. Then, PFBT-Br CPNs having an average diameter of 69 nm were integrated with the nanopillars via careful drop-casting and dried at 50 °C. Time-resolved and steady state fluorescence measurements were taken at the same temperatures. Subsequently, the CPNs decorating the nanopillars were converted into the polymer chains by adding small amounts of THF and then fully evaporating it. By doing so, we aimed to preserve the number of acceptor molecules in the hybrid system and make a fair comparison between both of the cases using exactly the same polymer chains. This experimental methodology is illustrated in Figure 9.3.

To ensure the validity of our results, it is necessary to make sure that there are enough acceptors surrounding the quantum wells. For this purpose, we carefully prepared the samples, and took their SEM image including CPNs immobilized around nanopillars (Figure 9.4(a)) as well as the THF-treated version of the hybrid structure in which the CPNs were made to defold into polymer chains using and fully evaporating THF (Figure 9.4(b)). As can be seen from the images of both cases, nanopillars are just fully covered. In addition, the same amount of PFBT-Br CPNs was also drop-casted on a quartz substrate and later THF was added onto this film, while again preserving the same number of polymer molecules.

Consequently, this systematic study allowed us to analyze the emission and NRET kinetics of these two different architectures of PFBT-Br molecules (as CPNs and polymer chains). Time-resolved fluorescence decays of all these films

were also recorded at the corresponding temperatures. The lifetimes were determined by fitting multi-exponential functions to the experimentally measured decay curves. In all of the cases, χ^2 remained within 0.9 and 1.1, mostly very close to 1.0, which indicates a strong correlation between the experimental data and the fitted exponential functions. The error in the lifetimes was calculated to be <7.6% and <5% for the nanopillars and acceptor molecules, respectively.

9.3 Results and Discussion

Aqueous dispersions of CPNs were prepared from PFBT-Br [229] using the reprecipitation method in which the polymer chains are collapsed into spherical nanoparticles upon exposure to a poor solvent (*e.g.*, water). The average size of the resultant CPNs were determined to be 69 nm using dynamic light scattering measurement (Figure 9.3(a) and Table 9.1). The fluorescence and absorbance spectra of PFBT-Br in THF and PFBT-Br CPNs in water are given in Figure 9.2(a). PFBT-Br CPNs were incorporated into the nanopillars to obtain nanostructured hybrid systems in which InGaN/GaN QWs serve as the donor and CPNs as the acceptor in the nonradiative energy transfer.

The donor peak emission wavelength is around 450 nm, whereas the peak emission wavelength of the acceptor is located around 550 nm. Following the characterization of the InGaN/GaN-CPN hybrids, CPNs coating the MQW nanopillars were made to defold in situ into polymer chains by carefully treating with a good solvent (*e.g.*, THF), which allows for preserving the amount of polymers to study the morphology-dependent energy transfer and emission kinetics of the hybrid system. The absorbance spectra of the PFBT-Br CPN and defolded PFBT-Br are presented in Figure 9.2(b) along with the photoluminescence spectrum of the InGaN/GaN nanopillars. The experimental procedure is illustrated in Figure 9.5, and the scanning electron microscopy (SEM) images of the hybrid system before and after THF treatment is given in Figure 9.4.

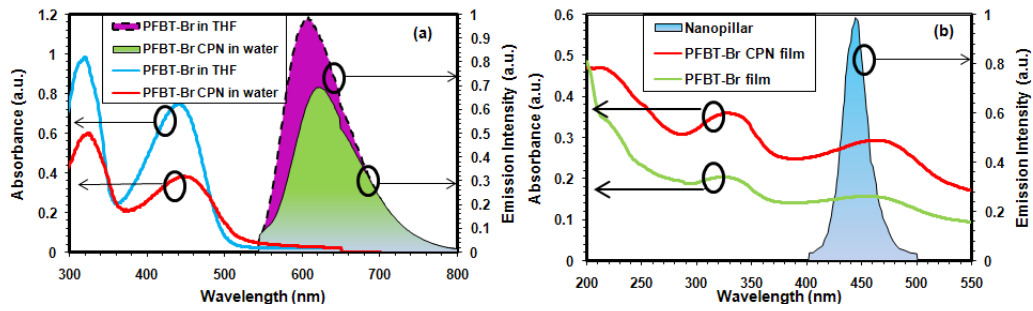


Figure 9.2. (a) Absorbance and fluorescence spectra of PFBT-Br in THF and PFBT-Br CPNs in water, and (b) absorbance spectra of PFBT-Br CPN film and de-folded PFBT-Br (while preserving the amount of polymers on quartz), together with the photoluminescence of InGaN/GaN QWs. Reproduced with permission from Ref. [100]. © American Chemical Society 2013.

Table 9.1. Emission (λ_{em}) and absorption (λ_{abs}) peaks and quantum efficiencies (Φ_f) of PFBT-Br in THF and PFBT-Br CPNs in water together with mean diameter, polydispersity index, and zeta potential of the nanoparticles.

	λ_{abs} (nm)	λ_{em} (nm)	Φ_f (%)	DLS		zeta
				diameter (mean) (nm)	polydispersity index	potential (mean) (nm)
PFBT- Br	319, 442	534	17	-	-	-
PFBT- Br CPNs	330, 473	544	0.5	69	0.294	-28.6

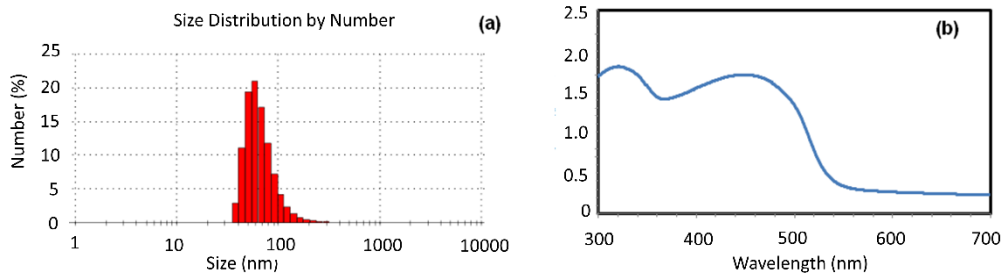


Figure 9.3. (a) Dynamic light scattering (DLS) histogram of PFBT-Br CPNs in water. The average diameter is 69 nm with a polydispersity index of 0.294, (b) the absorption spectrum of PFBT-Br film directly deposited on quartz. Reproduced with permission from Ref. [100]. © American Chemical Society 2013.

NRET efficiency (η) and NRET rate (γ_{NRET}) are calculated using Equations 9.1 and 9.2, respectively. Here, τ_{DA} stands for the lifetime of donors in the presence of acceptors and τ_D denotes the lifetime of donors in the absence of acceptors.

$$\eta = 1 - \frac{\tau_{DA}}{\tau_D} \quad (9.1)$$

$$\gamma_{NRET} = \frac{1}{\tau_{DA}} - \frac{1}{\tau_D} \quad (9.2)$$

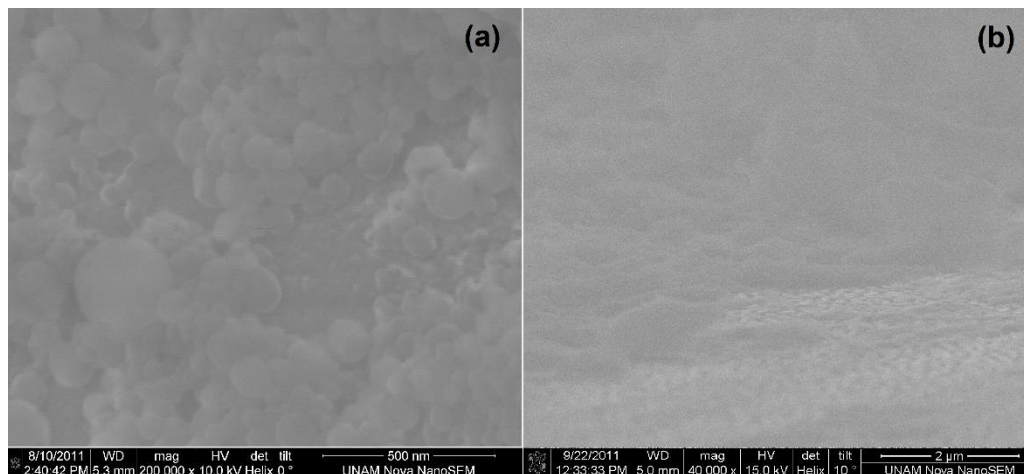


Figure 9.4. SEM images of (a) PFBT-Br nanoparticles on the nanopyllars and (b) PFBT-Br polymer chains on the nanopyllars (after the addition and evaporation of THF). The amount is carefully set such that the nanopyllars are almost fully covered in both cases to ensure the coverage of the emissive QW region inside the nanopyllars. Reproduced with permission from Ref. [100]. © American Chemical Society 2013.

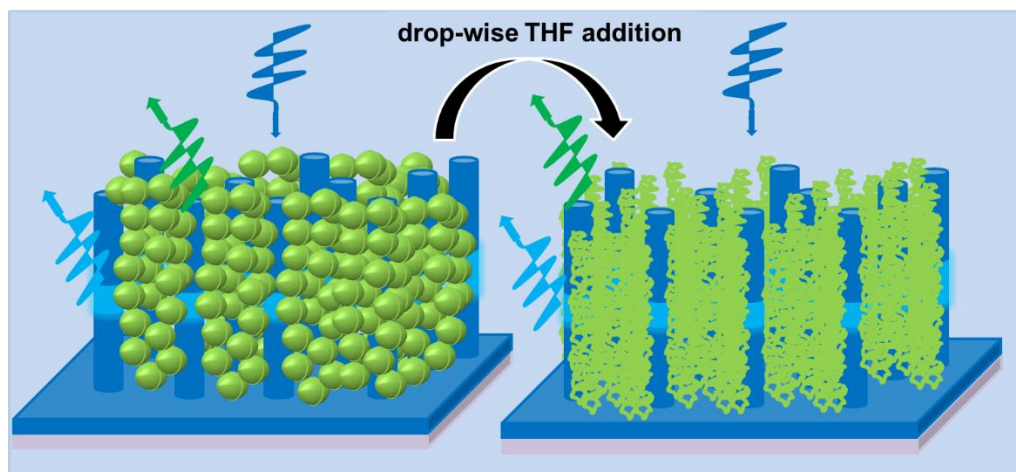


Figure 9.5. Illustration of the comparative study: First aqueous dispersion of nanoparticles is drop-casted on the nanopyllars and cryogenic time-resolved and steady state fluorescence measurements are taken at 296, 250, 200, 150, and 100 K. Later, THF is drop-wise added onto the nanoparticles on the nanopyllars to

defold them into polymer chains and then fully evaporated. The same measurements are repeated for the case of open polymers. Reproduced with permission from Ref. [100]. © American Chemical Society.

The corresponding lifetimes of the nanopillar–PFBT-Br hybrid systems at the donor peak emission wavelength are given in Figure 9.6 and listed in Table 9.2, together with the energy transfer efficiencies for CPNs and defolded polymer chains. Additionally, time-resolved fluorescence decay curves are presented at the donor and acceptor peak emission wavelengths in Figure 9.7 and Figure 9.8, respectively.

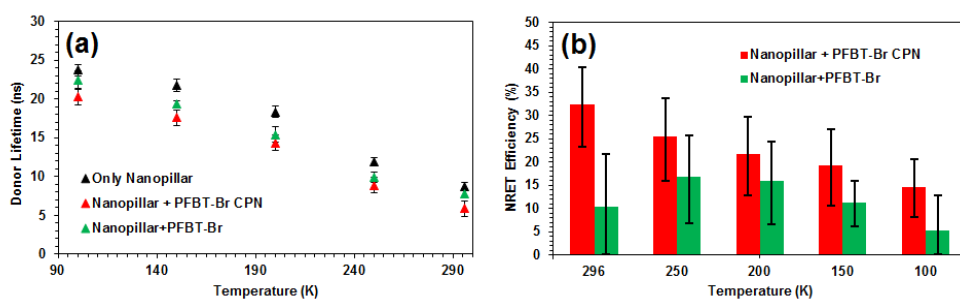


Figure 9.6. Temperature-dependent lifetimes of (a) nanopillars alone, nanopillars in the presence of PFBT-Br CPNs, and nanopillars in the presence of defolded PFBT-Br polymer chains, and (b) temperature-dependent NRET efficiency of the nanopillar-CPN hybrid and nanopillar defolded PFBT-Br hybrid. Black error bars indicate the measurement errors for (a), and the error bars in (b) were calculated using the information in (a). The minimum NRET efficiency was calculated by taking the minimum lifetime value of nanopillar and the maximum donor lifetime of acceptor including system. Similarly, the minimum NRET efficiency was found by using the maximum lifetime value of nanopillar and the minimum donor lifetime of acceptor including system. Reproduced with permission from Ref. [100]. © American Chemical Society 2013.

We observe a significant difference in the donor lifetimes and, consequently, in the energy transfer efficiencies after both (i) PFBT-Br CPN hybridization on InGaN/GaN nanopillars and (ii) PFBT-Br polymer chains obtained by defolding these CPNs *via* THF addition. Furthermore, the average donor lifetimes in the case of CPNs shorten more after hybridization than in the case of the defolded

polymers. This further lifetime shortening of nanopillars can possibly stem from the following: (a) an increase in the distance between the QWs of donor nanopillars and acceptor molecules after defolding, (b) a more successful surface passivation by defolded polymers compared to CPNs, or (c) a more successful energy transfer process in the case of CPNs compared to defolded polymer chains. Here the first problem was avoided during the experiment by drop-wise addition of THF without removing the defolded polymers away from the nanopillars. The SEM imaging revealed that the nanopillars were fully covered by CPNs before the THF treatment and a significant surface coverage was achieved after THF addition (Figure 9.4). With great care taken not to remove the polymers, the defolded polymers come even closer to the active region of the nanopillars. If the defolded polymers had the same NRET characteristics as the CPNs, one would expect to observe a stronger decrease in the lifetime of the nanopillars compared to CPNs.

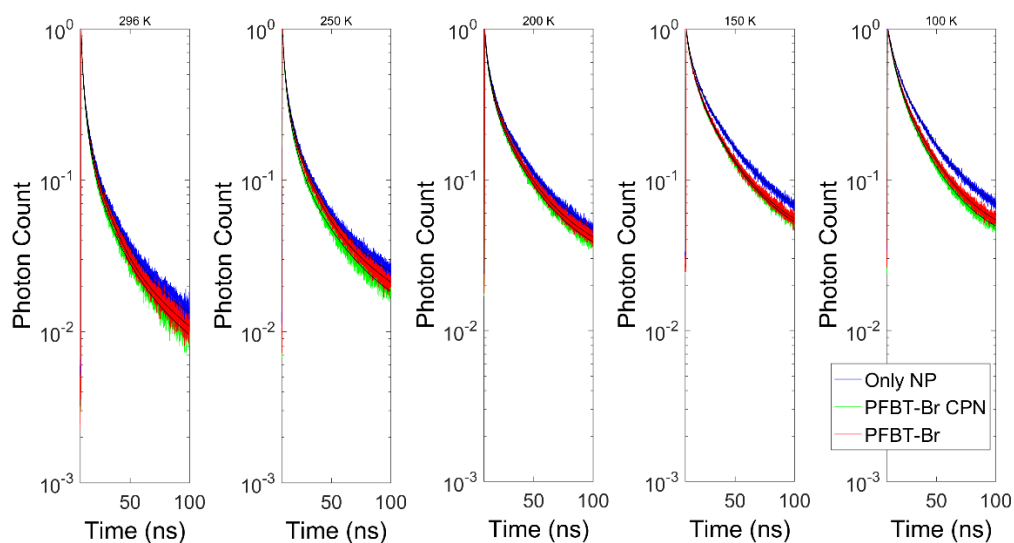


Figure 9.7. Time-resolved fluorescence decay curves of the nanopillars alone, the nanopillars hybridized with PFBT-Br CPNs and those hybridized with PFBT-Br polymer (after the addition and evaporation of THF) at 450 nm at temperatures of 296, 250, 200, 150, and 100 K. Black curves within the colored decay curves are the multi-exponential functions numerically fitted to the experimental data. Reproduced with permission from Ref. [100]. © American Chemical Society 2013.

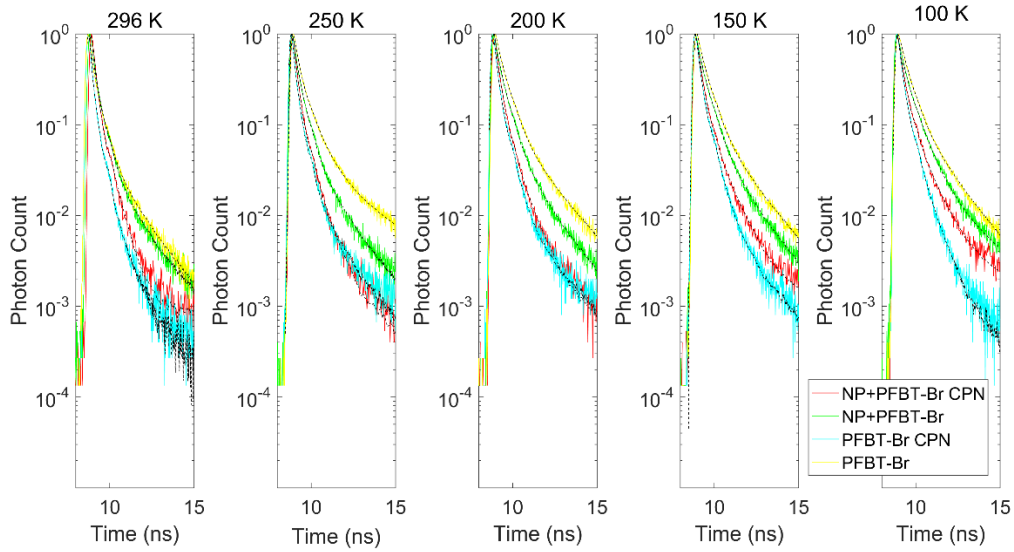


Figure 9.8. Time resolved fluorescence decay curves of PFBT-Br nanoparticles on quartz and on nanopillars, and defolded PFBT-Br polymer chains (after the addition of THF onto nanoparticles) on quartz and on nanopillars at 550 nm at temperatures 296 K, 250 K, 200 K, 150 K, and 100 K. Black lines indicate the fitted multi-exponential curves (4 exponentials). Reproduced with permission from Ref. [100]. © American Chemical Society 2013.

Table 9.2. Lifetimes (together with χ^2 -values) and energy transfer rates and efficiencies of (i) the hybrid system of the nanopillar and PFBT-Br CPNs and (ii) that of the nanopillar and PFBT-Br defolded polymer chains. τ_{DA} : lifetime of the donor in the presence of acceptor at 450 nm, τ_D : lifetime of the donor (in the absence of the acceptor) at 450 nm, and τ_A : lifetime of the acceptor (in the absence of the donor) at 550 nm.

		296 K	250 K	200 K	150 K	100 K
Nanopillar and PFBT-Br CPNs	τ_{DA} (ns) - χ^2	5.897-	8.907-	14.34-	17.622-	20.247-
	Error +/-	0.44/0.41	0.68/0.61	1.02/0.95	1.18/1.12	0.83/0.78
		8.736-	11.943-	18.34-	21.821-	23.714-
Nanopillar and PFBT-Br defolded polymer chains	τ_D (ns) - χ^2	1.097	1.041	1.084	1.009	0.993
	Error +/-	0.48/0.46	0.56/0.54	0.73/0.70	0.81/0.78	0.79/0.77
	τ_A (ns) - χ^2	0.288-	0.32-	0.352-	0.384-	0.416-

		1.017	0.987	0.940	0.914	1.098
	Error(x10 ⁻³)	7.50/7.50	9.90/7.70	13.0/12.3	18.2/17.8	19.3/19.0
	+/-					
	NRET					
	efficiency	32.5	25.5	19.7	23.8	19.4
	(%)					
	Error +/-	7.98/9.09	8.23/9.52	7.94/8.87	7.81/8.60	5.94/6.45
Nanopillar and defolded polymer chains	τ_{DA} (ns) -	7.830-	9.925-	15.410-	19.370-	22.440-
	χ^2	1.043	1.015	0.995	1.014	1.047
	Error +/-	0.65/0.61	0.68/0.64	1.08/1.00	0.38/0.38	1.17/1.09
	τ_D (ns) - χ^2	8.736-	11.943-	18.34-	21.821-	23.714-
		1.097	1.041	1.084	1.009	0.993
	Error +/-	0.48/0.46	0.56/0.54	0.73/0.70	0.81/0.78	0.79/0.77
	τ_A (ns) - χ^2	0.320-	0.384-	0.480-	0.544-	0.544-
		0.991	0.904	1.028	0.977	1.080
	Error(x10 ⁻³)	0.71/0.33	0.72/0.17	0.58/0.15	0.65/0.16	0.86/0.17
	+/-					
	NRET					
	efficiency	10.4	16.9	16.0	11.2	5.4
(%)						
Error +/-	11.3/10.4	8.81/9.93	8.43/9.41	4.85/5.10	7.48/5.37	

As the second possibility, the surface passivation issue was addressed during the preparation of samples. To eliminate this problem, nanopillar surfaces were carefully passivated *via* KOH and NH₄S surface treatment during the fabrication process. The proper passivation was verified by the increased intensity (I) of the nanopillars with respect to the planar case. We observed that the emission intensities are ordered in magnitude as $I_{before\ treatment} < I_{planar} < I_{after\ treatment}$, and the peak emission wavelength, which blue-shifts with the nanopillar etching, stays constant before and after the surface treatment, i.e., $\lambda_{planar} > \lambda_{before\ treatment} \sim \lambda_{after\ treatment}$. This means that the nanopillar etching leads to strain relaxation, which is expected to blue-shift the peak emission and increase the emission intensity. Once the nanopillars are formed, the surface treatment does not affect the spectral content of the emission, but only its intensity. This implies that the

surface states were in fact effective before the surface treatment, reducing the emission intensity substantially before passivating the pillar surfaces.

As a result, here we attribute this stronger lifetime shortening of nanopillars mainly to NRET process; however, an error analysis is still necessary. Such an analysis should be carried out considering Figure 9.6(b) and Figure 9.7 together. According to Figure 9.6(b), the minimum NRET efficiency of the nanopillar-CPN hybrid system at room temperature turns out to be higher than the maximum NRET efficiency of the defolded CPN hybrid system. At 250 and 200 K, the NRET efficiency error bars overlap more strongly, which is a consequence of the increasing NRET efficiency of the defolded CPN hybrid system together with the decrease in the NRET efficiency of the CPN hybrid system. A similar conclusion can be drawn by investigating the decay curves in Figure 9.7 where the decay curves of the both hybrid systems get closer. Nevertheless, CPN hybrid system is observed to attain a faster decaying trend at these two temperatures and at 150 and 100 K as well, although the overlap of the decays gets stronger. Considering this observation, we believe that assigning a higher NRET to CPN hybrid system is still qualitatively reasonable, especially down to 200 K, because the faster decay is a clear trend rather than noisy data points.

According to the analyses of the measured average lifetimes, the maximum NRET efficiency for the CPN hybridization is calculated to be 33% at room temperature, whereas this value drops to 10% when the nanoparticles are defolded into polymer chains *via* THF addition and evaporation. This is an indicator that here the CPNs within the nanopillars constitute a better NRET donor-acceptor pair compared to polymer chains. The absorption spectrum of CPNs yields 1.8 times higher overlap-integral [96] with the emission spectrum of nanopillars compared to that of defolded polymers (Figure 9.2(b)). However, our calculations reveal that this difference in the overlap integral can increase the NRET efficiency at most by 1.7 folds, which is not enough to explain almost 3-fold enhancement at room temperature. We reckon that the modified photophysical properties and exciton dynamics in the CPNs compared to the defolded polymer may play an important role in this observation. Other acceptor-related factors such as the refractive index and dipole orientation factors, which are closely related to the stacking, in other words, morphology of

the acceptor, should also have an important contribution to the change of the NRET efficiency.

While decreasing temperature, we further observe that NRET rate of the CPNs is a strong function of temperature (0.055 ns⁻¹ at 296 K, 0.029 ns⁻¹ at 250 K, 0.015 ns⁻¹ at 200 K, 0.011 ns⁻¹ at 150 K and 0.007 ns⁻¹ at 100 K) and NRET efficiencies of the system follow a slowly decreasing trend while taking the values of 33%, 25%, 22%, 19%, and 15% at the same temperatures, respectively (Figure 9.6). This observation can be explained by slightly stronger localization of excitons within QWs as the temperature decreases. Further investigation of the decay dynamics reveals that the lifetime of the bare nanopillar case (τ_D) increases as the temperature decreases down to 100 K. This is an expected behavior because of the suppression of the nonradiative transitions within the nanopillar as the temperature decreases. In the case that THF is added and defolded polymers are obtained, NRET rates decrease strongly to 0.013 ns⁻¹ at 296 K, 0.017 ns⁻¹ at 250 K, 0.010 ns⁻¹ at 200 K, 0.006 ns⁻¹ at 150 K, and 0.002 ns⁻¹ at 100 K, while the NRET efficiency first increases from 10% to 17% when the temperature decreases from room temperature to 250 K and remains closer to this value (16%) at 200 K. However, further decrease of temperature to 150 and 100 K decreases the NRET efficiency again down to 11% and 6%, respectively.

Nevertheless, the error bars of the NRET efficiencies calculated using the maxima and minima of the lifetimes reveal a strong overlap of the efficiencies. This prevents a healthy quantitative discussion on the change of morphology dependent energy transfer efficiency with respect to temperature. However, a qualitative analysis based on the decay curves reveals that the PFBT-Br exhibits a strong morphology-dependent energy transfer character. Based on the qualitative discussion carried out above, one can conclude that the realization of a higher NRET efficiency is highly probable with the PFBT-Br CPN hybridization of inorganic InGaN/GaN nanopillars compared to their hybridization with defolded CPNs especially at room temperature, 150 and 100 K. Here, although the change at cryogenic temperatures cannot be quantitatively assigned to the variation in the absorption due to the inability of our measurement setup, while it was possible to quantitatively relate this behavior at room temperature partly to the difference in the spectral overlap integral in

addition to other factors. We consider that the observed behavior may also occur due to the temperature related morphology changes of PFBT-Br leading to changes in its photophysical properties – mainly the available electronic states and the absorption – and the changes in the dipole orientation factor and the refractive index might contribute as well.

In the case that CPNs were hybridized and later defolded on nanopillars, we observe that the acceptor lifetimes (τ_A) increase monotonically and substantially as the temperature decreases. This can be an indicator for the dominance of the nonradiative recombinations in the films at room temperature because of the suppression of nonradiative transitions as the temperature decreases. For comparison purposes, the same lifetime characterization of PFBT-Br CPNs and polymer chains were repeated using quartz substrate. The corresponding lifetimes are shown in Figure 9.9, the tabulated values can be found in Tables 9.2 and 9.3, and the decay curves are presented in Figure 9.8. Here we observe that the lifetimes of the nanoparticles on quartz increase monotonically as the temperature decreases. This monotonic increase in the lifetime with the decreasing temperature is also consistent with the behavior of polymer chains generated by defolding the CPN structure into polymer chains. Nevertheless, the polymers exhibit much longer lifetimes compared to CPNs showing that CPN morphology enables additional nonradiative recombination pathways, whereas these pathways are suppressed in the defolded form of polymer chains on quartz. When compared with the acceptor lifetimes on nanopillars, we observe that the CPNs exhibit similar lifetimes on quartz, whereas defolded PFBT-Br films have completely different decay lifetimes. This observation clearly shows that the emission dynamics of PFBT-Br CPNs are less morphology-dependent than that of defolded PFBT-Br.

Table 9.3. Lifetimes of PFBT-Br nanoparticles and polymer chains on quartz at 550 nm.

Temperature	296 K	250 K	200 K	150 K	100 K
$\tau_{\text{PFBT-Br-CPN}}$	0.240-	0.272-	0.304-	0.336-	0.336-
(ns)- χ^2	1.074	1.084	0.972	0.993	0.937
Error ($\times 10^{-3}$) +/-	0.14/0.02	2.20/2.20	0.41/0.38	0.30/0.27	0.20/0.03
$\tau_{\text{PFBT-Br}}$ (ns)- χ^2	0.368-	0.464-	0.592-	0.608-	0.624-
	0.991	0.904	1.028	0.977	1.080
Error ($\times 10^{-3}$) +/-	0.43/0.10	0.02/0.11	0.83/0.38	0.70/0.12	1.00/0.15

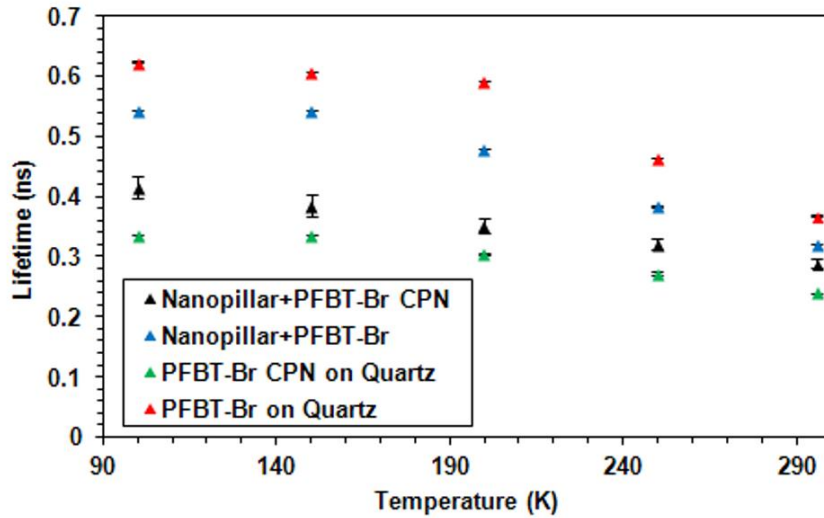


Figure 9.9. Temperature dependent fluorescence lifetimes of PFBT-Br CPNs and defolded PFBT-Br on the nanopillars and quartz. Reproduced with permission from Ref. [100]. © American Chemical Society 2013.

9.4 Summary

In this work we studied the hybrid excitonic structures of both PFBT-Br nanoparticles and their defolded polymer chains intimately integrated on the nanopillars of InGaN/GaN multiple quantum wells and investigated the

temperature dependent nonradiative energy transfer dynamics in these two hybrid architectures. We found that the nonradiative energy transfer from the quantum wells to the PFBT CPNs is more efficient compared to the defolded PFBT-Br polymer chains at the temperatures tested in this study. At room temperature, the CPNs exhibit the maximum NRET efficiency of 33% whereas this value decreases to 10% in the case of polymer chains. Another finding of this study is that the efficiency of the energy transfer decreases as the temperature decreases for the CPNs while the NRET efficiency shows an oscillating behavior in the case of defolded polymer chains. For comparison purposes, we further investigated the emission kinetics of the nanoparticles and polymer chains on the nanopillars and on a flat quartz substrate. We observed that in both type of substrates the nanoparticles reveal similar behavior. However, the open polymer chains are observed to feature significantly different emission kinetics depending on the substrate. In summary, this work demonstrates an efficient excitonic hybrid model system made of organic and inorganic nanostructured components, enabling new possibilities for future excitonic systems in light generation and harvesting as well as sensing.

Chapter 10

Conclusions

In this chapter, we present our thesis research work on the development of efficient and stable light-emitters for general lighting and display backlighting by employing colloidal semiconductors and conjugated polymer nanoparticles. Here we also list our contributions to the literature.

10.1 Contributions to scientific knowledge

Within the framework of this thesis, we studied the color science and photometry of nanoemitters with discrete and sharp emission that we use to evaluate the color quality and photometric performance of the white LEDs targeting general lighting and display backlighting applications.

In Chapter 3 of the thesis, we showed the potential of the discrete nanocrystal emitters for display backlighting applications and determined the necessary conditions for designing a display backlight of nanocrystals that helps maintaining our natural daily biological rhythm. With a focus to achieve a broader color gamut than the phosphor based LEDs, we demonstrated that the use of nanocrystals provides excellent opportunities when especially narrow green-emitting nanocrystals are employed. We also evaluated and revealed the effect of the nanocrystal based display backlights on the human biological rhythm. Our results showed that by employing strategically selected nanocrystal combinations, it is possible to improve the color definition of the displays by 34% while exhibiting 33% disruption on the biological rhythm compared phosphor based backlighting. Moreover, we found out that for a circadian rhythm friendly display backlighting, it is essential to choose the peak emission wavelengths of the blue and green color components at 465 and 535 nm, respectively with full-width at half-maximum values as narrow as 20 nm. As opposed to the requirements of the general lighting applications, surprisingly, the performance of the circadian rhythm friendly displays with a broad color gamut is not found to

require narrow emitters for the red color component. Here, for the first time in the literature we showed that employing nanocrystals for display backlighting enables obtaining a broad color gamut while minimizing the effect of the displays on the human biological rhythm at the same time. This thus leads to bio-friendly color enrichment.

The next problem, which we studied in Chapter 4 of this thesis work, was the significant energy waste of displays due to the use of polarizers with unpolarized backlighting. To address this issue, we aimed to produce polarized light and proposed the integration of magnetic nanowires together with semiconductor nanocrystals. We showed for the first time in the literature that the nanocrystals hybridized with magnetically aligned nanowires may possess polarization anisotropy despite the fact that the nanocrystals are intrinsically isotropic emitters. The obtained polarization ration of 15 shows that this material system may find a widespread use in the display industry as it significantly decreases the need for polarizers in the displays and offers a cost-effective fabrication methodology based on the magnetic alignment of the nanowires.

Subsequently, in Chapter 5 we focused on solving the low emission stability, incompatibility with the LED production line, incompatibility with the silicone encapsulants, and emission degradation at elevated temperatures and under high photon flux issues of the nanocrystals for their use on high power LED chips. As a solution, we proposed and demonstrated the incorporation of the nanocrystals into borax matrix that forms a protection layer around the nanocrystals against oxygen and humidity diffusion. We showed that these macrocrystals can be easily powdered and they can maintain their emission capabilities when integrated with silicones. With this approach, we solved the compatibility issues of the nanocrystals with the existing LED production line and with the commonly used silicones. Using the powders of these macrocrystals of nanocrystals and designing the device structure providing feedback from experiments and photometric calculations, we also demonstrated the most photometrically efficient white LED of the world, to the best of our knowledge. We further showed that this material system is also capable of solving the thermal stability and photostability problems of the nanocrystal emission when integrated with a high power LED. Considering all these findings, we believe

that the results of this work opened the way for a widespread use of nanocrystals in salt matrices for general lighting applications.

In Chapter 6, to increase the quantum efficiency of the nanocrystals in solid form we studied the potential of using plasmonic interaction. Within this framework, we successfully maintained the plasmonic character of the metal nanoparticles in sucrose matrix as opposed to salt matrices causing the aggregation of the metal nanoparticles. Protecting this plasmonic character was shown to enable plasmonic fluorescence enhancement of semiconductor nanocrystals upon their co-immobilization with metal nanocrystals. We found that the occurrence of this interaction requires a careful optimization of the semiconductor nanocrystal and metal nanoparticle concentrations. Another point that deserves attention regarding these plasmonic macrocrystals is the fact that a solid and robust plasmonic material system was made possible for the first time. In this work, we showed that plasmonic interaction may be conveniently utilized to improve the emission capability of the nanocrystals within macrocrystals and this material system may be employed as color converters for light-emitting diodes.

The straightforward techniques for preparing macrocrystals required the nanocrystals to be dispersed in aqueous environment. This necessitates the synthesis of the nanocrystals in water or a ligand exchange is needed. However, the quantum efficiency of the nanocrystals synthesized in water remains typically low and the ligand exchange of the nanocrystals is known to substantially decrease the quantum yield of the synthesized semiconductor nanocrystals. To avoid this decreasing efficiency problem so that the fabrication of efficient nanocrystal integrated LEDs becomes possible, in Chapter 7 of this thesis, we showed our novel methodology that involves the evaporation of the nanocrystal dispersion and LiCl solution mixture in tetrahydrofuran in vacuum. This method enabled the incorporation of the nanocrystals into the salt matrix without requiring ligand exchange process for the first time and allowed for maintaining the quantum efficiency of the nanocrystals in salt powders. We also showed that the emission stability of the nanocrystals at high temperatures and under high photon flux is also improved significantly within salt matrix. Considering all of these achievements we showed that this technique solves an important problem

of the nanocrystal incorporation into salts and makes this material system ready for use in LED fabrication.

In Chapter 8 of this thesis work, we investigated the potential of nonradiative energy transfer between the nanocrystals incorporated into salt matrix to further improve the nanocrystal emission. For this purpose, we utilized green- and red-emitting nanocrystal quantum dots within LiCl matrix and proved the occurrence of the exciton transfer by using steady state and time-resolved fluorescence spectroscopy for the first time. These excitonically improved nanocrystal integrated salt powders were integrated with a blue LED to form a violet LED that exhibited luminous efficiencies $>70 \text{ lm/W}_{\text{elect}}$, which are higher than the performance of the epitaxially grown violet LEDs. These excitonically improved powders are robust, their emission is stable, and they can be easily integrated with LEDs; therefore, we believe that they are excellent candidates for use in LEDs as color converters.

As part of the efforts for obtaining efficient soft color converters without cadmium content, in Chapter 9 we utilized the nonradiative energy transfer for improving the emission capabilities of the conjugated polymer nanoparticles. For this purpose, we used InGaN/GaN quantum well nanopillars as the donors and investigated the dependence of the energy transfer on the nanoparticle morphology by dissolving the nanoparticle in situ to obtain their polymers. We discovered that the conjugated polymer nanoparticles construct a better nonradiative energy transfer pair with the InGaN/GaN nanopillars compared to their polymer form. Our investigations revealed that the reason behind this observation is the improvement of the absorption capabilities of the nanoparticles compared to their de-folded polymer chains. We believe that this material system has the potential to be employed for excitonically improved light harvesting and generation applications if their emission stability problem is addressed in addition to compatibility issues with the LED fabrication techniques.

Overall, during this graduate study at Bilkent University we carried out research at the interface of electrical engineering, physics, chemistry, and materials science. We designed, implemented, and characterized light-emitting

devices for lighting and display applications with a special emphasis on increasing their efficiency and stability. For this purpose, we also investigated the near-field dynamics within various material systems. We showed that using nano-emitters the present disadvantages for generating high quality white light of using rare-earth ion based color converting phosphors can be overcome. Furthermore, the studies that we presented here enabled to solve the existing problems of the colloidal nano-emitters and improved their performance so that they can find ubiquitous use in high-quality and high-efficiency light-emitting devices.

10.2. Contributions to the literature

Below we list the SCI journal papers, refereed conference presentations, book chapters, and patents that we contributed during the graduate study at Bilkent University.

SCI Journal Publications:

1. **T. Erdem** and H. V. Demir, “Colloidal photonics of nanocrystals for light sources and displays: milestones and recent developments” *Nanophotonics* 5, 74 (2016).
2. **T. Erdem**, Z. Soran-Erdem, P. L. Hernandez-Martinez, V. K. Sharma, H. Akcali, I. Akcali, N. Gaponik, A. Eychmüller, H. V. Demir, “Sweet plasmonics: Sucrose macrocrystals of metal nanoparticles,” *Nano Research* 8, 860-869 (2015).
3. **T. Erdem**, Y. Kelestemur, Z. Soran-Erdem, Y. Ji, H. V. Demir, “Energy-saving quality road lighting with colloidal quantum dot nanophosphors” *Nanophotonics* 3, 373-381 (2014). *Selected as cover article*
4. **T. Erdem**, V. Ibrahimova, D. W. Jeon, I. H. Lee, D. Tuncel, H. V. Demir, “Morphology-dependent energy transfer of polyfluorene nanoparticles decorating InGaN/GaN quantum-well nanopillars,” *J. Phys. Chem. C* 117, 18613-18619 (2013).

5. **T. Erdem** and H. V. Demir, "Color science of nanocrystal quantum dots for lighting and displays," *Nanophotonics* 2, 57-81 (2013). *Selected as cover article*
6. **T. Erdem**, S. Nizamoglu, and H. V. Demir, "Computational study of power conversion and luminous efficiency performance for semiconductor quantum dot nanophosphors on light-emitting diode," *Optics Express* 20, 3275-3295 (2012).
7. **T. Erdem** and H. V. Demir, "Semiconductor nanocrystals as rare-earth alternatives," *Nature Photon.* 5, 126 (2011) (Letter).
8. **T. Erdem**, S. Nizamoglu, X.W. Sun, and H. V. Demir, "A photometric investigation of ultra-efficient LEDs with high color rendering index and high luminous efficacy employing nanocrystal quantum dot luminophores," *Optics Express* 18, 340 (2010).
9. **T. Erdem***, Z. Soran-Erdem*, Y. Kelestemur, N. Gaponik and H. V. Demir, "Excitonic improvement of colloidal nanocrystals in salt powder matrix for quality lighting and color enrichment," *Optics Express* 24, A74 (2016). *Equal contribution
10. **T. Erdem***, Z. Soran-Erdem*, V. K. Sharma, Y. Kelestemur, M. Adam, N. Gaponik and H. V. Demir, "Stable and efficient colour enrichment powders of nonpolar nanocrystals in LiCl," *Nanoscale* 7, 17611 (2015). *Selected as cover article*, *Equal contribution
11. Z. Soran-Erdem*, **T. Erdem***, K. Gungor, J. Pennakalathil, D. Tuncel, H. V. Demir, "High-stability, high-efficiency organic monoliths made of oligomer nanoparticles wrapped in organic matrix," *ACS Nano* 10, 5333 (2016). *Equal contribution
12. M. Adam*, **T. Erdem***, G. Stachowski, Z. Soran-Erdem, J. Lox, C. Bauer, J. Poppe, H. V. Demir, N. Gaponik, A. Eychmüller, "Implementation of high-quality warm-white light-emitting diodes by a model-experimental feedback approach using quantum dot-salt mixed crystals," *ACS Appl. Mater. Inter.* 7, 23364 (2015).
13. Z. Soran-Erdem*, **T. Erdem***, P. L. Hernandez-Martinez, M. Z. Akgul, N. Gaponik, H. V. Demir, "Macrocrystals of colloidal quantum dots in anthracene: exciton transfer and polarized emission," *J. Phys. Chem. Lett.* 6, 1767-1772 (2015).

14. C. Uran, **T. Erdem**, B. Guzelturk, N. Kosku Perkgöz, S. Jun, E. Jang, H. V. Demir, “Highly polarized light emission by isotropic quantum dots integrated with magnetically aligned segmented nanowires,” *Appl. Phys. Lett.* 105, 141116 (2014).
15. Y. Ji, W. Liu, **T. Erdem**, R. Chen, S. T. Tan, Z. H. Zhang, Z. G. Ju, X. L. Zhang, H. D. Sun, X. W. Sun, Y. J. Zhao, S. P. DenBaars, S. Nakamura, H. V. Demir, “Comparative study of field-dependent carrier dynamics and emission kinetics of InGaN/GaN light-emitting diodes grown on (1122) semipolar versus (0001) polar planes,” *Appl. Phys. Lett.* 104, 143506 (2014).
16. S. Nizamoglu, **T. Erdem**, X. W. Sun, and H. V. Demir, “Warm-white light-emitting diodes integrated with colloidal quantum dots for high luminous efficacy and color rendering: reply to comment,” *Optics Letters* 36, 15, 2852 (2011).
17. E.-J. Park, **T. Erdem**, V. Ibrahimova, S. Nizamoglu, H. V. Demir, and D. Tuncel, “White-emitting conjugated polymer nanoparticles with cross-linked shell for mechanical stability and controllable photometric properties in color-conversion LED applications,” *ACS Nano* 5, 2483 (2011).
18. S. Nizamoglu, **T. Erdem**, and H. V. Demir, “High scotopic/photopic ratio white-light-emitting diodes integrated with semiconductor nanophosphors of colloidal quantum dots,” *Optics Letters* 36, 1893 (2011).
19. S. Nizamoglu, **T. Erdem**, X. W. Sun, and H. V. Demir, “Warm-white light-emitting diodes integrated with colloidal quantum dots for high luminous efficacy and color rendering,” *Optics Letters* 35, 20, 3372 (2010).
20. V. K. Sharma, B. Guzelturk, **T. Erdem**, Y. Kelestemur, H. V. Demir, “Tunable white-light-emitting Mn-doped ZnSe nanocrystals,” *ACS Appl. Mater. Interfaces* 6, 3654-3660 (2014).
21. H. V. Demir, S. Nizamoglu, **T. Erdem**, E. Mutlugun, N. Gaponik, and A. Eychmüller, “Quantum dot integrated LEDs using photonic and excitonic color conversion,” *Nano Today* 6, 632 (2011).

22. H. Keita, B. Guzelturk, J. Pennakalathil, **T. Erdem**, H. V. Demir, D. Tuncel, "Construction of multi-layered white emitting core-shell type nanoparticles by clicking light emitting polymers," *J. Mater. Chem. C* 3, 10277 (2015).
23. S. Delikanli, B. Guzelturk, P. L. Hernández-Martínez, **T. Erdem**, Y. Kelestemur, M. Olutas, M. Z. Akgul and H. V. Demir, "Continuously Tunable Emission in Inverted Type-I CdS/CdSe Core/Crown Semiconductor Nanoplatelets" *Adv. Funct. Mater.* 25, 4282-4289 (2015).
24. V.K. Sharma, S. Gokyar, Y. Kelestemur, **T. Erdem**, E. Unal, H. V. Demir, "Manganese doped fluorescent paramagnetic nanocrystals for dual-modal imaging," *Small* 10, 4961-4966 (2014).
25. E. Mutlugun, P. L. Hernandez-Martinez, C. Eroglu, Y. Coskun, **T. Erdem**, V. K. Sharma, E. Unal, S. K. Panda, S. G. Hickey, N. Gaponik, A. Eychemüller, and H. V. Demir, "Large-area (over 50 cm × 50 cm) freestanding films of colloidal InP/ZnS quantum dots" *Nano Letters* 12, 3986-3993 (2012).

International Conferences:

1. Z. Soran-Erdem, **T. Erdem**, P. L. Hernandez-Martinez, M. Z. Akgul, N. Gaponik, H. V. Demir, "Macrocrystals of colloidal quantum dots in anthracene: Exciton transfer and polarized emission," *APS Meeting*, Baltimore, Maryland, USA, March 2016.
2. P. L. Hernandez-Martinez, S. Delikanli, B. Guzelturk, **T. Erdem**, Y. Kelestemur, M. Olutas, M. Z. Akgul, H. V. Demir, "Tunable Emission in Inverted Type-I CdS/CdSe Core/Crown Semiconductor Nanoplatelets," *APS Meeting*, Baltimore, Maryland, USA, March 2016.
3. **T. Erdem**, Y. Kelestemur, Z. Soran-Erdem, Y. Ji, H. V. Demir, "High-efficiency high-quality street lighting with colloidal quantum dot nanophosphors," *IEEE Photonics Conference*, Reston, VA, USA, October 2015.
4. Z. Soran-Erdem, **T. Erdem**, P. L. Hernandez-Martinez, M. Z. Akgul, N. Gaponik, H. V. Demir, "Exciton transfer and polarized emission in colloidal quantum dot – anthracene crystals," *IEEE Photonics Conference*, Reston, VA, USA, October 2015.

5. P. L. Hernandez-Martinez, **T. Erdem**, Z. Soran-Erdem, V. K. Sharma, H. Akcali, I. Akcali, N. Gaponik, A. Eychmüller, H. V. Demir, "Sweet plasmonics: Sucrose macrocrystals of metal nanoparticles" *APS Meeting*, San Antonio, Texas, USA, March 2015.
6. **T. Erdem** and H. V. Demir, "Biological rhythm friendly display backlighting with nanocrystals" *N4E Plenary Meeting*, Barcelona, Spain, December 2014.
7. **T. Erdem** and H. V. Demir, "Quality lighting with nanocrystal color enrichment" *Forum LED*, Paris, France, November 2014.
8. C. Uran, **T. Erdem**, and H. V. Demir, "Arrays of suspended plasmonic nanodiscs," *IEEE Photonics Conference*, Bellevue, WA, USA, September 2013.
9. **T. Erdem**, Z. Soran-Erdem, P. L. Hernandez-Martinez, V. K. Sharma, N. Gaponik, A. Eychmüller, and H. V. Demir, "Macrocrystals of co-immobilized semiconductor nanocrystals and metal nanoparticles," *NANAX 6*, Bad Hofgastein, Salzburg, Austria, May 2014.
10. **T. Erdem** and H. V. Demir, "Nanocrystal optoelectronics for semiconductor lighting and lasing," *N4E Plenary Meeting*, Stockholm, Sweden, November 2013.
11. **T. Erdem**, S. Nizamoglu, and H. V. Demir, "Power conversion and luminous efficiency performance of nanophosphor quantum dots on color-conversion LEDs for high-quality general lighting," *SPIE Photonics West*, San Francisco, CA, USA, January 2012.
12. E. Mutlugun, P. L. Hernandez Martinez, C. Eroglu, Y. Coskun, **T. Erdem**, V. K. Sharma, E. Unal, S. K. Panda, S. G. Hickey, N. Gaponik, A. Eychmüller, H. V. Demir, "Large-area ($> 50 \text{ cm} \times 50 \text{ cm}$), freestanding, flexible, optical membranes of Cd-free nanocrystal quantum dots," *IEEE Photonics Conference*, Burlingame, CA, USA, September 2012.
13. **T. Erdem**, S. Nizamoglu, and H. V. Demir, "Efficient and high quality warm white light generation using colloidal semiconductor quantum dots," *N4E Plenary Meeting*, Stockholm, Sweden, June 2011.
14. S. Nizamoglu, **T. Erdem**, X. W. Sun, and H. V. Demir, "Superior warm-white light-emitting diodes integrated with quantum dot nanophosphors

for high luminous efficacy and color rendering," *CLEO/IQEC Baltimore*, Maryland, USA, May 2011.

15. **T. Erdem**, S. Nizamoglu, and H. V. Demir, "Warm-white color-converting nanophosphors of semiconductor nanocrystals with high color rendering index and high luminous efficacy," *Proceedings of 23rd IEEE Annual Photonics Society Meeting*, Denver, CO, USA, November 2010.
16. B. Guzelturk, **T. Erdem**, E. Unal, S. Nizamoglu, D. Tuncel, and H. V. Demir, "Non-radiative energy-transfer-driven quantum dot LEDs," *Proceedings of 23rd IEEE Annual Photonics Society Meeting*, Denver, CO, USA, November 2010.

Other publications:

1. H. V. Demir, **T. Erdem**, S. Nizamoglu, and X. W. Sun, "Photometric design of color-conversion LEDs," SPIE Newsroom (2011).

Patents:

1. H. V. Demir, B. Guzelturk, E. J. Jang, C. Uran, **T. Erdem**, K. Gungor, "Optical elements and electronic devices including the same" Korean Patent, European Patent, and US Patent (20,160,027,963).

Book Chapter:

1. **T. Erdem** and H. V. Demir, "On-chip integration of functional hybrid materials and components in nanophotonics and optoelectronics," in *Ceramic Integration and Joining Technologies, From Macro to Nanoscale*, ed. M. Singh, T. Ohji, R. Asthana and S. Mathur, *John Wiley & Sons* (2011).

10.3 Challenges and future outlook

There are still some challenges of employing colloidal nanocrystals for solid-state lighting applications. Among them, the most well-known issue is the cadmium content of the efficient nanocrystals. To avoid the health and environmental risks of these materials, either a proper recycling method has to be developed or

proper cadmium-free alternatives have to be synthesized. The existing inorganic cadmium-free nanocrystals possess significantly lower efficiencies compared to their cadmium-containing counterparts. Furthermore, their emission spectra are significantly broader. Therefore, even if we can increase their efficiencies using methods such as incorporation into macrocrystals or near-field interactions, their emission spectra should be definitely narrowed. Otherwise, high-quality lighting cannot be realized using these materials. As an alternative, developing cadmium-free colloidal quantum wells may step forward if they can be made efficiently emitting. In addition to inorganic nano-emitters, the use of organic nanoparticles may also be utilized for solid-state lighting. However, their emission spectra have to be narrowed before they can be employed ubiquitously in solid-state lighting.

Another important issue related with the use of colloidal nanoparticles in solid-state lighting is the need for a significant amount of materials for integration on an LED, which makes it difficult to incorporate their powders on the LEDs. This basically stems from the relatively low absorption coefficients of the quantum dots. As a solution to this problem, the use of colloidal nanoplatelets or perovskites can be offered. Another advantage of using these materials is the possibility of achieving significantly narrow emission spectra enabling photometric optimization. However, the main difficulty of using these materials is the significant decrease in their efficiencies in their solid-films. This problem may be addressed in the future by incorporating them into crystalline matrices. Nevertheless, both of these materials are very sensitive to the variations in their environments. Therefore, novel methods need to be developed to embed them into macrocrystals.

In addition to the existing challenges of these materials, the methods that we developed here also offer unique opportunities. For example, we believe that the presented macrocrystal approach may be very important for optical gain and lasing applications in the future if the nanocrystals could be integrated in higher concentrations. Furthermore, the smart self-assembly methods may enable the formation of robust metamaterials inside a solid crystalline matrix and it would be also possible to produce some exotic optical components or even devices. These macrocrystals can be also very beneficial when they are used on solar cells for spectral concentration of the sun light. Considering that the macrocrystals

offer a robust platform for near-field interactions, they can be an interesting platform for studying nonlinear, plasmonic, and excitonic interactions involving various types of nanomaterials.

We believe that the challenges that are presented above may be addressed in the near-future by using the materials systems we presented here. Furthermore, the opportunities listed above should be able to be realized following the improvements in the structural and optical features of the nanomaterials. Considering these, we think that within the next decade we will witness an increasing use of the colloidal nanomaterials in optoelectronic devices including light-emitting diodes, displays, lasers, solar cells, photodetectors, and sensors.

Bibliography

- [1] UNESCO and DPG, “Jahr des Lichtes.” .
- [2] UNESCO, “The International Year of Light,” 2014. .
- [3] J. M. Phillips, M. E. Coltrin, M. H. Crawford, A. J. Fischer, M. R. Krames, R. Mueller-Mach, G. O. Mueller, Y. Ohno, L. E. S. Rohwer, J. A. Simmons, and J. Y. Tsao, “Research challenges to ultra-efficient inorganic solid-state lighting,” *Laser Photonics Rev.*, vol. 1, no. 4, p. 307, Dec. 2007.
- [4] M. R. Krames, O. B. Shchekin, R. Mueller-Mach, G. O. Mueller, L. Zhou, G. Harbers, and M. G. Craford, “Status and Future of High-Power Light-Emitting Diodes for Solid-State Lighting,” *J. Disp. Technol.*, vol. 3, no. 2, pp. 160–175, Jun. 2007.
- [5] US Department of Energy, “How much electricity is used for lighting in the United States?” [Online]. Available: <https://www.eia.gov/tools/faqs/faq.cfm?id=99&t=3>. [Accessed: 14-Jun-2010].
- [6] US Department of Energy, “Energy Savings Forecast of Solid-State Lighting in General Illumination Applications,” 2014.
- [7] US Department of Energy, “How Energy-Efficient Light Bulbs Compare with Traditional Incandescents.” [Online]. Available: <http://energy.gov/energysaver/how-energy-efficient-light-bulbs-compare-traditional-incandescents>. [Accessed: 14-Jun-2016].
- [8] R. Müller-Mach, G. O. Müller, M. R. Krames, and T. Trottier, “High-power phosphor-converted light-emitting diodes based on III-Nitrides,” *IEEE J. Sel. Top. Quantum Electron.*, vol. 8, no. 2, p. 339, 2002.
- [9] O. Graydon, “The new oil?,” *Nat. Photonics*, vol. 5, no. 1, p. 1, Jan. 2011.
- [10] T. Erdem and H. V. Demir, “Semiconductor nanocrystals as rare-earth alternatives,” *Nat. Photonics*, vol. 5, no. 1, p. 126, 2011.
- [11] T. Erdem, S. Nizamoglu, X. W. Sun, and H. V. Demir, “A photometric investigation of ultra-efficient LEDs with high color rendering index and

- high luminous efficacy employing nanocrystal quantum dot luminophores.,” *Opt. Express*, vol. 18, no. 1, pp. 340–7, Jan. 2010.
- [12] T. Erdem and H. V. Demir, “Color science of nanocrystal quantum dots for lighting and displays,” *Nanophotonics*, vol. 2, no. 1, pp. 57–81, 2013.
- [13] E. Jang, S. Jun, H. Jang, J. Lim, B. Kim, and Y. Kim, “White-light-emitting diodes with quantum dot color converters for display backlights.,” *Adv. Mater.*, vol. 22, no. 28, pp. 3076–3080, Jul. 2010.
- [14] Z. Luo, Y. Chen, and S.-T. Wu, “Wide color gamut LCD with a quantum dot backlight.,” *Opt. Express*, vol. 21, no. 22, pp. 26269–84, 2013.
- [15] D. Tuncel and H. V. Demir, “Conjugated polymer nanoparticles.,” *Nanoscale*, vol. 2, no. 4, pp. 484–494, 2010.
- [16] T. Erdem and H. V. Demir, “Colloidal nanocrystals for quality lighting and displays: milestones and recent developments,” *Nanophotonics*, vol. 5, no. 1, pp. 74–95, 2016.
- [17] F. W. Billmeyer, “Color Science: Concepts and Methods, Quantitative Data and Formulae, 2nd ed., by Gunter Wyszecki and W. S. Stiles, John Wiley and Sons, New York, 1982, 950 pp. Price: \$75.00,” *Color Res. Appl.*, vol. 8, no. 4, pp. 262–263, 1983.
- [18] Webvision, “The Organization of the Retina and Visual System.” [Online]. Available: <http://webvision.med.utah.edu/book/part-i-foundations/simple-anatomy-of-the-retina/>. [Accessed: 01-Jun-2016].
- [19] J. E. Dowling, “Organization of the vertebrate retina.,” *Nihon Seirigaku Zasshi.*, vol. 32, pp. 546–547, 1970.
- [20] E. F. Schubert, *Light-Emitting Diodes - 2nd Edition*. Cambridge University Press, 2006.
- [21] Osram Sylvania Corporation, “Lumens and mesopic vision,” 2000.
- [22] L. B. Johnson, “Upper limit of mesopic vision,” *Trans. Illum. Eng. Soc.*, vol. 32, pp. 646–650, 1937.
- [23] Y. LeGrand, *Handbook of sensory physiology. Vol. VII/4 Visual psychophysics*. Berlin: Springer-Verlag, 1972.

- [24] S. Kokoschka, “Das $V(\lambda)$ -Dilemma in der Photometrie,” in *Proceedings of 3. Internationales Forum für den lichttechnischen Nachwuchs*, 1997.
- [25] IESNA Illuminating Engineering Society of North America, *IESNA lighting handbook: reference and application*. New York: IESNA, 2000.
- [26] C. C. Bureau, “CIE 41:1978. Light as a true visual quantity: principles of measurement,” Vienna, 1978.
- [27] M. S. Rea, J. D. Bullough, J. P. Freyssinier-Nova, and A. Bierman, “A proposed unified system of photometry,” *Light. Res. Technol.*, vol. 36, no. 2, pp. 85–109, 2004.
- [28] M. Eloholma, M. Viikari, L. Halonen, H. Walkey, T. Goodman, J. Alferdinck, a Freiding, P. Bodrogi, and G. Várady, “Mesopic models—from brightness matching to visual performance in night-time driving: a review,” *Light. Res. Technol.*, vol. 37, no. 2, pp. 155–175, 2005.
- [29] T. Goodman, a Forbes, H. Walkey, M. Eloholma, L. Halonen, J. Alferdinck, a Freiding, P. Bodrogi, G. Varady, and a Szalmas, “Mesopic visual efficiency IV: a model with relevance to nighttime driving and other applications,” *Light. Res. Technol.*, vol. 39, no. 4, pp. 365–392, 2007.
- [30] “CIE Technical Report 191:2010. Recommended system for mesopic photometry based on visual performance,” Vienna, 2010.
- [31] S. Hattar, H. W. Liao, M. Takao, D. M. Berson, and K. W. Yau, “Melanopsin-containing retinal ganglion cells: architecture, projections, and intrinsic photosensitivity,” *Science (80-.)*, vol. 295, no. 5557, pp. 1065–1070, 2002.
- [32] D. M. Berson, F. A. Dunn, and M. Takao, *Phototransduction by retinal ganglion cells that set the circadian clock*, vol. 295, no. 557. 2002.
- [33] M. G. Figueiro and M. S. Rea, “Lack of short-wavelength light during the school day delays dim light melatonin onset (DLMO) in middle school students,” *Neuroendocrinol. Lett.*, vol. 31, no. 1, pp. 92–96, 2010.
- [34] M. S. Rea, M. G. Figueiro, A. Bierman, and J. D. Bullough, “Circadian light.,” *J. Circadian Rhythms*, vol. 8, no. 1, p. 2, 2010.

- [35] D. Gall, “Die Messung circadianer Strahlungsgrößen,” in *Proceedings of 3. Internationales Forum fur den lichttechnischen Nachwuchs*, 2004.
- [36] J. Al Enezi, V. Revell, T. Brown, J. Wynne, L. Schlangen, and R. Lucas, “A ‘melanopic’ spectral efficiency function predicts the sensitivity of melanopsin photoreceptors to polychromatic lights.,” *J. Biol. Rhythms*, vol. 26, no. 4, pp. 314–323, 2011.
- [37] T. M. Brown, J. Wynne, H. D. Piggins, and R. J. Lucas, “Multiple hypothalamic cell populations encoding distinct visual information.,” *J. Physiol.*, vol. 589, no. Pt 5, pp. 1173–94, 2011.
- [38] G. C. Brainard, J. P. Hanifin, J. M. Greeson, B. Byrne, G. Glickman, E. Gerner, and M. D. Rollag, “Action spectrum for melatonin regulation in humans: evidence for a novel circadian photoreceptor.,” *J. Neurosci.*, vol. 21, no. 16, pp. 6405–12, 2001.
- [39] K. Thapan, J. Arendt, and D. J. Skene, “An action spectrum for melatonin suppression: Evidence for a novel non-rod, non-cone photoreceptor system in humans,” *J. Physiol.*, vol. 535, no. 1, pp. 261–267, 2001.
- [40] M. Rea, M. Figueiro, A. Bierman, and R. Hamner, “Modelling the spectral sensitivity of the human circadian system,” *Light. Res. Technol.*, vol. 44, no. 4, pp. 386–396, 2011.
- [41] “CIE Commission Proceedings,” 1931.
- [42] I. C. A. Sandu, T. Busani, and M. H. De Sá, “The surface behavior of gilding layer imitations on polychrome artefacts of cultural heritage,” *Surf. Interface Anal.*, vol. 43, no. 8, pp. 1171–1181, 2011.
- [43] P. S. T. Raynham, “White light and facial recognition,” *Light. J.*, vol. 68, pp. 29–33, 2003.
- [44] “What is Color Rendering Index (CRI)?” [Online]. Available: <http://www.technolamp.com/faqs/>. [Accessed: 01-Jun-2016].
- [45] “CIE publication No. 15 – Colorimetry,” 1971.
- [46] “CIE publication No. 13.3 - Method of measuring and specifying color-

rendering of light sources,” 1995.

- [47] W. Davis and Y. Ohno, “Color quality scale,” *Opt. Eng.*, vol. 49, no. 3, p. 033602, 2010.
- [48] Y. Ohno and W. Davis, “Rationale of Color Quality Scale,” *Energy*, pp. 1–9, 2010.
- [49] Y. Ohno, “Color Quality of White LEDs,” *Top. Appl. Phys.*, vol. 126, pp. 349–371, 2013.
- [50] S. V. Gaponenko, *Optical Properties of Semiconductor Nanocrystals*. Cambridge University Press, 2005.
- [51] S. V. Gaponenko, *Introduction to Nanophotonics*. Cambridge University Press, 2010.
- [52] P. Reiss, M. Protière, and L. Li, “Core/shell semiconductor nanocrystals,” *Small*, vol. 5, no. 2. pp. 154–168, 2009.
- [53] N. Gaponik, S. G. Hickey, D. Dorfs, A. L. Rogach, and A. Eychmüller, “Progress in the light emission of colloidal semiconductor nanocrystals,” *Small*, vol. 6, no. 13. pp. 1364–1378, 2010.
- [54] X. Wang, X. Yan, W. Li, and K. Sun, “Doped quantum dots for white-light-emitting diodes without reabsorption of multiphase phosphors,” *Adv. Mater.*, vol. 24, no. 20, pp. 2742–2747, 2012.
- [55] N. Gaponik, D. V Talapin, A. L. Rogach, K. Hoppe, E. V Shevchenko, A. Kornowski, A. Eychmüller, and H. Weller, “Thiol-Capping of CdTe Nanocrystals: An Alternative to Organometallic Synthetic Routes,” *J. Phys. Chem. B*, vol. 106, no. 29, pp. 7177–7185, Jul. 2002.
- [56] W. K. Bae, K. Char, H. Hur, and S. Lee, “Single-step synthesis of quantum dots with chemical composition gradients,” *Chem. Mater.*, vol. 20, no. 2, pp. 531–539, 2008.
- [57] T. Erdem, S. Nizamoglu, X. W. Sun, and H. V. Demir, “A photometric investigation of ultra-efficient LEDs with high color rendering index and high luminous efficacy employing nanocrystal quantum dot luminophores,” *Opt. Express*, vol. 18, no. 1, pp. 340–347, 2010.

- [58] H. V. Demir, S. Nizamoglu, T. Erdem, E. Mutlugun, N. Gaponik, and A. Eychmüller, “Quantum dot integrated LEDs using photonic and excitonic color conversion,” *Nano Today*, vol. 6, no. 6, pp. 632–647, Dec. 2011.
- [59] T. Erdem, Y. Kelestemur, Z. Soran-Erdem, Y. Ji, and H. V. Demir, “Energy-saving quality road lighting with colloidal quantum dot nanophosphors,” *Nanophotonics*, vol. 3, no. 6, 2014.
- [60] T. Erdem, S. Nizamoglu, and H. V. Demir, “Computational study of power conversion and luminous efficiency performance for semiconductor quantum dot nanophosphors on light-emitting diodes,” *Opt. Express*, vol. 20, no. 3, pp. 3275–95, Jan. 2012.
- [61] ANSI, “American National Standard for Electric Lamps—Specifications for the Chromaticity of Solid State Lighting (SSL) Products,” 2008.
- [62] H.-F. Meng, “Overview of Semiconducting Conjugated Polymers,” in *Polymer Electronics*, H.-F. Meng, Ed. Stanford Publishing Pte. Ltd., 2013.
- [63] L. Feng, C. Zhu, H. Yuan, L. Liu, F. Lv, and S. Wang, “Conjugated polymer nanoparticles: preparation, properties, functionalization and biological applications,” *Chem. Soc. Rev.*, vol. 42, no. 16, pp. 6620–33, 2013.
- [64] E. J. Park, T. Erdem, V. Ibrahimova, S. Nizamoglu, H. V. Demir, and D. Tuncel, “White-emitting conjugated polymer nanoparticles with cross-linked shell for mechanical stability and controllable photometric properties in color-conversion LED applications,” *ACS Nano*, vol. 5, no. 4, pp. 2483–2492, 2011.
- [65] T.-Q. Nguyen, I. B. Martini, J. Liu, and B. J. Schwartz, “Controlling Interchain Interactions in Conjugated Polymers: The Effects of Chain Morphology on Exciton–Exciton Annihilation and Aggregation in MEH–PPV Films,” *J. Phys. Chem. B*, vol. 104, no. 2, pp. 237–255, 2000.
- [66] C. Szymanski, C. F. Wu, J. Hooper, M. A. Salazar, A. Perdomo, A. Dukes, and J. McNeill, “Single molecule nanoparticles of the conjugated polymer MEH-PPV, preparation and characterization by near-field scanning optical microscopy,” *J. Phys. Chem. B*, vol. 109, no. 18, pp. 8543–8546, 2005.

- [67] I. O. Hoyal, T. Ozel, U. Koldemir, S. Nizamoglu, D. Tuncel, and H. V. Demir, "White emitting polyfluorene functionalized with azide hybridized on near-UV light emitting diode for high color rendering index.," *Opt. Express*, vol. 16, no. 2, pp. 1115–1124, 2008.
- [68] I. O. Hoyal, U. Koldemir, T. Ozel, H. V. Demir, and D. Tuncel, "On the origin of high quality white light emission from a hybrid organic/inorganic light emitting diode using azide functionalized polyfluorene," *J. Mater. Chem.*, vol. 18, no. 30, p. 3568, 2008.
- [69] H. Keita, B. Guzelturk, J. Pennakalathil, T. Erdem, H. V. Demir, and D. Tuncel, "Construction of multi-layered white emitting organic nanoparticles by clicking polymers," *J. Mater. Chem. C*, vol. 3, no. 39, pp. 10277–10284, 2015.
- [70] I. Fischer and A. P. H. J. Schenning, "Nanoparticles Based on π Conjugated Polymers and Oligomers for Optoelectronic, Imaging, and Sensing Applications: The Illustrative Example of Fluorene-Based Polymers and Oligomers," in *Organic Electronics: Emerging Concepts and Technologies*, C. Cicoira, Fabio; Santato, Ed. Wiley-VCH Verlag GmbH & Co. KGaA, 2013, pp. 1–25.
- [71] R. . S. de List, E.J.; Guentner and U. Freitas, P.; Scherf, "The Effect of Keto Defect Sites on the Emission Properties of Polyfluorene-Type Materials," *Adv. Mater.*, vol. 14, no. 5, pp. 374–378, 2002.
- [72] T. Kietzke, D. Neher, M. Kumke, O. Ghazy, U. Ziener, and K. Landfester, "Phase separation of binary blends in polymer nanoparticles," *Small*, vol. 3, no. 6, pp. 1041–1048, 2007.
- [73] K. B. Burke, A. J. Stapleton, B. Vaughan, X. Zhou, a L. D. Kilcoyne, W. J. Belcher, and P. C. Dastoor, "Scanning transmission x-ray microscopy of polymer nanoparticles: probing morphology on sub-10 nm length scales.," *Nanotechnology*, vol. 22, no. 26, p. 265710, 2011.
- [74] J. Gao and J. K. Grey, "Spectroscopic studies of energy transfer in fluorene co-polymer blend nanoparticles," *Chem. Phys. Lett.*, vol. 522, pp. 86–91, 2012.
- [75] C. M. Davis, E. S. Childress, and E. J. Harbron, "Ensemble and single-particle fluorescence photomodulation in diarylethene-doped conjugated

- polymer nanoparticles,” *J. Phys. Chem. C*, vol. 115, no. 39, pp. 19065–19073, 2011.
- [76] Z. Tian, W. Wu, and A. D. Q. Li, “Photoswitchable fluorescent nanoparticles: preparation, properties and applications,” *ChemPhysChem*, vol. 10, no. 15, pp. 2577–2591, 2009.
- [77] N. Kurokawa, H. Yoshikawa, N. Hirota, K. Hyodo, and H. Masuhara, “Size-dependent spectroscopic properties and thermochromic behavior in poly(substituted thiophene) nanoparticles,” *ChemPhysChem*, vol. 5, no. 10, pp. 1609–1615, 2004.
- [78] S. Nizamoglu, T. Erdem, X. Wei Sun, and H. Volkan Demir, “Warm-white light-emitting diodes integrated with colloidal quantum dots for high luminous efficacy and color rendering: reply to comment,” *Opt. Lett.*, vol. 36, no. 15, pp. 3372–3374, Aug. 2011.
- [79] T. J. Sappala, “Samsung’s high-end TVs use nanocrystals for better color, efficiency,” 2015. [Online]. Available: <http://www.engadget.com/2015/01/05/ces2015-samsung-suhd/>. [Accessed: 11-Dec-2015].
- [80] G. Morrison, “What is Samsung’s SUHD?,” *CNet*, 2015. [Online]. Available: <http://www.cnet.com/news/what-is-samsung-suhd/>. [Accessed: 16-Feb-2016].
- [81] J. Condliffe, “Sony’s New Triluminous TVs Will Be Powered by Quantum Physics,” *Gizmodo*, 2013. [Online]. Available: <http://gizmodo.com/5976341/sonys-new-triluminous-tvs-will-be-powered-by-quantum-physics>. [Accessed: 16-Feb-2016].
- [82] Nanosys, “Welcome to a revolution in color.” [Online]. Available: <http://www.nanosysinc.com/lcd-revolution/>. [Accessed: 11-Dec-2015].
- [83] T. Otto, M. Müller, P. Mundra, V. Lesnyak, H. V. Demir, N. Gaponik, and A. Eychmüller, “Colloidal nanocrystals embedded in macrocrystals: Robustness, photostability, and color purity,” *Nano Lett.*, vol. 12, no. 10, pp. 5348–5354, 2012.
- [84] T. Erdem, Z. Soran-Erdem, P. L. Hernandez-Martinez, V. K. Sharma, H. Akcali, I. Akcali, N. Gaponik, A. Eychmüller, and H. V. Demir, “Sweet

- plasmonics: Sucrose macrocrystals of metal nanoparticles,” *Nano Res.*, vol. 8, no. 3, pp. 860–869, Mar. 2015.
- [85] T. Erdem, Z. Soran-Erdem, Y. Kelestemur, N. Gaponik, and H. V. Demir, “Excitonic improvement of colloidal nanocrystals in salt powder matrix for quality lighting and color enrichment,” *Opt. Express*, vol. 24, no. 2, p. A74, 2016.
- [86] Z. Soran-Erdem, T. Erdem, P. L. Hernandez-Martinez, M. Z. Akgul, N. Gaponik, and H. V. Demir, “Macrocrystals of Colloidal Quantum Dots in Anthracene: Exciton Transfer and Polarized Emission,” *J. Phys. Chem. Lett.*, vol. 6, no. 9, pp. 1767–1772, 2015.
- [87] M. Adam, T. Erdem, G. M. Stachowski, Z. Soran-Erdem, J. F. L. Lox, C. Bauer, J. Poppe, H. V. Demir, N. Gaponik, and A. Eychmüller, “Implementation of High-Quality Warm-White Light-Emitting Diodes by a Model-Experimental Feedback Approach Using Quantum Dot–Salt Mixed Crystals,” *ACS Appl. Mater. Interfaces*, vol. 7, no. 41, pp. 23364–23371, Oct. 2015.
- [88] T. Erdem, Z. Soran-Erdem, V. K. Sharma, Y. Kelestemur, M. Adam, N. Gaponik, and H. V. Demir, “Stable and efficient colour enrichment powders of nonpolar nanocrystals in LiCl,” *Nanoscale*, vol. 7, no. 42, pp. 17611–17616, 2015.
- [89] S. Kalytchuk, O. Zhovtiuk, S. V. Kershaw, R. Zbořil, and A. L. Rogach, “Temperature-Dependent Exciton and Trap-Related Photoluminescence of CdTe Quantum Dots Embedded in a NaCl Matrix: Implication in Thermometry,” *Small*, vol. 12, no. 4, pp. 466–476, 2016.
- [90] M. Müller, M. Kaiser, G. M. Stachowski, U. Resch-Genger, N. Gaponik, and A. Eychmüller, “Photoluminescence quantum yield and matrix-induced luminescence enhancement of colloidal quantum dots embedded in ionic crystals,” *Chem. Mater.*, vol. 26, no. 10, pp. 3231–3237, 2014.
- [91] M. Adam, Z. Wang, A. Dubavik, G. M. Stachowski, C. Meerbach, Z. Soran-Erdem, C. Rengers, H. V. Demir, N. Gaponik, and A. Eychmüller, “Liquid-Liquid Diffusion-Assisted Crystallization: A Fast and Versatile Approach Toward High Quality Mixed Quantum Dot-Salt Crystals,” *Adv. Funct. Mater.*, vol. 25, no. 18, pp. 2638–2645, May 2015.

- [92] H. J. Meyer, “Kristallisation,” *Meyers Großes Konversations-Lexikon*, no. Bd. 16. Bibliographisches Institut, p. 1, 1909.
- [93] M. Adam, R. Tietze, N. Gaponik, and A. Eychmüller, “QD-Salt Mixed Crystals: the Influence of Salt-Type, Free-Stabilizer, and pH,” *Zeitschrift für Phys. Chemie*, vol. 229, no. 1–2, pp. 109–118, Jan. 2015.
- [94] D. L. Dexter, “A Theory of Sensitized Luminescence in Solids,” *J. Chem. Phys.*, vol. 21, no. 5, pp. 836–850, 1953.
- [95] B. Guzelturk, P. L. Hernandez-Martinez, Q. Zhang, Q. Xiong, H. Sun, X. W. Sun, A. O. Govorov, and H. V. Demir, “Excitonics of semiconductor quantum dots and wires for lighting and displays,” *Laser Photonics Rev.*, vol. 8, no. 1, pp. 73–93, 2014.
- [96] T. Förster, “Experimentelle und theoretische Untersuchung des zwischenmolekularen Übergangs von Elektronenanregungsenergie,” *Zeitschrift für Naturforsch. - Sect. A J. Phys. Sci.*, vol. 4, no. 5, pp. 321–327, 1949.
- [97] J. R. Lakowicz, *Principles of fluorescence spectroscopy*. 2006.
- [98] R. M. Clegg, “Fluorescence resonance energy transfer,” *Curr. Opin. Biotechnol.*, vol. 6, no. 1, pp. 103–110, 1995.
- [99] P. L. Hernandez-Martinez, A. O. Govorov, and H. V. Demir, “Generalized theory of Förster-type nonradiative energy transfer in nanostructures with mixed dimensionality,” *J. Phys. Chem. C*, vol. 117, no. 19, pp. 10203–10212, 2013.
- [100] T. Erdem, V. Ibrahimova, D. Jeon, and I. Lee, “Morphology-Dependent Energy Transfer of Polyfluorene,” *J. Phys. Chem. C Physical Chem.*, vol. 117, pp. 18613–18619, 2013.
- [101] S. A. Maier, *Plasmonics: Fundamentals and applications*. Springer-Verlag, 2007.
- [102] H. A. Atwater and A. Polman, “Plasmonics for improved photovoltaic devices,” *Nat. Mater.*, vol. 9, no. 10, pp. 865–865, 2010.
- [103] A. Brolo, “Plasmonics for future biosensors,” *Nat. Photonics*, vol. 6, no.

November, pp. 709–713, 2012.

- [104] Kern, “Perspective on plasmonics,” *Nat. Photonics*, vol. 6, no. 11, pp. 714–715, 2012.
- [105] J. D. Jackson, *Classical Electrodynamics*, 3rd ed. 1999.
- [106] C. F. Bohren and D. R. Huffman, *Absorption and scattering of light by small particles*, vol. 98. 1983.
- [107] A. O. Govorov, G. W. Bryant, W. Zhang, T. Skeini, J. Lee, N. A. Kotov, J. M. Slocik, and R. R. Naik, “Exciton-plasmon interaction and hybrid excitons in semiconductor-metal nanoparticle assemblies,” *Nano Lett.*, vol. 6, no. 5, pp. 984–994, 2006.
- [108] M. Figueiro, “An Overview of the Effects of Light on Human Circadian Rhythms: Implications for New Light Sources and Lighting Systems Design,” *J. Light Vis. Environ.*, vol. 37, no. 2, pp. 51–61, 2013.
- [109] J. S. Terman, M. Terman, E. S. Lo, and T. B. Cooper, “Circadian time of morning light administration and therapeutic response in winter depression.,” *Arch. Gen. Psychiatry*, vol. 58, no. 1, pp. 69–75, 2001.
- [110] M. G. Figueiro, M. S. Rea, P. Boyce, R. White, and K. Kolberg, “The effects of bright light on day and night shift nurses’ performance and well-being in the NICU,” *Intensive Care*, vol. 14, no. 1, pp. 29–33, 2001.
- [111] R. R. Auger, H. J. Burgess, R. a. Dierkhising, R. G. Sharma, and N. L. Slocumb, “Light Exposure Among Adolescents With Delayed Sleep Phase Disorder: A Prospective Cohort Study,” *Chronobiol. Int.*, vol. 28, no. 10, pp. 911–920, 2011.
- [112] A. Wilhelmsen-Langeland, I. W. Saxvig, S. Pallesen, I.-H. Nordhus, Ø. Vedaa, A. J. Lundervold, and B. Bjorvatn, “A randomized controlled trial with bright light and melatonin for the treatment of delayed sleep phase disorder: effects on subjective and objective sleepiness and cognitive function.,” *J. Biol. Rhythms*, vol. 28, no. 72, pp. 306–21, 2013.
- [113] R. G. Stevens and S. Davis, “The melatonin hypothesis: Electric power and breast cancer,” *Environmental Health Perspectives*, vol. 104, no. SUPPL. 1. pp. 135–140, 1996.

- [114] N. F. Ruby, T. J. Brennan, X. Xie, V. Cao, P. Franken, H. C. Heller, and B. F. O'Hara, "Role of melanopsin in circadian responses to light," *Science (80-.)*, vol. 298, no. 5601, pp. 2211–2213, 2002.
- [115] B. Thomas-Aguilar, "Screen Fiends | Infographic Reveals Shocking Truths on Technology Usage and Screen Time." [Online]. Available: <http://blog.pgi.com/2013/10/screen-fiends-infographic-reveals-shocking-truths-technology-usage-screen-time/>. [Accessed: 03-Jun-2010].
- [116] M. G. Figueiro, B. Wood, B. Plitnick, and M. S. Rea, "The impact of light from computer monitors on melatonin levels in college students," *Neuroendocrinol. Lett.*, vol. 32, no. 2, pp. 158–163, 2011.
- [117] B. Wood, M. S. Rea, B. Plitnick, and M. G. Figueiro, "Light level and duration of exposure determine the impact of self-luminous tablets on melatonin suppression," *Appl. Ergon.*, vol. 44, no. 2, pp. 237–240, 2013.
- [118] C. Cajochen, S. Frey, D. Anders, J. Späti, M. Bues, A. Pross, R. Mager, A. Wirz-Justice, and O. Stefani, "Evening exposure to a light-emitting diodes (LED)-backlit computer screen affects circadian physiology and cognitive performance," *J. Appl. Physiol.*, vol. 110, no. 5, pp. 1432–1438, 2011.
- [119] "F.lux." [Online]. Available: <https://justgetflux.com/>. [Accessed: 03-Jun-2016].
- [120] "RedShift." [Online]. Available: <http://jonls.dk/redshift/>. [Accessed: 03-Jun-2010].
- [121] S. Nizamoglu, T. Erdem, X. Wei Sun, and H. Volkan Demir, "Warm-white light-emitting diodes integrated with colloidal quantum dots for high luminous efficacy and color rendering: reply to comment," *Opt. Lett.*, vol. 36, no. 15, p. 2852, Jul. 2011.
- [122] E. Jang, S. Jun, H. Jang, J. Lim, B. Kim, and Y. Kim, "White-light-emitting diodes with quantum dot color converters for display backlights," *Adv. Mater.*, vol. 22, no. 28, pp. 3076–3080, 2010.
- [123] Lumileds, "Luxeon DCC for LCD backlighting," 2005.
- [124] C. Uran, T. Erdem, B. Guzelturk, N. K. Perkgöz, S. Jun, E. Jang, and H.

- V. Demir, “Highly polarized light emission by isotropic quantum dots integrated with magnetically aligned segmented nanowires,” *Appl. Phys. Lett.*, vol. 105, no. 14, p. 141116, 2014.
- [125] S. Lal, S. Link, and N. J. Halas, “Nano-optics from sensing to waveguiding,” *Nat. Photonics*, vol. 1, no. 11, pp. 641–648, 2007.
- [126] R. Oldenbourg, “A new view on polarization microscopy,” *Nature*, vol. 381, no. 6585, pp. 811–812, Jun. 1996.
- [127] C. Weder, “Incorporation of Photoluminescent Polarizers into Liquid Crystal Displays,” *Science (80-.)*, vol. 279, no. 5352, pp. 835–837, 1998.
- [128] H. R. Gwon and S. H. Lee, “Spectral and Angular Responses of Surface Plasmon Resonance Based on the Kretschmann Prism Configuration,” *Mater. Trans.*, vol. 51, no. 6, pp. 1150–1155, 2010.
- [129] K. Bourzac, “Energy harvesting displays.” [Online]. Available: <https://www.technologyreview.com/s/425024/energy-harvesting-displays/>. [Accessed: 05-Jun-2016].
- [130] E. Optics, “Ultra broadband Wire-Grid Polarizers.” [Online]. Available: <http://www.edmundoptics.com/optics/polarizers/wire-grid-polarizers/>. [Accessed: 05-Jun-2016].
- [131] J. J. Wang, W. Zhang, X. Deng, J. Deng, F. Liu, P. Sciortino, and L. Chen, *High-performance nanowire-grid polarizers.*, vol. 30, no. 2. 2005.
- [132] S. Saraf, R. L. Byer, and P. J. King, “High-extinction-ratio resonant cavity polarizer for quantum-optics measurements.,” *Appl. Opt.*, vol. 46, no. 18, pp. 3850–3855, 2007.
- [133] T. Ozel, S. Nizamoglu, M. A. Sefunc, O. Samarskaya, I. O. Ozel, E. Mutlugun, V. Lesnyak, N. Gaponik, A. Eychmuller, S. V. Gaponenko, and H. V. Demir, “Anisotropic emission from multilayered plasmon resonator nanocomposites of isotropic semiconductor quantum dots,” *ACS Nano*, vol. 5, no. 2, pp. 1328–1334, 2011.
- [134] S.-T. Wu, U. Efron, and L. D. Hess, “Birefringence measurements of liquid crystals,” *Appl. Opt.*, vol. 23, pp. 3911–3915, 1984.

- [135] L. Zhang, J. Teng, S. J. Chua, and E. A. Fitzgerald, “Design and fabrication of subwavelength nanogratings based light-emitting diodes,” *Appl. Phys. A*, vol. 103, no. 3, pp. 827–830, 2011.
- [136] M. Ma, D. S. Meyaard, Q. Shan, J. Cho, E. F. Schubert, G. B. Kim, M.-H. Kim, and C. Sone, “Polarized light emission from GaInN light-emitting diodes embedded with subwavelength aluminum wire-grid polarizers,” *Appl. Phys. Lett.*, vol. 101, no. 6, p. 061103, 2012.
- [137] J. Feng, Y. Zhao, X.-W. Lin, W. Hu, F. Xu, and Y.-Q. Lu, “A transfective nano-wire grid polarizer based fiber-optic sensor,” *Sensors (Basel)*, vol. 11, no. 3, pp. 2488–95, Jan. 2011.
- [138] B. Schnabel, E.-B. Kley, and F. Wyrowski, “Study on polarizing visible light by subwavelength-period metal-stripe gratings,” *Opt. Eng.*, vol. 38, no. 2, p. 220, 1999.
- [139] J. J. Wang, L. Chen, X. Liu, P. Sciortino, F. Liu, F. Walters, and X. Deng, “30-nm-wide aluminum nanowire grid for ultrahigh contrast and transmittance polarizers made by UV-nanoimprint lithography,” *Appl. Phys. Lett.*, vol. 89, no. 14, p. 141105, 2006.
- [140] D. Whang, S. Jin, Y. Wu, and C. M. Lieber, “Large-scale hierarchical organization of nanowire arrays for integrated nanosystems,” *Nano Lett.*, vol. 3, no. 9, pp. 1255–1259, 2003.
- [141] C. Uran, E. Unal, R. Kizil, and H. V. Demir, “On-chip integrated nanowire devices with controllable nanogap for manipulation, capturing, and electrical characterization of nanoparticles,” in *Conference Proceedings - Lasers and Electro-Optics Society Annual Meeting-LEOS*, 2009, pp. 217–218.
- [142] J. J. Boote and S. D. Evans, “Dielectrophoretic manipulation and electrical characterization of gold nanowires,” *Nanotechnology*, vol. 16, no. 9, pp. 1500–1505, 2005.
- [143] C. M. Hangarter, Y. Rheem, B. Yoo, E.-H. Yang, and N. V. Myung, “Hierarchical magnetic assembly of nanowires,” *Nanotechnology*, vol. 18, no. 205305, p. 7, 2007.
- [144] M. G. Bellino, E. J. Calvo, and G. J. Gordillo, “Nanowire manipulation

on surfaces through electrostatic self-assembly and magnetic interactions,” *Phys. Status Solidi - Rapid Res. Lett.*, vol. 3, no. 1, pp. 1–3, 2009.

- [145] H. Weller, U. Koch, M. Gutiérrez, and A. Henglein, “Photochemistry of Colloidal Metal Sulfides. 7. Absorption and Fluorescence of Extremely Small ZnS Particles (The World of the Neglected Dimensions),” *Berichte der Bunsengesellschaft für Phys. Chemie*, vol. 88, no. 7, p. 649, Jul. 1984.
- [146] M. L. Steigerwald, A. P. Alivisatos, J. M. Gibson, T. D. Harris, R. Kortan, A. J. Muller, A. M. Thayer, T. M. Duncan, D. C. Douglass, and L. E. Brus, “Surface Derivatization and Isolation of Semiconductor Cluster Molecules,” *J. Am. Chem. Soc.*, vol. 110, no. 10, p. 3046, May 1988.
- [147] L. E. Brus, “Electron–electron and electron-hole interactions in small semiconductor crystallites: The size dependence of the lowest excited electronic state,” *J. Chem. Phys.*, vol. 80, no. 9, pp. 4403–4409, 1984.
- [148] M. Achermann, M. A. Petruska, D. D. Koleske, M. H. Crawford, and V. I. Klimov, “Nanocrystal-based light-emitting diodes utilizing high-efficiency nonradiative energy transfer for color conversion.,” *Nano Lett.*, vol. 6, no. 7, p. 1396, Jul. 2006.
- [149] C. Sun, Y. Zhang, Y. Wang, W. Liu, S. Kalytchuk, S. V. Kershaw, T. Zhang, X. Zhang, J. Zhao, W. W. Yu, and A. L. Rogach, “High color rendering index white light emitting diodes fabricated from a combination of carbon dots and zinc copper indium sulfide quantum dots,” *Appl. Phys. Lett.*, vol. 104, no. 26, p. 261106, Jun. 2014.
- [150] “QD Vision.” .
- [151] A. L. Rogach, N. Gaponik, J. M. Lupton, C. Bertoni, D. E. Gallardo, S. Dunn, N. Li Pira, M. Paderi, P. Repetto, S. G. Romanov, C. O’Dwyer, C. M. Sotomayor Torres, and A. Eychmüller, “Light-emitting diodes with semiconductor nanocrystals,” *Angew. Chem. Int. Ed. Engl.*, vol. 47, no. 35, p. 6538, Jan. 2008.
- [152] P. O. Anikeeva, J. E. Halpert, M. G. Bawendi, and V. Bulović, “Quantum dot light-emitting devices with electroluminescence tunable over the entire visible spectrum,” *Nano Lett.*, vol. 9, no. 7, pp. 2532–2536, 2009.

- [153] B. N. Pal, Y. Ghosh, S. Brovelli, R. Laocharoensuk, V. I. Klimov, J. A. Hollingsworth, and H. Htoon, “‘Giant’ CdSe/CdS core/shell nanocrystal quantum dots as efficient electroluminescent materials: strong influence of shell thickness on light-emitting diode performance.,” *Nano Lett.*, vol. 12, no. 1, p. 331, Jan. 2012.
- [154] M. Müller, M. Kaiser, G. M. Stachowski, U. Resch-Genger, N. Gaponik, and A. Eychmüller, “Photoluminescence quantum yield and matrix-induced luminescence enhancement of colloidal quantum dots embedded in ionic crystals,” *Chem. Mater.*, vol. 26, no. 10, pp. 3231–3237, 2014.
- [155] S. Kalytchuk, O. Zhovtiuk, and A. L. Rogach, “Sodium chloride protected CdTe quantum dot based solid-state luminophores with high color quality and fluorescence efficiency,” *Appl. Phys. Lett.*, vol. 103, no. 10, p. 103105, 2013.
- [156] T. H. Kim, F. Wang, P. McCormick, L. Wang, C. Brown, and Q. Li, “Salt-embedded carbon nanodots as a UV and thermal stable fluorophore for light-emitting diodes,” *J. Lumin.*, vol. 154, p. 1, Oct. 2014.
- [157] W. K. Bae, J. Kwak, J. Lim, D. Lee, M. K. Nam, K. Char, C. Lee, and S. Lee, “Multicolored Light-Emitting Diodes Based on All-Quantum-Dot Multilayer Films Using Layer-by-Layer Assembly Method,” *Nano Lett.*, vol. 10, no. 7, pp. 2368–2373, Jul. 2010.
- [158] S. Tamang, G. Beaune, I. Texier, and P. Reiss, “Aqueous Phase Transfer of InP/ZnS Nanocrystals Conserving Fluorescence and High Colloidal Stability,” *ACS Nano*, vol. 5, no. 12, pp. 9392–9402, Dec. 2011.
- [159] C. Würth, M. Grabolle, J. Pauli, M. Spieles, and U. Resch-Genger, “Relative and absolute determination of fluorescence quantum yields of transparent samples.,” *Nat. Protoc.*, vol. 8, no. 8, p. 1535, Aug. 2013.
- [160] J. Wang, “Stripping analysis at bismuth electrodes: A review,” *Electroanalysis*, vol. 17, p. 1341, 2005.
- [161] C. Prior and G. S. Walker, “The use of the bismuth film electrode for the anodic stripping voltammetric determination of tin,” *Electroanalysis*, vol. 18, p. 823, 2006.
- [162] *Commission delegated directive amending, for the purposes of adapting to*

technical progress, Annex III to Directive 2011/65/EU of the European Parliament and of the Council as regards an exemption for cadmium in illumination and display lighting. European Union, 2014.

- [163] V. V. Breus, C. D. Heyes, and G. U. Nienhaus, “Quenching of CdSe-ZnS Core-Shell Quantum Dot Luminescence by Water-Soluble Thiolated Ligands,” *J. Phys. Chem. C*, vol. 111, no. 50, p. 18589, Dec. 2007.
- [164] D. R. Lide, *Handbook of Chemistry and Physics*, 89th ed. Taylor & Francis Group, 2008, 2008.
- [165] P. D. Wadhavane, R. E. Galian, M. A. Izquierdo, J. Aguilera-Sigalat, F. Galindo, L. Schmidt, M. I. Burguete, J. Pérez-Prieto, and S. V Luis, “Photoluminescence enhancement of CdSe quantum dots: a case of organogel-nanoparticle symbiosis,” *J. Am. Chem. Soc.*, vol. 134, no. 50, p. 20554, Dec. 2012.
- [166] J. R. Lakowicz, *Principles of Fluorescence Spectroscopy*, 3rd ed. Springer, 2009.
- [167] “American National Standard for electric lamps – Specifications for the chromaticity of solid state lighting products.” American National Standards Institute, 2011.
- [168] S. Nie, “Probing Single Molecules and Single Nanoparticles by Surface-Enhanced Raman Scattering,” *Science (80-.)*, vol. 275, no. February, pp. 1102–1106, 1997.
- [169] M. Pelton, J. Aizpurua, and G. Bryant, “Metal-nanoparticle plasmonics,” *Laser and Photonics Reviews*, vol. 2, no. 3. pp. 136–159, 2008.
- [170] V. V Temnov, “Ultrafast acousto-magneto-plasmonics,” *Nat. Photonics*, vol. 6, no. OCTOBER, pp. 728–736, 2012.
- [171] T. Ozel, P. L. Hernandez-Martinez, E. Mutlugun, O. Akin, S. Nizamoglu, I. O. Ozel, Q. Zhang, Q. Xiong, and H. V. Demir, “Observation of selective plasmon-exciton coupling in nonradiative energy transfer: Donor-selective versus acceptor-selective plexcitons,” *Nano Lett.*, vol. 13, no. 7, pp. 3065–3072, 2013.
- [172] M. Xiao, R. Jiang, F. Wang, C. Fang, J. Wang, and J. C. Yu, “Plasmon-

- enhanced chemical reactions,” *J. Mater. Chem. A*, vol. 1, no. 19, pp. 5790–5805, 2013.
- [173] A. D. Boardman and A. V. Zayats, “Nonlinear plasmonics,” *Handb. Surf. Sci.*, vol. 4, pp. 329–347, 2014.
- [174] M. Durach, A. Rusina, M. I. Stockman, and K. Nelson, “Toward full spatiotemporal control on the nanoscale,” *Nano Lett.*, vol. 7, no. 10, pp. 3145–3149, 2007.
- [175] M. Israelowitz, J. Amey, T. Cong, and R. Sureshkumar, “Spin coated plasmonic nanoparticle interfaces for photocurrent enhancement in thin film si solar cells,” *J. Nanomater.*, vol. 2014, 2014.
- [176] Y. Kim, R. C. Johnson, and J. T. Hupp, “Gold Nanoparticle-Based Sensing of ‘Spectroscopically Silent’ Heavy Metal Ions,” *Nano Lett.*, vol. 1, no. 4, pp. 165–167, 2001.
- [177] Y. Teng, K. Ueno, X. Shi, D. Aoyo, J. Qiu, and H. Misawa, “Surface plasmon-enhanced molecular fluorescence induced by gold nanostructures,” *Ann. Phys.*, vol. 524, no. 11, pp. 733–740, 2012.
- [178] W. W. Yu, L. Qu, W. Guo, and X. Peng, “Experimental determination of the extinction coefficient of CdTe, CdSe, and CdS nanocrystals,” *Chem. Mater.*, vol. 15, no. 14, pp. 2854–2860, 2003.
- [179] G. Frens, “Controlled Nucleation for the Regulation of the Particle Size in Monodisperse Gold Suspensions,” *Nat. Phys. Sci.*, vol. 241, no. 105, pp. 20–22, Jan. 1973.
- [180] W. Haiss, N. T. K. Thanh, J. Aveyard, and D. G. Fernig, “Determination of size and concentration of gold nanoparticles from UV-Vis spectra,” *Anal. Chem.*, vol. 79, no. 11, pp. 4215–4221, 2007.
- [181] A. Glauert, “Epoxy resins: an update on their selection and use,” *Microsc. Anal.*, no. September, pp. 15–20, 1991.
- [182] N. Albon, “The observation of growth steps on sucrose crystals,” *Acta Cryst.*, vol. 12, pp. 219–221, 1959.
- [183] S. Kalytchuk, O. Zhovtiuk, and A. L. Rogach, “Sodium chloride protected

- CdTe quantum dot based solid-state luminophores with high color quality and fluorescence efficiency,” *Appl. Phys. Lett.*, vol. 103, no. 10, pp. 103105–4, 2013.
- [184] “Nanocrystals in their prime,” *Nat Nano*, vol. 9, no. 5, p. 325, May 2014.
- [185] X. Michalet, F. F. Pinaud, L. A. Bentolila, J. M. Tsay, S. Doose, J. J. Li, G. Sundaresan, A. M. Wu, S. S. Gambhir, and S. Weiss, “Quantum Dots for Live Cells, in Vivo Imaging, and Diagnostics,” *Science (80-.)*, vol. 307, no. 5709, p. 538, 2005.
- [186] C. Dang, J. Lee, C. Breen, J. S. Steckel, S. Coe-Sullivan, and A. Nurmikko, “Red, green and blue lasing enabled by single-exciton gain in colloidal quantum dot films,” *Nat. Nanotechnol.*, vol. 7, no. 5, pp. 335–339, 2012.
- [187] B. Guzelturk, Y. Kelestemur, M. Z. Akgul, V. K. Sharma, and H. V. Demir, “Ultralow threshold one-photon- and two-photon-pumped optical gain media of blue-emitting colloidal quantum dot films,” *J. Phys. Chem. Lett.*, vol. 5, no. 13, pp. 2214–2218, 2014.
- [188] B. Guzelturk, Y. Kelestemur, K. Gungor, A. Yeltik, M. Z. Akgul, Y. Wang, R. Chen, C. Dang, H. Sun, and H. V. Demir, “Stable and Low-Threshold Optical Gain in CdSe/CdS Quantum Dots: An All-Colloidal Frequency Up-Converted Laser,” *Adv. Mater.*, vol. 27, no. 17, pp. 2741–2746, 2015.
- [189] S. Jun, J. Lee, and E. Jang, “Highly luminescent and photostable quantum dot-silica monolith and its application to light-emitting diodes,” *ACS Nano*, vol. 7, no. 2, pp. 1472–1477, 2013.
- [190] J. C. de Mello, H. F. Wittmann, and R. H. Friend, “An improved experimental determination of external photoluminescence quantum efficiency,” *Adv. Mater.*, vol. 9, no. 3, pp. 230–232, 1997.
- [191] K. H. Ibnaouf, S. Prasad, M. S. Al Salhi, A. Hamdan, M. B. Zaman, and L. El Mir, “Influence of the solvent environments on the spectral features of CdSe quantum dots with and without ZnS shell,” *J. Lumin.*, vol. 149, pp. 369–373, 2014.
- [192] G. Nienhuis and C. T. J. Alkemade, “Atomic radiative transition

- probabilities in a continuous medium,” *Phys. B+C*, vol. 81, no. 1, pp. 181–188, 1976.
- [193] R. J. Glauber and M. Lewenstein, “Quantum optics of dielectric media,” *Phys. Rev. A*, vol. 43, no. 1, pp. 467–491, 1991.
- [194] J. Knoester and S. Mukamel, “Intermolecular forces, spontaneous emission, and superradiance in a dielectric medium: Polariton-mediated interactions,” *Phys. Rev. A*, vol. 40, no. 12, pp. 7065–7080, 1989.
- [195] M. Crenshaw and C. Bowden, “Effects of local fields on spontaneous emission in dielectric media,” *Phys. Rev. Lett.*, vol. 85, pp. 1851–4, 2000.
- [196] S. F. Wuister, C. de Mello Donega, and A. Meijerink, “Local-field effects on the spontaneous emission rate of CdTe and CdSe quantum dots in dielectric media,” *J. Chem. Phys.*, vol. 121, no. 9, pp. 4310–4315, 2004.
- [197] Z. A. Talib, W. M. Daud, Y. N. Loh, and H. A. A. Sidek, “Optical and electrical characteristics of $(\text{LiCl})_x(\text{P}_2\text{O}_5)_{1-x}$ glass,” *Ionics (Kiel)*, vol. 15, no. 3, pp. 369–376, 2009.
- [198] A. Sarkar and S. Mahapatra, “Novel hydrophobic vaterite particles for oil removal and recovery,” *J. Mater. Chem. A*, vol. 2, no. 11, pp. 3808–3818, 2014.
- [199] P. J. Masset, “Thermogravimetric study of the dehydration reaction of $\text{LiCl} \cdot \text{H}_2\text{O}$,” *J. Therm. Anal. Calorim.*, vol. 96, no. 2, pp. 439–441, 2009.
- [200] J. Y. Kim, O. Voznyy, D. Zhitomirsky, and E. H. Sargent, “Colloidal Quantum Dot Materials and Devices: a Quarter-Century of Advances,” *Adv. Mater.*, vol. 25, no. 36, pp. 4986–5010, 2013.
- [201] T.-H. Kim, K.-S. Cho, E. K. Lee, S. J. Lee, J. Chae, J. W. Kim, D. H. Kim, J.-Y. Kwon, G. Amaratunga, S. Y. Lee, B. L. Choi, Y. Kuk, J. M. Kim, and K. Kim, “transfer printing,” *Nat. Photonics*, vol. 5, no. February, pp. 176–182, 2011.
- [202] V. Sukhovatkin, S. Hinds, L. Brzozowski, and E. H. Sargent, “Colloidal quantum-dot photodetectors exploiting multiexciton generation,” *Science*, vol. 324, no. 5934, pp. 1542–1544, 2009.

- [203] E. H. Sargent, “Colloidal quantum dot solar cells,” *Nat. Photonics*, vol. 6, no. 3, pp. 133–135, 2012.
- [204] P. V. Kamat, “Quantum dot solar cells. Semiconductor nanocrystals as light harvesters,” *J. Phys. Chem. C*, vol. 112, no. 48, pp. 18737–18753, 2008.
- [205] S. Nizamoglu, T. Erdem, X. Wei Sun, and H. Volkan Demir, “Warm-white light-emitting diodes integrated with colloidal quantum dots for high luminous efficacy and color rendering: reply to comment.,” *Opt. Lett.*, vol. 36, no. 15, p. 2852, 2011.
- [206] P. Zhong, G. He, and M. Zhang, “Optimal spectra of white light-emitting diodes using quantum dot nanophosphors,” *Opt. Express*, vol. 20, no. 8, p. 9122, 2012.
- [207] O. Chen, J. Zhao, V. P. Chauhan, J. Cui, C. Wong, D. K. Harris, H. Wei, H.-S. Han, D. Fukumura, R. K. Jain, and M. G. Bawendi, “Compact high-quality CdSe-CdS core-shell nanocrystals with narrow emission linewidths and suppressed blinking.,” *Nat. Mater.*, vol. 12, no. 5, pp. 445–51, 2013.
- [208] R. Koeppe and N. S. Sariciftci, “Photoinduced charge and energy transfer involving fullerene derivatives.,” *Photochem. Photobiol. Sci.*, vol. 5, no. 12, pp. 1122–31, 2006.
- [209] S. Nizamoglu, E. Sari, J. H. Baek, I. H. Lee, and H. V. Demir, “Nonradiative resonance energy transfer directed from colloidal CdSe/ZnS quantum dots to epitaxial InGaN/GaN quantum wells for solar cells,” *Phys. Status Solidi - Rapid Res. Lett.*, vol. 4, no. 7, pp. 178–180, 2010.
- [210] R. Abdul Nur Aida, W. McDaniel, K. Bardou, S. Srinivasan, V. Vickerman, P. T. C. So, and J. H. Moon, “Conjugated Polymer Nanoparticles for Two-Photon Imaging of Endothelial Cells in a Tissue Model.,” *Adv. Mater.*, vol. 21, no. 34, pp. 3492–3496, 2009.
- [211] J. H. Moon, W. McDaniel, P. MacLean, and L. F. Hancock, “Live-cell-permeable poly(p-phenylene ethynylene),” *Angew. Chemie - Int. Ed.*, vol. 46, no. 43, pp. 8223–8225, 2007.
- [212] P. Howes, R. Thorogate, M. Green, S. Jickells, and B. Daniel, “Synthesis,

- characterisation and intracellular imaging of PEG capped BEHP-PPV nanospheres.,” *Chem. Commun.*, no. 18, pp. 2490–2492, 2009.
- [213] C. Wu, B. Bull, K. Christensen, and J. McNeill, “Ratiometric single-nanoparticle oxygen sensors for biological imaging,” *Angew. Chemie - Int. Ed.*, vol. 48, no. 15, pp. 2741–2745, 2009.
- [214] J. H. Moon, P. MacLean, W. McDaniel, and L. F. Hancock, “Conjugated polymer nanoparticles for biochemical protein kinase assay.,” *Chem. Commun.*, no. 46, pp. 4910–4912, 2007.
- [215] T. Piok, S. Gamerith, C. Gadermaier, H. Plank, F. P. P. Wenzl, S. Patil, R. Montenegro, T. Kietzke, D. Neher, U. Scherf, K. Landfester, E. J. W. List, and Others, “Organic Light-Emitting Devices Fabricated from Semiconducting Nanospheres,” *Adv. Mater.*, vol. 15, no. 10, pp. 800–804, 2003.
- [216] T. Kietzke, D. Neher, K. Landfester, R. Montenegro, R. Güntner, and U. Scherf, “Novel approaches to polymer blends based on polymer nanoparticles.,” *Nat. Mater.*, vol. 2, no. 6, pp. 408–12, 2003.
- [217] T. Kietzke, D. Neher, M. Kumke, R. Montenegro, K. Landfester, and U. Scherf, “A nanoparticle approach to control the phase separation in polyfluorene photovoltaic devices,” *Macromolecules*, vol. 37, no. 13, pp. 4882–4890, 2004.
- [218] I. O. Ozel, T. Ozel, H. V. Demir, and D. Tuncel, “Non-radiative resonance energy transfer in bi-polymer nanoparticles of fluorescent conjugated polymers.,” *Opt. Express*, vol. 18, no. 2, pp. 670–84, 2010.
- [219] G. Mauthner, K. Landfester, A. Köck, H. Brückl, M. Kast, C. Stepper, and E. J. W. List, “Inkjet printed surface cell light-emitting devices from a water-based polymer dispersion,” *Org. Electron. physics, Mater. Appl.*, vol. 9, no. 2, pp. 164–170, 2008.
- [220] E. Fisslthaler, S. Sax, U. Scherf, G. Mauthner, E. Moderegger, K. Landfester, and E. J. W. List, “Inkjet printed polymer light-emitting devices fabricated by thermal embedding of semiconducting polymer nanospheres in an inert matrix,” *Appl. Phys. Lett.*, vol. 92, no. 18, 2008.
- [221] E. Fisslthaler, A. Blümel, K. Landfester, U. Scherf, and E. J. W. List,

- “Printing functional nanostructures: a novel route towards nanostructuring of organic electronic devices via soft embossing, inkjet printing and colloidal self assembly of semiconducting polymer nanospheres,” *Soft Matter*, vol. 4, no. 12, p. 2448, 2008.
- [222] I. O. Huyal, T. Ozel, D. Tuncel, and H. V Demir, “Quantum efficiency enhancement in film by making nanoparticles of polyfluorene,” *Opt. Express*, vol. 16, no. 17, pp. 13391–13397, 2008.
- [223] G. R. Hayes, I. D. W. Samuel, and R. T. Phillips, “Exciton dynamics in electroluminescent polymers studied by femtosecond time-resolved photoluminescence spectroscopy,” *Phys. Rev. B*, vol. 52, no. 16, 1995.
- [224] J. I. Basham, G. K. Mor, and C. A. Grimes, “Förster resonance energy transfer in dye-sensitized solar cells,” *ACS Nano*, vol. 4, no. 3, pp. 1253–1258, 2010.
- [225] M. Achermann, M. a Petruska, S. Kos, D. L. Smith, D. D. Koleske, and V. I. Klimov, “Energy-transfer pumping of semiconductor nanocrystals using an epitaxial quantum well,” *Nature*, vol. 429, no. 6992, pp. 642–646, 2004.
- [226] D. Basko, G. C. La Rocca, F. Bassani, and V. M. Agranovich, “Forster energy transfer from a semiconductor quantum well to an organic material overlayer,” *Eur. Phys. J. B - Condens. Matter Complex Syst.*, vol. 8, no. 3, pp. 353–362, 1999.
- [227] S. Chanyawadee, P. G. Lagoudakis, R. T. Harley, M. D. B. Charlton, D. V. Talapin, H. W. Huang, and C. H. Lin, “Increased color-conversion efficiency in hybrid light-emitting diodes utilizing non-radiative energy transfer,” *Adv. Mater.*, vol. 22, no. 5, pp. 602–606, 2010.
- [228] S. Nizamoglu, B. Guzelturk, D. W. Jeon, I. H. Lee, and H. V. Demir, “Efficient nonradiative energy transfer from InGaN/GaN nanopillars to CdSe/ZnS core/shell nanocrystals,” *Appl. Phys. Lett.*, vol. 98, no. 16, 2011.
- [229] V. İbrahimova, S. Ekiz, Ö. Gezici, and D. Tuncel, “Facile synthesis of cross-linked patchy fluorescent conjugated polymer nanoparticles by click reactions,” *Polym. Chem.*, vol. 2, no. 12, p. 2818, 2011.